Novel Techniques for Characterisation and Control of Magnetostriction in G.O.S.S

PhD Thesis

Piotr Klimczyk

A thesis submitted to the Cardiff University in candidature for the degree of Doctor of Philosophy

Wolfson Centre for Magnetics

Cardiff School of Engineering

Cardiff University

Wales, United Kingdom

October 2012

Acknowledgements

This work was carried out at the Wolfson Centre for Magnetics, Cardiff School of Engineering and Cardiff University to which I am grateful for providing the resources needed to complete this project.

Special thanks to my both academic supervisors Professor Anthony Moses and Dr Philip Anderson. I am very grateful for their guidance and encouragement from the beginning to end of my PhD studies. Their supervision and professional expertise improved my work and knowledge significantly.

I wish to thank to Cogent Power Ltd, especially to Dr Martyn Davies, Mr Keith Jenkins and Mr Andrew Nolan for supporting the project and contributing industrial expertise and experience into my research.

Collaboration with my colleague Dr Sakda Somkun also fulfilled this project.

Thanks also to my friends and colleagues from Wolfson Centre for Magnetics for friendly atmosphere and help.

I wish to express my greatest thanks to my father Krzysztof, my mother Elzbieta, my sister Agnieszka, and my brother Grzegorz for their love, support and motivation.

Summary of Thesis

The magnetostriction of the core laminations is one of the primary causes of transformer acoustic noise. The magnetostriction of grain oriented silicon steel is extremely sensitive to compressive stress applied along its rolling direction which increases the magnitude of magnetostriction drastically. A measurement system using piezoelectric accelerometers has been built and optimised for magnetostriction measurements under stress within the range of 10 MPa to -10 MPa. This system was used for characterisation of wide range of samples which were prepared and processed under different thermal and mechanical conditions.

In this study the influence of factors such as strip thickness, coating stress, annealing under tension, cutting stress and rotational magnetisation on the magnetostriction of silicon steel under stress were investigated.

It was observed that the increase of strip thickness leads to the decrease of the magnetostatic energy and therefore a reduction in the volume of closure domains in the stress patterns leading to magnetostriction under stress increasing in proportion with the thickness.

Also a gradual increase in coating weight resulted in an effective increase of tensile stress introduced to the surface of the steel which was evaluated by analysis of the stress shift of the magnetostriction curve.

An investigation of sample cutting techniques showed that the water jet cutting introduced an advantageous tensile stress along the cut edge in the RD of the steel.

Measurement of the pk-pk magnetostriction under rotational magnetisation was shown to be significantly higher than due to uniaxial magnetisation under high compression.

The acquired data was used to develop a new prediction model based on the Boltzmann function capable of evaluating the influence of those factors on magnetostriction in GO steel. The final model was able to accurately describe the effect of all studied aspects being present during the production of the steel and affecting the magnetostriction sensitivity of the final material.

List of Contents

Chapter 1 Introduction

1.1 Introduction

The magnetic cores of power transformers are assembled from laminations of grain oriented, 3% silicon steel. Magnetostriction (linear, rotational and under stress) together with magnetostatic forces (lamination flapping or in plane attraction), and core resonance is commonly considered as one of primary causes of transformer acoustic noise [1].

Increasing numbers of transformer units are being located in urban areas where such noise is of environmental concern. Therefore there is a strong need to obtain a better understanding of magnetostriction in silicon steel and to ultimately reduce it.

The magnetostriction of grain oriented silicon steel was found to be extremely sensitive to compressive stress applied along the rolling direction (RD) or by tensile stress along the transverse (TD) [2]. Regions of compressive stress in RD can be introduced in the core stack during manufacture due to a variety of factors including non-flat laminations, non-uniform clamping stress and the mass of the top yoke. This compressive stress would increase the magnitude of magnetostriction drastically. Therefore it is beneficial to apply a tensile stress in the RD to the electrical steel which can reduce the harmful noise in the core. This creates a need of developing reliable technique for characterisation magnetostriction in grain oriented silicon steel under various stress conditions.

1.2 Objectives

The aim of this research is to characterise and control factors which have an influence on magnetostriction of electrical steel under stress. A magnetostriction measurement system will be developed to measure repeatable magnetostriction under applied stress from 10 MPa to -10 MPa at a magnetisation frequency 50 Hz and flux density 1.0 T, 1.5 T and 1.7 T. The selected flux densities and frequency are the established industrial references to compare and develop the silicon steel materials with different grades at these particular magnetisation conditions. The influence of the

following parameters on magnetostriction under stress will be investigated in order to characterise magnetostriction in grain oriented silicon steel (GOSS):

a) Influence of strip thickness
b) Influence of applied coating stress
c) Influence of annealing under tension
d) Influence of applied cutting stress
e) Influence of rotational magnetisation

These investigations will be carried out on the full range of commercially available and laboratory developed grain oriented silicon steels supplied by Orb Electrical Steels.

Also a prediction model based on the selected factors with the highest impact on the shape of the stress sensitivity curve will be developed and correlated with measurement data. This will aid the development of future low magnetostriction steels since the magnetostriction will be able to be predicted based on a range of physical parameters.

1.3 Reference

[1] R. Girgis, *et al.*, "The sound of silence: Designing and producing silent transformers," *ABB Review*, vol. 2, 2008.

[2] L. J. Dijkstra and U. M. Martius, "Domain patterns in silicon iron under stress," *Reviews of Modern Physics*, vol. 25, pp. 146-150, 1953.

Chapter 2 Grain Oriented Silicon Steel

2.1 Introduction to the Grain Oriented Silicon Steel (GOSS)

The addition of a silicon to high purity steel was first investigated by Hadfield, Barret and Brown in 1902 [1]. A small amount of silicon in low carbon steel prevents aging of the steel and increases the electrical resistivity, which causes reduction in eddy currents. It has been proven by experiments that large single grains of silicon steel have high permeability and low hysteresis loss. Also the magnetic induction varies depending upon the direction in which the crystal is magnetised.

Grain oriented silicon steel (GOSS) was first described by Goss in 1934 [2]. The GOSS texture is characterised by a cubic structure with crystals aligned on their edges with (110) planes along the sheet plane, where the cubes <100> axis are close to the rolling direction of the steel strip. The first grain oriented steel with an average misorientation of 7° to the rolling direction was put into production by Armco Steel Corporation in 1940 and was called conventional grain oriented "CGO" steel. The further development in texture of the GOSS was made by Nippon Steel Company which developed a high permeability silicon steel with an average misorientation of around 3° [3]. This high permeability steel was branded as "HiB" (also called highly grain oriented "HGO") steel.

2.2 The Production Cycle of the CGO and HiB Silicon Steel

2.2.1 Steel Making

Oxygen steelmaking is a method where the molten, rich in carbon, pig-iron is made into steel. When alloying, the concentration levels of carbon, sulphur and nitrogen must be as low as possible to prevent oxidation. Furthermore oxygen is blown through the molten alloy to reduce the carbon content, which would combine with iron to create carbides.

The difficulty with the alloy is that it rapidly ages by the creation of intermetallic particles with a new phase, termed precipitates, at elevated temperatures

[2, 4]. Therefore to avoid aging of the steel a small amount of silicon is added, which also minimises eddy currents induced during ac magnetisation by increasing the resistivity of the steel. In grain oriented electrical steel, silicon reaches 2% to about 4.5% of the alloy [5]. The carbon content in the alloy should not exceed more than 0.003%, to avoid magnetic aging [5].

The difference between CGO and HiB steel is not only the processing of the steel but also the additions to the alloy which have an effect on the grain growth process as shown in Table 2.1.

Table 2.1. Classification of grain oriented steel [6]

<table>
<tr><th>Classification by inhibitor preparation</th><th>Slab reheating temperature</th><th>Main inhibitors</th><th>Final cold rolling reduction</th><th colspan="2">Remarks</th></tr>
<tr><td rowspan="2">Inherent inhibitor method
(Solid solution method, Extra high temperature slab reheating method)</td><td rowspan="2">Extra high (>1300˚C)</td><td>MnS</td><td>Light (50%)</td><td>Armco method</td><td>CGO</td></tr>
<tr><td>MnS, AlN</td><td>Heavy (>85%)</td><td>Nippon Steel method</td><td rowspan="2">HiB</td></tr>
<tr><td>Acquired inhibitor method
(Extra low temperature slab reheating method)</td><td>Extra low (1100 - 1200˚C)</td><td>MnS, AlN (Nitriding)</td><td>Heavy (>85%)</td><td>Nippon Steel method</td></tr>
</table>

CGO utilizes approximately 0.06% by weight of manganese sulphide to inhibit primary grain growth during the high temperature coil annealing process. However HiB steel contains manganese sulphide and aluminium nitride with weights of 0.08% and 0.03%, respectively [7]. The alloy is cast into 250 mm thick ingots and then is reheated up to 1400°C to put the inhibitors in to solution. The AlN enables the secondary recrystalization of the (110)[001] orientation with about 3° of misorientation between the <100> axes and the rolling direction [3]. The strain energy required by the additional inhibitors in HiB means that single stage of heavy cold reduction is utilised.

2.2.2 First Steel Gauge Reduction - Hot Rolling

The cast of the steel with an initial thickness of 250 mm is hot rolled to a gauge of 1.9 mm. Next, by fast quenching to 600˚C the steel is coiled. The hot rolled coil is then exported to the electrical steel works where the strip is side-trimmed and continuously annealed at 950˚C for CGO and 1100˚C for HiB. The surface iron oxide is removed by a wheel abrator using iron shot fired at the strip surfaces. Finally the surface is cleaned with a high pressure wash, followed by a hot dip in an alkaline oil solution. Fig 2.1 shows the example of a hot rolling line.

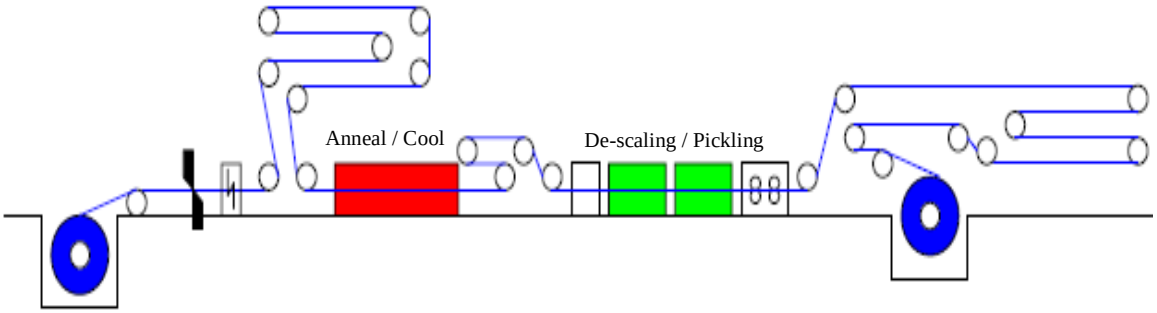

Fig 2.1. Hot rolling line with annealing and de-scaling [6].

2.2.3 Second and Third Steel Gauge Reduction - Cold Rolling

At this stage the gauge reduction due to the cold rolling process is different for CGO and HiB steel as presented in Table 2.2.

Table 2.2 Cold rolling process for CGO and HiB steel

<table>
<tr><th>CGO</th><th>HiB</th></tr>
<tr><td>1. Primary cold rolling – gauge reduction between 0.5 and 0.7 mm</td><td rowspan="3">1. Primary cold rolling - heavy 85 % reduction</td></tr>
<tr><td>2. Intermediate anneal 950˚C</td></tr>
<tr><td>3. Secondary cold rolling – 50 % reduction</td></tr>
<tr><td colspan="2">Final gauge of 0.23 mm to 0.35 mm</td></tr>
</table>

The thickness reduction of the CGO requires primary and secondary cold rolling process. The primary rolling reduces the thickness of the steel to the intermediate gauge

of between 0.5 mm and 0.7 mm by passing the steel for a few times through a reversing mill as shown in Fig 2.2.

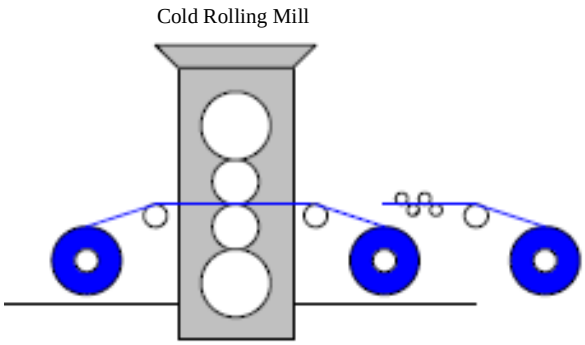

Fig 2.2 Cold rolling reversing mill [6].

The high density of dislocations in well oriented grains and stresses applied by the cold rolling process require secondary recrystallisation, which is procured by an intermediate anneal. Afterwards the CGO steel is secondary cold rolled by two passes through the reversing mill in order to achieve the final gauge of 0.23 to 0.35 mm. However HiB steel in contrast to CGO is cold rolled once. The cold rolling process applies additional energy to the strip which affects the GOSS texture development during the high temperature coil annealing.

2.2.4 Decarburising and First Layer Coat of the Steel

The coil with the final strip gauge is processed through a decarburising line as shown in Fig 2.3.

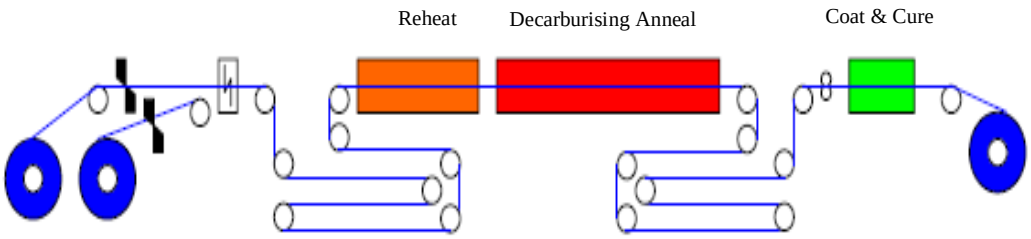

Fig 2.3 Decarburising line with first coating application [6].

An open furnace on the entry of this line burns off a residue of the rolling oil from the strip surface. Subsequently the strip is continuously annealed in an atmosphere of

hydrogen and nitrogen, mixed in the ratio 3:1, at a temperature of around 850˚C in order to remove the relatively high level of carbon in the steel which degrades the magnetic properties. The decarburising annealing causes the recrystallisation of the grains, previously cold rolled, as well as the formation of an oxide layer on the surface of the strip. The oxide reacts with the silicon iron forming the layer of Fayalite (Fe_2SiO_4) on the surface of the strip. At the final part of the decarburising line a slurry coating of magnesium oxide of weight approximately 3 g/m^2 per side is applied to the surface of the steel and cured in the furnace at 850˚C. At this stage of production the steel includes very small grains with a size of approximately 150 microns in diameter. Also the grains have a very low orientation to the rolling direction.

2.2.5 High Temperature Coil Anneal (HTCA)

The coil, previously coated with magnesium oxide is inserted into a furnace for high temperature coil annealing (HTCA). The furnace has 4 inner covers, where each includes 2 sets of coils placed vertically on the separated base plates with a pillar in the middle as shown in Fig 2.4.

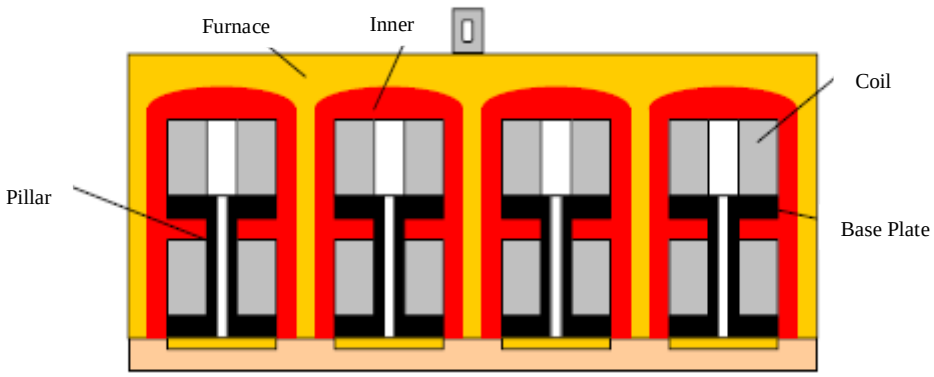

Fig 2.4 High temperature coil annealing chamber [6].

The coils are left in the furnace for five days of continuous annealing in an atmosphere of dry hydrogen. During the annealing all coils are heated to 1200˚C for at least two hours. The primary grain growth, due to the rising temperature, is inhibited by the addition of manganese sulphide to the CGO and manganese sulphide with aluminium nitride to the HiB steel. When the temperature reaches around 900˚C the inhibitors go into solution and the energy stored in the strip from the cold rolling process causes secondary grain growth at the expense of those grains which surround it.

One of the roles of the magnesium oxide coating is to separate the laps to ensure that they do not stick together, especially during the high temperature anneal. Furthermore the magnesium oxide reacts with the Fayalite forming the Forsterite ($2MgO_2SiO_2$) layer. When the steel cools down the top coating consists mostly of the Forsterite layer with elements including manganese, sulphur and oxygen liberated from the steel during the high temperature soak in the hydrogen atmosphere. This coating is also commonly referred to as a "glass film" which works as an insulator between the lamination in a transformer core to prevent the build up of eddy currents [8] and also applies a small amount of tension to the surface of the steel during thermal contraction. Also at the interface between the forsterite coating and the base metal, especially in HiB steel which includes AlN, the MgAl oxide composite spinel ($MgAl_2O_4$) is formed. The spinel occurs in the forsterite coating, mainly in the bottom interface layer between the coating and the steel, and degrades adhesion [9].

2.2.6 Second Coat and Thermal Flattening Process of the Steel

The coil after HTCA is transported to the final part of the production line as shown in Fig 2.5, where at the beginning of the line the strip surface is cleaned by washing and brushing off the excessive magnesium oxide powder.

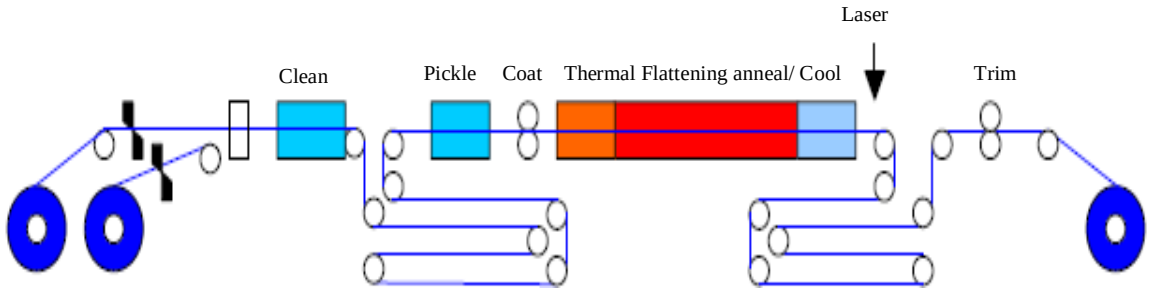

Fig 2.5 Final part of production line [6].

Subsequently the steel with the glass film coating is coated with a slurry phosphate coating of weight approximately 4 g/m^2 per side and then cured at a temperature of approximately 650˚C. This is followed by the thermal flattening process to eliminate curvature in the strip caused by the high temperature coil annealing. The thermal flattening process takes a place in the furnace at approximately 850˚C and in an atmosphere of nitrogen, where the strip is under tension from the drive rolls. The flattening is obtained by four rolls penetrating with a certain depth below the strip pass

line. When the strip is cooled, the differential contraction between strip and coatings increases the tension, initially applied by the glass film which improves magnetic properties. At the end of the line the strip is trimmed and wound into a coil.

2.3 References

[1] W. Barret, *et al.*, "Researches on different alloys of iron," *Journal of the Institute of Electrical Engineers,* vol. 31, p. 674, 1902.

[2] N. Goss, "Electrical sheet and method and apparatus for its manufacture and test," US Patent 1965559, 1934.

[3] S. Taguchi, *et al.*, "Process for production single-oriented silicon steel sheet having a high magnetic induction " US Patent 3287183, 1966.

[4] D. William and D. Callister, "Materials science and engineering," *John Wiley & Sons*, 2007.

[5] J. W. Schoen, *et al.*, "High permeability grain oriented electrical steel," US Patent 7887645 A1, 2011.

[6] M. Cichuta, "Trends and developments in grain oriented steels," *Internal presentation of Cogent Power Ltd.*, 2009.

[7] A. J. Moses, "Electrical steels: past, present and future developments," *IEE Proceedings-Science Measurement and Technology,* vol. 137, pp. 233-245, 1990.

[8] T. Ichida, *et al.*, "Method of forming a forsterite insulating film on the surface of grain-oriented silicon steel sheet," US Patent 4249966, 1981.

[9] Y. Kubo, *et al.*, "Grain-oriented electrical steel sheet excellent in coating adhesion and method of producing the same," US Patent 2010/0055481 A1, 2011.

Chapter 3 Ferromagnetism in Silicon Steel

The term ferromagnetism is used to characterise a material which exhibits spontaneous net magnetisation in the absence of the external magnetic field. Each electron in an atom has an electronic magnetic moment, resulting from two components: an orbital magnetic moment due to orbital momentum, and a spin magnetic moment due to electron spin [1].

The exchange interaction between adjacent magnetic moments has the same source as the exchange interaction of neighbouring electrons in the same atom, which can cause alignment of spins to be parallel or antiparallel [2]. The energy associated with an interaction between adjacent atoms is minimised when all magnetic moments are aligned parallel. The spontaneous magnetisation disappears at temperatures higher than the Curie temperature, below which the material is ferromagnetically ordered.

3.1 Energies of the Ferromagnet

3.1.1 Magnetocrystalline Anisotropy Energy

The term magnetic anisotropy is used when the internal energy depends on the direction of spontaneous magnetisation with respect to the crystallographic axes of the material [3]. The easy magnetisation directions of a single iron crystal are <100> as shown in Fig 3.1 which indicates the direction of the spontaneous domain magnetisation in the demagnetised state [4].

The <110> and <111> are the medium and hard directions, where magnetisation in these directions requires application of a higher magnetic field, than in <100> direction, in order to reach magnetic saturation.

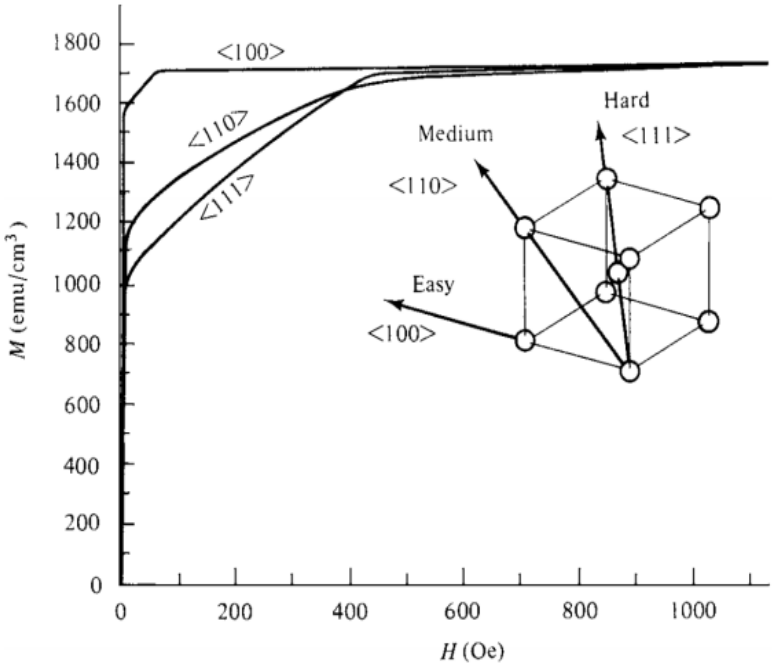

Fig 3.1 Magnetisation along three directions of a single iron crystal (magnetisation of 1 emu/cm3 = 1000 A/m and magnetic field of 1 Oe = 79.58 A/m) [5].

Grain oriented silicon steel has a body centre cubic structure with easy axes along the cube edge. Most of the grains are aligned in a cube on edge orientation close to the rolling direction (RD) which is the direction close to the easy direction <100> [001]. The magnetocrystalline anisotropy energy is minimum when domains are located parallel to the certain crystallographic <100> directions [6]. This dependence which results from spin-orbit interaction can be described by the magnetocrystalline anisotropy energy E_k given by [7]:

$$E_k = K_0 + K_1(\alpha_1^2\alpha_2^2+\alpha_2^2\alpha_3^2+\alpha_3^2\alpha_1^2) + K_2(\alpha_1^2\alpha_2^2\alpha_3^2) \quad (3.1)$$

Where K_0, K_1, K_2 are anisotropy constants and α_1, α_2 and α_3 are the direction cosines of magnetisation with respect to the <100> directions which for the single crystal of grain oriented steel are shown in Fig 3.2. K_0 can be ignored if only a change in the energy E_k, when the magnetisation vector (Ms) rotates from one direction to another, is considered [5].

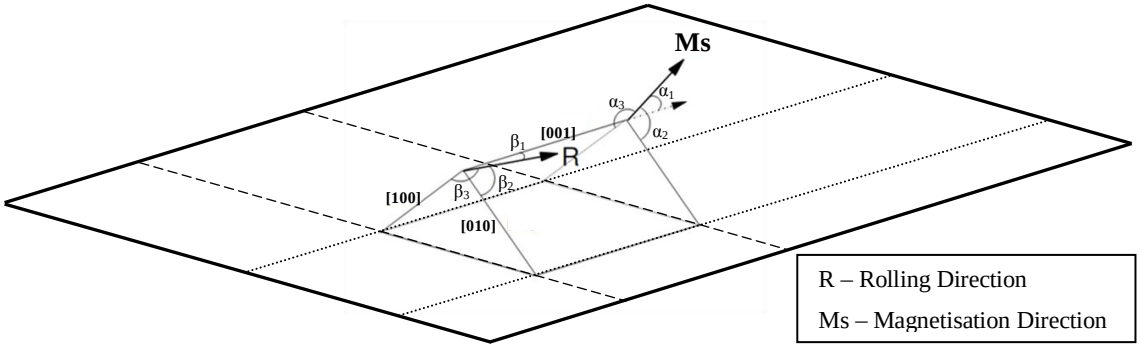

Fig 3.2 Direction cosines (α, β) for the silicon iron crystal.

Table 3.1 gives values of E_k when the Ms is parallel to important directions [uvw].

Table 3.1 Crystal anisotropy energies for various directions in a cube crystal (a, b and c are angles between Ms direction and [uvw] directions) [5]

[u v w]	a	b	c	α_1	α_2	α_3	E_k
[100]	0	90°	90°	1	0	0	K_0
[110]	45°	45°	90°	$1/\sqrt{2}$	$1/\sqrt{2}$	0	$K_0 + K_1/4$
[111]	54.7°	54.7°	54.7°	$1/\sqrt{3}$	$1/\sqrt{3}$	$1/\sqrt{3}$	$K_0 + K_1/3 + K_2/27$

3.1.2 Magnetostatic Energy

If a bulk of ferromagnetic material contains only one domain which is saturated along the [001] axis as shown in Fig 3.3, then the ends of the domains would act as free magnetic poles which would create a large internal magnetic field [7]. Therefore this single domain would become a permanent magnet.

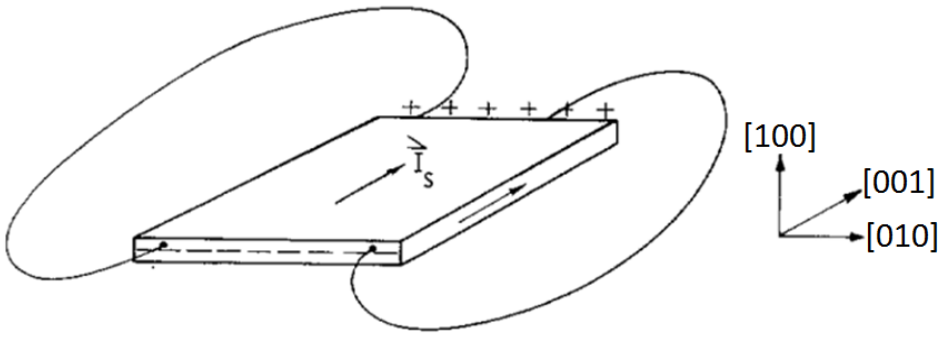

Fig 3.3 Ferromagnetic sheet saturated along the [001] direction with areas of magnetostatic charges [7].

The energy of the domain bulk in its own field is called as magnetostatic energy, which can be expressed as:

$$E_m = \frac{1}{2} N_D M^2 \qquad (3.2)$$

where E_m is the magnetostatic energy, N_D is the demagnetisation factor and M is the magnetisation of the sample. The demagnetisation factor depends on the shape of the sample. For instance, N_D is zero for an infinitely long thin specimen magnetised along its longitudinal axis, whereas it obtain a large value for a thick and short specimen [3].

The magnetostatic energy can be reduced if more domains magnetised in the opposite directions are formed in the crystal (single grain) as shown in Fig 3.4.

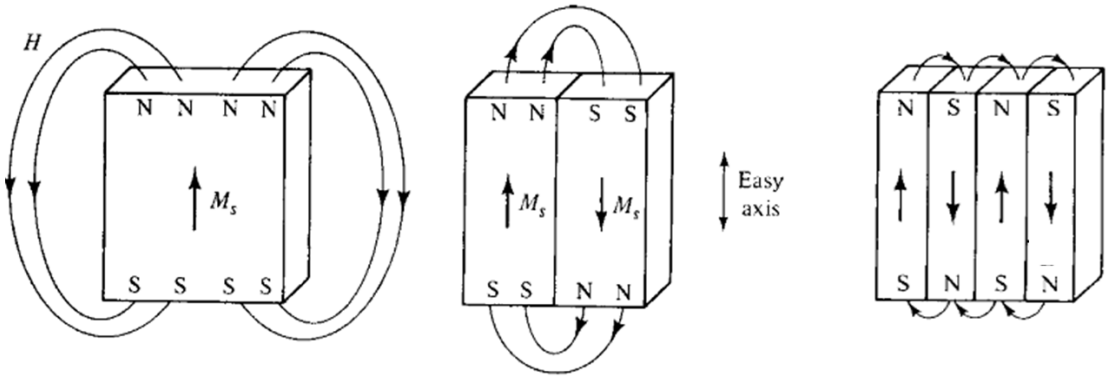

Fig 3.4 Magnetostatic energy reduction by division of a crystal into domains [5].

The spatial extent of the H field is decreased by placing the newly created opposite poles close to each other [5]. The magnetostatic energy can be reduced more, by increasing the number of domains in the grain. The number of domains is limited by the introduction of additional free energy in the domain walls as discussed in the following section.

3.1.3 Domain Wall Energy

A domain wall in a bulk material is the interface between two regions in which the spontaneous magnetisation has different directions as shown in Fig 3.5 [5].

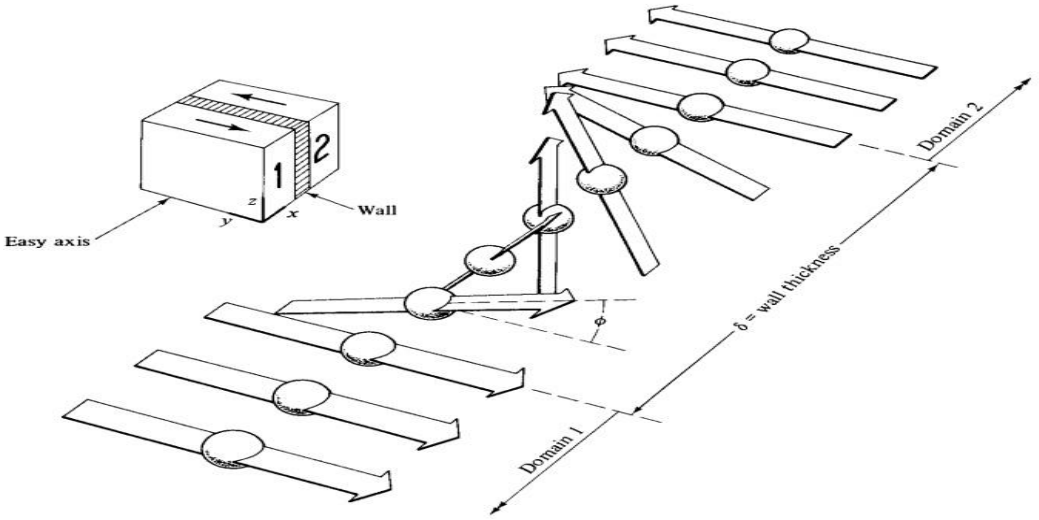

Fig 3.5 Structure of a 180˚ domain wall (bloch wall) in a bulk material [5].

The energy stored in the domain wall due to the neighbouring domains separation is the domain wall energy [3]. The magnetisation in the wall changes the direction from one easy crystallographic direction to another by 180˚ rotation. The ferromagnet has a minimum energy state when adjacent spins (magnetic moments) are parallel due to the exchange energy.

The total domain wall energy is the sum of the anisotropy and exchange energies. Therefore the wall would have a large exchange energy when adjacent moments are aligned antiparallel. If the moments within the wall rotate away from the easy direction the crystal anisotropy energy of the wall increases.

The increasing exchange energy tries to make the domain wall as wide as possible, in order to decrease the angle Ø (shown in Fig 3.5). However the anisotropy energy causes the opposite effect trying to make the wall as thin as possible by decreasing the number of spin, aligned away from the easy directions.

Finally as a result of this competition, the wall has a definite width and structure with a minimum energy state, and this type of wall is referred to as a Bloch wall [5].

3.1.4 Magnetoelastic Energy and Spontaneous Magnetostriction

The atomic moment interactions caused by magnetic anisotropy and magnetisation force, introduce strain to the lattice which introduces magnetoelastic energy [3, 7]. This can be observed when a single magnetic domain with all magnetic moments aligned along an easy direction is heated above the Curie temperature, where the thermal energy agitates the alignment of atoms and the ferromagnetic properties disappear. This is then cooled in order to restore the previous atomic configuration and as a consequence applies the strain to the lattice. This strain is called as the spontaneous magnetostriction. Fig 3.6 shows change in the length (L) of grains of the silicon iron steel above and below the Curie temperature during spontaneous magnetostriction.

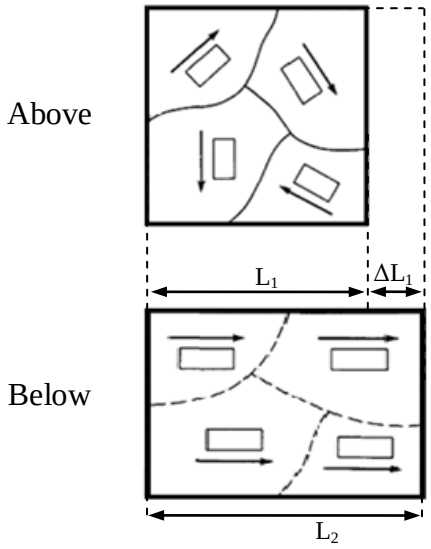

Fig 3.6 Mechanism of spontaneous magnetostriction of silicon steel [5].

The spontaneous magnetostriction along the domain magnetisation direction in a grain is equal to the saturation magnetostriction (λ_s) giving a magnetoelastic energy (E_λ). For an isotropic material, it is given by:

$$E_\lambda = -\frac{3}{2}\lambda_s \sigma sin^2\theta \qquad (3.3)$$

where θ is the angle between the direction of magnetisation and direction of the applied stress, ±σ. The magnetostriction for the silicon steel with the cube on edge orientation (as shown in Fig 3.2) has a strong interaction between the domain orientation and residual or applied stress.

It can be expressed using the Becker Döring equation [8]:

$$\lambda = \frac{3}{2}\lambda_{100}\left(\alpha_1{}^2\beta_1{}^2+\alpha_2{}^2\beta_2{}^2+\alpha_3{}^2\beta_3{}^2-\frac{1}{3}\right) + 3\lambda_{111}\left(\alpha_1\alpha_2\beta_1\beta_2+\alpha_2\alpha_3\beta_2\beta_3+\alpha_3\alpha_1\beta_3\beta_1\right) \quad (3.4)$$

where α_1, α_2 and α_3 are the directions cosines of the magnetisation direction and β_1, β_2 and β_3 are the directions cosines of the strain direction with respect to the cube edges. λ_{100} and λ_{111} are the saturation magnetostriction constants in the [100] and [111] directions respectively.

3.2 Magnetic Domain Structure of Grain Oriented Steel

All the magnetic domain configurations in grains of silicon steel are based on minimisation of the total free energy of the system. To reduce the magnetostatic energy in a grain, a multi domain structure is created as shown in Fig 3.4. Furthermore to eliminate the flux leakage (high charge density of poles) and therefore reduce the magnetostatic energy to zero, closure flux domains are formed at the ends to lead the flux within the specimen in the closed path as shown in Fig 3.7 [5]. The closure domains have a magnetisation aligned parallel to the crystal surface.

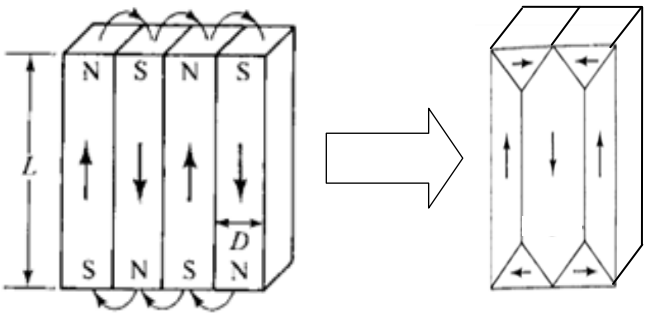

Fig 3.7 Closure flux domains in the cubic crystal [5].

A cubic crystal exhibits magnetostriction, $\lambda_{100,}$ which for the iron is positive, then the closure domains in [100] direction with a constant volume, tend to elongate parallel to the crystal surface as shown by the dotted lines in Fig 3.8. Therefore some of

the magnetoelastic energy is stored due to compression of the triangular closure domains [3].

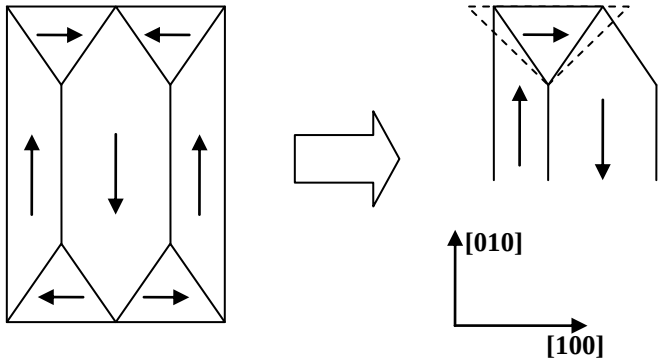

Fig 3.8 Magnetostrictive elongation of a surface closure domain [3, 5].

In grain oriented silicon steel, such domains as presented in Fig 3.8 cannot occur because of the large magnetocrystalline anisotropy energy associated with the transverse domains. The grain to grain variation of orientation in the sheet plane generates free magnetic poles (with an associated demagnetising field) which increase the magnetostatic energy.

Therefore to minimise the energy, surface dagger domains as shown in Fig 3.9 will appear. These domains are commonly called as lancet or spike domains, and run through the thickness of the strip [9].

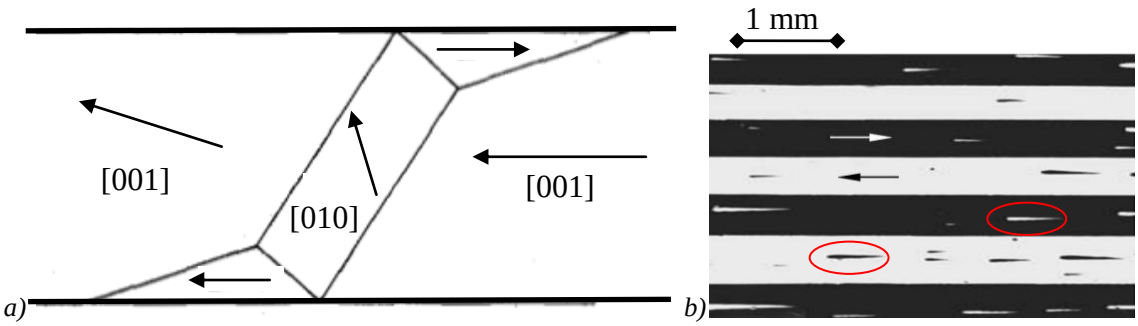

Fig 3.9 Lancet domains structure presented through the sheet thickness (a) and on the sheet surface (b) [7].

The transverse [010] domain on both surfaces is connected to closure domains [001], oppositely magnetised to the adjacent domains, therefore the flux is closed and magnetostatic energy minimised in the grain. The increase in density of closure domains is related to an increase of the dip angle, δ, of domain magnetisation out of the strip plane. When δ is about 4˚, the lancet domains are to be aligned in rows and this

structure is called a lancet combo structure [10]. In this structure the group of aligned lancet closure domains use the same main transverse domain.

The misorientation of the grain to the rolling direction along the sheet plane would also create supplementary domains at the grain boundaries. If the net magnetisation directions of two grains separated by the grain boundary follow the easy axes (irrespective of the polarization) then the charge density of domains is zero as shown in Fig 3.10 (a), where the domain continuity is observed through the grain boundary [4]. However, the appearance of charges (magnetic poles), caused by the misorientation from the easy direction, would create closure structures at the grain boundary (Fig 3.10 (b)). The charges can be reduced by rotation of the magnetisation away from the easy axes. With stronger charges, more complicated flux closure domains are introduced in the neighbourhood of the grain boundary as shown in Fig 3.10 (c, d).

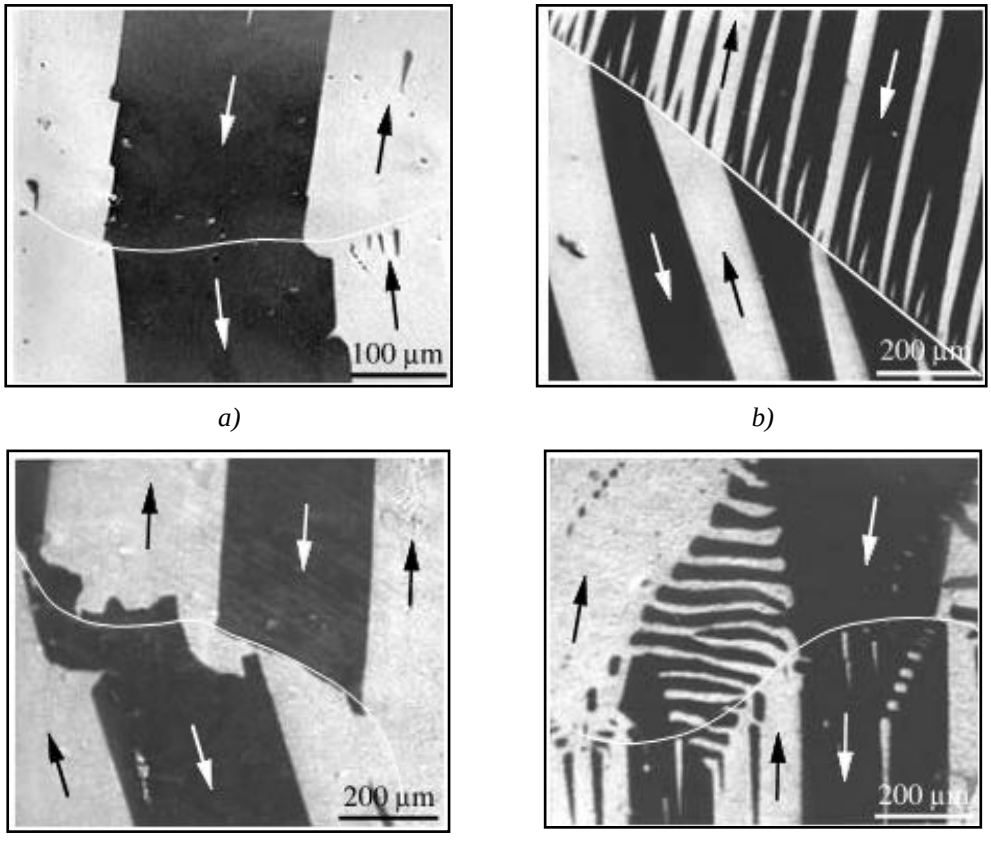

a) *b)*

c) *d)*

Fig 3.10 Domain structure in the neighbourhood of the grain boundary: (a) domain continuity, (b) spike-shape domains, (c, d) closure with internal transverse domains [4].

Closure domains are based on the internal transverse domains as shown in Fig 3.11.

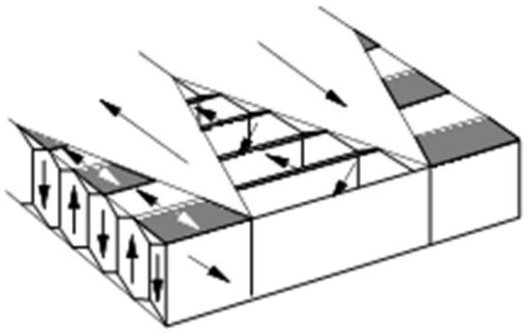

Fig 3.11 Schematic of closure domains at a grain boundary [4].

3.3 Effect of Applied Field

A ferromagnetic material in the demagnetised state contains domains where each is spontaneously magnetised to saturation. The magnetisation process under external applied field, of sufficient magnitude to saturate the material, converts the strip from a multi-domain state to a single domain, magnetised in the same direction as the field [5].

In silicon steel, magnetisation occurs by the 180˚and 90˚ domain wall movement through the material until the net energy is minimised [5]. If magnetic moments within a domain are initially rotated out of the easy axes, which result in higher magnetocrystalline anisotropy energy, and also out of the direction of applied field (H) as shown in Fig 3.12(a, b), then a higher applied field would be required to rotate the magnetic moments to the magnetisation (M) direction (Fig 3.12(c, d)).

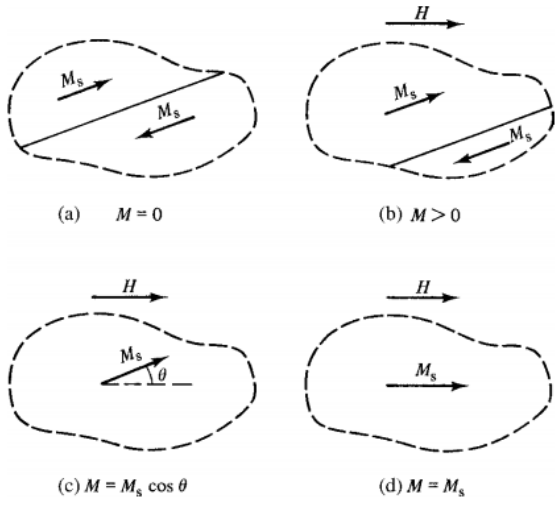

Fig 3.12 Magnetisation process in silicon steel [5].

M and H contribute to a magnetic induction or magnetic flux density B which is expressed as [11]:

$$B = \mu_0(H + M) \tag{3.5}$$

where B is in Tesla, and $\mu_0 = 4\pi \cdot 10^{-7}$ is permeability of free space in henrys per meter.

In free space $\mu_0 M$ also known as magnetic polarisation (J) is zero. Moreover the magnetic flux density in a magnetic material such as the grain oriented silicon steel is equal:

$$B = \mu_0 \mu_r H \tag{3.6}$$

where μ_r is relative permeability of the magnetic material.

The process of domain wall movement, and then single domain magnetisation rotation to the direction of applied field in the silicon steel can be presented as an ideal magnetisation curve as shown in Fig 3.13.

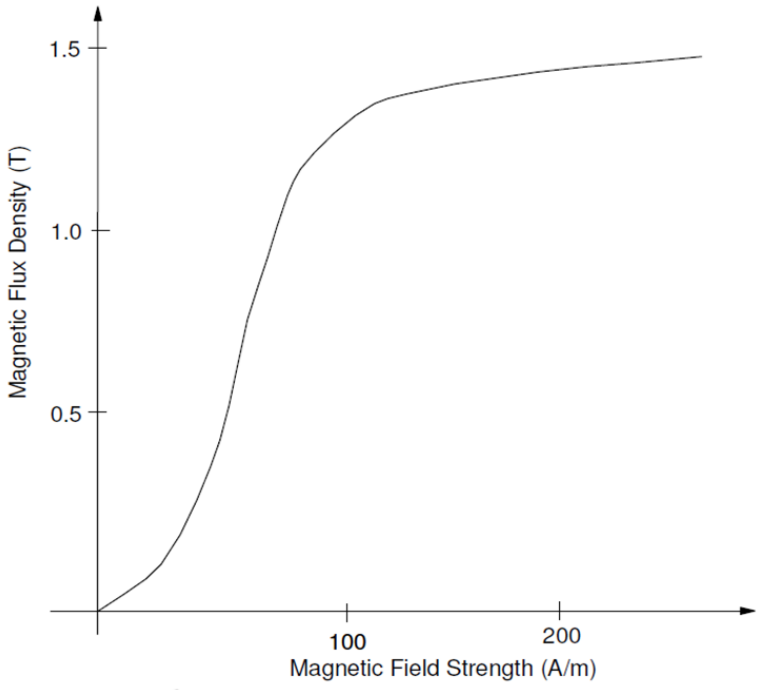

Fig 3.13 Ideal magnetisation curve of the silicon steel [12].

High permeability is observed at low fields, where magnetisation causes 180˚ domain wall motion, and then after the 'knee' of the curve when the permeability drops due to rotation of domain magnetisation.

In materials such as silicon steel, domain wall motion is not reversible. If the field is reduced to zero from a saturated magnetisation state, the magnetisation is not reduced to zero. This is due to sites including dislocations and non magnetic inclusions, which pin the moving domain wall until the increased magnetic field can overcome it. These pinning sites cause local variations in magnetoelastic, wall and magnetostatic energies. Irreversibility or so-called hysteresis of the magnetisation curve is shown in Fig 3.14.

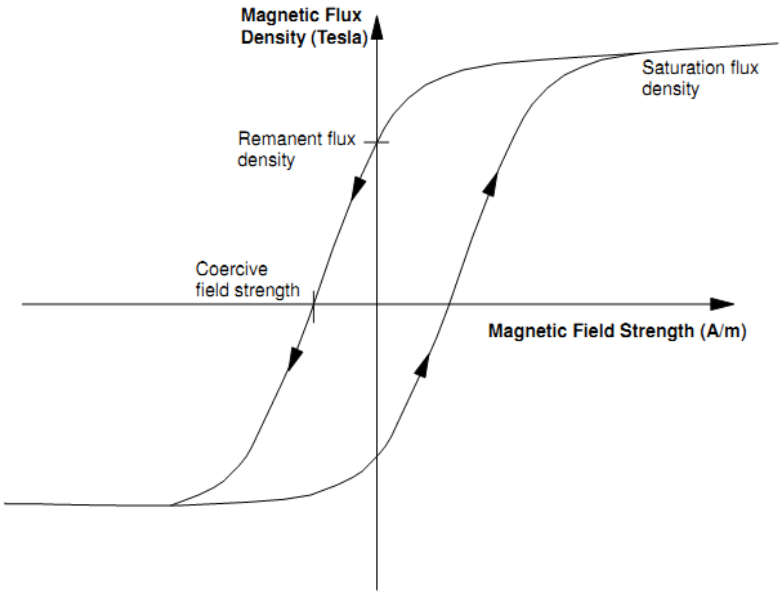

Fig 3.14 Hysteresis magnetisation loop of silicone steel [12].

The area inside the hysteresis loop is equivalent to the energy required to cycle the magnetisation around the loop and is called the hysteresis loss.

3.4 Magnetostriction under Applied Field

In highly grain oriented steel domains are strained along the direction of spontaneous magnetisation (below the Curie temperature). Any rearrangement of the domain structure, for instance by the application of an external field may cause a change in the net strain of the material. This appears when the grain structure contains closure

domains with 90˚ walls which under higher magnetic field rotate to the direction of the applied field as shown in Fig 3.15. This strain causes a change in the geometrical shape of the material and is called magnetostriction. Silicon steel with positive magnetostriction elongates in the direction of an applied filed.

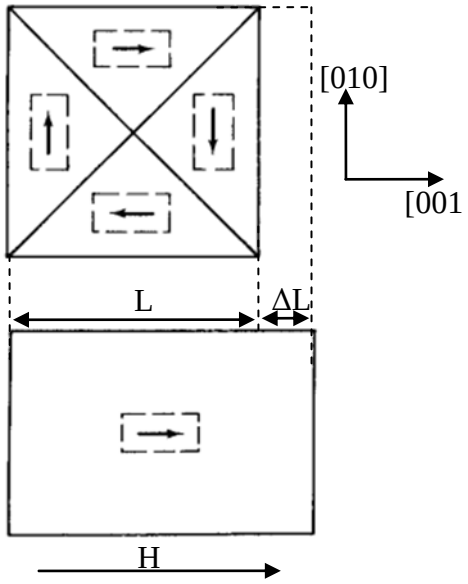

Fig 3.15 Magnetostriction (ΔL/L) of the iron crystal in the [001] direction [5].

However under 180˚ domain wall movement magnetostriction does not occur because the magnetic moments under external field stay in the same direction as the spontaneous magnetisation. Using equation (3.4), the magnetostriction for 180˚ domain wall movement can be expressed as:

$$\Delta\lambda = \lambda_{final} - \lambda_{initial} = \frac{3}{2}\lambda_{100}\left((-1)^2{\beta_3}^2 - \frac{1}{3}\right) - \frac{3}{2}\lambda_{100}\left((1)^2{\beta_3}^2 - \frac{1}{3}\right) = 0 \qquad (3.7)$$

The domains with magnetisation aligned in the $[00\bar{1}]$ direction are switched to $[001]$ and inversely, then in the initial condition $\alpha_1=\alpha_2=0$, $\alpha_3=1$ and in the final $\alpha_1=\alpha_2=0$, $\alpha_3=-1$. However the direction of applied field stayed unchanged, consequently β_1, β_2 and β_3 are not affected.

In the case of 90˚ domains aligned in the transverse [010] or [100] directions which are switched to [001] direction, the initial condition is $\alpha_1=1$, $\alpha_2=\alpha_3=0$, and in the final $\alpha_1=\alpha_2=0$, $\alpha_3=1$.

$$\Delta\lambda = \lambda_{final} - \lambda_{initial} = \frac{3}{2}\lambda_{100}\left((1)^2{\beta_3}^2 - \frac{1}{3}\right) - \frac{3}{2}\lambda_{100}\left((1)^2{\beta_1}^2 - \frac{1}{3}\right)$$
$$= \frac{3}{2}\lambda_{100}\left({\beta_3}^2 - {\beta_1}^2\right)$$

(3.8)

The magnetic moments switch to the [001] direction under applied field, then β_1=1 and β_3=0. Therefore the change in the magnetostriction is given by:

$$\Delta\lambda = \frac{3}{2}\lambda_{100} \qquad (3.9)$$

For the GOSS material λ_{100} = 24 x 10^{-6} [13], then change in magnetostriction $\Delta\lambda$ = 36 x 10^{-6}.

3.5 References

[1] D. Jiles, "Introduction to magnetism and magnetic materials," *Chapman and Hall,* 1991.

[2] K. Buschow and F. D. BOER, "Physics of magnetism and magnetic materials," *Kluwer Academic Publishers,* 2003.

[3] S. Chikazumi, "Physics of magnetism," *Robert E. Krieger Publishing Company,* 1978.

[4] A. Hubert and R. Shafer, "Magnetics domains," *Springer-Verlag Berlin Heidelberg,* 1998.

[5] B. Cullity and C. Graham, "Introduction to magnetic material," *John Wiley & Sons,* 2009.

[6] J. W. Shilling, "Domain-structures in 3 percent Si-Fe single-crystals with orientation near (110)001," *IEEE Transactions on Magnetics,* vol. MAG9, pp. 351-356, 1973.

[7] J. W. Shilling and G. L. Houze, "Magnetic proprties and domain structure in gain-oriented 3% Si-Fe," *IEEE Transactions on Magnetics,* vol. MAG10, pp. 195-223, 1974.

[8] R. Becker and W. Döring, "Ferromagnetism," *Springer,* 1939.

[9] W. S. Paxton and T. G. Nilan, "Domain configurations and crystallographic orientation in grain-oriented silicon steel," *Journal of Applied Physics,* vol. 26, pp. 994-1000, 1955.

[10] J. W. Shilling and G. L. Houze, "Magnetic properties and domain structure in gain-oriented 3% Si-Fe," *IEEE Transactions on Magnetics,* vol. MA10, pp. 195-223, 1974.

[11] D. Jiles, "Introduction to Magnetism and Magnetic Materials," *Chapman and Hall,* 1991.

[12] P. Anderson, "A novel method of measurement and characterisation of magnetostriction in electrical steels," PhD Thesis, Cardiff University, Cardiff, 2000.

[13] R. Gersdorf, "Uniform and non-uniform form effect in magenetostriction," *Physica,* vol. 26, pp. 553-574, 1960.

Chapter 4 Domain Structure under Stress in Grain Oriented Silicon Steel

4.1 Domain Structures under Applied Stress

The domain structures presented in this chapter occur under stress in the elastic region of grain oriented silicon steel. Fig 4.1 shows directions of the cube on edge crystal in grain oriented steel. A tensile or compressive stress is applied along the rolling [001] and the transverse [110] direction.

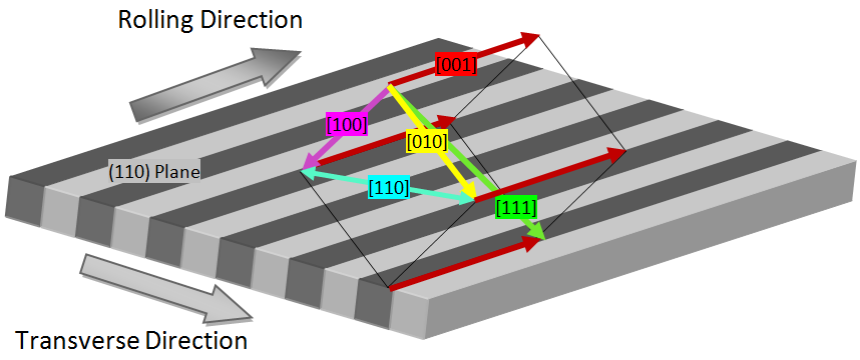

Fig 4.1 Directions of the cubic crystal in the grain oriented steel.

4.1.1 Tensile Stress in the Rolling Direction

A tensile stress applied along the rolling direction in a well oriented grain causes a refinement to longitudinal main domains aligned in [001] direction. Supplementary transverse [010] or [100] domains attached to the main domains will be removed by the tension which also refines the domains wall spacing. The magnetoelastic energy of transverse domains under tensile stress applied in the rolling direction increases, whilst it simultaneously decreases in the longitudinal domains.

Consequently the longitudinal domains grow at the expense of the transverse domains which lead to an increase in magnetostatic energy. At a certain value of applied tensile stress the [001] domains will start narrowing in order to reduce the demagnetising field and consequently magnetostatic energy.

4.1.2 Compressive Stress in the Rolling Direction

Compressive stress applied along the [001] direction increases the magnetoelastic energy of longitudinal [001] domains and decreases that of the supplementary [010] or [100] domains. Therefore the volume of supplementary domains increases [1]. This type of domain structure under compressive stress was first observed by Dijkstra and Martius [2]. They described two characteristic patterns which were named as stress pattern *I* and stress pattern *II*. These two patterns appear within the elastic range of the material and disappear when the load is removed.

Stress pattern *I* is the simplest of the two structures, where the main domains under compression switch from [001] to [100] direction and consist a small flux closure domains, still aligned in the [001] direction as presented in Fig 4.2.

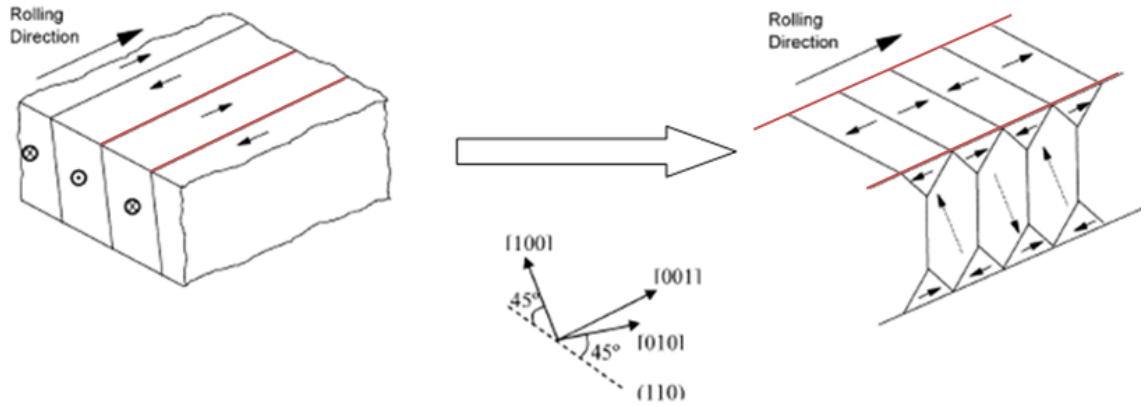

Fig 4.2 Transition from the unstressed state to stress pattern I.

In a similar fashion to supplementary transverse domains under tension, the compressive stress increases the magnetoelastic energy which causes the expansion of the [100] main domains by decreasing the volume of the closure [001] domains. Therefore increase in the compressive stress narrows the bulk domain wall spacing in order to reduce the magnetostatic energy. The main domains wall energy in stress pattern *I* and the closure domain spacing increase with increasing stress [3].

Stress pattern *II* appears under higher compression. An improved understanding of transition from stress pattern *I* to stress pattern *II* was offered by Corner and Mason [3]. They proposed that the main domains stayed in the same [100] direction but the domain walls changed from 90° to 45° to the rolling direction which is the [010] direction as shown in Fig 4.3.

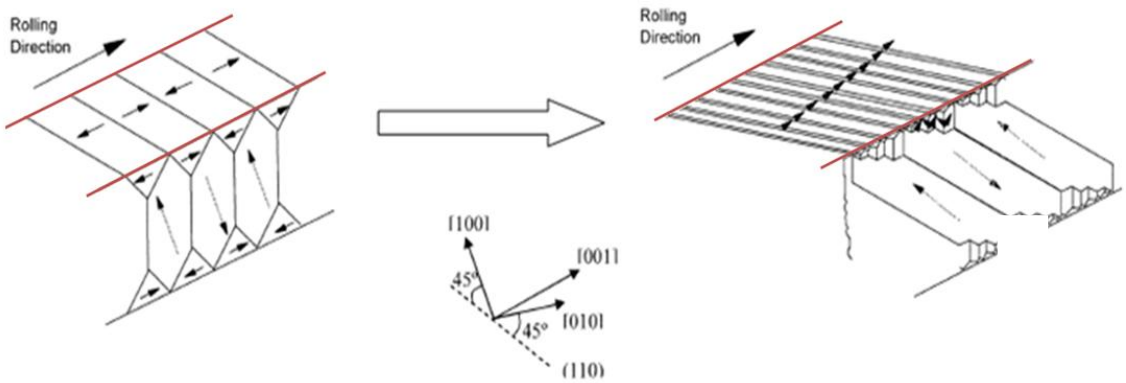

Fig 4.3 Transition from stress pattern I to stress pattern II [4].

The growth of main domains and reduction of flux closure domains are the same as in stress pattern *I*. Corner and Mason noted that the domain wall energy of stress pattern *II* decreases with increasing stress which is opposite to that in pattern *I*. The closure domain structure in stress pattern *II* can be observed on the surface as characteristic zigzag patterns. However regardless of complicated domain structure, the closure flux in these two types of patterns is completed [2].

4.1.3 Compressive and Tensile Stress Applied in the Transverse Direction

When a compressive stress is applied in the rolling direction, the main [001] domains switch to [100] or [010] directions which are at 45° to the [110] direction. The domains cannot align along the [110] direction because of its high energy state so they align to one of the other easy crystal axes ([100] or [010]) to minimize the energy. Tensile stress applied in the transverse direction in the ideal grain has the same effect as compressive stress in the longitudinal direction. According to Banks and Rawlinson the transverse stress should have the same effect on the grain oriented SiFe steel as the application of a longitudinal stress of half the magnitude [5]. Perpendicular compressive stress applied on the sheet surface will have a similar effect as a tensile stress along the rolling direction and vice versa.

4.2 The Influence of a Magnetic Field on Domain Structures under Applied Stress

In this section the influence of a magnetic field applied either along the rolling or transverse direction of GOSS on the magnetic domain structures under applied stress is examined.

4.2.1 Domains under Tensile Stress Applied in the Rolling Direction

The reduction of supplementary transverse domains e.g. dagger, chevrons and lancet domains, improves average misorientation of the domain structures under applied tensile stress along the [001] direction. This gives a similar domain structure to that in an ideal unstressed grain. The difference appears under higher flux density, above 1 Tesla, when the previously removed supplementary domains reappear [6].

The 180˚ domain wall movement due to the magnetisation increases the magnetostatic energy to the point where the sum of the magnetostatic and magnetoelastic energies is reduced by the reappearance of supplementary domains [1]. This reappearance of closure domains has the effect of causing a drop in the permeability as shown in Fig 4.4 [7].

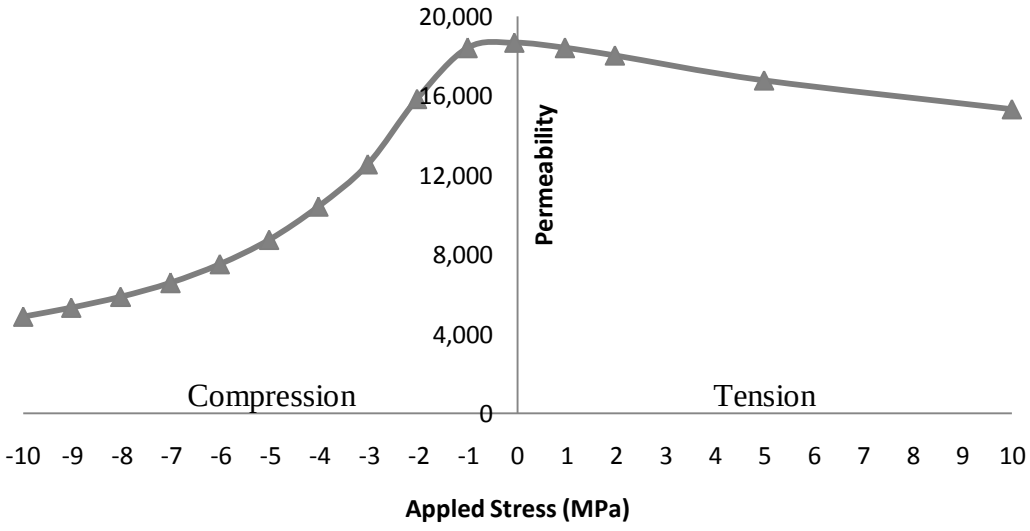

Fig 4.4 Permeability characteristic of the GOSS under tensile and compressive stress (1.7T, 50 Hz).

4.2.2 Domains under Compressive Stress Applied in the Rolling Direction

Increasing compressive stress along the rolling direction creates characteristic stress patterns *I* and *II*. Applied magnetic field in the [001] direction, the same direction as compressive stress, generates the magnetisation force which firstly produces 90° domain wall movement in order to align main domains to the [001] direction. This means that the closure [001] domains grow at the expense of the main [100] domains as shown in Fig 4.5. Secondly, under higher magnetisation 180° domain wall motion occurs [8].

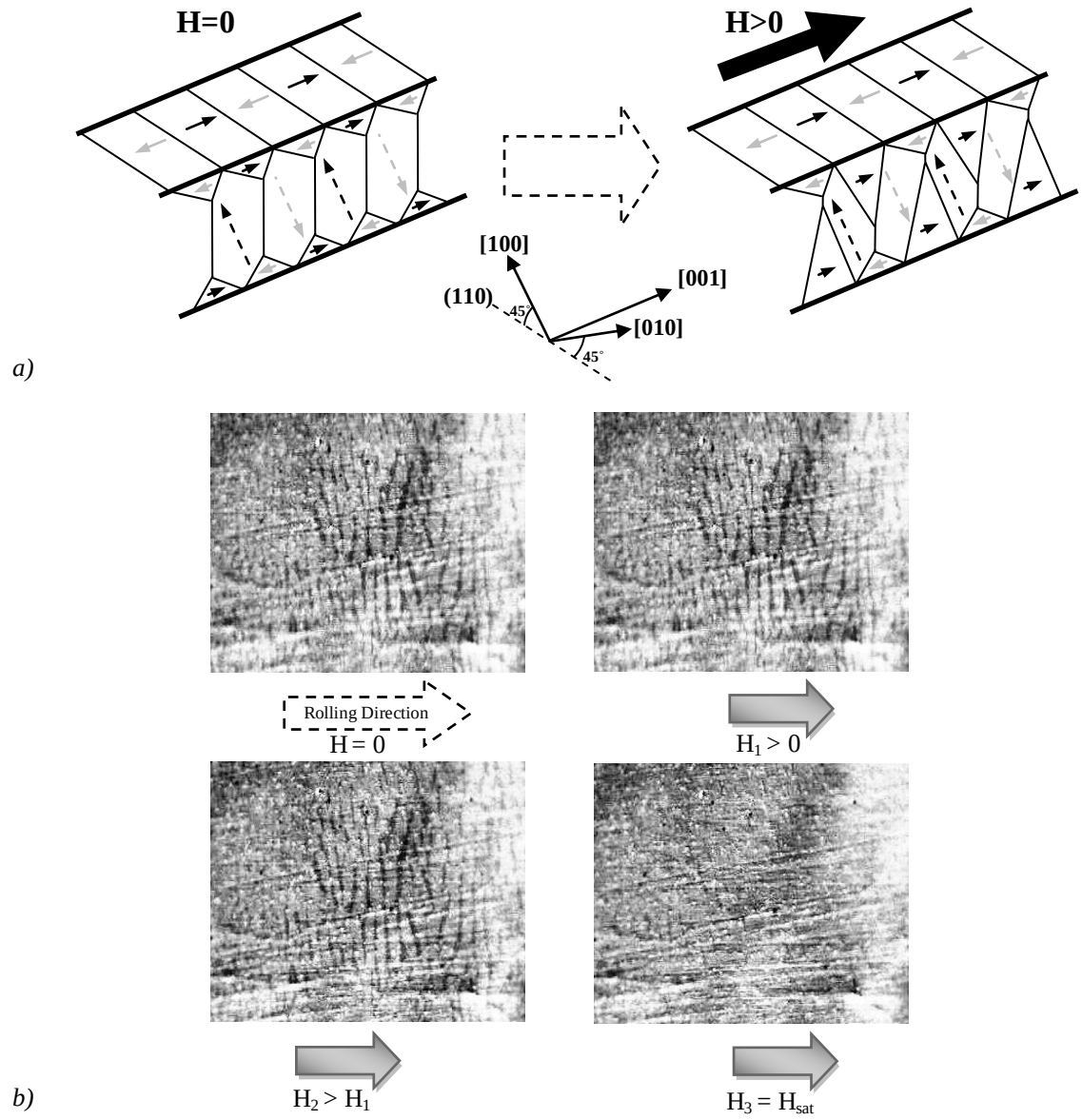

Fig 4.5 The 90˚ domain wall movement in stress pattern I during magnetisation along the [001] by schematic (a) and domain observation (b).

It was observed by Corner and Mason that the width of surface domains does not change under increasing magnetisation until 180° domain wall motion is initiated [3]. Also the drop in permeability is observed due to the magnetisation of stress patterns as shown in Fig 4.4. The reduction is greater than that under tensile stress due to the much larger volume of 90° domains.

4.2.3 Domains under Applied Stress in the Transverse Direction

Tensile or compressive stress applied in the transverse direction [110] (Fig 4.1) is half of the magnitude of the longitudinal [001] direction [5]. Therefore domain structures under stress are comparable with those explained in 4.2.1 and 0 but with the opposite effect. It means that the tensile stress in this case causes stress patterns *I* or *II*.

Tensile stress applied in the transverse [110] direction causes the movement of main domains from the [001] direction to the [100] direction which is at 45° to the [110] direction. The flux closure domains are still in the [001] direction. The magnetisation in the [110] direction will increase the volume of main [100] domains at the expense of the closure [001] domains, therefore the closure domains will switch to the [110] direction and the main domains from [100] to [110]. Under a high magnetic field, all of the domains become saturated in the [110] direction by 180° domain wall motion as shown in Fig 4.6.

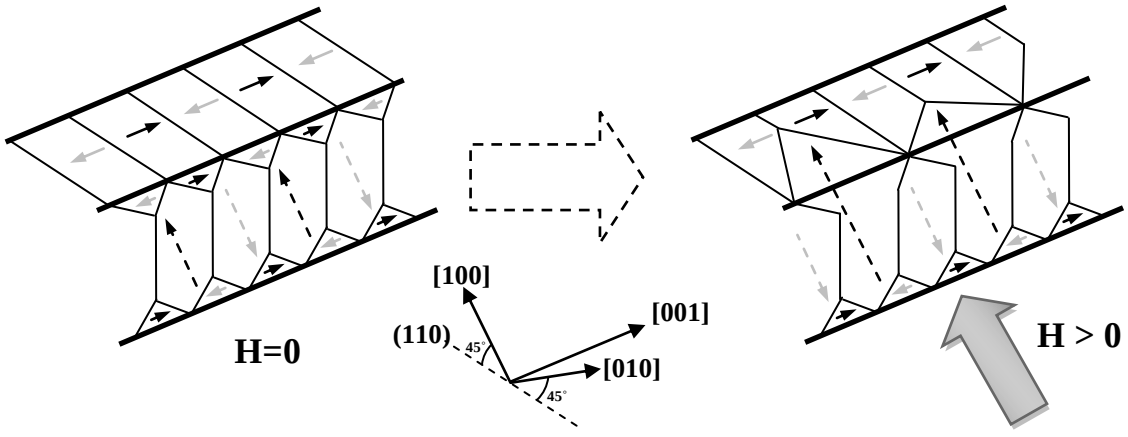

Fig 4.6 Magnetisation in the [110] direction of domains under applied tensile stress in the [110] direction.

However, compressive stress applied in the [110] direction improves the orientation of the domains to the [001] direction, then due to magnetisation in [110] direction the

domains move from [001] direction to the [110] direction causing 90°, and then 180° domain wall motion as shown in Fig 4.7.

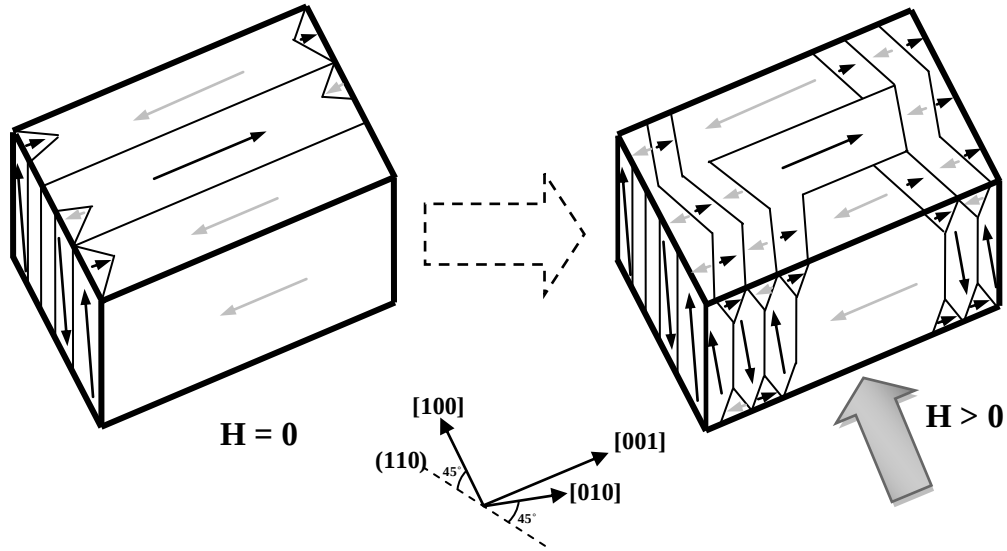

a)

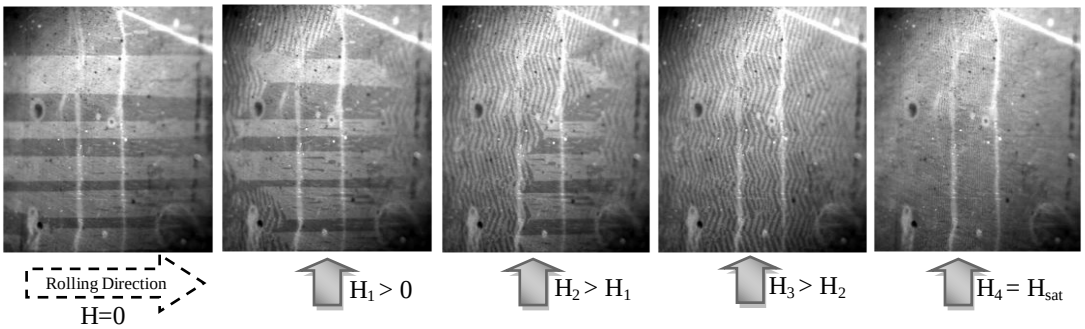

b)

Fig 4.7 Magnetisation in the [110] direction of domains under applied compressive stress in the [110] direction by schematic (a) and domain observation (b).

4.3 Effect of Domain Structures under Stress on Magnetostriction

Applied tensile or compressive stress causes a change in the magnetostriction of grain oriented silicon steel. A typical relation between magnetostriction under tensile and compressive stress of grain oriented steel is presented in Fig 4.8. An understanding of this characteristic can be gained by studying the changing domain structures under magnetisation and in particular 90 degree domain wall motion which is the primary generator of magnetostriction in these materials [3].

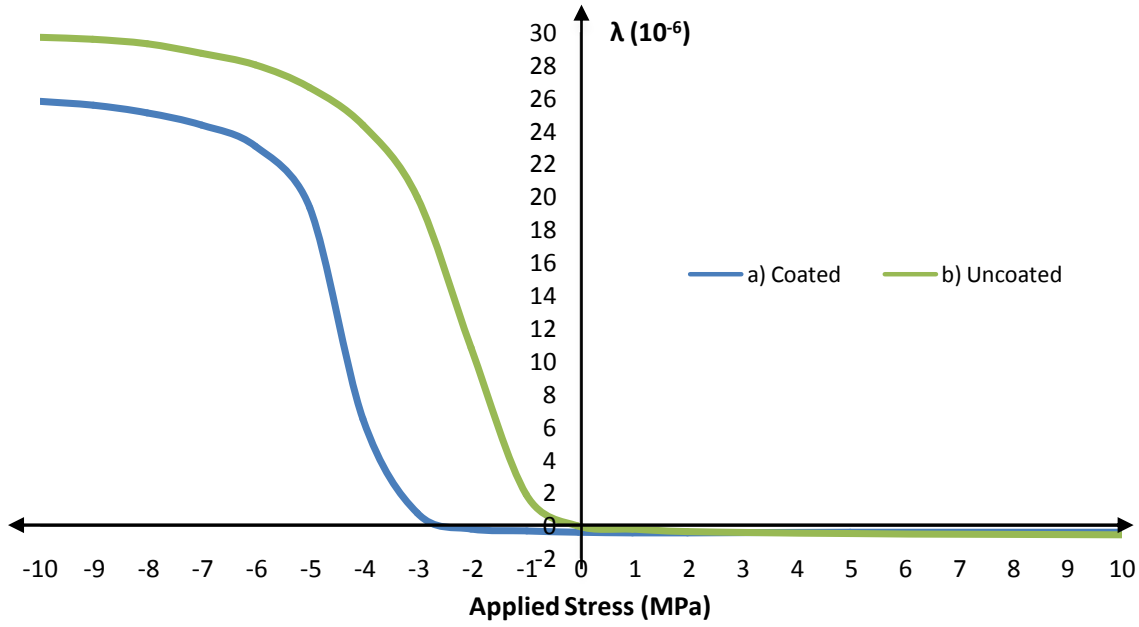

Fig 4.8 Typical Magnetostriction versus stress characteristic of grain oriented silicon steel: a) coated, b) uncoated.

4.3.1 Domains under Applied Tensile Stress in the Rolling Direction

Domain structures magnetised under applied tensile stress in the rolling direction are described in section 4.2.1. It was observed by Shilling [9] that transverse supplementary domains previously removed by tension, reappear during the magnetisation process. The reorganisation in the structure from [001] domains to transverse domains, where magnetic moments are directed out of plane in the [010] or [100] direction (e.g. Fig 3.9), produces a small negative magnetostriction as presented in Fig 4.8.

4.3.2 Domains under Applied Compressive Stress in the Rolling Direction

As presented in section 4.1.2 stress patterns occur in the GOSS under compressive stress applied along the rolling direction. The magnetisation process changes the magnetoelastic energy by rotation the main [100] domains to the [001] direction. This 90˚ domain switch generates the positive magnetostriction in grain oriented silicon steel. The average misorientation of the domains from the rolling direction in conventional grain oriented steel is 7˚ which results in a variation of the magnetoelastic energy from grain to grain. The result of this is that the stress patterns will not occur simultaneously in all of the grains giving the smooth shape to the characteristic.

4.4 Magnetostriction Model of Domains under Compressive Stress in GO Steel

Simmons and Thompson [10] proposed a model to calculate the effect of magnetisation on the material under compressive stress. This model describes the switch to stress pattern I where the average width of closure domains, d, strip thickness, t, and angle θ between the diagonal of the closure domain (parallel to the [111] direction) and the surface as shown in Fig 4.9 are used in the analysis. Three assumptions were made in order to simplify the model:

a) All grains in the material exhibit the same layout of the stress pattern I.
b) All grains under compression contain only [001] and [100] domains.
c) Values of domains misorientation to the RD, Ø, at the unstressed condition and closure domain width d appeared under compression are an average values for all of the grains.

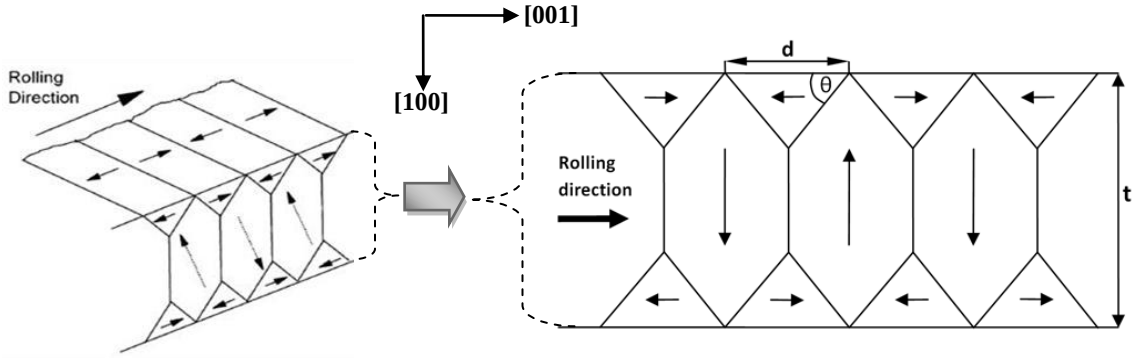

Fig 4.9 Longitudinal section through a grain exhibiting stress pattern I.

The volume fraction, V_f, of closure domains aligned in the [001] direction can be calculated by examination of Fig 4.9 as

$$V_f = 2 \times \frac{d}{2} \times \frac{d}{2} tan\theta \times \frac{1}{dt} \qquad (4.1)$$

$$= \frac{d}{2t} tan\theta$$

The magnetostriction in each domain presented in Fig 4.9 can be calculated using equation (3.4).

Magnetostriction for the closure domains along the [001] direction is measured for, α_1=0, α_2=0, α_3=1, and β_3=cos Ø is given by,

$$\lambda_{closure} = \frac{3}{2}\lambda_{100}\left(cos^2\emptyset - \frac{1}{3}\right) \qquad (4.2)$$

Magnetostriction for main bulk domains along [100] direction is measured for, α_1=1, α_2=0, α_3=0, and β_3=sin Ø is given by,

$$\lambda_{bulk} = \frac{3}{2}\lambda_{100}\left(sin^2\emptyset - \frac{1}{3}\right) \qquad (4.3)$$

The initial magnetostriction along the [001] direction is the strain when the domain structure is entirely stress pattern I and it can be calculated by summing the magnetostriction of each type of domains.

$$\lambda_{initial} = \frac{3}{2}\lambda_{100}\left(cos^2\emptyset - \frac{1}{3}\right)V_f + \frac{3}{2}\lambda_{100}\left(sin^2\emptyset - \frac{1}{3}\right)(1 - V_f) \quad (4.4)$$

Then,

$$\lambda_{initial} = \lambda_{100}(cos2\emptyset)\frac{3d}{4t}tan\theta + \frac{3}{2}\lambda_{100}\left(sin^2\emptyset - \frac{1}{3}\right) \quad (4.5)$$

The magnetostriction after the stressed sample is subsequently magnetised, can hence be calculated. When the sample is magnetically saturated (at a flux density B_s) each grain comprises only [001] domains aligned along the magnetisation direction, then the volume fraction of [001] domains under measured flux density, B, can be described as:

$$V_f{}' = \frac{B}{B_s}cos\emptyset \quad (4.6)$$

Therefore the final magnetostriction can be expressed as:

$$\lambda_{final} = \frac{3}{2}\lambda_{100}\left(cos^2\emptyset - \frac{1}{3}\right)V_f{}' + \frac{3}{2}\lambda_{100}\left(sin^2\emptyset - \frac{1}{3}\right)(1 - V_f{}') \quad (4.7)$$

Then,

$$\lambda_{final} = \frac{3}{2}\frac{B}{B_s}cos\emptyset\,\lambda_{100}\left(cos2\emptyset - \frac{1}{3}\right) + \frac{3}{2}\lambda_{100}\left(sin^2\emptyset - \frac{1}{3}\right) \quad (4.8)$$

The magnetostriction of the strip under applied magnetic field can be finally calculated as:

$$\lambda_{measured} = \lambda_{final} - \lambda_{initial} \quad (4.9)$$

$$\lambda_{measured} = \frac{3}{2}\frac{B}{B_s}cos\emptyset\,\lambda_{100}\left(cos2\emptyset - \frac{1}{3}\right) + \frac{3}{2}\lambda_{100}\left(sin^2\emptyset - \frac{1}{3}\right) - \lambda_{100}(cos2\emptyset)\frac{3d}{4t}tan\theta - \frac{3}{2}\lambda_{100}\left(sin^2\emptyset - \frac{1}{3}\right) \quad (4.10)$$

Then,

$$\lambda_{measured} = \frac{3}{2}\lambda_{100} cos2\emptyset \left(\frac{B}{B_s} cos\emptyset - \frac{d}{2t} tan\theta\right) \quad (4.11)$$

The measured magnetostriction based on the misorientation, change in the closure domains, and magnetic flux density can be estimated using the equation (4.11). However d, and ∅ must be obtained by experimental domain observations under stress.

4.5 The Effect of Domain Structures under Stress on Loss

The change in the domain structure would also lead to a change in the power loss due to the increase in domain wall motion. Tensile stress applied along the [001] direction would improve the net misorientation of the domain, however the effect on loss is not as significant as compressive stress applied along the [001] direction.

4.5.1 Domains under Applied Compressive Stress

A magnetic field applied along the [001] direction when a compressive stress is applied along the same direction, initially causes 90° domain wall movement in order to align main domains of stress pattern (*I* or *II*) along the [001] direction. This means that the closure [001] domains grow at the expense of the main [100] domains. As the field is increased, 180° domain walls movement is executed [8]. This transition from 90° to 180° wall movement can be observed as a distortion in the B-H loop (1.7 T, 50 Hz) of the grain oriented steel under compressive stress in the RD as shown in Fig 4.10 [11].

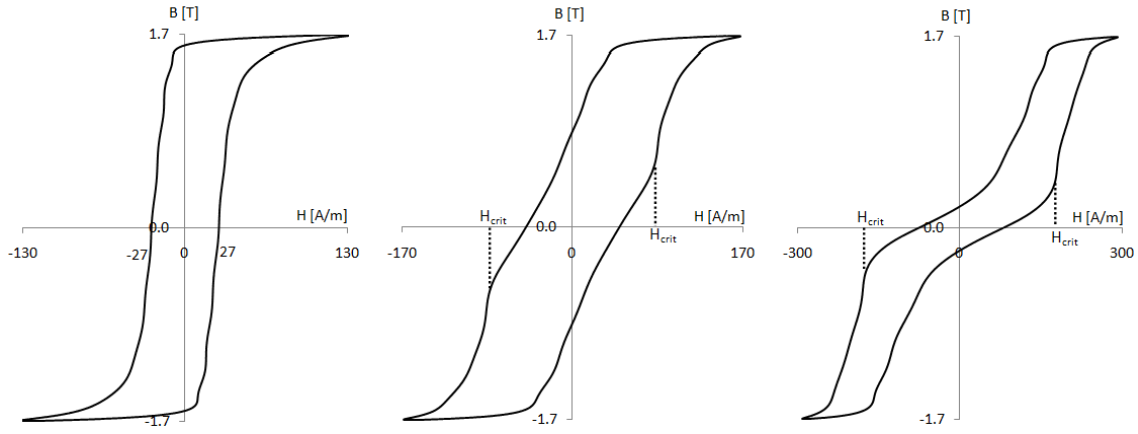

a) H_{crit}=0 A/m *b) H_{crit}=90 A/m* *c) H_{crit}=180 A/m*

Fig 4.10 B-H Loops under compressive stress applied along the RD of: a) 0 MPa, b) -5 MPa, c) -10 MPa.

To magnetise the compressed sample, that is to initiate the 180° domain walls movement, to the saturation level a certain value of magnetic field, the critical field, H_{crit} (Fig 4.10b, c), is required. The H_{crit} is proportional to the applied compressive stress and is given by [12]:

$$H_{crit} = \frac{3\lambda_{100}\sigma}{2B_s} \qquad (4.12)$$

where σ is the compressive stress.

4.6 References

[1] J. W. Shilling and G. L. Houze, "Magnetic proprties and domain structure in gain-oriented 3% Si-Fe," *IEEE Transactions on Magnetics,* vol. MAG10, pp. 195-223, 1974.

[2] L. J. Dijkstra and U. M. Martius, "Domain patterns in silicon iron under stress," *Reviews of Modern Physics,* vol. 25, pp. 146-150, 1953.

[3] W. D. Corner and J. J. Mason, "Effect of stress on domain structure of goss textured silicon iron," *British Journal of Applied Physics,* vol. 15, pp. 709-722, 1964.

[4] P. Anderson, "A novel method of measurement and characterisation of magnetostriction in electrical steels," PhD Thesis, Cardiff University, Cardiff, 2000.

[5] P. J. Banks and E. Rawlinson, "Dynamic magnetostriction and mechanical strain in oriented 3% silicon iron sheet subject to combined longitudinal and transverse stresses," *Proceedings of the Institution of Electrical Engineers-London,* vol. 114, pp. 1537-1546, 1967.

[6] J. W. Shilling, "Domain structure during magnetisation of grain oriented 3% SiFe as a function of applied tensile stress," *Journal of Applied Physics,* vol. 42, pp. 1787-1789, 1971.

[7] P. I. Anderson, *et al.*, "Assessment of the stress sensitivity of magnetostriction in grain-oriented silicon steel," *IEEE Transactions on Magnetics,* vol. 43, pp. 3467-3476, 2007.

[8] R. Perryman, "Effects of tensile and compressive sterss on 3 percent grain-oriented silicon iron," *Journal of Physics D-Applied Physics,* vol. 8, pp. 1901-1909, 1975.

[9] J. W. Shilling, "Domain structure during megnetization of (100) [001] grain-oriented 3% Si-Fe," *IEEE Transactions on Magnetics,* vol. MAG7, pp. 557-560, 1971.

[10] G. H. Simmons and J.E. Thompson, "Magnetic properties of grain oriented silicon iron," *Proceedings of the IEE,* vol. 118, pp. 1302-1306, 1971.

[11] A. J. Moses, "Effects of applied stresses on the magnetic properties of high permeability silicon iron," *IEEE Transactions on Magnetics,* vol. 15, pp. 1575-1579, 1979.

[12] A. J. Moses and D. Davies, "Influance of compressive stress on magnetic properties of comercial (110) [001] oriented silicon-iron," *IEEE Transactions on Magnetics*, vol. 16, pp. 454-460, 1980.

Chapter 5 Magnetostriction Measurement System

5.1 Magnetostriction Measurement Techniques for GO Steel

5.1.1 Measurement of Magnetostriction

Magnetostriction of a ferromagnetic material is defined as the fractional change in dimensions ($\Delta L/L$) and can be measured under dynamic AC or DC magnetisation conditions. When the strip is magnetised under AC magnetisation for instance, at 50 Hz, the fundamental frequency of magnetostriction is at 100 Hz with harmonics at integer multiples of this. Therefore the magnetostriction measurement sensor should be capable of picking up the signal with a characteristic bandwidth from 100 Hz to 1 KHz.

Grain oriented silicon steel has a peak value of magnetostriction in the order of 10^{-6} (μstrain). This very small displacement requires selection of an extremely sensitive transducer which will produce a signal proportional to the magnitude of the vibratory motion of the free end of a steel strip.

5.1.2 Review of Measurement Techniques

A transducer converts one form of energy to another. For measurement of magnetostrictive vibration, a transducer that converts mechanical energy to an electrical signal is needed.

In this section several transducers are reviewed in order to select the most suitable one to measure magnetostriction under stress.

5.1.2.1 Linear Variable Differential Transformers

The linear variable differential transformer (LVDT) is used for measuring linear displacement. It is an electro-mechanical device including a primary excitation coil and two secondary coils which produce an AC voltage output proportional to the

displacement of the soft magnetic core as shown in Fig 5.1. The core is placed inside the coils at the centre. Movement of the core changes the flux linkage in the secondary coils which appears as a differential voltage output. The sensor has a high resolution up to 0.01 x 10^{-6}.

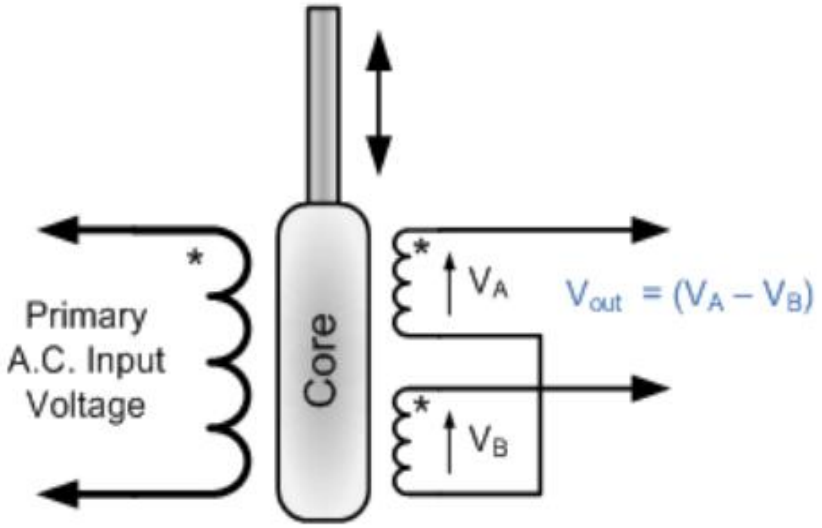

Fig 5.1 Linear variable differential transformer (LVDT) [1].

A magnetostriction measurement system using an LVDT was evaluated by Stanbury [2] who observed that the sensor picks up a stray field during the measurement. Also difficulties of adjustment of the sensor in the zero position before each measurement was encountered. An increase of the LVDT temperature would result in an increase in the resistance of the copper wire used in the primary and secondary coils [3].

5.1.2.2 Capacitive Displacement Sensors

The capacitive displacement sensor measures the capacitance change between two parallel plates of the capacitor which is proportional to its displacement. Fig 5.2 shows a measurement system with a capacitive displacement sensor attached.

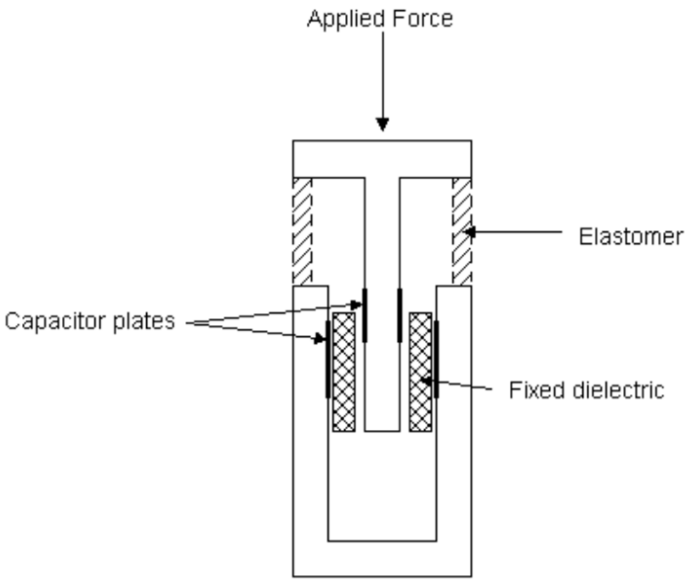

Fig 5.2 Measurement system with attached capacitive displacement sensor [4].

This type of sensor was previously investigated by Whittaker [5], Birss [6] and George [7], where one plate of the capacitor was fixed to the free end of a sample in order to measure magnetostrictive vibration. The change of sample length is proportional to the change of the capacitance which is converted by the demodulator circuit to a change in the voltage proportional to the fixed capacitor plate displacement. This type of transducer has a very high resolution up to 0.0001×10^{-6} and it is not affected by stray magnetic field.

Magnetostriction measurements using capacitive displacement sensors have several disadvantages such as setting the air gap in the capacitor before each measurement is time consuming and the capacitor dielectric is air so its permittivity would vary with temperature and humidity [8].

5.1.2.3 Resistance Strain Gauge

The resistance strain gauge is a widely used, well known, strain measurement method [9] [10] [11]. The strain element can be a wire or foil resistive pattern whose shape and size depends on the application. The resistive pattern is mounted on a backing material and bonded on the sample surface. The gauge with a defined resistance is connected with an electronic circuit which can exist in quarter, half or full bridge configurations.

The selection of a bridge configuration depends on the quantity of active elements required for the strain measurement as shown in Fig 5.3.

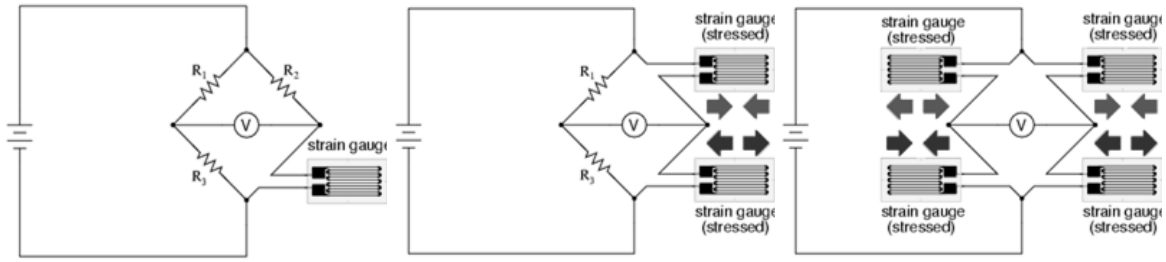

a) *b)* *c)*

Fig 5.3 Strain gauge circuits: a) quarter-bridge b) half-bridge c) full-bridge [12].

Under extension or contraction of the substrate, the length of the resistive pattern gauge changes and this is proportional to the change of the gauge resistance as shown in Fig 5.4.

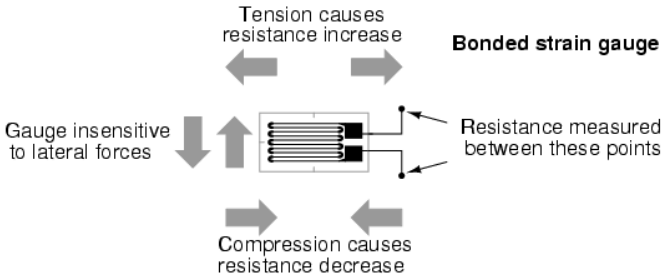

Fig 5.4 Resistance strain gauge [12].

The resolution of the strain gauge is approximately 0.1 x 10^{-6}. The strain gauge has become common technique because of simplicity of strain measurement.

The resistance strain gauge as a magnetostriction measurement technique was investigated by Anderson [13] who presented a several disadvantages of the strain gauge in magnetostriction measurements under stress (±10 MPa). The gauge needs to be bonded to the sample surface using an epoxy resin and also the output wires of the gauge have to be soldered to the gauge terminals. This is a time consuming procedure and requires good manual skills. Also it was observed [13] that the strain gauge was extremely sensitive to vertical vibrations and bending stress for the strip under applied compressive stress. Furthermore a low output signal to noise ratio was obtained during strain detection, even up to 3 micrometers. Temperature and pick up field can be cancelled by using a compensating dummy gauge.

5.1.2.4 Optical Measurement Techniques

The Laser Doppler Velocimeter (Homodyne laser system) makes use of the Doppler Effect in a single laser beam to measure the vibratory motion of a reflecting target as shown in Fig 5.5.

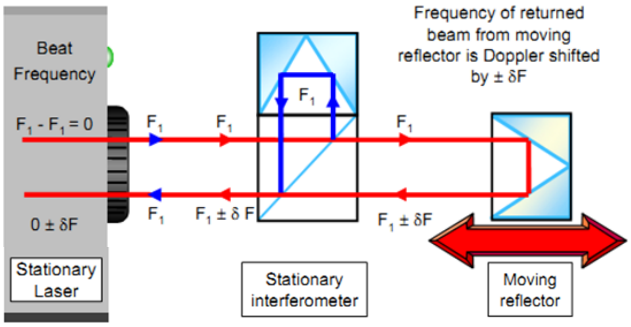

Fig 5.5 Homodyne laser system [14].

The first use of the laser Doppler technique to measure magnetostriction of silicon steel strip was reported by Nataka et al [15] who fixed two mirrors in the some distance apart on the strip surface in order to reflect the laser beam. The modulated frequency of the reflected laser beam was integrated to provide a differential displacement of the mirrors. The obtained resolution of the laser was 0.04×10^{-6}.

Further investigation of laser techniques was carried out by Nakase et al [16], who compared magnetostriction measurements using a single beam laser Doppler velocimeter (Fig 5.5) with a two beam Heterodyne laser interferometer as shown in Fig 5.6. One beam of the Heterodyne laser was focused on a reference fixed target, and the second one on a moving target fixed to the unclamped end of a strip surface.

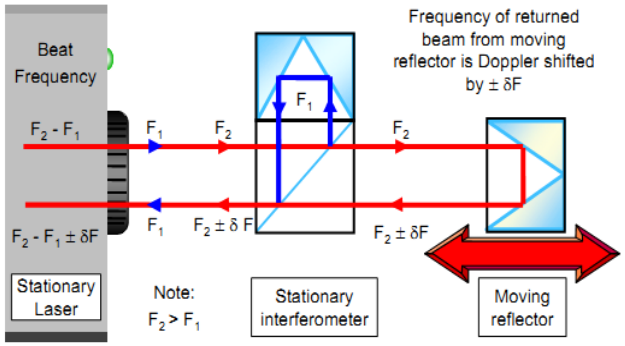

Fig 5.6 Heterodyne laser system [14].

The modulated frequencies of the two beams were subtracted and processed in a similar way to Doppler laser. The resolution for both types of laser was 0.04 x 10^{-6}. The advantage of this measurement technique is its non-contact nature which means that the laser is not exposed to changes in temperature and magnetic field.

However in these investigations the laser technique was only considered for testing samples without applying external stress. Moreover a magnetisation coil wrapped on the sample would cause difficulties in access during placing the mirrors on the sample surface.

5.1.2.5 Piezoelectric Displacement Transducer

Piezoelectric displacement transducers consist of a pin mechanically connected with a piezoelectric transducer similar to a record player pick-up shown in Fig 5.7.

Fig 5.7 Record player pick-up [17].

Magnetostriction measurement using this type of transducer was developed by Brownsey and Maples [18], Simmons and Thompson [19] and then followed by Mapps and White [20]. Each measured magnetostriction between two points on the sample surface, where two sharp styli were placed as shown for instance in Fig 5.8.

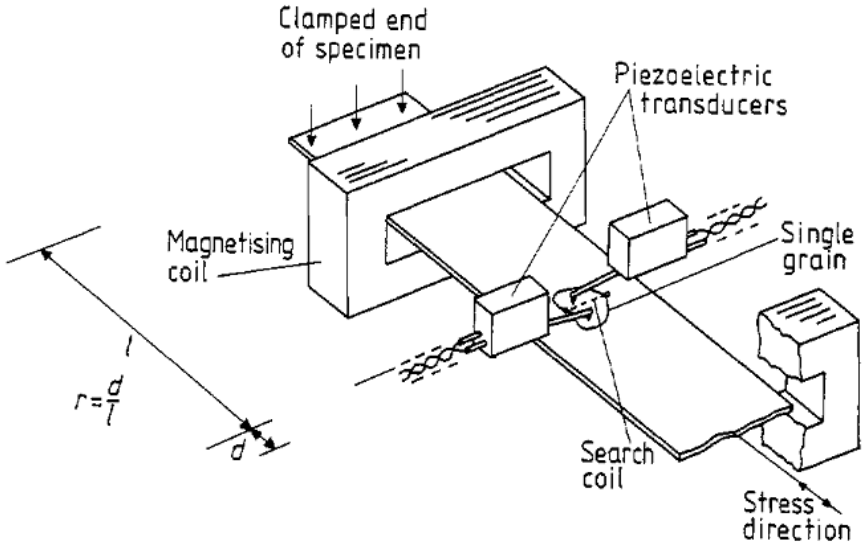

Fig 5.8 Schematic diagram of the magnetostriction measurement system with two piezoelectric transducers [20].

The magnetostriction was measured under applied stress up to 6 MPa. The resolution of the transducer obtained by Mapps and White was 0.002 x 10^{-6}. The piezoelectric displacement transducer is not susceptible to stray magnetic fields and offers a wider operating temperature range.

The low force the stylus applied to the surface should not affect the measurement. The transducer is sensitive to transverse and vertical vibrations which can be partially eliminated by the stereo phonograph cartridge with the series connected outputs [18]. Also in this case the measurement under applied stress, similar to the target of the laser, would introduce a problem resulting from the direct contact of the sensor with the sample surface.

5.1.2.6 Piezoelectric Accelerometer

The piezoelectric accelerometer includes the sensing element that is a seismic mass attached to the polarised ferroelectric piezo-ceramic element as shown in Fig 5.9.

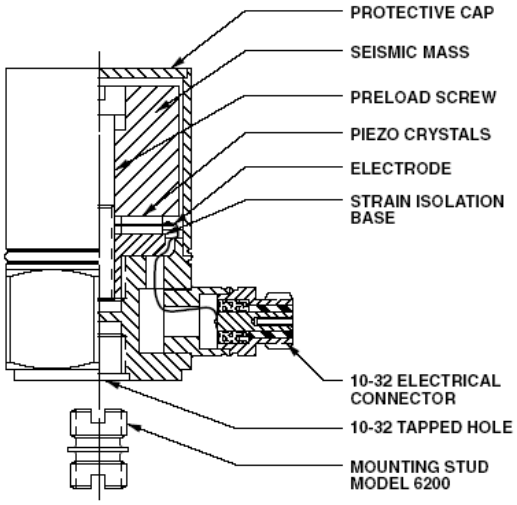

Fig 5.9 Cross section of a piezoelectric accelerometer [21].

Under external vibrations the seismic mass is mechanically stressed and it generates an electric charge proportional to the applied force. This type of accelerometer often has a charge amplifier (converts the charge to voltage) which when connected with a control system gives an acceleration output signal which after double integration provides a displacement. The accelerometer requires a direct contact with the magnetised material and is shielded by aluminium housing.

A system using two accelerometers to measure magnetostriction under stress (±10 MPa) was first built by Stanbury [2] and further developed by Anderson [22] as shown in Fig 5.10. The system showed that piezoelectric accelerometers, where the first accelerometer is fixed to the clamp of the pneumatic cylinder connected together with as free end of the sample and the second one is connected with the fixed end, shows a stable response and a resolution of less than 0.01 x 10^{-6}. The advantage of this measurement technique is that the sample requires little set up time. Also the piezoelectric accelerometer offers a wide operating temperature range and it is not susceptible to changes in magnetic field [23].

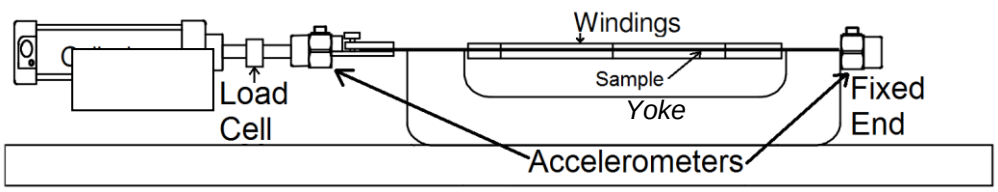

Fig 5.10 A system to measure magnetostriction under stress by using two piezoelectric accelerometers[22].

5.1.3 The Final Selection of the Transducer for Magnetostriction Measurement under Applied Stress

It is proposed to use a transducer with a minimum resolution of approximately 0.01×10^{-6}. Measurement of uniaxial magnetostriction requires the sensor to have a very low, ideally zero sensitivity in directions other than the measurement direction. The sensor should also be insensitive to stray magnetic field which could be introduced by the surrounding environment, and change in temperature. The system should require little or no setting up or calibration of the sensor by the operator which is important when a large quantity (several thousand) of samples is to be measured. Advantages and disadvantages of reviewed techniques to be used to measure magnetostriction under stress are presented in Table 5.1.

Table 5.1 Advantages and disadvantages of reviewed techniques for magnetostriction measurements under stress

Measurement technique	**Resolution**	**disadvantage**	**advantage**
Linear Variable Differential Transformers	0.01×10^{-6}	• affected by stray field and temperature • difficulties of adjustment • direct contact of the sensor with the sample surface	• high resolution • relatively low cost
Capacitive Displacement Sensors	0.0001×10^{-6}	• difficulties of adjustment • direct contact of the sensor with the sample	• very high resolution • relatively low cost • not susceptible to changes in magnetic field
Strain Gauge	0.1×10^{-6}	• time consuming fixing procedure and requires good manual skills • extremely sensitive to vertical vibrations and bending stress for the strip under applied compressive stress	• relatively low cost for small range of tested samples • simple measurement procedure

		• low output signal to noise ratio • direct contact of the sensor with the sample surface. • large quantity of strain gauges is required for range of tested samples which makes this technique very expensive • lower resolution for larger gauges	
Optical Measurement Techniques	0.04×10^{-6}	• direct contact of the mirrors with the sample surface. • high cost	• high resolution • not susceptible to changes in magnetic field • wide range of operating temperature
Piezoelectric Displacement Transducer	0.002×10^{-6}	• direct contact of the sensor with the sample surface	• high resolution • wide range of operating temperature • relatively low cost
Piezoelectric Accelerometer	0.01×10^{-6}	• direct contact of the sensor with the sample	• high resolution • sample requires little set up time • wide range of operating temperature • not susceptible to changes in magnetic field • relatively low cost

A transducer with the highest quantities of advantages is the piezoelectric accelerometer. The accelerometer is an industrial measurement device used for the

industrial applications. It is not sensitive to atmosphere, and also has a high range of operating temperatures and relatively low cost.

The in-contact nature of accelerometer would not affect the magnetostriction measurement, because of its small size and light weight. Also the magnetostriction measurement under stress requires clamping a sample on both ends. Therefore the accelerometer could be fixed to the one of the clamps.

Taking into consideration all of these arguments the accelerometer was selected to be the most suitable for magnetostriction measurement under applied stress. More detailed description of this technique is presented in section 5.2.1.

5.2 Magnetostriction Measurement System

A magnetostriction measurement system as shown in Fig 5.11 was designed and constructed developing on previous systems [22, 24] discussed in section 5.1.2.6. A strip (305 x 30 mm) of electrical steel is inserted into the support, which is enwrapped by secondary and primary windings with number of turns 179 and 274, respectively. The H is measured by the current i_h passing through the primary (magnetising) coil and B is a voltage V_b measured from the secondary (search) coil. During magnetisation, flux is closed through the steel yoke and stress is applied to the sample via a clamp, which is connected to a pneumatic cylinder. The opposite end of the strip is fixed. A load cell sensor is positioned between the clamp and the cylinder to control the stress applied to the sample. The magnetostriction of the sample is calculated by double integration of the output of two piezoelectric accelerometers

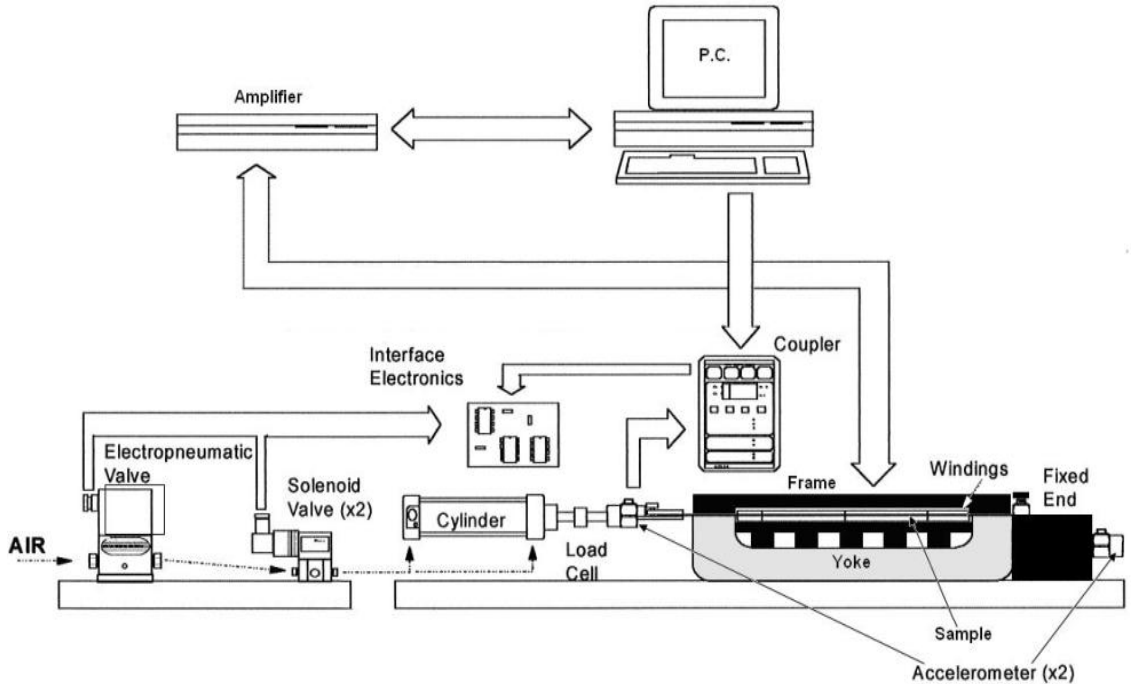

Fig 5.11. Schematic diagram of a developed system to measure magnetostriction in single Epstein strips under applied longitudinal tension or compression.

The accelerometers are supplied with a constant current and their outputs are coupled by a suitable Coupler. All signals are controlled and analysed by the LabView Virtual Instrument (VI) software.

The system includes a measurement and control unit connected with the stressing and magnetising rig. The measurement unit shown in Fig 5.12 includes:

a) Pc desktop with two National Instruments data acquisition cards
b) BNC connectors for I/O
c) Power supply coupler
d) Power supply (+12V)
e) Amplifier
f) Two solenoid switching valves
g) Electro-pneumatic valve (pressure regulator)
h) Insulation transformer

a) Front *b) Rear*

Fig 5.12 Front and rear side of a measurement and control unit.

The system has been tested using CGO and HiB Epstein strips provided by Cogent Power Ltd in order to assess its magnetostriction and also power loss under stress.

5.2.1 Piezoelectric Accelerometer

The magnetostriction vibrations are measured from the difference of outputs from the two accelerometers located at the free and fixed ends of the strip. The differential output signal is double integrated to obtain the magnetostriction of the strip.

The chosen Piezo-Beam accelerometer is a sensing element consisting of a ceramic bimorph beam supported by a centre post that when bending occurs as a result of being subjected to vibration, the cantilevered beam element yields an electrical charge as shown in Fig 5.13.

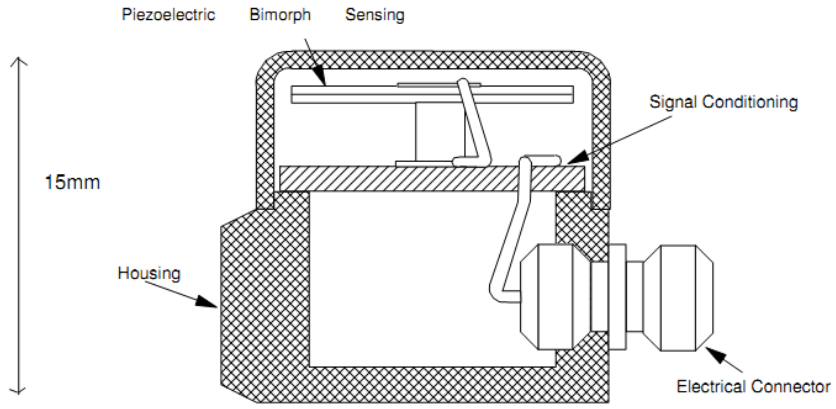

Fig 5.13 Cross section of the piezo-beam bimorph accelerometer [22].

A high impedance level of the charge mode signal in pico-Coulomb per acceleration relative to free-fall (pC/g), generated by the piezo ceramics is converted to a low impedance voltage mode signal (V/C) by a charge amplifier, built inside the sensor. The input acceleration of the sensor is converted by the seismic mass into analogous stress applied to the piezo ceramics [25]. The output charge signal is proportional to the acceleration. The low impedance type requires an external power supply coupler to energize the electronics and decouple the subsequent DC bias voltage from the output signal. The sensitivity of the accelerometer is 1000 mV/g. The voltage outputs from two accelerometers are passed through a summing amplifier and then integrated using LabView software.

To choose the most suitable accelerometer for this system with required resolution, some calculations had to be made. The resolution required for the system is 0.01 µm in order to measure magnetostriction of the GO steel. Therefore the peak magnetostriction for the sample with magnetising path of 0.27 mm equals 0.0027 µm. The peak acceleration can be calculated by double differentiation (5.3) of displacement (5.1) using equation (5.4)

$$x = Asin(\omega t) \tag{5.1}$$

$$\frac{dx}{dt} = A\omega cos(\omega t) \tag{5.2}$$

$$\frac{d^2x}{dt^2} = -A\omega^2 sin(\omega t) \quad (5.3)$$

Therefore,

$$a = -\omega^2 x = -(2 \times \pi \times f)^2 \times \lambda \times L \quad (5.4)$$

where,

a = Acceleration (m/s^2)

x = Displacement (m)

A = Constant

ω = Angular frequency (Rad/s)

t = Time (s)

f = Magnetostriction fundamental frequency (Hz)

λ = Measured magnetostriction (microstrain)

L = Magnetised length of a strip (m)

For the minimum magnetostriction of 0.0027 µm with fundamental frequency 100 Hz the minimum measured acceleration is 1.18 x 10^{-3} m/s^2.To define the acceleration range of the sensor, the maximum acceleration, measured in g (1g = 9.81 m/s^2), for the saturation magnetostriction of GO steel in the [001] direction can be calculated using equation (5.4). Table 5.2 Acceleration at a range of frequencies for magnetostriction of 24 µm (peak)Table 5.2shows the change in acceleration for saturation magnetostriction of 24 µstrain under various fundamental frequencies.

Table 5.2 Acceleration at a range of frequencies for magnetostriction of 24 µm (peak)

Magnetisation frequency (Hz)	**Magnetostriction fundamental frequency (Hz)**	**Acceleration (m/s^2)**	**Acceleration (g)**
50	100	2.9	0.3
70	140	5.7	0.6
90	180	9.4	1.0
120	240	16.6	1.7
140	280	22.6	2.3
160	320	29.6	3.0
180	360	37.4	3.8
200	400	46.2	4.7
210	420	50.9	5.2

The chosen accelerometer with the lowest mass and required sensitivity is the 8636C5 Kistler Piezo-Beam. The Piezo-Beam accelerometer offers sensitivity 1 V/g and acceleration range of ±5 g which satisfies the specification needs shown in Table 5.3. The acceleration frequency range reaches up to 3 kHz which makes the accelerometer sufficient to measure the acceleration signal to the 30^{th} harmonic. The resonant frequency, transverse sensitivity and operating temperature rate as presented in Table 5.3 satisfy the measurement requirements.

The two 8636C5 accelerometers were placed in the system as shown in Fig 5.11 are connected with four channel power supply coupler (model number 5134).

Table 5.3 Specifications of 8636C5 piezo-beam accelerometer [26]

Specifications	**Kistler 8636C5** **Piezo-Beam Accelerometers**
Acceleration range	± 5 g
Acceleration limit	± 8 g
Threshold (nom.)	120 μg_{rms}
Sensitivity	1 V/g
Frequency Range (± 5 % limit)	0.8 Hz to 3 kHz
Resonant Frequency (nom.)	9 kHz
Operating temperature range	0 to 65 °C
Mass	5 g
Transverse sensitivity	< 1 %

5.2.2 Stressing System

The stress is applied to the strip by a pneumatic cylinder [27] with three guides as shown in Fig 5.14. The maximum pressure supplied by the compressor to the cylinder is 0.8 MPa. Therefore the cylinder can apply maximum 43.5 MPa of tension and 33.5 MPa of compression to the Epstein strip. The applied stress is measured by the load cell which is fixed to the middle guide of the cylinder (Fig 5.14). The load cell can measure the maximum applied stress to the Epstein strip up to 22.2 MPa [28].

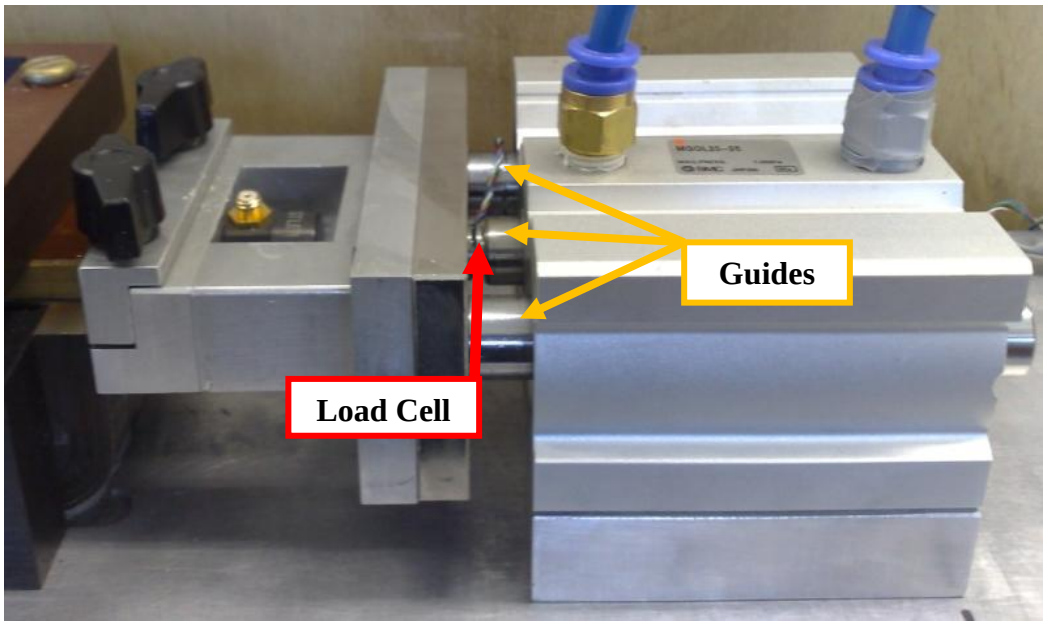

Fig 5.14 Pneumatic cylinder with load cell fixed to the middle guide.

To calculate the stress σ applied to the strip the following formula was used:

$$\sigma = \frac{V \times \delta \times l}{S_l \times m} \tag{5.5}$$

where,

V = Load cell output voltage (V)

δ = Sample density (kg/m^3)

l = Length of the sample (m)

S_l = Load cell sensitivity (mV/N)

m = Sample mass (kg)

5.2.3 LabView Virtual Instrument Control System

All of the input (measured) and output (generated) signals are connected with the National Instrument data acquisition card (DAQ). This card is controlled by LabView (VI) software. Fig 5.15 shows the front panel of the LabView VI displayed on a PC desktop screen.

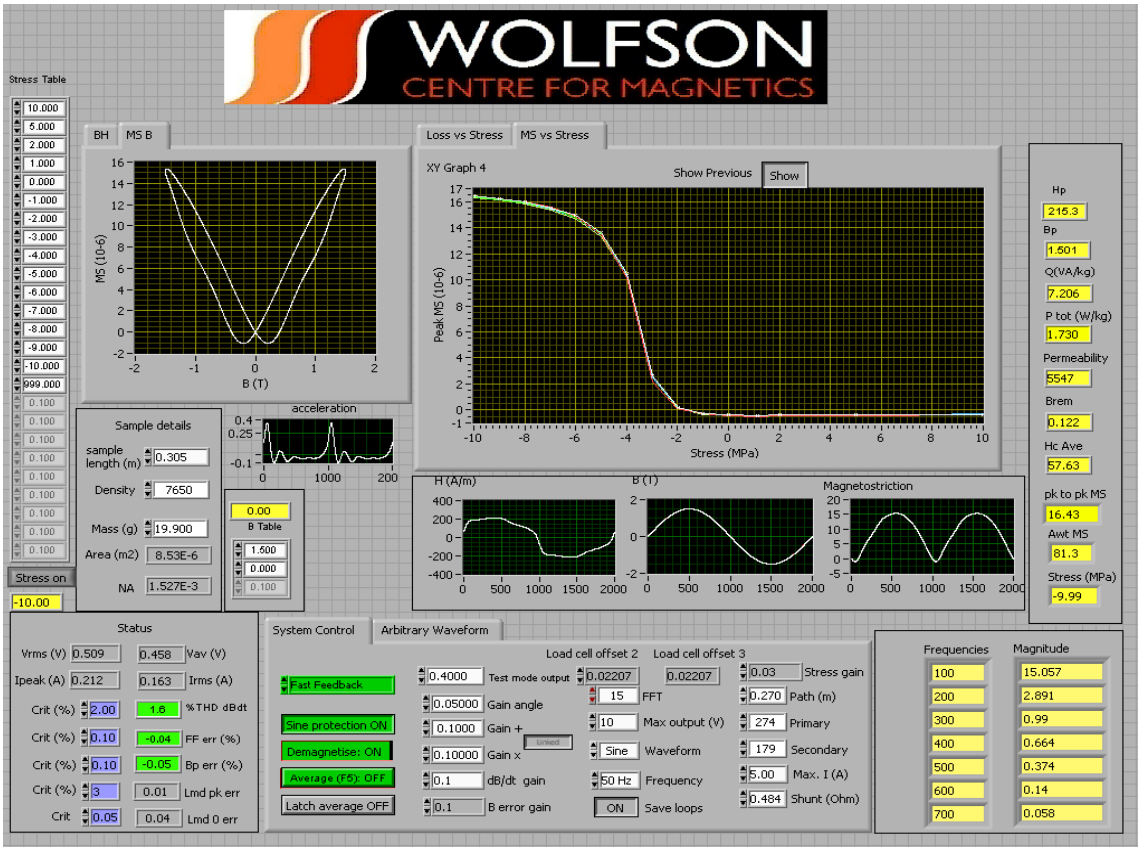

Fig 5.15 The Front panel of the LabView VI software.

The measured waveforms of H, B, acceleration, displacement and also the B vs. magnetostriction are plotted on the LabView front panel in real time. The values of pk-pk magnetostriction and specific total loss (which is expressed as Watt per kg) against applied stress are presented as measured points after a full cycle of the measurement. The measured parameters and controlled signal waveforms are saved in a file which is compatible with Microsoft Excel.

The peak to peak magnetostriction is given by

$$\lambda = \frac{1}{\omega^2} \times \frac{g}{G \times S_a} \times \frac{1}{L} \times V \times 10^6 \qquad (5.6)$$

where,

g = calibration value equal 9.81 m/s^2

G = Coupler gain (1-100)

S_a = Accelerometer sensitivity (V/g)

V = double integrated Coupler output (V)

The algorithm based on equation (5.6) was written as a sub VI in the main LabView VI and is presented in Fig 5.16.

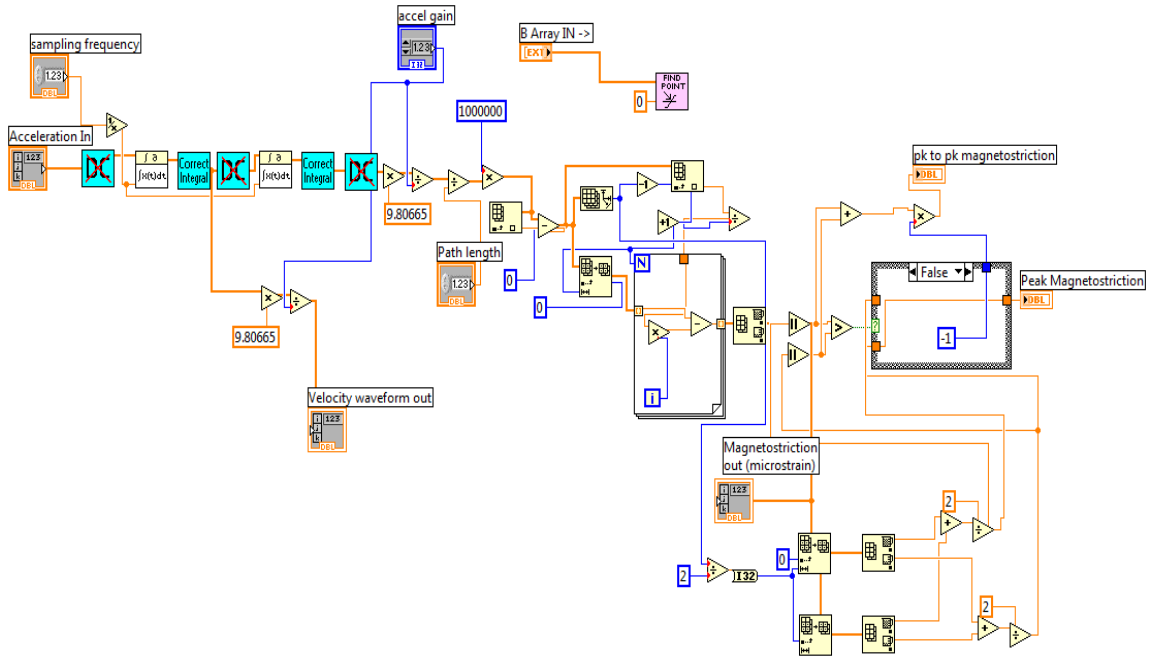

Fig 5.16 LabView VI algorithm to calculate pk-pk magnetostriction with double integration of acceleration.

The average specific total power loss $\left[\frac{W}{kg}\right]$ per unit mass and frequency is measured using [29]

$$P = \frac{f}{\delta}\int_0^{1/f} H(t)\frac{dB(t)}{dt}dt \tag{5.7}$$

Fig 5.17 shows the sub VI algorithm to calculate the specific total loss (5.7) of the measured sample.

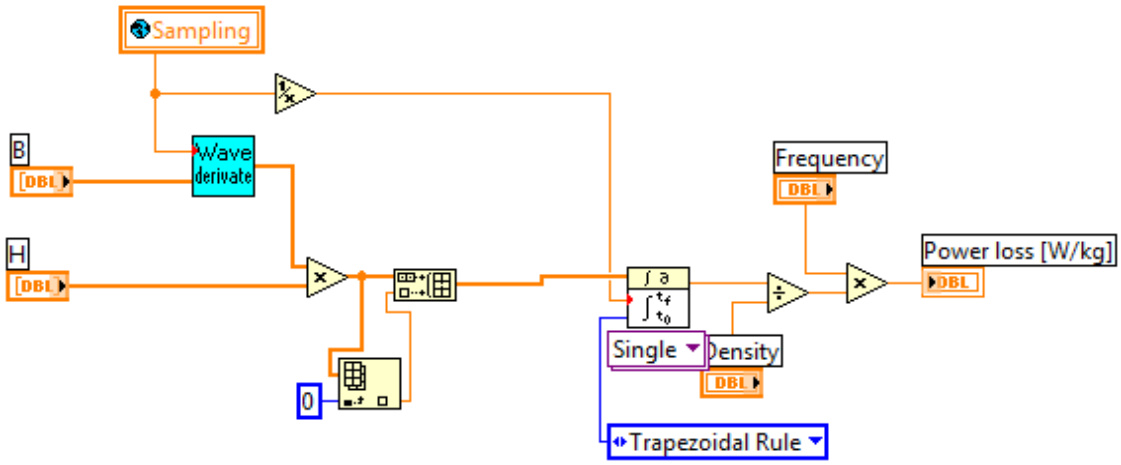

Fig 5.17 LabView VI algorithm to calculate specific total loss.

The parameters as frequency, flux density and applied stress are defined by a user before the full cycle of measurement.

Fig 5.18 shows an example of sensitivity curves of pk-pk magnetostriction and specific total loss against applied stress (±10 MPa) of CGO measured under 1.7 T and 50 Hz.

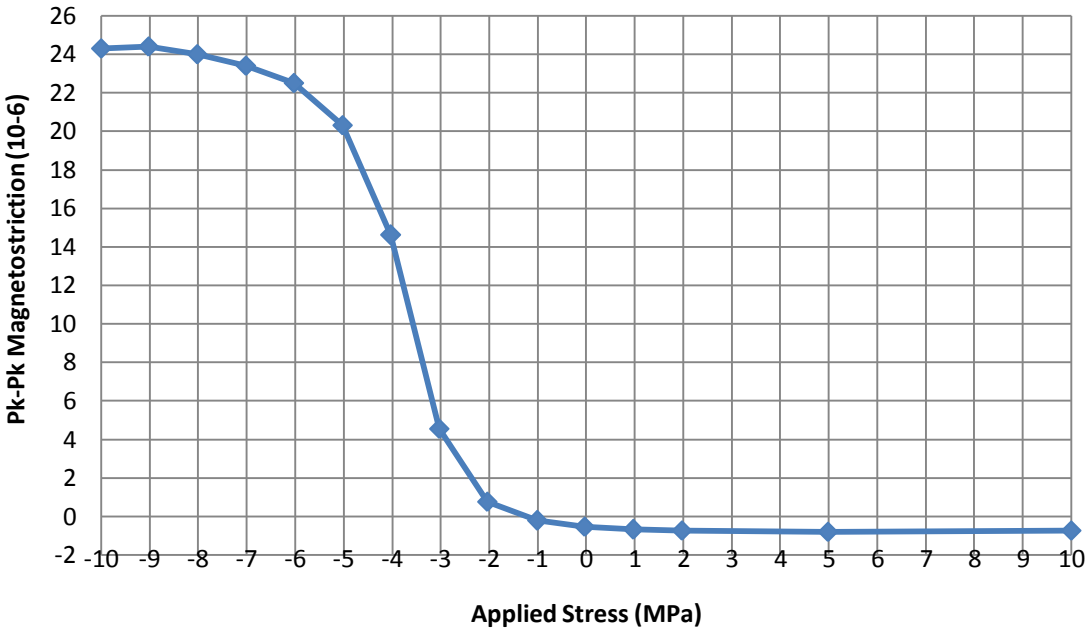

a)

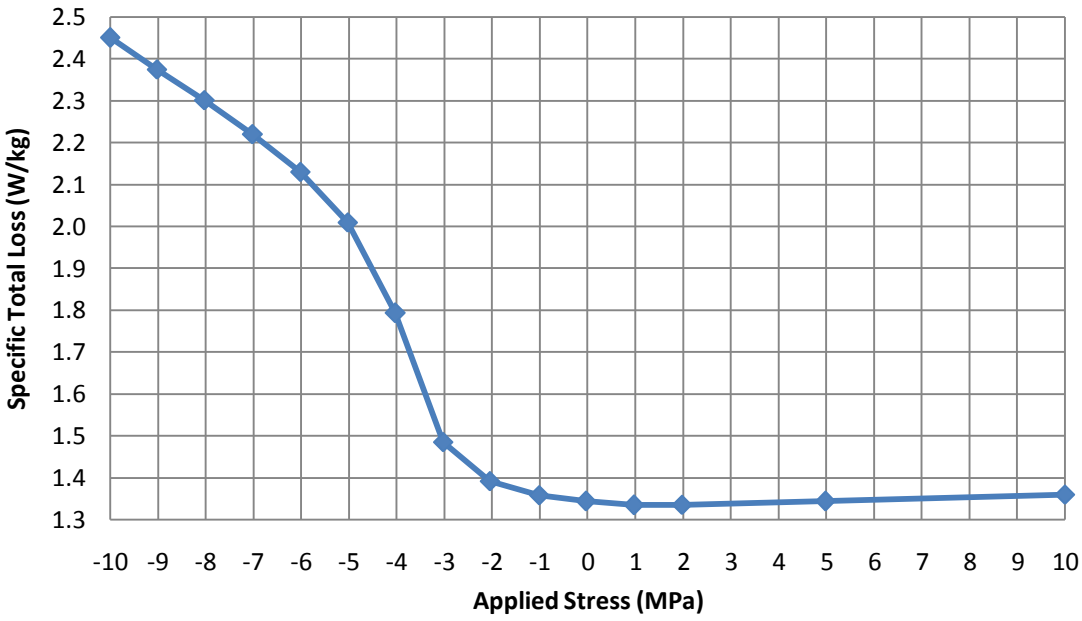

b)

Fig 5.18 Peak to peak magnetostriction (a) and specific total loss (b) under ±10 MPa of stress.

5.3 Development of the Measurement System

5.3.1 Challenges in System Construction

One of the challenges of magnetostriction measurement is to achieve uniform and repeatable applied stress, particularly compression. Therefore some mechanical issues have to be addressed during design and construction of the magnetostriction measurement system.

It was found that an acetal (copolymer) bed under the sample together with a frame applied to the top surface had to be perfectly aligned in order to avoid the sample bending. The frame must apply slight pressure to the sample surface to keep the strip flat under compression. If this pressure is too high it can create difficulty in inserting the sample into the frame and more importantly, reduce the measured magnetostriction. Fig 5.19 shows that this is particularly noticeable under -10 MPa of compression where magnetostriction is attenuated by 50 % of a typical strip of HiB magnetised under 1.7T at 50 Hz.

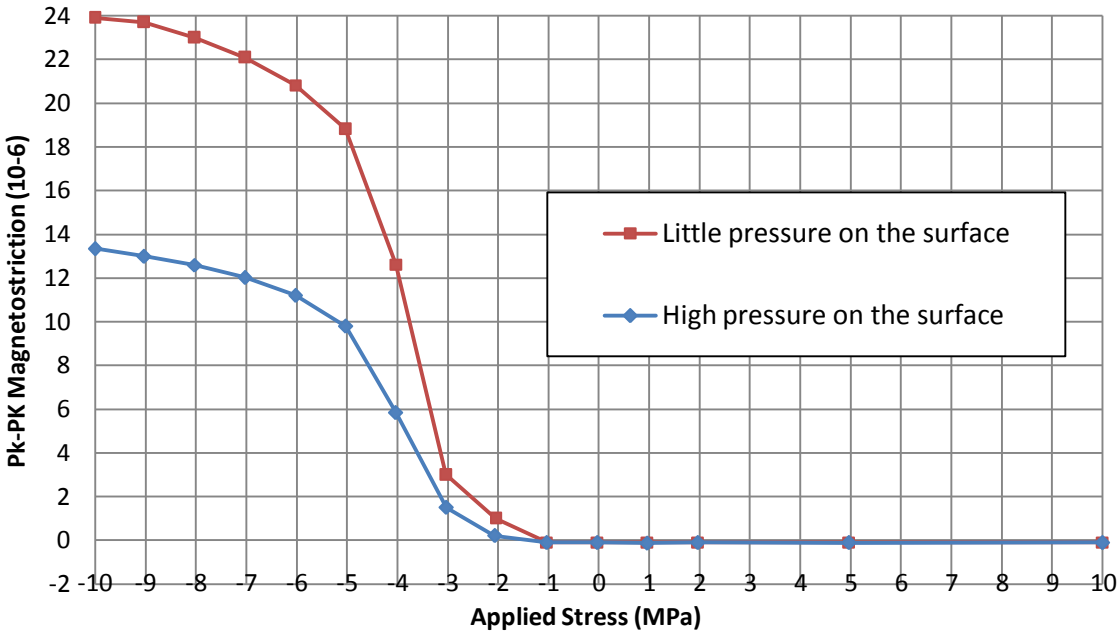

Fig 5.19. Pk-pk magnetostriction measured at 1.7T (50Hz) on a strip with little and high pressure applied to the surface.

It was necessary for the sample to be capable of accommodating strips ranging in thickness from 0.23 mm to 0.5 mm. To achieve this, Tufnol strips of different thicknesses were fabricated and inserted as shown in Fig 5.20 to eliminate free air gaps between the sample and the frame

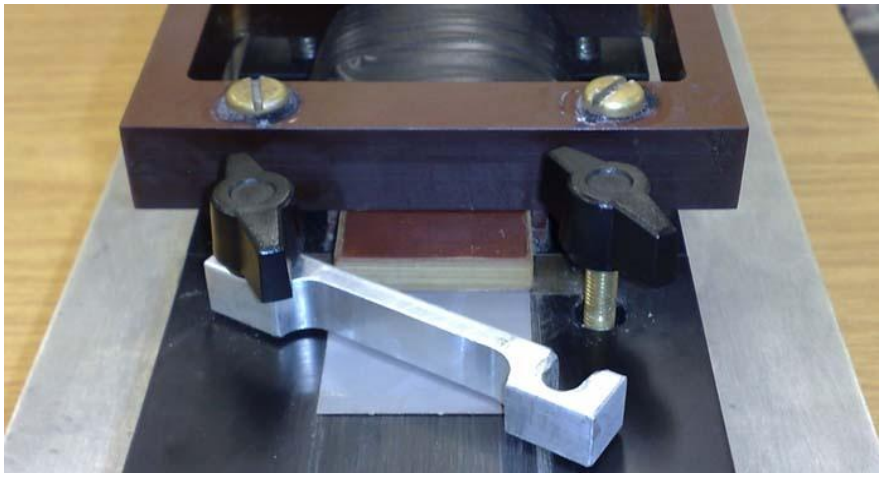

Fig 5.20 Sample restrain from buckling.

To reduce any torsion from the direction of the applied stress, guides were used to limit both sample rotation and out of plane stress (Fig 5.14). Fig 5.21 shows newly designed and constructed test system.

Fig 5.21 Newly designed and constructed test system.

5.3.2 Operational Challenges of the Measurement System

When a measurement is to be repeated, the sample has to be removed and reinserted in order to release any residual stress due to clamping or previous stress cycling. In practice it can be difficult to insert and clamp the strip in an identical position in the test system. This can lead to unequal distribution of applied stress in the clamped strip. The repeatability of five cycles (series 1 to 5) of the magnetostriction measurement on a typical single strip of CGO with using a precise technique of clamping and adjusting the sample before each test is shown in Fig 5.22. After each series the sample was removed from the system and inserted again.

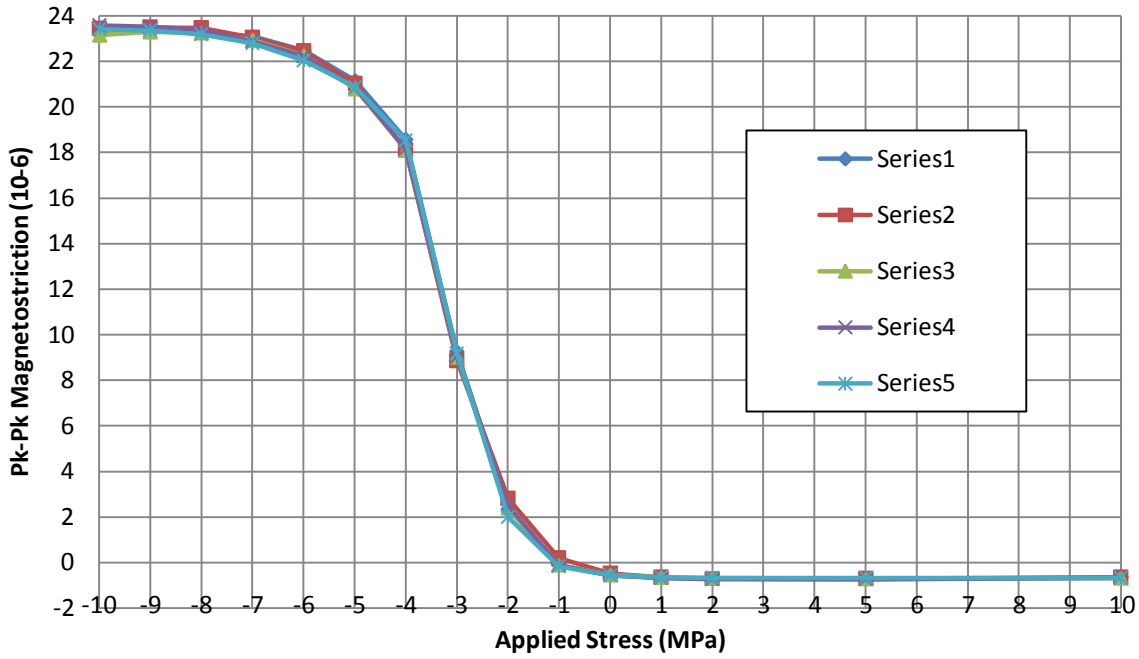

Fig 5.22 Typical repeatability of the magnetostriction measurement system on a CGO sample 1.7 T, 50 Hz.

5.3.3 Importance of Physical State of the Specimen

Magnetostriction depends not only on the accuracy of the system but also on the physical condition of the sample which may not be visible to the naked eye. If, before measurement, a strip is slightly twisted or has damaged edges or burrs, the damage can be increased as a result of stress cycling so the magnetostriction can change as shown in Fig 5.23. The magnetostriction in this slightly damaged sample was found to increase by 10% after each measurement (series). After the each series of measurement the sample was removed from the system and inserted again.

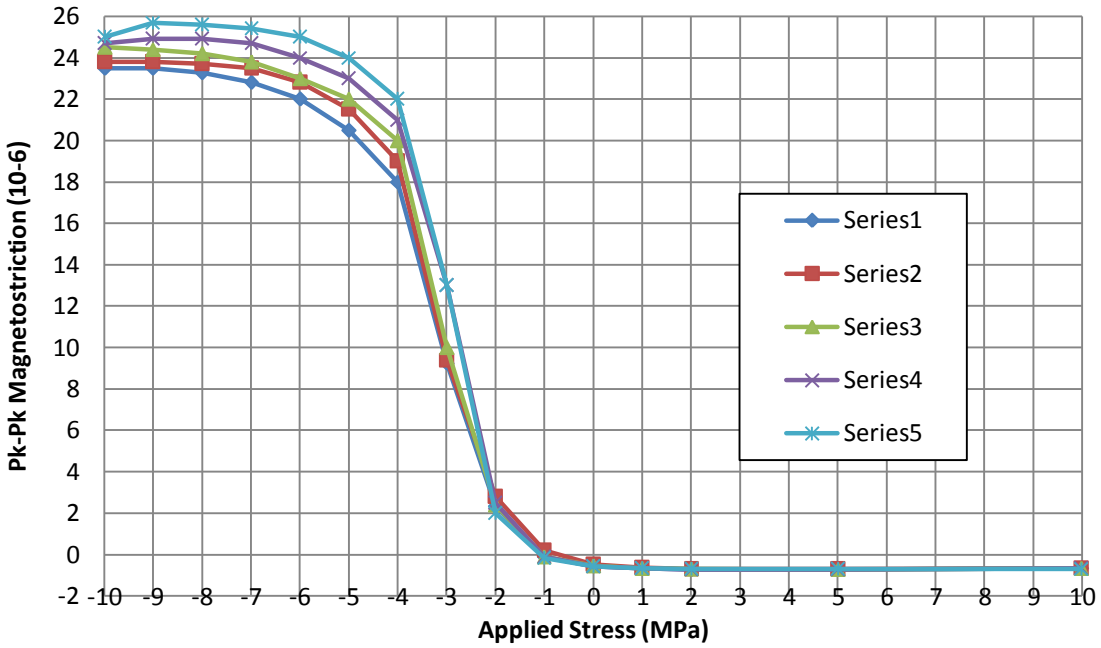

Fig 5.23 Poor repeatability of measurement caused by increasing damage to a CGO sample during repeated testing (1.7 T, 50 Hz).

5.3.4 Resonance of the Magnetostriction Measurement System

It is important to be aware of the effect of resonant modes of any vibration measurement system. The natural frequency f_n of an Epstein strip can be calculated from the following standard mechanical resonance equation

$$f_n = \frac{n}{4L}\sqrt{\frac{E}{\delta}} \qquad (5.8)$$

Using a value of Young's modulus, E, of 110 x 10^9 Pa for GO steel in the RD, strip length, L, of 0.305 m and density, δ, of 7650 kgm^{-1} the natural resonance frequency of a strip is 3.1 kHz (where n=1 for the first resonant mode). It is more complex to evaluate natural frequency for the complete system as it would require a model incorporating both mass and springs [30]. However it is difficult to estimate the value of stiffness factor, mass and spring constant of the pneumatic cylinder. The system itself exhibited resonance at a magnetisation frequency of 170 Hz and fundamental magnetostriction 340 Hz under applied compressive stress. This was found by magnetostriction measurements at various magnetisation frequencies. The natural frequency of the system is much lower than the sample alone. Measured vibration under

resonance frequency of the system, can increase magnetostriction under compressive stress of GO steel by up to 300% as shown in Fig 5.24.

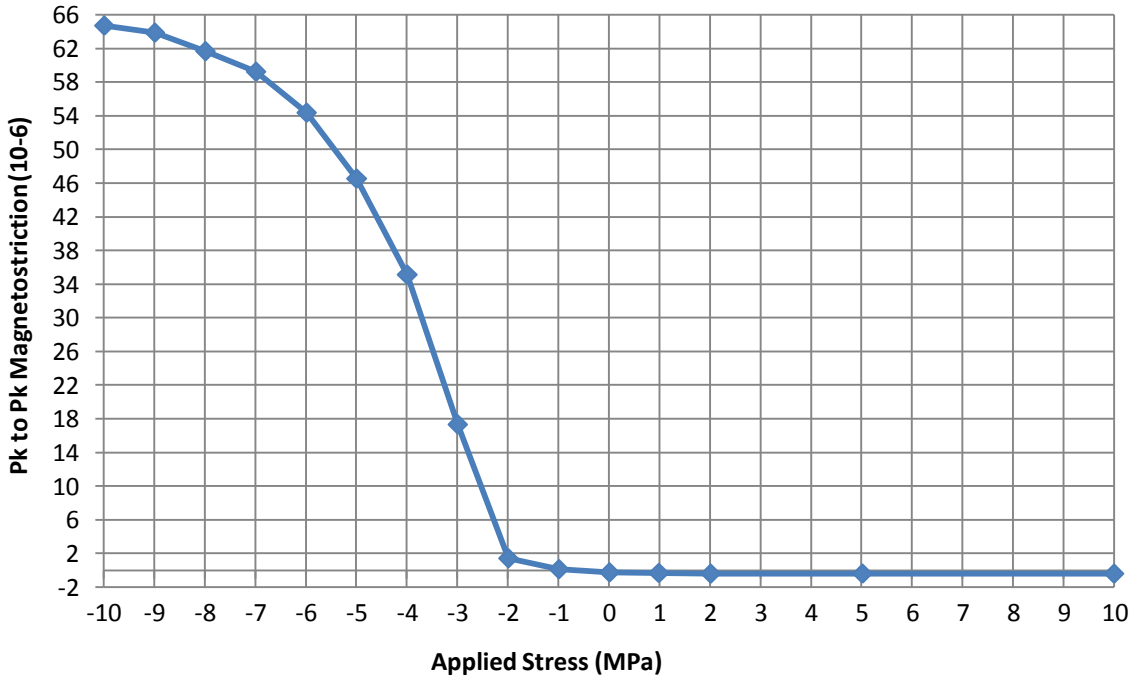

Fig 5.24 Influence of the resonance on the magnetostriction under applied stress at 1.7 T and 170 Hz of magnetisation in GO steel.

The effects of resonance on the harmonics of magnetostriction under compressive stress are not fully understood. The higher harmonics, above 400 Hz of magnetostriction under compression increases at magnetisation frequency of 60 Hz and above. Therefore all magnetostriction and loss measurements under stress on the system were carried out under 50 Hz of magnetisation.

5.4 Specification of the System

- The system was built to measure Epstein strips: length 305 mm, width 30 mm with gauges (thicknesses) : 0.23 mm; 0.27 mm; 0.30 mm; 0.35 mm; 0.50 mm.
- The range of average flux density B (T): 0.1 T - 1.9 T with accuracy up to 0.001T.
- Applied stress: +10 MPa tensile to -10 MPa compressive with accuracy up to 0.01 MPa.
- Frequency of magnetisation:
    a) Without stress 1 Hz - 1 kHz

b) Under stress 25 Hz - 70 Hz

- In the real time LabView program is presenting on screen:
  a) Pk to pk of magnetostriction and specific total loss versus stress, as an example shown in Fig 5.25,

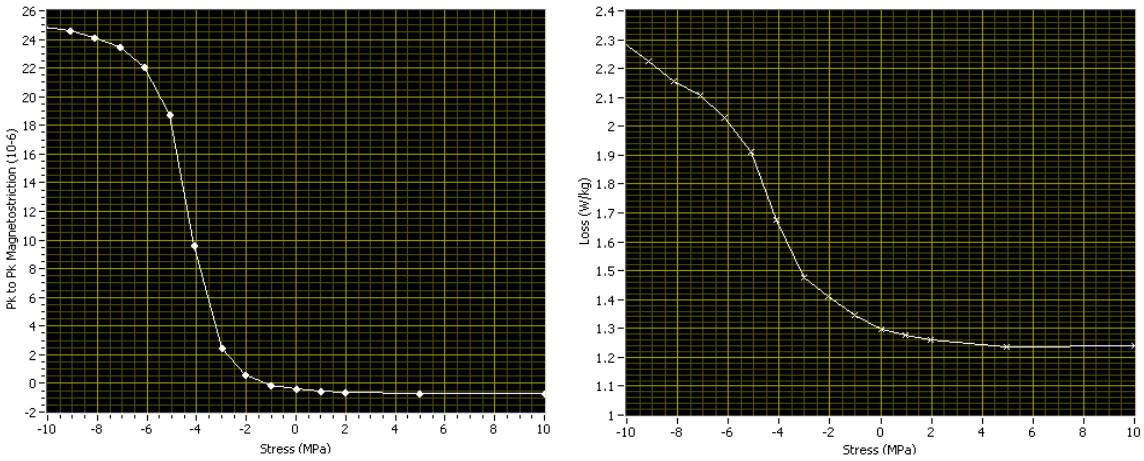

a) *b)*

Fig 5.25 Pk-pk magnetostriction (a) and specific total loss (b) sensitivity curves presented on screen in the LabView software (1.7T, 50 Hz).

b) harmonics of magnetostriction,

c) Waveforms per period of: H (A/m), B (T) and double integrated acceleration (μσ), as an example shown in Fig 5.26,

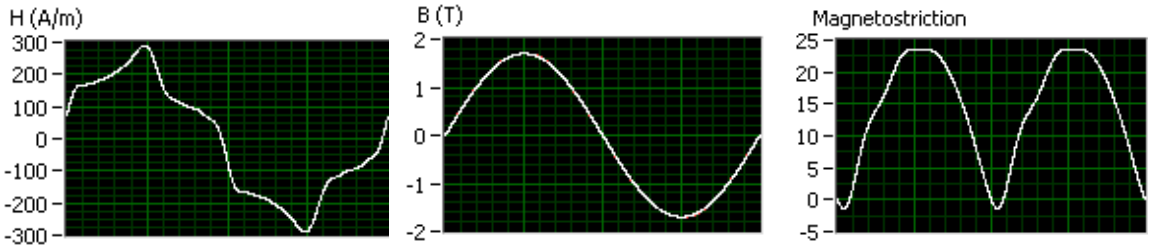

a) *b)* *c)*

Fig 5.26 Waveforms per period of H (a), B (b) and magnetostriction (c).

d) Loops of flux density vs. magnetostriction and magnetic field, as an example shown in Fig 5.27.

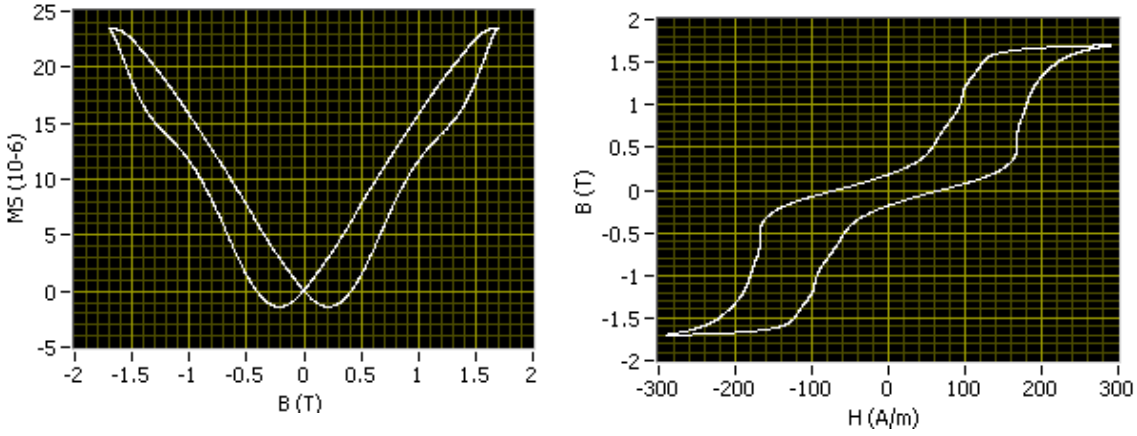

a) *b)*

Fig 5.27 Loops of flux density vs. magnetostriction and magnetic field under -10 MPa at 1.7 T, 50 Hz.

5.5 Operational Mode

Before the system is run, the user must specify in the LabView program values of:

1. Sample mass (g)
2. Sample density (kg/m^3)
3. Sample length (m)
4. Range of stress to apply (MPa)
5. Value of peak of B (T)
6. Value of magnetisation frequency (Hz)
7. The total harmonic distortion of the dB/dt waveform (THD % - within 4%)
8. The form factor of the detected B waveform (FF % - within 0.1%)
9. The peak value of the detected B waveform (B_{peak}% - within 0.1%).

The procedure of inserting and clamping a sample inside the stressing rig (Fig 5.28) has to be followed by steps:

1. Insert the sample in to the rig,
2. Ensure the sample is firmly pressed to the edge of the sample holder which has been machined to ensure perfect sample alignment.
3. Clamp the one end of the sample to the system bed,
4. Use a spacer to keep the constant distance between the clamp and the end of the yoke,

5. Start the LabView software,
6. When the offset of the load cell is measured by the software then fully clamp and tighten up the sample.
7. Press enter to start the measurement process.

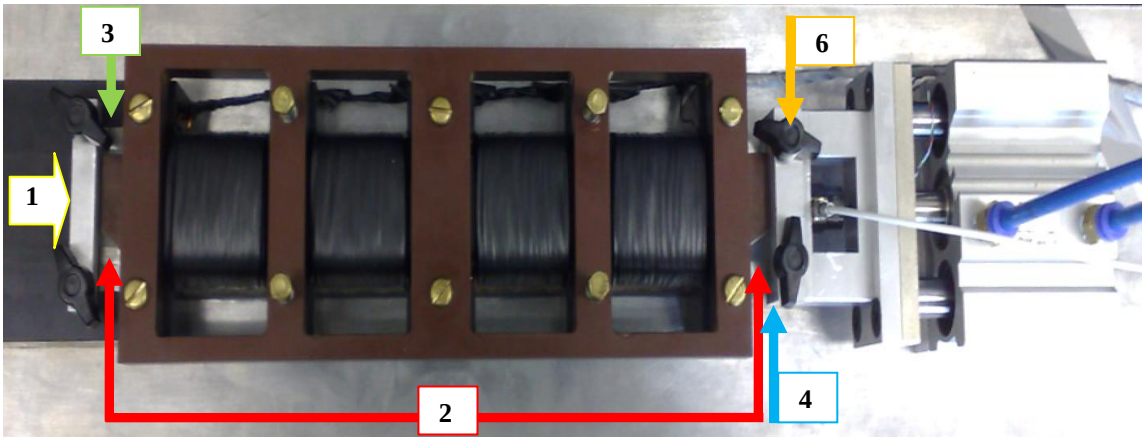

Fig 5.28 The procedure in steps of inserting and clamping a sample inside the stressing rig.

The full cycle of measurement is carried out by the LABVIEW programme in following steps:

1. The first value (the highest tension) from the stress table is applied to the sample,
2. When the stress is reached, the solenoid valve closes the pressure inside the pneumatic cylinder to keep it constant,
3. Next the sample is magnetised at predefined values of peak magnetic flux density and magnetostriction is measured,
4. When values of THD%, FF% and Bpeak% errors reach the minimum required, then the program saves data in the temporary file,
5. Finally the sample is demagnetised by subjecting to an equal or greater AC current which is reduced over a fixed period of time (typically 18 seconds) until zero output current is reached, and then stress changes to the next set value.

The process is repeated till the sample is magnetised under the final value of stress in the table. When the full cycle of measurement for all set points is completed, the program saves data of:

a) Peak B (T)

b) Applied stress (MPa)
c) Pk-pk of magnetostriction (μm)
d) Peak H (A/m)
e) Power loss (W/kg)
f) Magnetostriction harmonics (10 harmonics at integer multiples of fundamental)
g) Waveforms of magnetostriction vs. time
h) B-H loops

5.6 Measurement Uncertainty and Repeatability

The uncertainties of the magnetostriction measurement system were calculated on the basis of recommendations given in UKAS M3003, "The Expression of Uncertainty and Confidence in Measurement" [31].

The measured y is the function of the input quantities of x_1, x_2, ..., x_n.

$$y = f(x_1, x_2, \dots, x_n) \tag{5.9}$$

The mean value of function y can be measured using (5.10), where x_i is the measured value of y.

$$\bar{x} = \frac{1}{n}\sum_{i=1}^{n} x_i \tag{5.10}$$

The standard deviation is defined as

$$s = \sqrt{\frac{\sum_{i=1}^{n}(x_i - \bar{x})^2}{n-1}} \tag{5.11}$$

The uncertainty of u(y) is derived from the standard deviation over the n times of repeated measurement as

$$u(y) = \frac{s}{\sqrt{n}} \qquad 5.12$$

The sensitivity coefficient, c_i, is the partial derivative of the y with respect to x_i and is given by

$$c_i = \frac{\partial y}{\partial x_i} \qquad 5.13$$

When the input uncertainties are combined, a normal distribution referred to the standard deviation was obtained. The combined input uncertainties was expressed at the standard deviation level with coverage factor k_{95}=2. However some of the inputs were expressed as limited values with the rectangular distribution which is expressed as a standard uncertainty with $k_{95}=\sqrt{3}$.

The standard uncertainty of measurement associated to the input value x_i is

$$U_i = \frac{u(y)c_i}{k_{95}} \qquad 5.14$$

The effective degrees of freedom v_{eff} of the combined standard uncertainty is based on the degrees of freedom, v_i, of the individual standard uncertainty of the u(y). Also the v_{eff} was used to determine k_{95} from the t-distribution table [31]. When the k_{95}= 2 the v_{eff} is often infinity.

$$V_{eff} = \frac{u^4(y)}{\sum_{i=1}^{N} \frac{U_i^4(y)}{v_i}} \qquad 5.15$$

$U_c(y)$ is a combined standard uncertainty,

$$U_c(y) = \sum_{i=1}^{n} \sqrt{U_i} \qquad 5.16$$

The expanded uncertainty, $U_e(y)$, is found by taking the square root of the total combined standard uncertainty (6.16) which provides the evaluated uncertainty with a confidence level at 95% of the normal distribution.

$$U_e(y) = k_{95} U_c(y) \qquad 5.17$$

Table 5.4 to Table 5.8 show the uncertainty budget of B_{peak}, applied stress and magnetostriction under 5 MPa, -5 MPa and -10 MPa.

Table 5.4 Determination of the uncertainties in the peak of magnetic flux distribution (B_{peak})

Source of uncertainty	Value ± %	Probability distribution	Divisor	C_i	U_i ± %	Vi or Veff
Card calibration	0.1500	Normal	2.00	1.00	0.0750	∞
Frequency setting	0.0100	Rectangular	1.73	1.00	0.0058	∞
Mass (Balance calibration)	0.0100	Normal	2.00	1.00	0.0050	∞
Length (Rule calibration)	0.0250	Normal	2.00	1.00	0.0125	∞
Length (Reading uncert of rule)	0.0700	Rectangular	1.73	1.00	0.0404	∞
Epstein frame air flux	0.0600	Rectangular	1.73	1.00	0.0346	∞
Repeatability	0.0500	Rectangular	1.73	1.00	0.0289	
Sum of squares					0.0095	
Combined uncertainty					0.0975	
Expanded uncertainty					0.1950	
Declared uncertainty in Bpeak					**0.2**	
at a confidence level of 95 %						

Table 5.5 Determination of the uncertainties in value of applied stress to the 0.30mm thick Epstein strip

Source of uncertainty	Value ± %	Probability distribution	Divisor	C_i	U_i ± %	Vi or Veff
Load cell calibration	0.2000	Normal	2.00	1.00	0.1000	∞
Load cell drift	0.0500	Rectangular	1.73	1.00	0.0289	∞
Length	0.0250	Normal	2.00	1.00	0.0125	∞
Mass	0.0100	Normal	2.00	1.00	0.0050	∞
Non uniformity of stress	0.5000	Rectangular	1.73	1.00	0.2887	∞
Card calibration	0.1500	Normal	2.00	1.00	0.0750	∞
Repeatability	0.5000	Rectangular	1.73	1.00	0.2887	-
Sum of squares					0.1833	
Combined uncertainty					0.4281	
Expanded uncertainty					0.8563	
Declared uncertainty in stress					**0.9**	
at a confidence level of 95 %						

Table 5.6 Determination of the uncertainty in pk-pk magnetostriction under +5 MPa of tension

Source of uncertainty	Value ± %	Probability distribution	Divisor	C_i	U_i ± %	Vi or Veff
Accelerometer calibration	0.2000	Normal	2.00	1.00	0.1000	∞
Card calibration	0.2000	Normal	2.00	1.00	0.1000	∞
Integration error	0.2000	Rectangular	1.73	1.00	0.1155	∞
Repeatability of measuring magnetostriction	0.1000	Normal	2.00	1.00	0.0500	-
length	0.2000	Normal	2.00	1.00	0.1000	∞
J setting	0.2000	Normal	2.00	1.22	0.1218	∞
Stress setting	0.9000	Normal	2.00	0.01	0.0045	
Sum of squares					0.0607	
Combined uncertainty					0.2464	
Expanded uncertainty					0.4927	
Declared uncertainty in stress (5MPa)					**0.5**	
at a confidence level of 95 %						

Table 5.7 Determination of the uncertainty in magnetostriction under -5 MPa of compression

Source of uncertainty	Value ± %	Probability distribution	Divisor	C_i	U_i ± %	Vi or Veff
Accelerometer calibration	0.2000	Normal	2.00	1.00	0.1000	∞
Card calibration	0.2000	Normal	2.00	1.00	0.1000	∞
Integration error	0.2000	Normal	2.00	1.00	0.1000	∞
Repeatability of measuring magnetostriction	0.1000	Normal	2.00	1.00	0.0500	-
length	0.2000	Normal	2.00	1.00	0.1000	∞
J setting	0.2000	Normal	2.00	14.70	1.4700	∞
Stress setting	0.9000	Normal	2.00	5.13	2.3069	∞
Sum of squares					7.5251	
Combined uncertainty					2.7432	
Expanded uncertainty					5.4864	
Declared uncertainty in stress (-5MPa)					**5.5**	
at a confidence level of 95 %						

Table 5.8 Determination of the uncertainty in magnetostriction under -10 MPa of compression

Source of uncertainty	Value ± %	Probability distribution	Divisor	C_i	U_i ± %	Vi or Veff
Accelerometer calibration	0.2000	Normal	2.00	1.00	0.1000	∞
Card calibration	0.2000	Normal	2.00	1.00	0.1000	∞
Integration error	0.2000	Normal	2.00	1.00	0.1000	∞
Repeatability of measuring magnetostriction	0.1000	Normal	2.00	1.00	0.0500	-
length	0.2000	Normal	2.00	1.00	0.1000	∞
J setting	0.2000	Normal	2.00	21.35	2.1350	∞
Stress setting	0.9000	Normal	2.00	0.25	0.1104	∞
Sum of squares					4.6129	
Combined uncertainty					2.1478	
Expanded uncertainty					4.2955	
Declared uncertainty in stress (-10MPa)					**4.3**	
at a confidence level of 95 %						

The sensitivity coefficients (C_i) of "J setting" and "stress setting" at three stress regions are predominant in the uncertainty budget. The calculation methods are shown in Table 5.9 and Table 5.10.

Table 5.9 Calculation of sensitivity coefficient of J setting

Stress (MPa)	**J (T)**	**Variation in J (T)**	**Pk-pk magnetostriction (10^{-6})**	**Variation in magnetostriction (10^{-6})**	**C_i**
5.00	1.50	0.20	-0.58	0.24	**1.22**
	1.70		-0.82		
-5.00	1.50	0.20	14.25	2.94	**14.70**
	1.70		17.19		
-10.00	1.50	0.20	20.31	4.27	**21.35**
	1.70		24.58		

Table 5.10 Calculation of sensitivity coefficient of stress setting

J (T)	**Stress (MPa)**	**Variation in stress (MPa)**	**Pk-pk magnetostriction (10^{-6})**	**Variation in magnetostriction (10^{-6})**	**C_i**
1.70	6.00	2.00	-0.84	0.01	**<0.01**
	4.00		-0.83		
1.70	-4.00	2.00	10.82	10.27	**5.13**
	-6.00		21.07		
1.70	-8.00	2.00	24.38	0.49	**0.25**
	-10.00		24.88		

Declared uncertainties for the magnetostriction measurement system at a confidence level of 95 % in:

a) B_{peak} = ± 0.2 %
b) Applied stress = ± 0.9 %
c) The uncertainty of magnetostriction was evaluated for the three stress regions shown in Fig 5.29:
   - under stress at 5MPa = ± 0.5 %
   - under stress at - 5 MPa = ± 5.5 %
   - under stress at - 10 MPa = ± 4.3 %

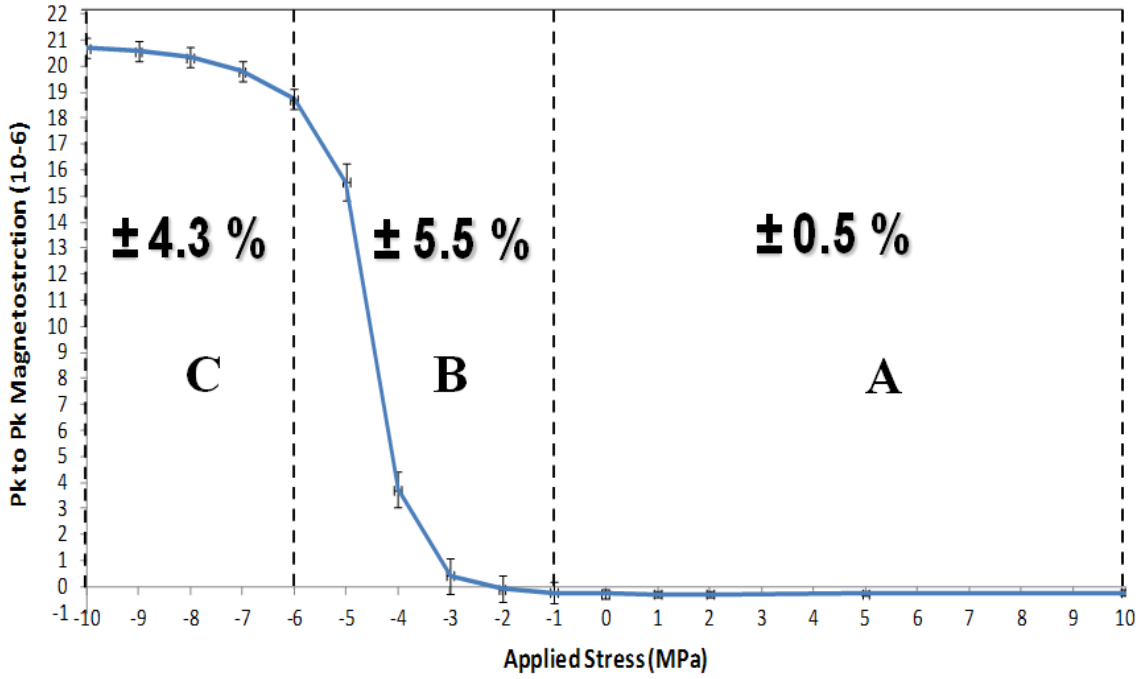

Fig 5.29 The regions of varies uncertainty on the stress sensitivity curve.

5.7 Correlation between Measured and Calculated Magnetostriction

Verification of the measurement was essential to provide confidence in the measured characteristic when assessing material characteristics and effects of coating. Therefore several experiments were undertaken to verify results of magnetostriction measurements GO material.

Stress uniformity was assessed through the application of strain gauges along the length of the measured strip (a modified top plate was created to accommodate the gauges and connecting wires). No variation in stress could be observed along the magnetised length of the sample after following the steps concerning alignment outlined in section 5.2.

Confirmation of measured magnetostriction under applied stress was achieved through static domain observations with no magnetising windings in place. A magnetic domain viewer [32] utilising the Bitter technique was used together with a digital camera to acquire static domain images at applied stresses from -10 MPa to +10 MPa. These images were analysed by LabView Vision software, as shown in Fig 5.30, to calculate the percentage increase of stress patterns in comparison to the total area of the observed surface.

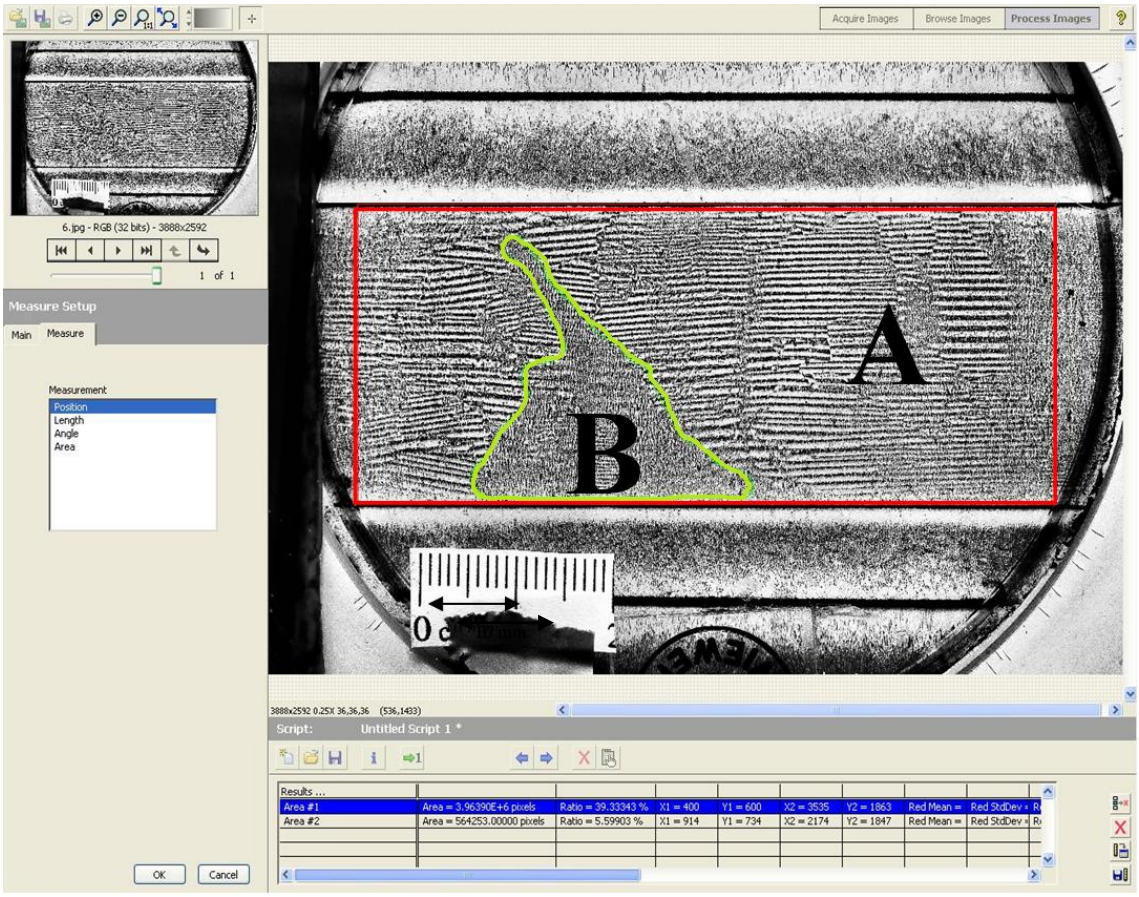

Fig 5.30 Calculations of percentage increase of stress patterns according to the total area by LabView vision software.

Fig 5.30 shows the total observed area "A" of the sample surface marked with the red line and area "B" of stress patterns separated by the green line.

The following equation based on the coverage of stress patterns (C%) was used to calculate magnetostriction ($\lambda_{measured}$) under stress

$$\lambda_{measured} = \frac{\lambda_{maximum} * C\%}{100\%} \quad (5.18)$$

where $\lambda_{maximum}$ is the maximum magnetostriction of a sample subjected to a compressive stress just sufficient to produce saturation magnetostriction.

Domain observations were carried out on two samples of the CGO and two of the HiB steel under stress with two thicknesses 0.27 mm and 0.30 mm. The percentage of stress pattern *I* was estimated on the samples surfaces under compression up to -10 MPa. These are shown for several applied compressive stress levels in Table 5.11.

Table 5.11 Percentage increase (C%) of stress pattern I under compressive stress

Compressive Stress (MPa)	**CGO 0.27 mm (C%)**	**CGO 0.30 mm (C%)**	**HiB 0.27 mm (C%)**	**HiB 0.30 mm (C%)**
0	0	0	0	0
-2	0	0	0	0
-4	35	39	0	5
-6	96	86	53	72
-8	98	90	93	90
-10	100	100	100	100

After observing the domains, the same samples were tested on the system at 1.7 T under compressive stress up to -10 MPa which was sufficient to achieve saturation magnetostriction. Values of pk-pk magnetostriction at -10 MPa of compression for both materials are presented in Table 5.12.

Table 5.12 Maximum measured magnetostriction under compressive stress at 1.7T, 50 Hz

Type of Steel	**$\lambda_{maximum}$ (10^{-6})**
0.27 mm CGO	22.9
0.30 mm CGO	23.3
0.27 mm HiB	22.5
0.30 mm HiB	22.3

The pk-pk magnetostriction under stress curve obtained from the measurement on the system and magnetostriction calculated from the percentage increase of stress pattern *I* according to the maximum measured magnetostriction is presented in Fig 5.31

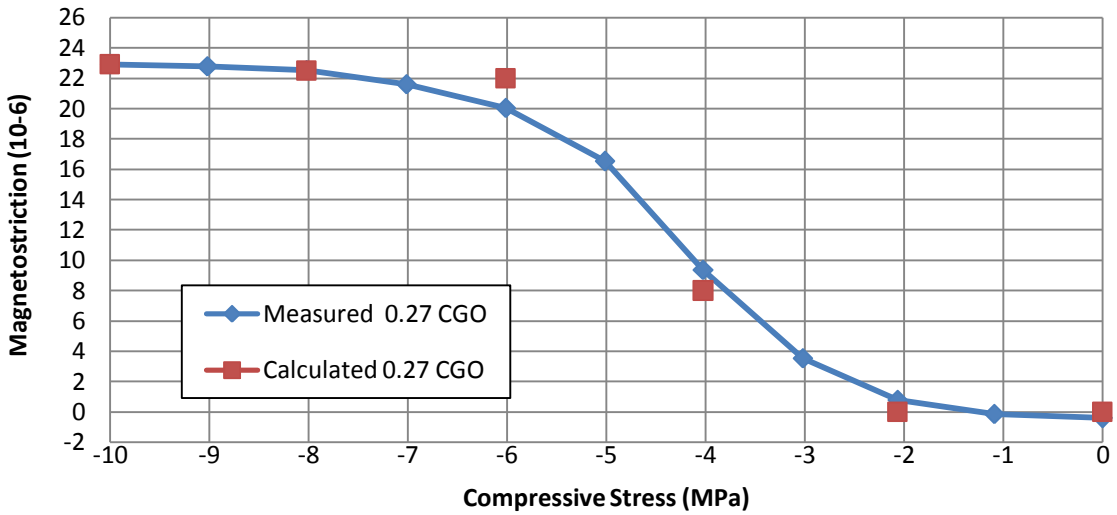
Magnetostriction (10-6)
26
24
22
20
18
16
14
12
10
8
6
4
2
0
-2
-10
-9
-8
-7
-6
-5
-4
-3
-2
-1
0
Compressive Stress (MPa)
Measured 0.27 CGO
Calculated 0.27 CGO

a)

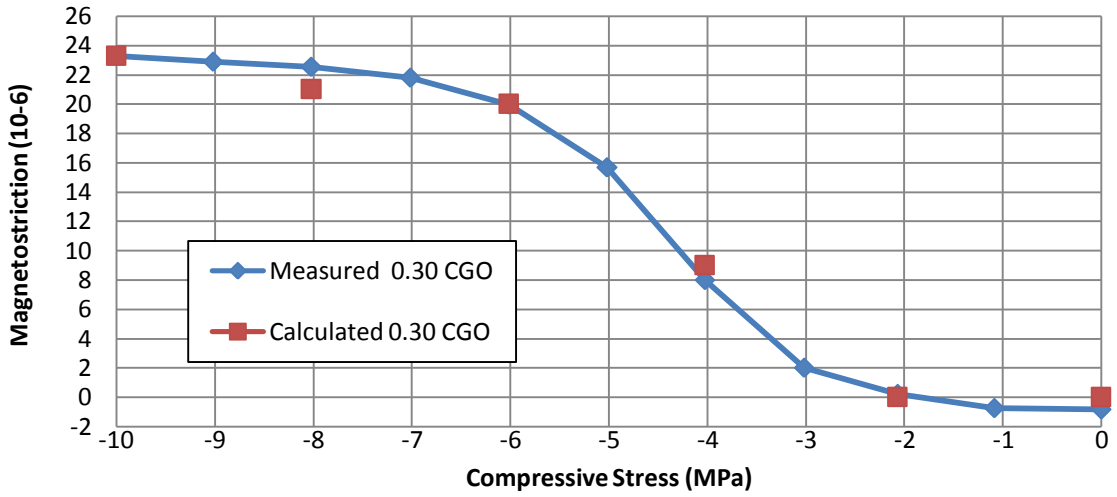
Magnetostriction (10-6)
26
24
22
20
18
16
14
12
10
8
6
4
2
0
-2
-10
-9
-8
-7
-6
-5
-4
-3
-2
-1
0
Compressive Stress (MPa)
Measured 0.30 CGO
Calculated 0.30 CGO

b)

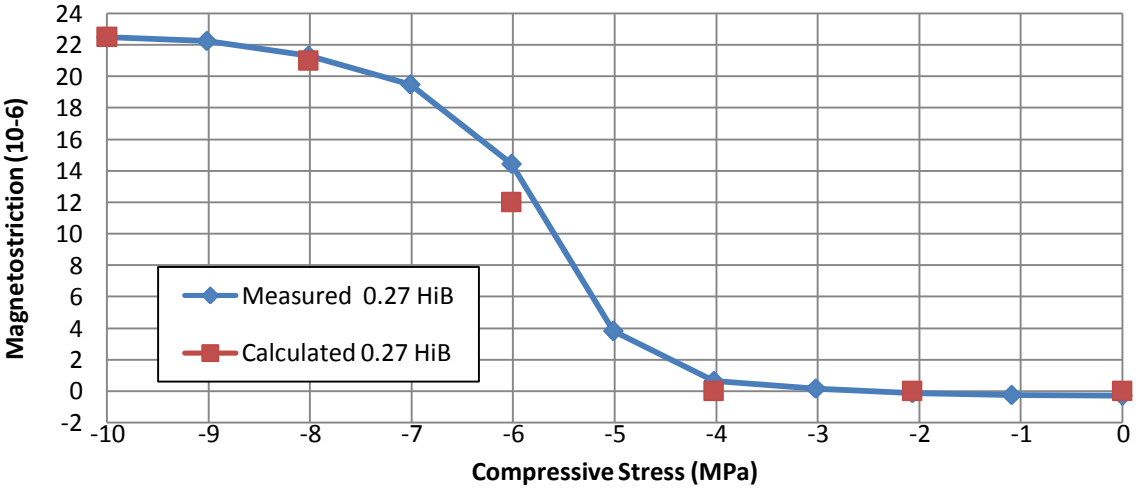
Magnetostriction (10-6)
24
22
20
18
16
14
12
10
8
6
4
2
0
-2
-10
-9
-8
-7
-6
-5
-4
-3
-2
-1
0
Compressive Stress (MPa)
Measured 0.27 HiB
Calculated 0.27 HiB

c)

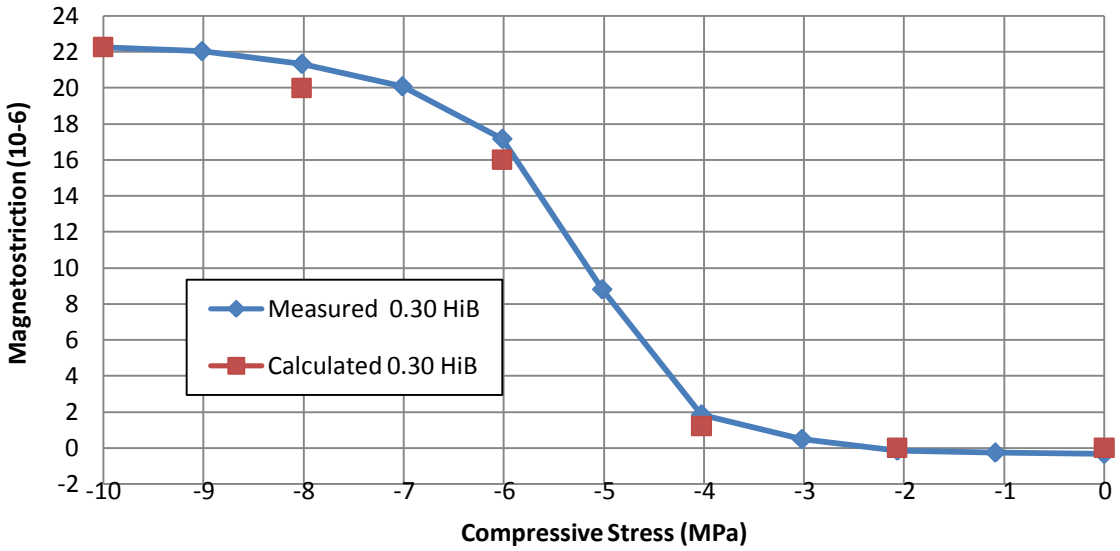

d)

Fig 5.31 Correlation between measured (1.7 T, 50 Hz) and calculated magnetostriction under compressive stress with thicknesses: a) 0.27 mm CGO , b) 0.30 mm CGO, c) 0.27 mm HiB, d) 0.30 mm HiB.

As can be seen the magnetostriction measured using the magnetostriction measurement system and calculated, based on the domain patterns observations agrees within uncertainty of the measurement system as shown in section 5.6.

5.8 References

[1] *Linear variable differential transformer (LVDT)*. Available: http://www.electronics-tutorials.ws/io/io_2.html.

[2] H. J. Stanbury, "Magnetostriction effects at angles to the rolling direction in grain oriented silicon steel," PhD Thesis, University of Wales, Cardiff, 1984.

[3] R. Repas. (2007). *The hot and cold of LVDTs*. Available: http://machinedesign.com/article/the-hot-and-cold-of-lvdts-0510.

[4] "Capacitive displacement sensor," in *http://www.southampton.ac.uk*.

[5] J. Whittaker, "Magnetostriction in steel measurement methods for electrical sheet," *Electrical Times,* vol. 137, pp. 675-677, 1960.

[6] R. Birss, *et al.*, "A capacitive instrument for the measurement of a large range of magnetostriction at low temperatures and high magnetic fields " *Journal of Physics E: Scientific Instruments* vol. 11, pp. 928-934, 1978.

[7] W. R. George, *et al.*, "Magnetostriction in grain-oriented silicon-iron," *Proceedings of the IEE - Part A: Power Engineering* vol. 109, pp. 101-108, 1961.

[8] L. K. Baxter, "Capacitive sensors: design and applications," *Institute of Electrical & Electronics Engineering,* pp. 61–80, 1997.

[9] A. J. Moses and D. Davies, "Influance of compressive stress on magnetic properties of comercial (110) [001] oriented silicon-iron," *IEEE Transactions on Magnetics,* vol. 16, pp. 454-460, 1980.

[10] P. J. Banks and E. Rawlinson, "Dynamic magnetostriction and mechanical strain in oriented 3% silicon iron sheet subject to combined longitudinal and transverse stresses," *Proceedings of the Institution of Electrical Engineers-London,* vol. 114, pp. 1537-1546, 1967.

[11] R. D. Greenough and C. Underhill, "Strain gauges for the measurement of magnetostriction in the range 4K to 300K," *Journal of Physics E: Scientific Instruments,* vol. 9, pp. 451-454, 1976.

[12] "Strain Gauge Circuits," in *http://www.sensorland.com/HowPage002.html*.

[13] P. Anderson, "Evaluation of magnetostriction measurement techniques," MSc Thesis, University of Wales, Cardiff, 1996.

[14] M. Chapman. Heterodyne and homodyne interferometry. *Renishaw Plc, Apply Innovation*. Available: http://www.olympus-controls.com/documents/GEN-NEW-0117.pdf.

[15] T. Nakata, *et al.*, "Magnetostriction measurements with a laser-doppler velocimeter," *IEEE Transactions on Magnetics,* vol. 30, pp. 4563-4565, Nov 1994.

[16] T. Nakase, *et al.*, "Measuring system for magnetostriction of silicon steel sheet under AC excitation using optical methods," *IEEE Transactions on Magnetics,* vol. 34, pp. 2072-2074, Jul 1998.

[17] *Record player pick-up*. Available: http://www.123rf.com/photo_3970179_long-playing-record.html.

[18] C. M. Brownsey and G. C. Maples, "Magnetostriction characteristics of 3.1% grain-oriented silicon iron transformer steel," *Proceedings of the Institution of Electrical Engineers-London,* vol. 113, pp. 1859-1862, 1966.

[19] G. H. Simmons and J. E. Thompson, "Magnetic properties of grain-oriented silicon iron . Part 1 use of ceramic displacement transducers for measurement of magnetostriction," *Proceedings of the Institution of Electrical Engineers-London,* vol. 115, pp. 1835-1839, 1968.

[20] D. J. Mapps and C. E. White, "Magnetostriction harmonics measurement using a double pizoelectric transducer technique," *Journal of Physics E-Scientific Instruments,* vol. 17, pp. 472-476, 1984.

[21] Dytran Instruments. *Introduction to charge mode accelerometers*. Available: http://www.dytran.com/go.cfm/en-us/content/tech-education-a7/x.

[22] P. Anderson, "A novel method of measurement and characterisation of magnetostriction in electrical steels," PhD Thesis, Cardiff University, Cardiff, 2000.

[23] Visong Test. *Technical support: piezo-accelerometer selection guide* Available: http://www.visongtest.com/technical%20support1.htm.

[24] P. I. Anderson, *et al.*, "An automated system for the measurement of magnetostriction in electrical steel sheet under applied stress," *Journal of Magnetism and Magnetic Materials,* vol. 215, pp. 714-716, 2000.

[25] Dytran Instruments. *Introduction to Charge Mode Accelerometers*. Available: http://www.dytran.com/go.cfm/en-us/content/tech-education-a7/x.

[26] *8630C & 8636 C PiezoBEAM Accelerometers*. Available: http://www.intertechnology.com/Kistler/pdfs/Accelerometer_Model_8630C_8636C.pdf.

[27] *SMC: An integrated guide style air cylinder that achieves lateral load resistance and high non-rotating accuracy*. Available: http://content2.smcetech.com/pdf/MGQ_EU.pdf.

[28] M. Specialties. *Force Sensor - ELFF Series Load Cell*. Available: http://www.meas-spec.com/product/t_product.aspx?id=2420.

[29] F. Fiorillo, *Measurement and characterization of magnetic materials*: Elsevier Inc., 2004.

[30] J. Inman, "Engineering vibration," *Prentice Hall*, pp. 451-489, 2000.

[31] UKAS, "The expression of uncertainty and confidence in measurement," M3003, 2007.

[32] R. Taylor, "Magnetic pattern viewer," European Patent 0388712A2, 1990.

Chapter 6 Approach to an Experimental Investigation of Factors Influencing Magnetostriction

The following factors which have an influence on magnetostriction under applied stress were investigated:

a) Influence of strip thickness
b) Influence of applied coating stress
c) Influence of annealing under tension
d) Influence of applied cutting stress
e) Influence of rotational magnetisation

The first three (a-c) are pertinent to the production process and cutting stress could be introduced when coiled steel is cut in to laminations. However the effect of rotational magnetisation is directly relevant to transformer core T-joints.

These investigations required the use of a wide range of grades of electrical steel samples with different shape and thicknesses which are presented in details in Table 6.1. The discussion gives an idea of how to find a way of controlling the magnetostriction when subjected to external applied tensile or compressive stress in the RD and the TD.

Table 6.1 Range of samples to be used in the experiments in this study

Chapter	Type of steel	Size	Thickness
Influence of Strip Thickness on Magnetostriction in GO Steel (chapter 7)	CGO	Epstein Strip 305 mm x 30 mm	0.23 mm 0.27 mm 0.30 mm 0.35 mm 0.50 mm
Influence of Coating Stress on Surface of GO Steel on Magnetostriction and Loss (chapter 8)	HiB	305 mm x 30 mm	0.27 mm

Influence of Annealing under Tension on Magnetostriction and Loss in GO Steel (chapter 9)	HiB	305 mm x 30 mm	0.30 mm
Influence of Cutting Stress on Magnetostriction in GO Steel (chapter 10)	CGO	305 mm x 30 mm	0.30 mm
Influence of Rotational Magnetisation on Magnetostriction in GO and NO Steel (chapter 11)	CGO and HiB	305 mm x 30 mm	0.30 mm
	NO	305 mm x 30 mm	0.35 mm 0.50 mm
	CGO and HiB	Disc 80 mm diameter	0.30 mm
	NO	80 mm diameter	0.35 mm 0.50 mm

6.1 Introduction to the Experiments

6.1.1 Influence of Strip Thickness on Magnetostriction in GO Steel (Covered in Chapter 7)

The final thickness of GO steel is determined by cold rolling, as explained in chapter 2. A previous investigation of the magnetostriction characteristic under stress on various Epstein strip thicknesses carried out by Anderson [1] compared the measured magnetostriction of 0.23 mm, 0.27 mm and 0.30 mm thick HiB strips under stress with calculated values using the magnetostriction model proposed by Simmons and Thompson [2].

In this research a new comprehensive model of magnetostriction under stress taking into account variation in angle θ between the width of closure domain observed on the strip surface and the closure domain walls has been developed. It is based on surface domain observations under stress carried out over a wide thickness range of the CGO steel.

6.1.2 Influence of Coating Stress on Surface of GO Steel on Magnetostriction and Loss (Covered in Chapter 8)

Compressive stress applied to the laminations due to the assembly of a transformer core can be reduced or even eliminated when an external tensile stress is applied to the steel along the RD by application of a coating to the steel surface. The coating stress also contributes to a reduction of the power loss [3].

Grain oriented silicon steel in a coil is insulated by two layers of coatings. The first layer is applied before the high temperature coil annealing (HTCA) process, and second one is applied at the final stage of production as described in chapter 2. The differential thermal contraction between the steel and coatings due to the cooling process after the curing a coating at 850˚C, applies a tensile stress to the steel surface along the RD.

To fully understand this process Young`s modulus, yield strength and thermal expansion coefficient of GO bare steel were measured. Also single or multilayer coating application, curing process and different types of coatings with various thicknesses were investigated to help evaluate the stress applied to the steel surface at each stage.

The stress model based on the mechanical properties of the anisotropic steel and isotropic coating in the RD and TD is also presented.

6.1.3 Influence of Annealing under Tension on Magnetostriction and Loss in GO Steel (Covered in Chapter 9)

Grain oriented steel is constantly under an applied tensile stress during the production process. This tension is controlled by varying the speed of the driving rolls on the production line. The coil after HTCA is sent to the final stage where the second coating is applied and the steel is thermally flattened at 850˚C when additional compressive or tensile stress can be set up in the steel.

In this investigation strips cut from a coil after HTCA were annealed under a variety of tensions in an atmosphere of either nitrogen or compressed air. Also to investigate the effect of the thermal flattening process on magnetostriction the steel on the production line was thermally flattened with different depths of the penetrating rollers below the strip pass line. These penetrating rollers flatten the strip through a

local application of stress which is a function of the penetration depth, line tension and roller diameters.

6.1.4 Influence of Cutting Stress on Magnetostriction in GO Steel (Covered in Chapter 10)

It is important that the method of cutting electrical steel into sheets for magnetostriction measurement has a minimal effect on their magnetic properties. Compressive stress set up during cutting causes surface static magnetic domain stress patterns to appear. When a strip is magnetised, this initial stress domain pattern is overcome resulting in high pk-pk magnetostriction.

In this investigation the shift between curves of pk-pk magnetostriction against stress was used to estimate the stress condition of cut Epstein strips using commercially available guillotining, electrical discharge machining (EDM), laser and water jet cutting. Also B-H loops were plotted for strips after cutting and after subsequent stress relief annealing to investigate their influence on the magnetic properties of the steel.

6.1.5 Influence of Rotational Magnetisation on Magnetostriction in GO and NO Steel (Covered in Chapter 11)

The magnetic domain structures of electrical steels under dynamically rotating magnetisation alternate between well known bar patterns and a more complex distribution at certain times in the magnetising cycle [4]. This characteristic complex structure resembles that of stress pattern *I* and pattern *II* and is described in chapter 4.

Magnetostriction studies have been carried out on Epstein strips and discs of non-oriented and grain-oriented electrical steels under uniaxial and rotational magnetisation.

The investigation on the effect of rotational magnetisation on magnetostriction was carried out in collaboration with colleague Somkun who designed a two dimensional magnetostriction measurement system and tested disc samples under rotational and uniaxial magnetisation [5].

6.2 References

[1] P. I. Anderson, *et al.*, "Assessment of the stress sensitivity of magnetostriction in grain-oriented silicon steel," *IEEE Transactions on Magnetics,* vol. 43, pp. 3467-3476, 2007.

[2] G. H. Simmons and J.E. Thompson, "Magnetic properties of grain oriented silicon iron," *Proceedings of the IEE,* vol. 118, pp. 1302-1306, 1971.

[3] E. Beyer, *et al.*, "The influence of compressive stress applied by hard coatings on the power loss of grain oriented electrical steel sheet," *Journal of Magnetism and Magnetic Materials,* pp. 1985-1991, 2011.

[4] F. McQuade, *et al.*, "Domain observation under two dimensional magnetisation," *Proc. 4th, International Workshop on 2 Dimensional Magnetisation Problems,* 1995.

[5] S. Somkun, "Magnetostriction and magnetic anisotropy in non-oriented electrical steels and stator core laminations," PhD Thesis, Cardiff University, Cardiff, 2011.

Chapter 7 Influence of Strip Thickness on Magnetostriction in the GO Steel

7.1 Samples Selection

Epstein strips (305 mm x 30 mm) cut along the RD and then stress relief annealed at a temperature of 810˚C for 2 hours in an atmosphere of 2% hydrogen and 98% nitrogen, after visual inspection of physical condition, were selected from five batches of CGO strips of thickness 0.23 mm, 0.27 mm, 0.30 mm, 0.35 mm and 0.50 mm. Each selected batch comprised five strips.

The average grain sizes of the strips of thickness 0.23 mm, 0.27 mm, 0.30 mm, 0.35 mm and 0.50 mm were 5 mm, 6 mm, 7 mm, 6 mm and 6 mm respectively.

7.2 Static Domain Observations under Compressive Stress

The Domain Viewer was used to observe static domains on one surface of a demagnetised strip of each thickness under applied compressive stress. This method enabled surface domains to be observed without removing the surface stress coating which would have changed the internal stress in the strips. Fig 7.1 shows an image of surface stress pattern *I* on 0.30 mm thick CGO strip under compressive stress of -10 MPa.

These images of the observed areas were captured by a digital camera and afterwards analysed by LabView Vision software as shown in Fig 7.2, to measure a width of stress patterns appeared on the surface.

Analysis of the images showed there was no evidence of stress patterns *II* in all observed samples with various thicknesses. The recognised pattern in all of the samples under high compressive stress was stress pattern *I*.

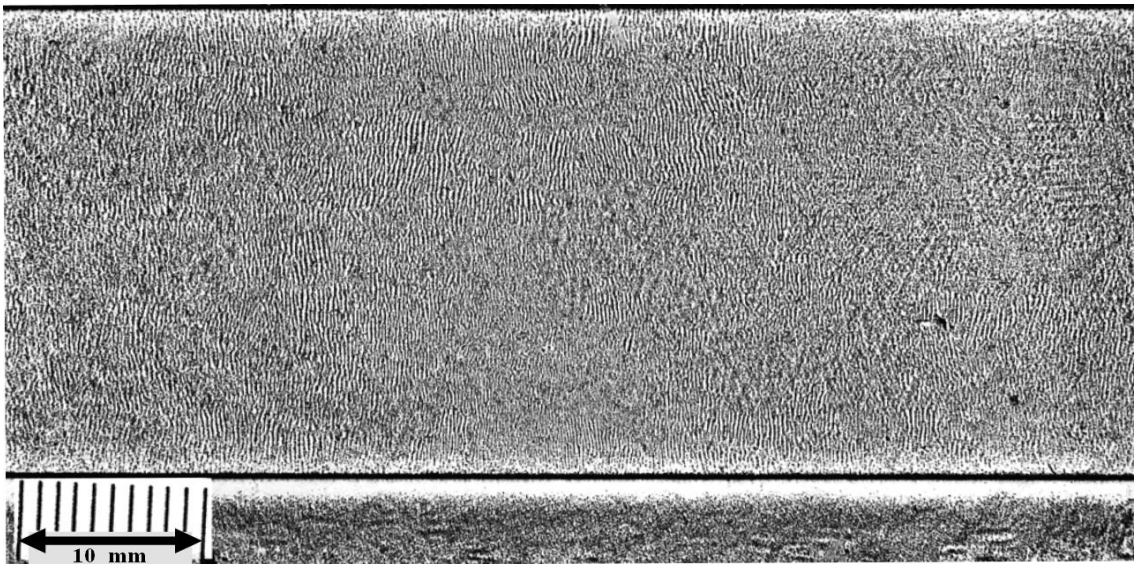

Fig 7.1 Stress pattern I observed on the surface of 0.30 mm thick CGO strip under compressive stress of -10 MPa.

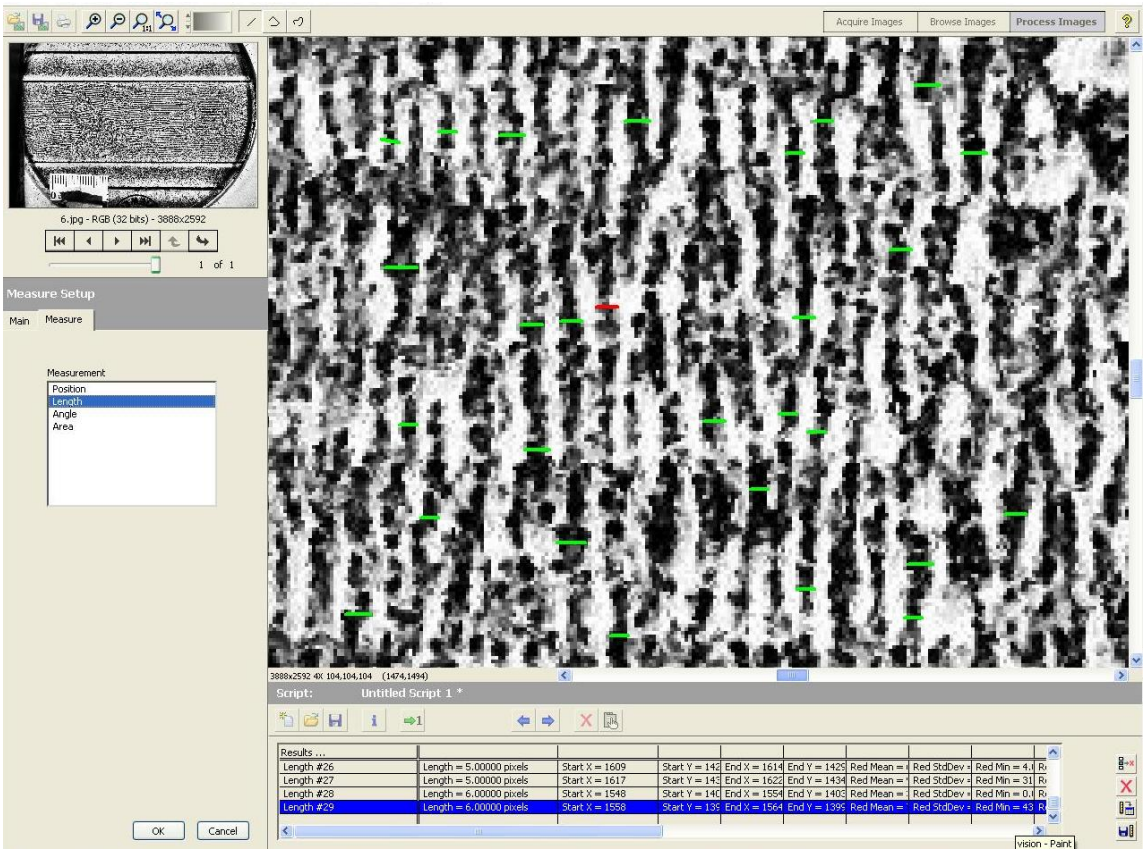

Fig 7.2 Example of domain image analysed by LabView Vision software to measure a width of stress patterns appeared on a strip surface.

7.3 Theoretical Approach to the Influence of Strip Thickness on Magnetostriction in the GO Steel

Magnetisation along the RD in the presence of a linear tensile stress in the same direction creates a small negative magnetostriction [1]. In contrast, application of compressive stress results in a rapid increase in magnetostriction as shown previously in chapter 4. This increase in magnetostriction is caused by a rearrangement of domains in order to minimise the total free energy of the steel when magnetoelastic stored energy is added to the magnetocrystalline, magnetostatic and domain wall components of free energy.

Consider a sample of GO populated entirely by grains containing domains in the stress pattern *I* configuration shown in Fig 7.3, first described by Dijkstra and Martius [2]. Fig 7.3 shows a schematic view of a longitudinal section through a perfectly oriented single grain of a sheet of grain oriented electrical steel with thickness t, showing the static domain structure developed to minimize the total free energy [3] under compression along the [001] direction of the single grain. The θ is the angle between the width of closure domain observed on the strip surface and the closure domain walls.

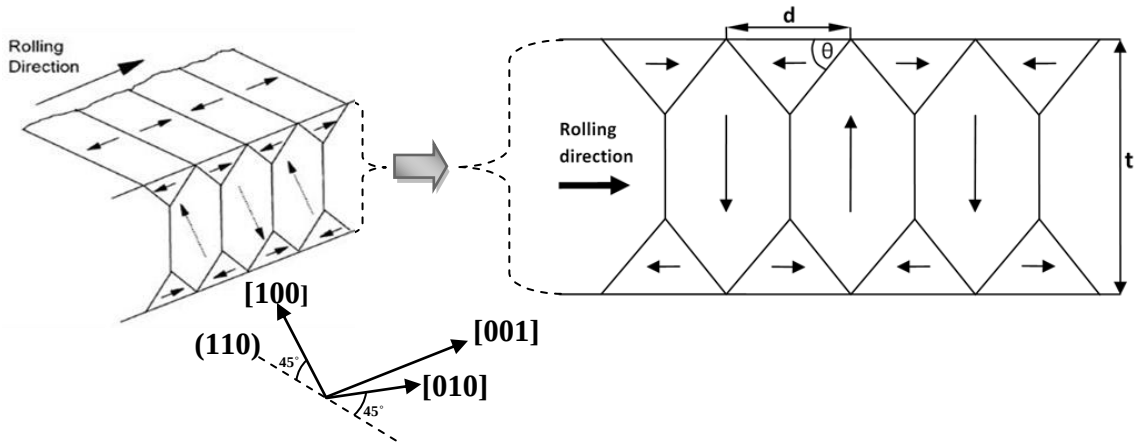

Fig 7.3 Longitudinal section of domain structure through a grain exhibiting stress pattern I [4].

When the sheet is magnetised along its rolling direction ([001]) high magnetostriction occurs as the main transverse domains initially oriented along [010] and [100] directions rotate into [001] directions. The value of magnetostriction along

the rolling direction depends on the volume weighted proportion of domains oriented in these principle axes.

The magnetostrictive strain, when an external magnetic field is applied along the RD, can now be calculated from (7.1) similar to that presented in details in section 4.4, with reference to the cross section through the grain shown in Fig 7.3. It must be assumed that, at magnetic saturation, B_s, the grain consists only of [001] domains. At an applied magnetic flux density B the volume fraction of [001] closure domains is $\frac{B}{B_s}\cos\emptyset$. Equation (7.1) used to calculate $\lambda_{measured} = \lambda_{final} - \lambda_{initial}$ the maximum measured magnetostriction under compressive stress assuming initially the material only comprised [001] bar domains, i.e. λ_{final} is zero and, $\lambda_{initial}$ is calculated from the stress pattern *I* domain volume distribution.

$$\lambda_{maximum} = \lambda_{final} - \lambda_{initial} = \frac{3}{2}\lambda_{100} cos2\emptyset \left(\frac{B}{B_s} cos\emptyset - \frac{d}{2t} tan\theta\right) \qquad (7.1)$$

For the CGO steel at 20˚C, λ_{100} = 24 x 10^{-6}, B_S = 2.03 T, and a typical value of average misorientation of the grains from the [001] direction, ∅, is 7˚.

7.4 Investigation of Effect of Strip Thickness on Magnetostriction

The magnetostriction of each of the strips in each batch was measured 3 times over the flux density 1.7 T at stress up to ± 10 MPa. Fig 7.4 shows the average values of pk – pk magnetostriction in all the batches characterized as stress sensitivity curves magnetised at 1.7 T, 50 Hz. Each data point is the average magnetostriction in each of the 5 strips in each batch measured three times. Similar characteristics were found at 1.5 T.

A marked variation can be observed where increasing strip thickness leads to an increase in magnetostriction under high compressive stress and also causes vertical and horizontal shift of the stress sensitivity curves.

To obtain the influence of strip thickness on the vertical and horizontal (stress) shift the all points on each of average pk-pk magnetostriction sensitivity curves were divided by

its maximum value of magnetostriction under compression, e.g. each point on the stress sensitivity curve of 0.23 mm thick strip was divided by 20 (μstrain). These curves are shown in Fig 7.5. The difference in curves shifts between Fig 7.4 and Fig 7.5 show that vertical shifts are caused by the change of strip thicknesses, while the horizontal (stress) shift remains almost unchanged. These stress shifts especially between 0.35 mm and 0.50 mm thick strips could be caused due to differences in a coating stresses, when a similar coating thickness is applied to the surface of each strip thickness. The vertical shifts of the sensitivity curves (Fig 7.4) at -10 MPa of compression show approximately 1.5 μstrain shift for a change of 0.5 mm in the strip thickness in the range of thicknesses 0.23 mm to 0.35 mm. However magnetostriction shift between the thicknesses of 0.35 mm and 0.50 mm is approximately 1.5 μstrain.

Table 7.1 shows the average percentage of surface area of five strips from each batch covered by closure domains indicating the presence of stress pattern *I*.

Table 7.1 Percentage increase of stress pattern I on the surface under compressive stress

Thickness (mm)	***-2 MPa (%)***	***-5 MPa (%)***	***-8 MPa (%)***	***-10 MPa (%)***
0.23	0	70	98	100
0.27	0	70	98	100
0.30	5	70	90	100
0.35	10	80	100	100
0.50	20	70	98	100

As expected the area with stress domain patterns increases with compressive stress. Some qualitative correlation can be seen between the percentage of stress pattern *I* present and the stress sensitivity curves in Fig 7.4. For example, at -2 MPa virtually no stress patterns were observed in the three thicknesses of steel where the magnetostriction was relatively low at this stress level whereas 20% of the area is affected in the 0.5 mm thick material which has the steepest and earliest rapid increase in magnetostriction attributed to the presence of the stress pattern. Also at -10 MPa the pk-pk magnetostriction in all batches has levelled out since stress pattern *I* is observed on all the surfaces. The average value of the closure domain width (d in Fig 7.3) at -10 MPa was measured using a travelling microscope with an accuracy ± 0.01 mm.

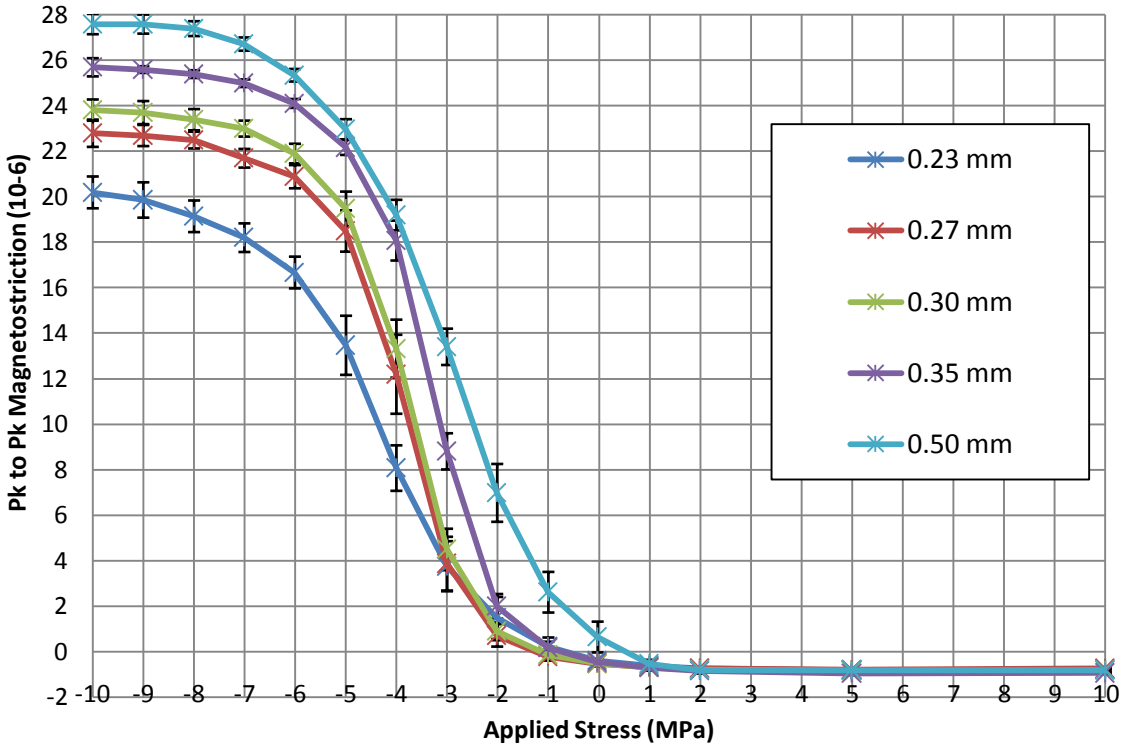

Fig 7.4 Variation of magnetostriction sensitivity curves for Epstein strips of thickness from 0.23 mm to 0.50 mm measured under1.7T, at 50 Hz.

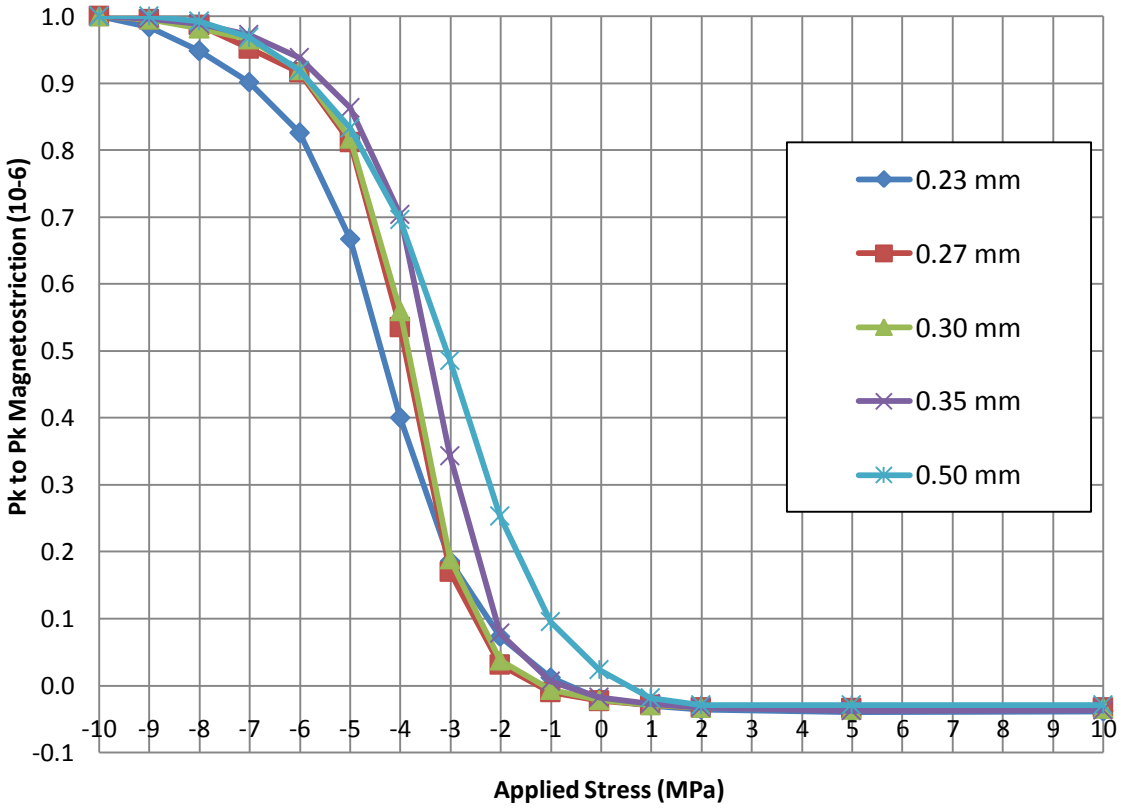

Fig 7.5 Magnetostriction sensitivity curves from Fig 7.4 divided by peak magnetostriction under stress.

Table 7.2 shows the mean value of d of five strips for each steel thickness.

Table 7.2 Measured average width of stress pattern I for each steel thickness

Thickness (mm)	***d (mm)***
0.23	0.07
0.27	0.07
0.30	0.07
0.35	0.07
0.50	0.07

Since the high pk – pk magnetostriction under high compression occurs due to the change from stress pattern *I* domain structure to predominantly [001] domains (particularly at high flux density) during the magnetising cycle, its dependence on thickness can only occur due a change in the value of θ shown in Fig 7.3.

The value of calculated maximum magnetostriction is critically dependent on the value of θ. Previously a constant value of 55˚ has been assumed as described in chapter 4. If this value is used in equation (7.1) to obtain maximum magnetostriction also value of d is constant for all thicknesses, then a good agreement with measurements is observed only for average values of 0.27 mm and 0.30 mm thick strips as shown in Fig 7.6.

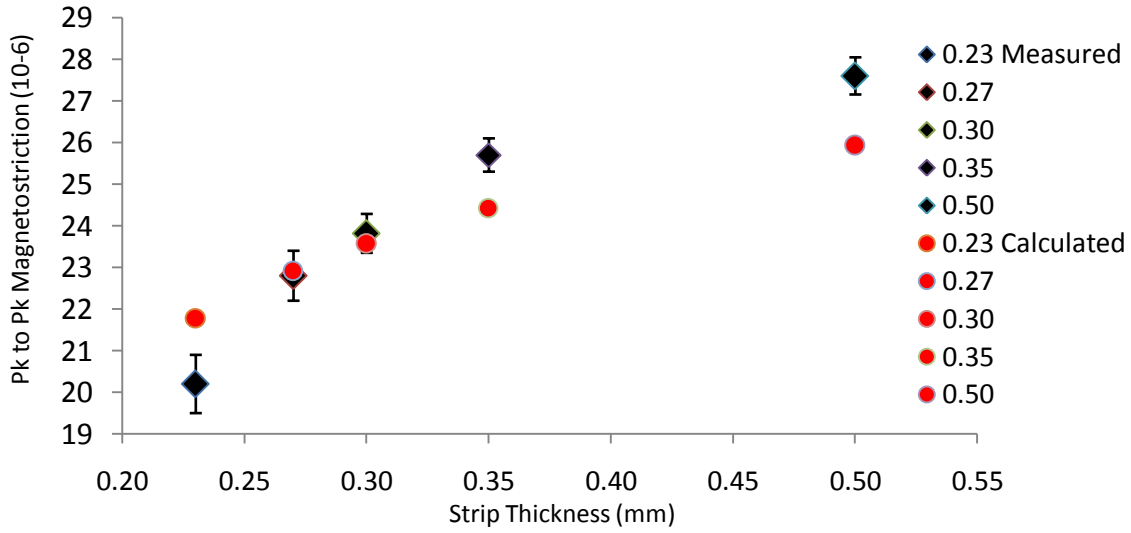

Fig 7.6 Comparison of the measured (1.7 T, 50 Hz) and calculated (1.7 T) variation of pk-pk magnetostriction with thickness for constant value of θ = 55˚.

A better fit between measured and calculated magnetostriction can be obtained if it is assumed that θ can varies with sheet thickness.

However, as the strip thickness increases the magnetostatic energy due to the [100] domains will decrease leading to a reduction in the closure domain volume and hence the angle θ (since the domain spacing can be seen to remain unchanged through studies using a domain viewer). Experimental validation of this dependence is not possible to achieve since non-destructive domain observation techniques such as the Bitter technique give only the surface domain patterns. Techniques such as those using the scanning electron microscope [5] require careful sample preparation which would have a significant effect on the observed domain patterns.

Therefore the assumption has to be taken:

Consider the closure domain with a triangular shape structure through a grain which altitude, h, as shown in Fig 7.7 can be calculated by equation (7.2)

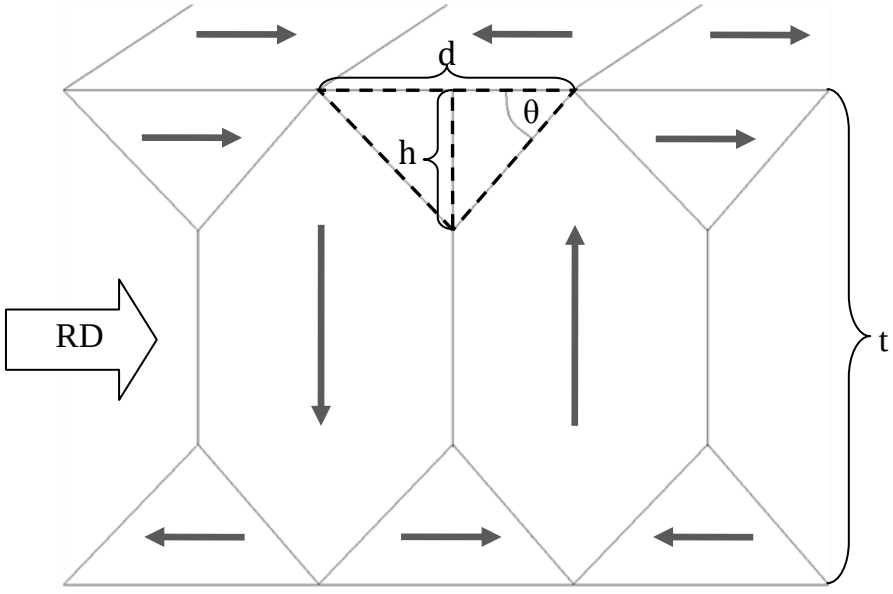

Fig 7.7 Longitudinal section of domain structure through a grain exhibiting stress pattern I.

$$h = \frac{d}{2}\, tan\theta \qquad (7.2)$$

Then closure domain area can be expressed as

$$A_c = \frac{d}{2}\, h \tag{7.3}$$

Therefore,

$$A_c = \frac{d^2}{4}\, tan\theta \tag{7.4}$$

The closure domain area is inverse proportional to the thickness of the steel,

$$A_c = \frac{K}{t} \tag{7.5}$$

Where K is a constant.

Therefore,

$$tan\theta = \frac{4\,K}{t\,d^2} \tag{7.6}$$

Then equation (7.1) of maximum magnetostriction can be converted to

$$\lambda`_{maximum} = \frac{3}{2}\,\lambda_{100}\, cos2\emptyset \left(\frac{B}{B_s}\, cos\emptyset - \frac{4\,K}{2\,t^2\,d}\right) \tag{7.7}$$

A close correlation can be made between the measured and modelled data by using a value for K of approximately $5x10^{-13}$.

Table 7.3 shows the calculated values of θ based on the value of strip thickness, and width of stress pattern *I*.

Table 7.3 Calculated values of θ based on the value of strip thickness, and width of stress pattern I

Thickness	***d***	***Θ***
(mm)	***(mm)***	***(˚)***
0.23	0.07	61
0.27	0.07	57
0.30	0.07	54
0.35	0.07	49
0.50	0.07	32

When the values given in Table 7.3 are used good correlation between measured and calculated pk-pk magnetostriction is achieved as shown in Fig 7.8.

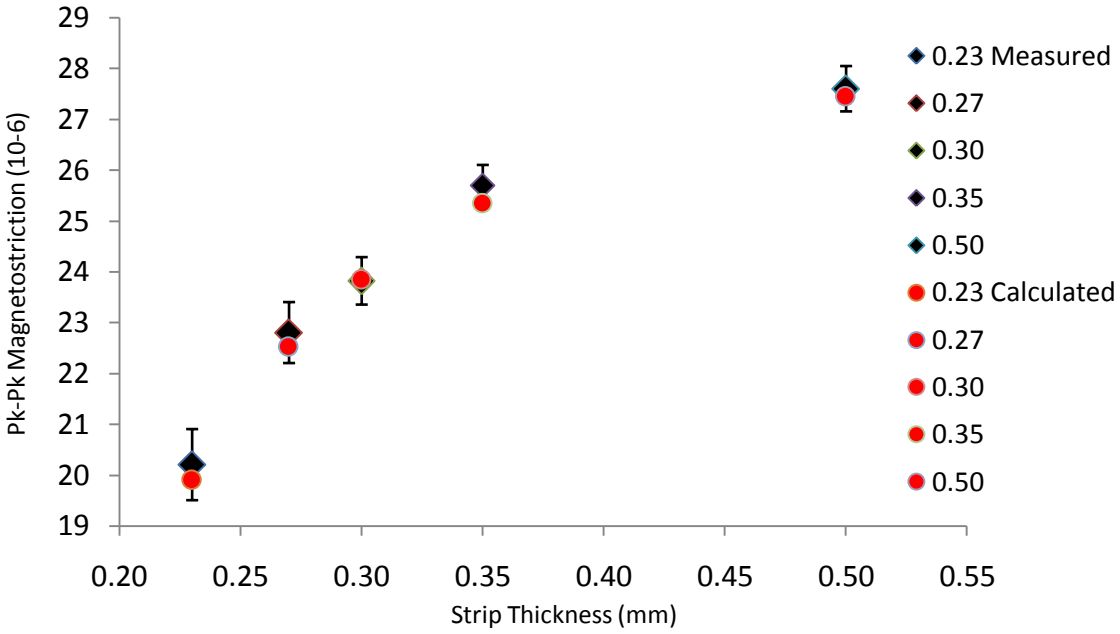

Fig 7.8 Comparison of the measured (1.7 T, 50 Hz) and calculated (1.7 T) variation of pk –pk magnetostriction with thickness using different values of θ for the different strip thicknesses.

7.5 Summary of the Effect of Strip Thickness on Domain Patterns and Magnetostriction.

The width of surface closure domains was found to be constant and independent of thickness in all the strips investigated. Magnetostriction measurements on a range of strips under stress show that a change in thickness causes vertical shift in magnetostriction vs. stress sensitivity curves under high compression. An increase in the measured magnetostriction under high compressive stress is approximately proportional to the strip thickness of the range from 0.23 mm to 0.35 mm.

The magnetostriction model of stress pattern *I* using various angles θ to calculate maximum magnetostriction shows a good correlation with magnetostriction measurements under -10 MPa of compressive stress. The angle θ was estimated to be inversely proportional to the strip thickness. Therefore it is shown that the increase in strip thickness decreases the magnetostatic energy leading to a reduction in the volume of closure domains. As a result the magnetostriction of GO steel becomes more sensitive to applied stress.

7.6 References

[1] P. Allia, *et al.*, "Theory of negative magnetostriction in grain-oriented 3% SiFe for various inductions and applied stresses," *IEEE Transactions on Magnetics,* vol. MAG-14, pp. 362 - 364, 1978.

[2] L. J. Dijkstra and U. M. Martius, "Domain patterns in silicon iron under stress," *Reviews of Modern Physics,* vol. 25, pp. 146-150, 1953.

[3] W. D. Corner and J. J. Mason, "Effect of stress on domain structure of goss textured silicon iron," *British Journal of Applied Physics,* vol. 15, pp. 709-722, 1964.

[4] P. I. Anderson, *et al.*, "Assessment of the stress sensitivity of magnetostriction in grain-oriented silicon steel," *IEEE Transactions on Magnetics,* vol. 43, pp. 3467-3476, 2007.

[5] M. Ardenne, "Improvements in electron microscopes," British Patent 511204, 1939.

Chapter 8 Influence of Coating Stress on Surface of GO Steel on Magnetostriction and Loss

8.1 Mechanical Properties of CGO and HiB Steel

To investigate the effect of coating stress by application of several coatings on the GO steel surface, and also to create a thermal contraction model of coating stresses, measurements of mechanical properties such as Young`s modulus, yield point and expansion coefficient of GO steel along the RD and the TD were carried out.

8.1.1 Measurement of the Young`s Modulus

The elastic modulus, also called Young`s modulus (E) is the linear relation between stress and strain values in the range of the material elasticity. This modulus is a constant value and can be expressed as [1]

$$E = \frac{\sigma}{\varepsilon} \tag{8.1}$$

where ε is the strain whose values can be obtained from stress vs. strain measurement. To evaluate Young`s modulus of 0.30 mm thick CGO and the HiB steel in the RD and the TD directions, two sheets were cut in to strips with dimensions 305 mm x 24 mm in the RD [001] and the TD [110] direction. After cutting, the strips were stress relief annealed and then pickled in to 20% sodium hydroxide to remove top coatings from the strip surfaces. The uncoated bare steel strips were finally tested on the Avery-Denison tensile testing machine which is shown in Fig 8.1.

Fig 8.1 Tensile tester used to evaluate Young`s modulus of the CGO and HiB steel.

The average values of Young`s modulus of 2 strips are presented in the Table 8.1.

Table 8.1. Young`s modulus (E) of 0.30 mm thick CGO and HiB steel in the RD and the TD

Type of the Silicon Steel	**Young`s Modulus (GPa)**
CGO in the RD	114
HiB in the RD	113
CGO in the TD	196
HiB in the TD	195

The long axis of precipitates in the steel, elongated due to the process of hot and cold rolling (chapter 2), is aligned close to the [001] direction of the cubic crystal as shown in Fig. 4.1 For this reason the Young`s modulus along the [001] direction is smaller than along the [110] direction. Therefore the increase of the elastic energy is lower when participates elongate parallel to the [001] direction.

8.1.2 Measurement of the Yield Strength

The yield strength is the stress at which a material begins to deform plastically. To find a position of a limit of proportionality on the stress vs. strain curve a proof stress was defined [1]. The 0.2 % proof stress is required to produce a permanent strain of 0.002 mm.

The yield strength based on the tensile test results from the section 8.1.1 was estimated by the 0.2 % proof stress in the rolling and the transverse direction for the same steel used to evaluate Young`s modulus, and is presented in the Table 8.2.

Table 8.2. Yield strength measured in the RD and TD by 0.2 % proof stress

Type of Steel	Yield Strength (MPa)
CGO in the RD	289
HiB in the RD	310
CGO in the TD	295
HiB in the TD	320

8.1.3 Measurement of the Thermal Expansion Coefficient

The linear thermal expansion coefficient α_L of the material is defined by [2]:

$$\alpha_L = \frac{1}{L} \cdot \frac{\Delta L}{\Delta T} \qquad (8.2)$$

where ΔL is the increase in length of a unit length L for an increase in temperature ΔT. A dilatometer shown in shown in Fig 8.2 was designed to test strip with dimensions 10 mm x 4 mm. The size of a strip tested in the dilatometer was in the range of a single grain of the HiB steel. Therefore to obtain the average value of thermal expansion coefficient a part of the bare CGO sheet (top coating was removed) with the smallest selected grains was cut in to strips.

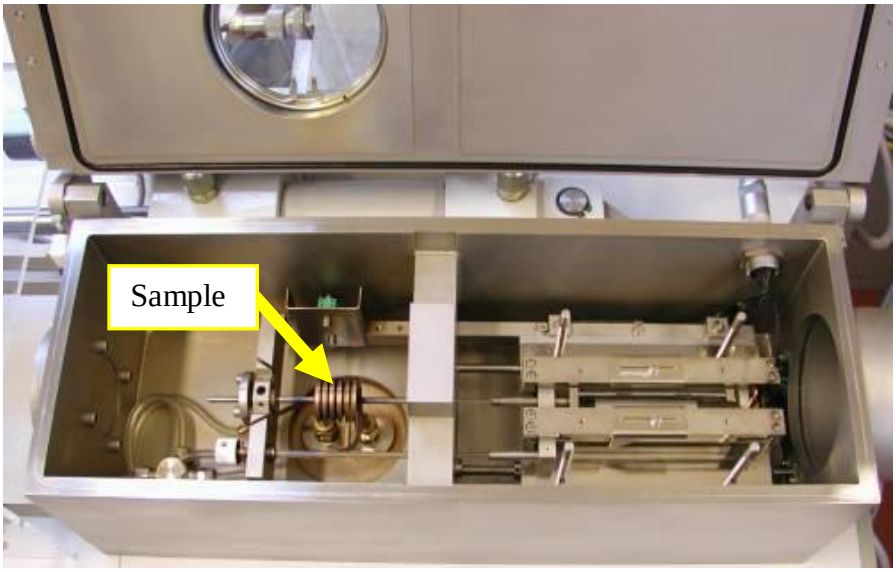

Fig 8.2 Chamber of dilatometer used to heat and measure thermal expansion of the CGO strip.

Two strips of 0.30 mm thick CGO, with the long axis parallel to the rolling and the transverse direction, were tested. The strips were then pickled in a 20% sodium hydroxide solution and stress relief annealed. During the measurement each strip was heated up to 850˚C and an expansion of the steel along its length was measured. The curves of the expansion due to change in the temperature are presented in Fig 8.3.

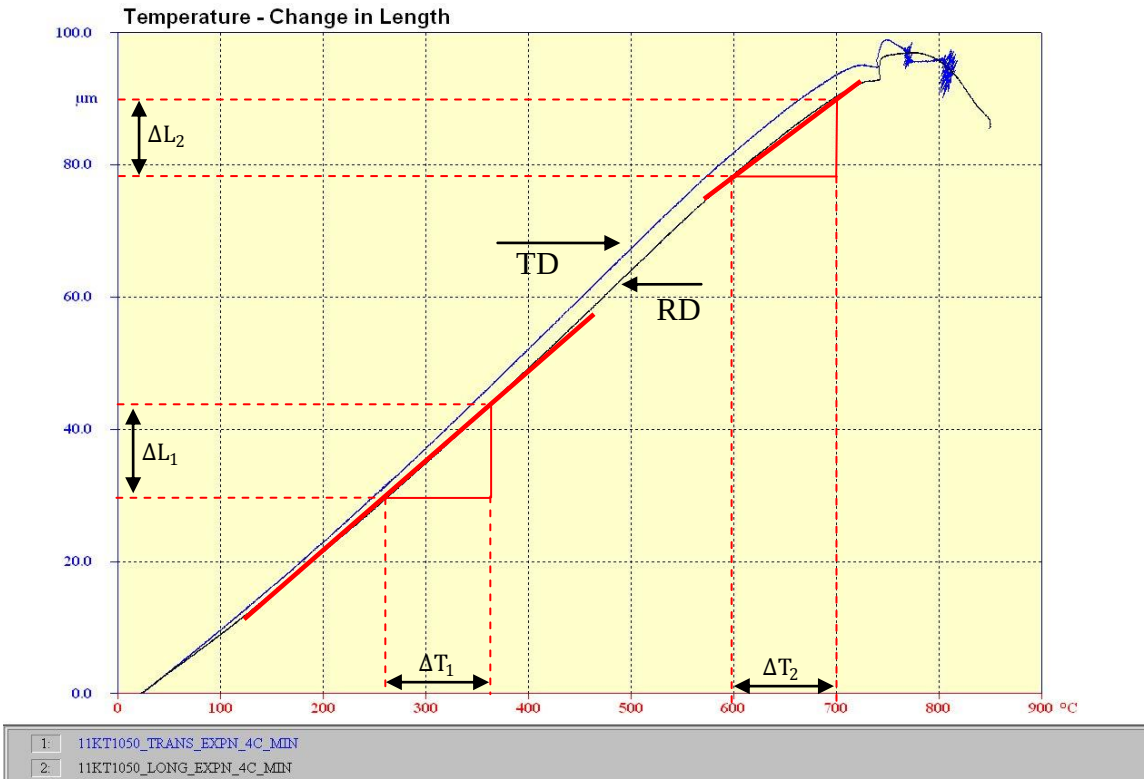

Fig 8.3 Thermal expansion characteristic in the rolling and the transverse direction of the CGO.

The measured coefficients are presented in Table 8.3.

Table 8.3. Linear thermal expansion coefficients α_L of the CGO steel strips

Temperature Range (˚C)	**α_L in the RD (10^{-6}/˚C)**	**α_L in the TD (10^{-6}/˚C)**
20 - 400	13.1	13.8
600 - 700	11.0	11.1

8.2 Application of Thermal Stresses in the Steel

The steel with a slurry coating on the surface expands by a similar amount in the RD and the TD under increasing temperature. During the cooling process from 850°C the steel and coating contract at different rates (the coating has a lower thermal expansion coefficient than the steel). The ceramic coatings extend the applicability of the brittle-coating at the temperature approximately 400°C [2]. It is assumed that at this temperature isotropic stresses are introduced by the coatings to the surface of the GO steel.

Strain caused by the thermal contraction of the steel is almost the same in the RD and TD direction (Table 8.3) therefore different Young`s moduli in these directions under further decrease (below 400°C) in temperature introduces an almost twice higher stress in the TD (Young`s modulus 196 GPa) than in the RD (Young`s modulus 114 GPa) direction. By applying the Poisson ratio for the GO steel which is approximately 0.38 [3], a compressive stress in the TD and a tensile in the RD direction are applied to the surface as shown in Fig 8.4.

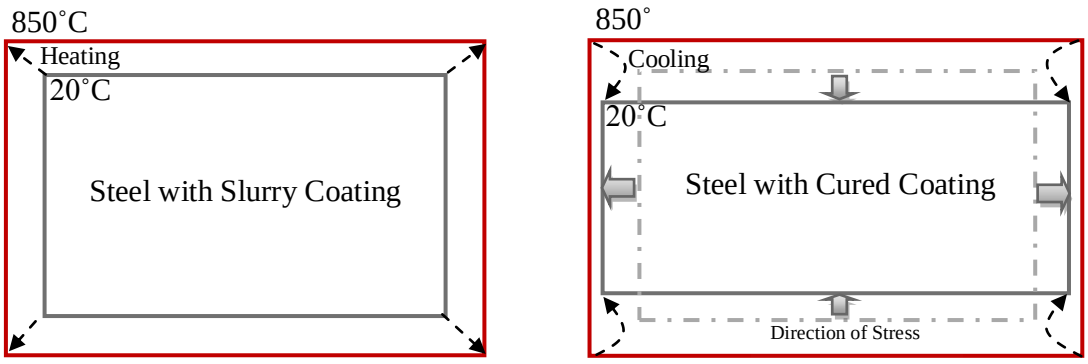

a) *b)*

Fig 8.4 Creation of thermal stresses to the surface by (a) heating and (b) cooling the steel including top coating.

Arrows with dotted curved lines in the Fig 8.4b show that cooling a sample down to a certain temperature causes contraction of the steel in both directions. Continued decrease in temperature causes further contraction in the TD and initiate expansion in the RD which is the result of the isotropic Young`s modulus of the coating and Poisson ratio of the steel.

8.3 Sample Preparation and Coating Application

A coating application was performed on the HiB material after the final stage of the production cut in to 0.27 mm thick Epstein strips which were pickled for approximately 10 minutes (this time was estimated by surface observations) in a 20% sodium hydroxide solution to remove the phosphate coating from both sides in order to leave only the glass film coating on the steel surfaces. In some cases it was necessary to remove both the phosphate coating and glass film by pickling in sulphuric (7%) and hydrofluoric (1%) solution for approximately 4 minutes (this time was estimated by surface observations) in order to achieve bare steel.

8.3.1 Type of Coatings

All coating preparation and application was carried out by the investigator in the Chemistry Laboratory at Cogent Power Ltd., prior to testing on the magnetostriction system described in section 6.1. The investigation focused on the tensile stress set up in the steel by four types of coatings currently available for laboratory testing at Cogent Power:

a) **Glass film** (forsterite coating) - magnesium oxide and colloidal silica (SiO_2 + MgO)

b) **Mix4** - aluminium orthophosphate and colloidal silica ($AlPO_4$ + SiO_2)

c) **Mix26b3** - aluminium orthophosphate, colloidal silica and magnesium orthophosphate ($AlPO_4$ + SiO_2 + $MgPO_4$)

d) **S2** - aluminium orthophosphate, colloidal silica and chromium trioxide ($AlPO_4$ + SiO_2 + CrO_3)

The coating weights of samples with coating weight up to 8 g/m^2 were measured using Fourier transform infrared spectroscopy (FTIR) [4]. Above this coating weight, up to 110 g/m^2 a Deltascope [5] device was used. This was obtained by an investigation of coating thickness measurement. Both devices were calibrated to present a coating weight in g/m^2.

8.3.2 Procedure for Coating Application

The coating as a slurry was applied by a device which comprises two mechanical rolls applying coating to the top and the bottom surface of the steel as shown in Fig 8.5.

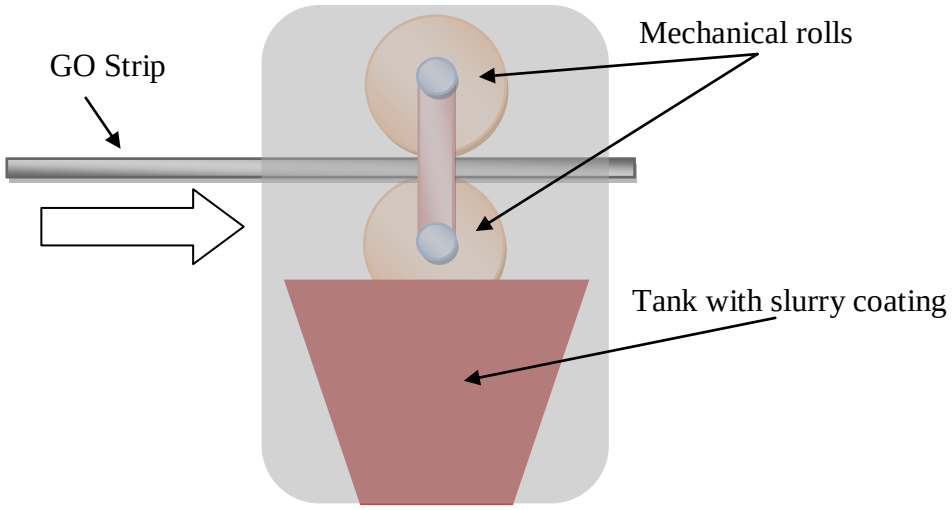

Fig 8.5 Double roller coating application machine.

The coated steel was placed on a tray (where only the 2 edges of the sample are in contact with the tray), then inserted into the furnace and heated at 850°C for 30 seconds. Subsequently, the sample and tray were taken out and cooled to room temperature (approximately 20°C) in 5 minutes, where the coating changed from slurry to a solid. After this curing process the sample was stress relief annealed (SRA) by heating at 400˚C/h to 850°C holding for 1 hour then cooling to the room temperature at100˚C/h. The thickness of the applied coating would vary between the top and bottom surface and also along the length of the coated strip. This variation depends also on the thickness of the applied coating which for the thick layer would vary up to approximately 15%. Therefore the thickness on the ends and in the middle part of the

sample on both surfaces was measured and the average coating thickness of the measured points was evaluated.

8.4 Investigation of the Coating Stress

The stress shift between magnetostriction sensitivity curves was used as a measure of the effect of stress applied to the steel by coatings. A correlation was achieved between magnetostriction under stress measurements and static domain observations under stress as described in section 5.7. This gave a basis to say that a shift between two points of stress where curves at zero magnetostriction can be used to assess the maximum stress applied to the sample surface by the coating as shown in Fig 8.6. These initial compressive stresses applied in the RD, generating stress patterns on the samples surface which causes an increase in magnetostriction.

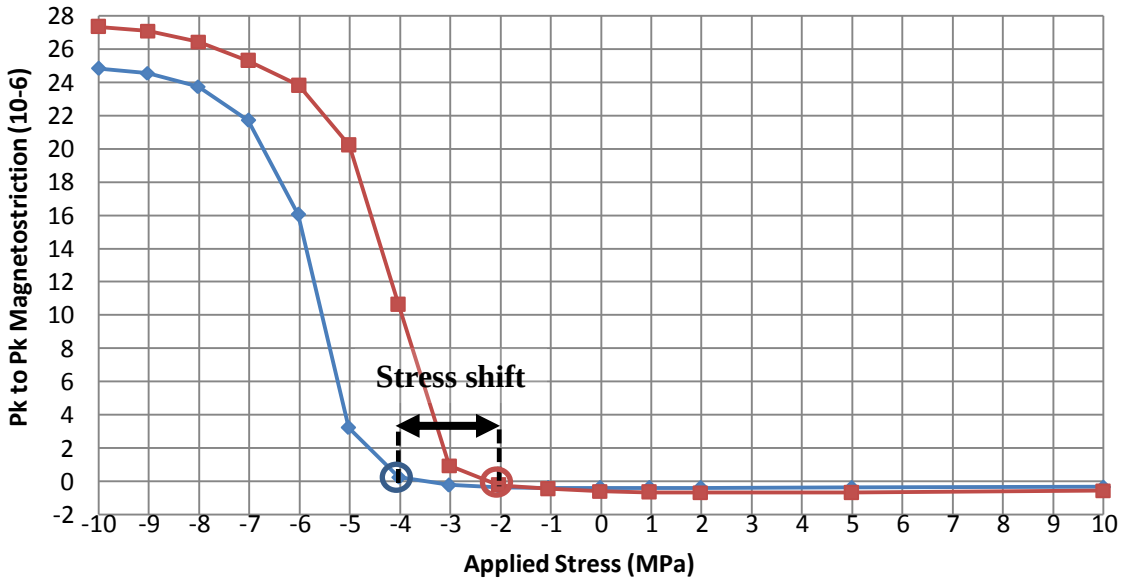

Fig 8.6 Evaluation of the stress shift between the magnetostriction vs. stress curves of the HiB steel measured under 1.7 T and 50Hz.

At this stage the effect of the coating stress on the power loss is also investigated. The gradient of the stress sensitivity curve of loss, especially under tensile stress, differs from that of the magnetostriction curve. Therefore the maximum stress shift for loss is measured between the stress points of two curves included in the lower range of compressive stress as shown in Fig 8.7.

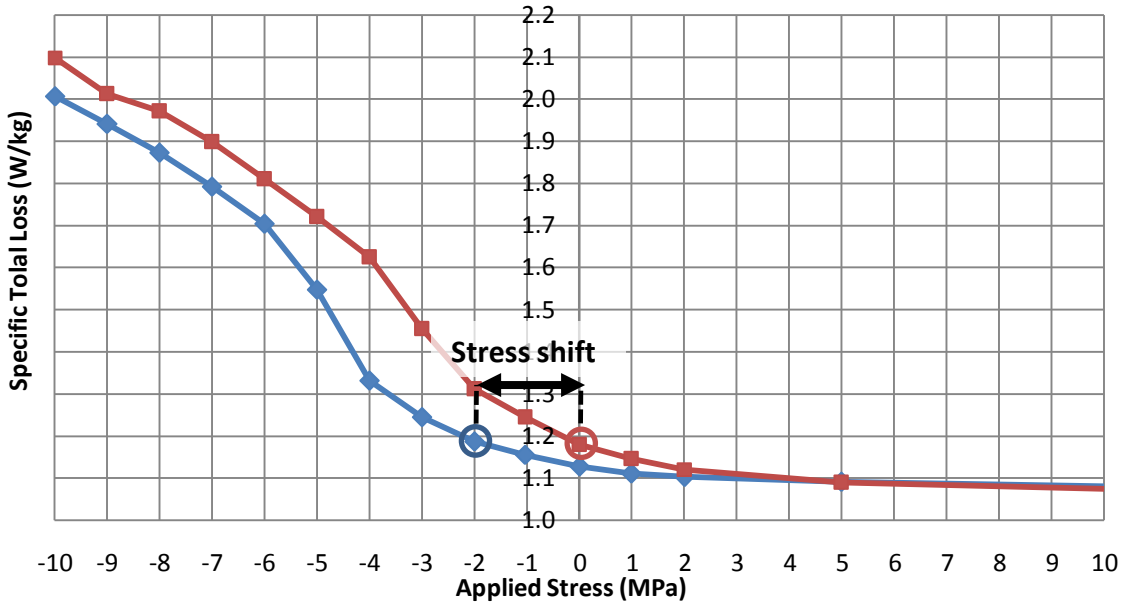

Fig 8.7 Evaluation of the stress shift between loss vs. stress curves of the HiB steel measured under 1.7 T and 50Hz.

8.4.1 Importance of the SRA

To investigate the effect of the curing and SRA on the stress applied to the steel surface during the coating application, four samples were coated and measured after the stages shown in Table 8.4.

Table 8.4 Four stages of HiB sample preparation

Stage 1	Stage 2	Stage 3	Stage 4
Sample from production line coated with Mix4	Pickled to remove only the Mix4 coating	Coated with slurry Mix4 in the laboratory and cured	SRA

The Mix4 coating was applied with a coating weight of 4 g/m^2 per side to the sample surface on the production line and also in the laboratory. Fig 8.8 shows magnetostriction and loss characteristics of average values of 5 HiB strips tested on the magnetostriction measurement system after the each stage (Table 8.4).

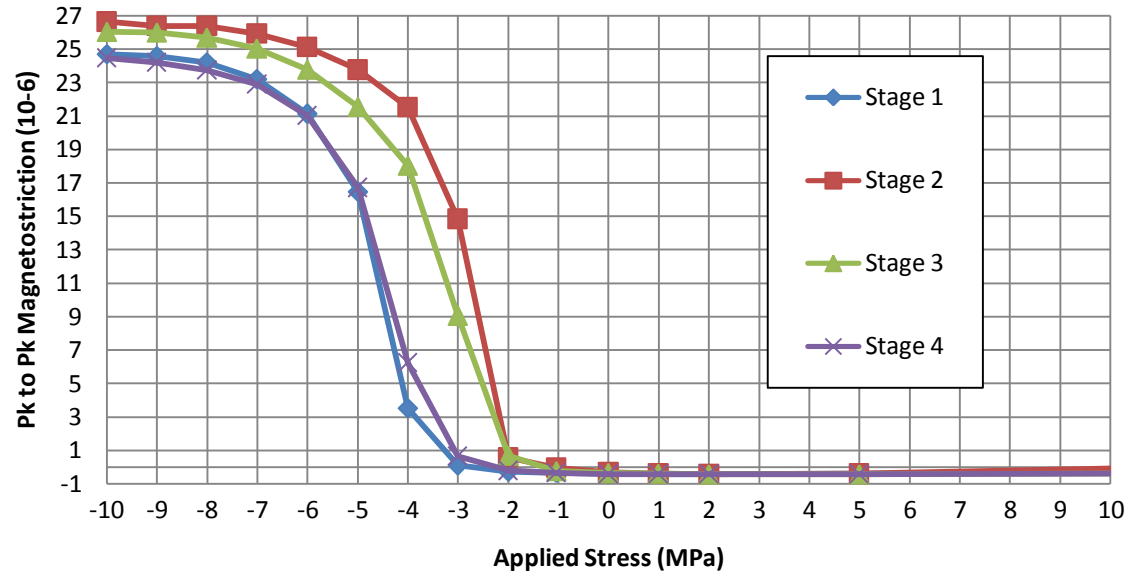

a)

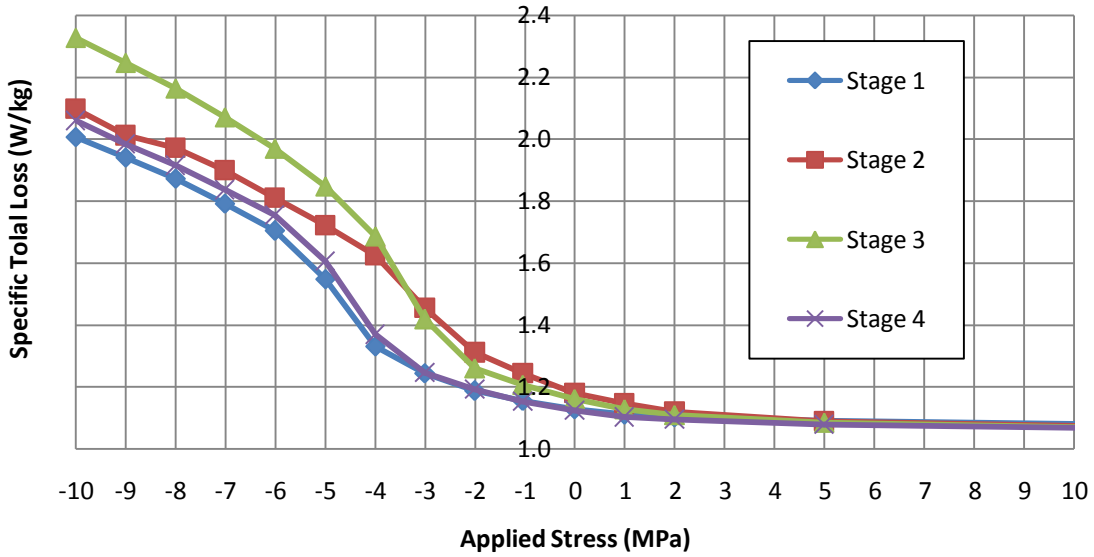

b)

Fig 8.8 Average magnetostriction and loss characteristics of 5 HiB strips coated on production line and in the laboratory with Mix4 coating, according to Table 8.4 (tested at 1.7 T and 50 Hz).

The Mix4 coating after the curing process applied a very low tension to the surface of the steel. The stress shift of up to 2 MPa between stage 2 (only glass film) and stage 4 (glass film with Mix4) was obtained for magnetostriction and loss under stress characteristics. It was also observed that after SRA the maximum coating tension was achieved.

The slurry phosphate coating applied to the HTCA material on the production line was cured at 850˚C for 30 seconds, and was then cooled to room temperature with a

slow rate when the final material is coiled and transferred from the production line. This cooling rate can be similar to that obtained in the laboratory environment (after SRA) as the magnetostriction and loss stress sensitivity curves for the remaining samples were similar to those presented in the Fig 8.8 (especially stage 1 and stage 4).

8.4.1.1 SRA Application After Each Applied Coating Layers

In this stage the effect of SRA after each applied coating layers were investigated. Two batches of three samples including glass film were double coated with the S2 coating in two ways:

a) SRA once - coating applied in five steps as presented in Table 8.5:

Table 8.5 Five steps of coating application process

Step 1	**Step 2**	**Step 3**	**Step 4**	**Step 5**
First layer of slurry coating	Cure	Second layer of slurry coating	Cure	SRA

b) SRA twice - coating applied in six steps as presented in Table 8.6:

Table 8.6 Six steps of coating application process

Step 1	**Step 2**	**Step 3**	**Step 4**	**Step 5**	**Step 6**
First layer of slurry coating	Cure	SRA	Second layer of slurry coating	Cure	SRA

Fig 8.9 shows average values of magnetostriction and loss measured under stress of three samples from each batch with average total coating weights (bottom plus top coating) of 15 g/m^2.

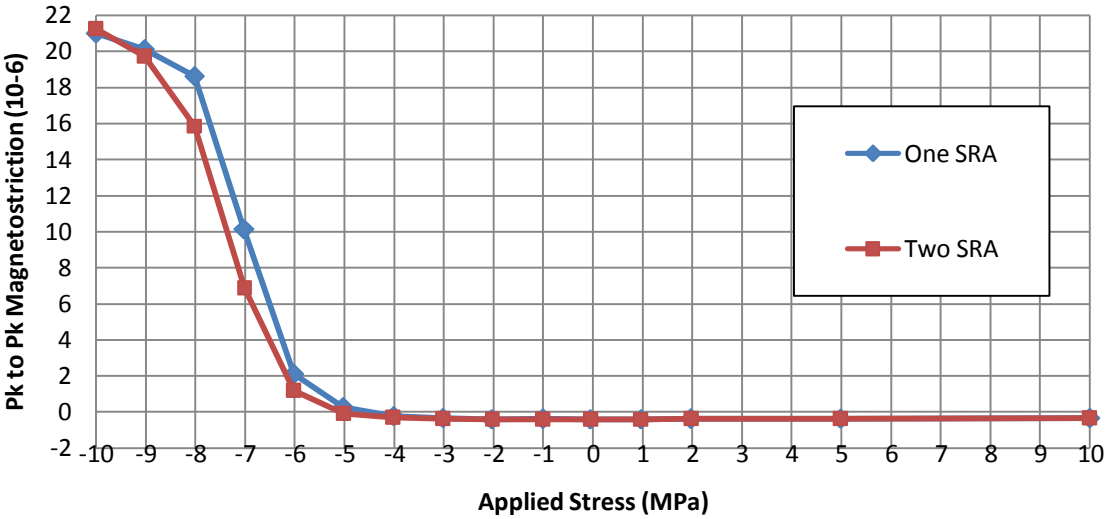

a)

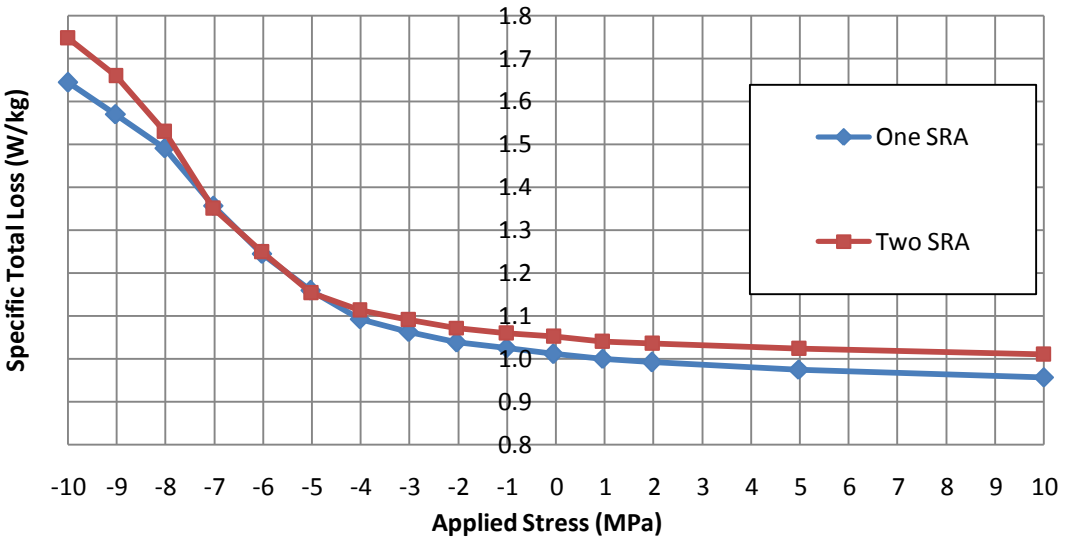

b)

Fig 8.9 Magnetostriction (a) and loss (b) sensitivity curves of the HiB with S2 coating of average total weight 15 g/m^2 on the surface measured under 1.7 T at 50 Hz.

A small variation between stress sensitivity curves of magnetostriction and loss measurements was obtained (as shown in Fig 8.9a, b). These could be caused by lower uniformity of the coating thickness along the samples length, therefore they should not be considered as significant changes.

This stage shows that SRA carried out once or twice during multilayer coating application does not affect magnetostriction and loss measured under stress.

8.4.2 Importance of the Glass Film as the Base Coating

8.4.2.1 Glass Film as the Single Coating Layer

To establish a stress applied to the steel surface using the glass film coating, the stress shift between magnetostriction and loss characteristics was measured. Three fully processed samples cut from the production line were pickled in 20% sodium hydroxide solution to remove the top coating i.e. Mix4, and were then tested on the magnetostriction measurement system. Subsequently the samples were pickled in a sulphuric and hydrofluoric acid solution to obtain completely bare steel. The magnetostriction measurements were repeated on the bare steel samples. The average values of three samples of magnetostriction and loss stress sensitivity curves are presented in Fig 8.10.

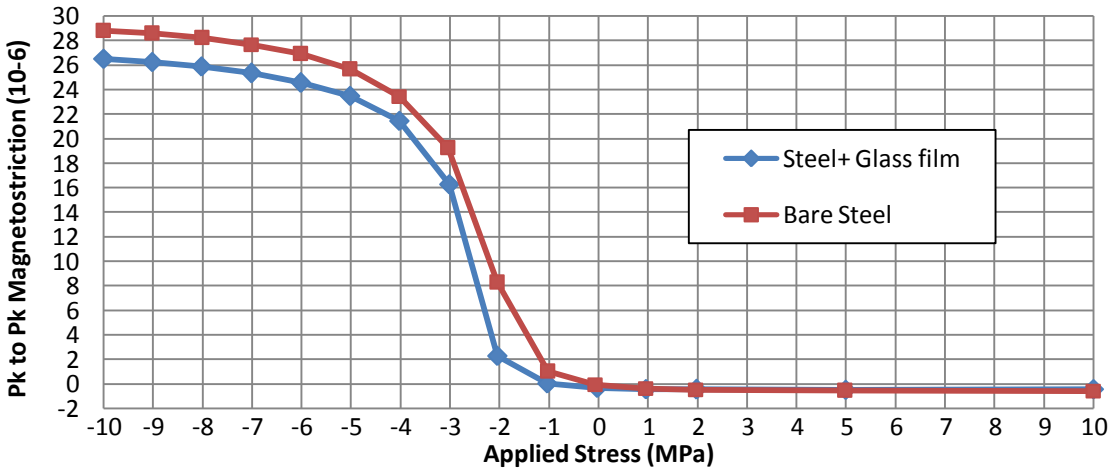

a)

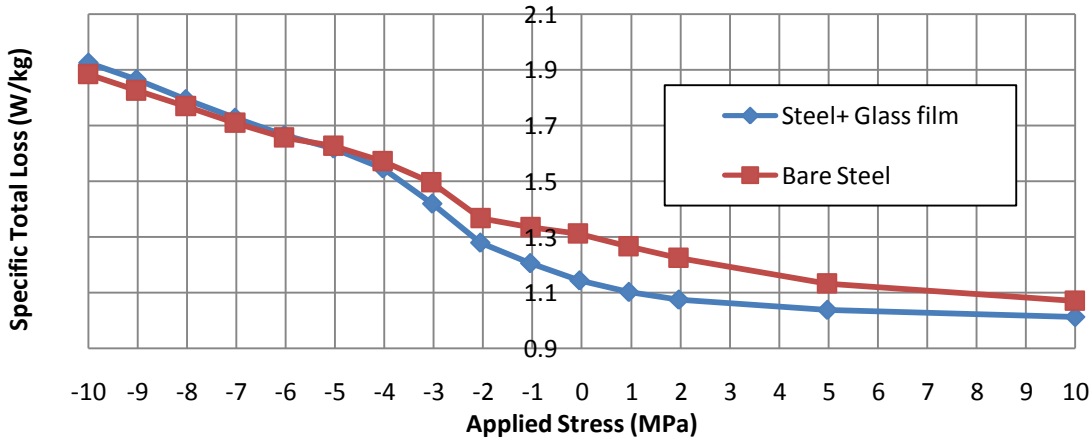

b)

Fig 8.10 Magnetostriction (a) and loss (b) sensitivity curves of the HiB with glass film coating of average total weight 6 g/m^2 on the surface measured under 1.7 T at 50 Hz.

The glass film coating with weight 3 g/m^2 applied a shift up to 1 MPa in magnetostriction as shown in Fig 8.10a. The characteristic variation in loss (10% reduction) for steel with and without glass film, especially under zero stress was similar for all three tested samples, in the stress region from 2 MPa to -2 MPa (Fig 8.10 (b)). The forsterite coating during its formation in the HTCA (section 2.2.5) penetrates into the steel subsurface as shown in Fig 8.11. Therefore after curing and subsequent thermal contraction of the coating, a stress on the surface and in the subsurface of the steel affects the loss as observed in Fig 8.10 (b).

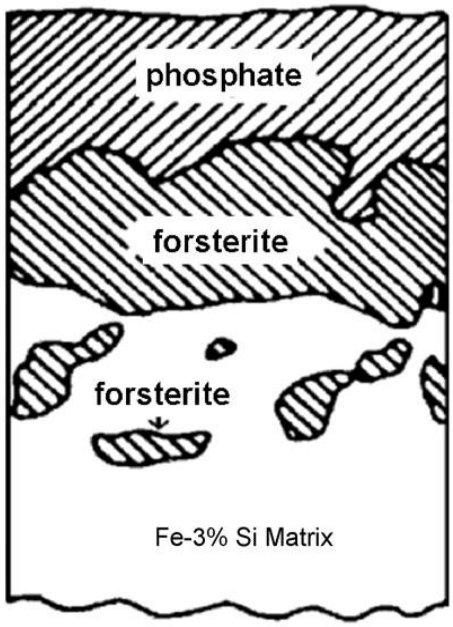

Fig 8.11 Composition of the forsterite coating in commercially produced GO steel [6].

8.4.2.2 Glass Film as the Base Coating

To investigate the importance of the glass film as a primer coating on the stress applied to the steel surface, two batches of three samples each were coated. A single layer of Mix26b3 and S2 coatings were applied to the samples surfaces with and without the primer. The weight of a single layered coating applied to the bare steel was equal to the total weight of two coatings, i.e. weight of "glass film + Mix26b3" was equal to the weight of "only Mix26b3" as presented in Fig 8.12 and Fig 8.13.

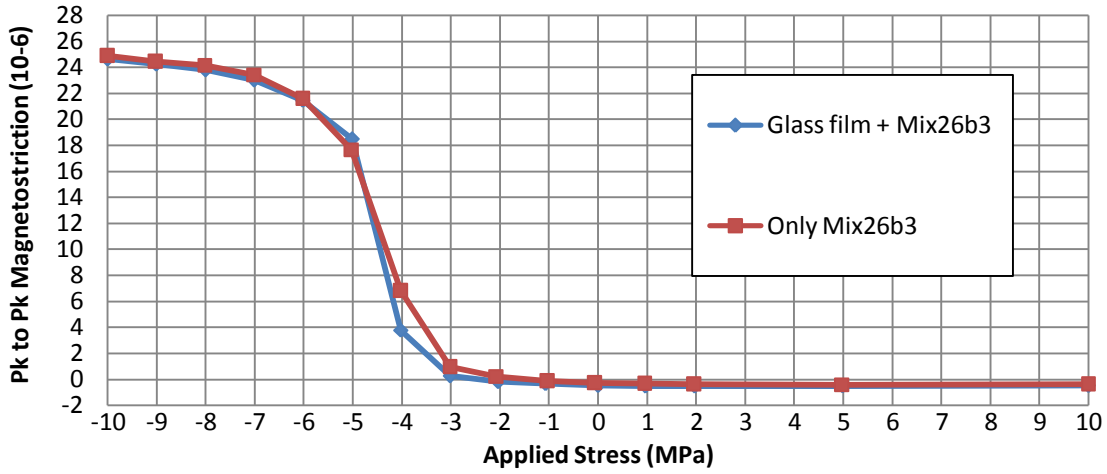

a)

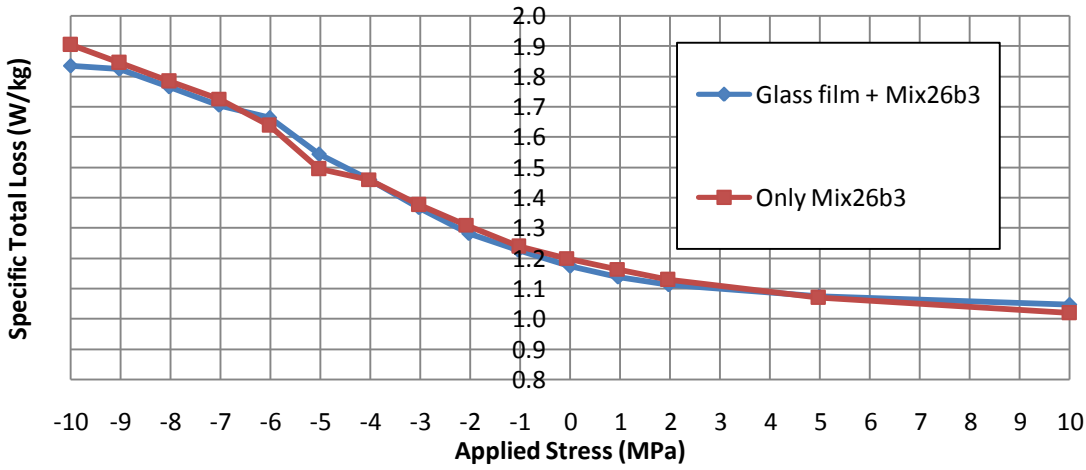

b)

Fig 8.12 Magnetostriction (a) and loss (b) sensitivity curves of the HiB with Mix26b3 coating of average total weight 12 g/m^2 on the surface measured under 1.7 T at 50 Hz.

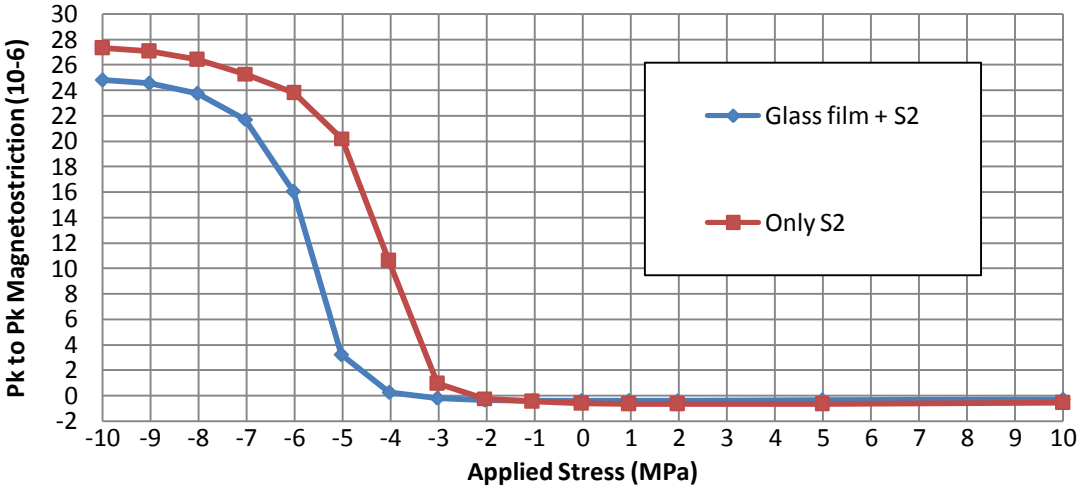

a)

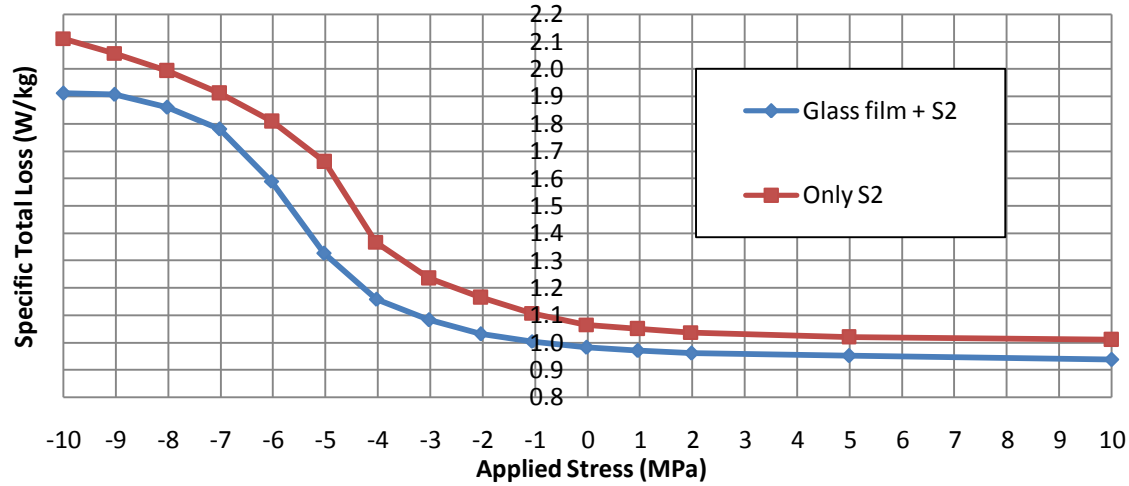

b)

Fig 8.13 Magnetostriction (a) and loss (b) sensitivity curves of the HiB with S2 coating of average total weight 13 g/m^2 on the surface measured under 1.7 T at 50 Hz.

The coating Mix26b3 applied to the bare steel surface with and without the primer, does not affect the magnetostriction and loss under stress as shown in Fig 8.12.

The S2 coating applied as the primer coating characterises with comparable stress sensitivity curves of magnetostriction and loss to Mix26b3 coating. However S2 coating applied as the second layer on the glass film improves significantly the coating stress applied to the steel surface by generating an additional 2 MPa shift in magnetostriction and loss sensitivity curves (Fig 8.13). It seems that the magnesium and colloidal silica (also included in S2 coating) as ingredients of the glass film provide better adhesion to the steel surface, therefore when bonded with S2 coating it applies higher stress to the steel surface.

8.4.3 Multilayer Coating Application

The condition and quality of the coating applied to each sample was observed by visual inspection: colour and adhesion. The maximum weight of a single layer of coating that could be applied to each surface was 8 g/m^2. The quality of the coating applied as a single layer at its maximum weight was very poor for all investigated coatings with the coating flaked off. A multilayered method was necessary to increase the coating thickness to be more than 8 g/m^2 per side.

8.4.3.1 Importance of Multilayer Coating Application (Mix26b3 and S2 Coating)

To investigate the behaviour of a coating in a form of single or double layered with a similar total coating weight applied to the surface of the steel including the primer, two batches of three samples were prepared. Two types of coatings, Mix26b3 and S2, were applied to two batches of samples initially coated with glass film. Each batch was given a single and double layered coating with the SRA at the end of the multilayered coating application process. Fig 8.14 and Fig 8.15 present comparison of stress sensitivity characteristics of magnetostriction and loss measurements of two samples with average 12 g/m^2 total coating weights.

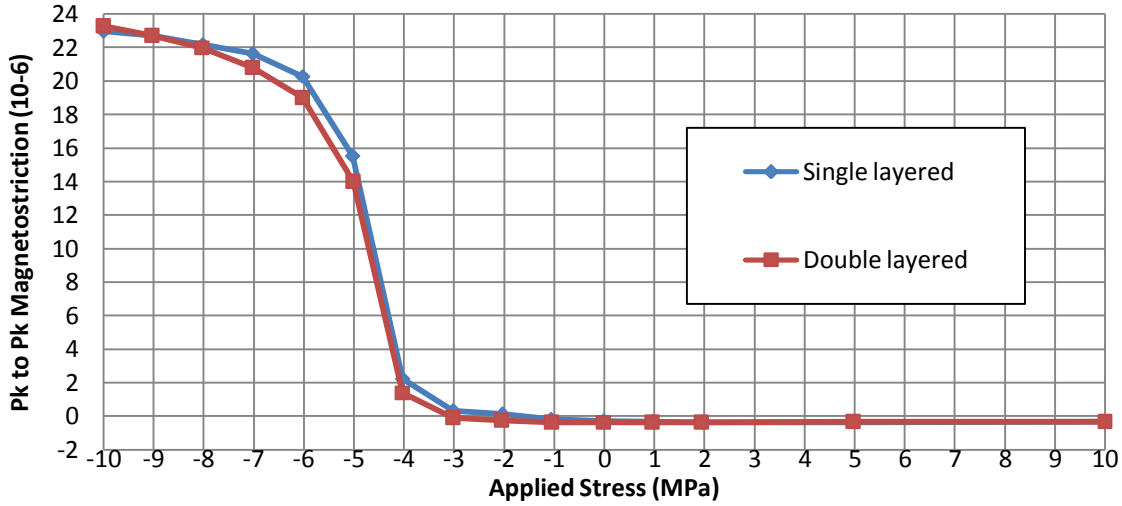

a)

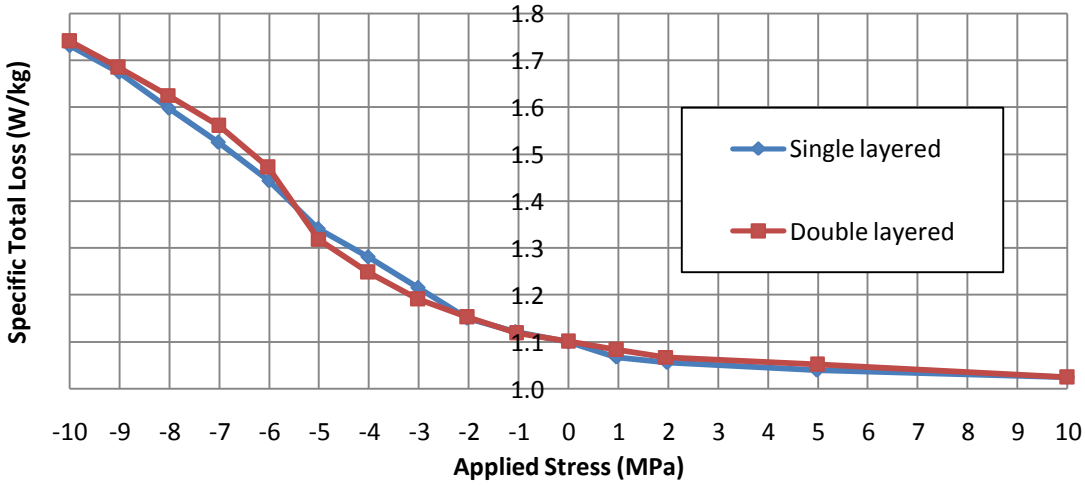

b)

Fig 8.14 Magnetostriction (a) and loss (b) sensitivity curves of the HiB with single and double layered Mix26b3 coating of average total weight 12 g/m^2 on the surface measured under 1.7 T at 50 Hz.

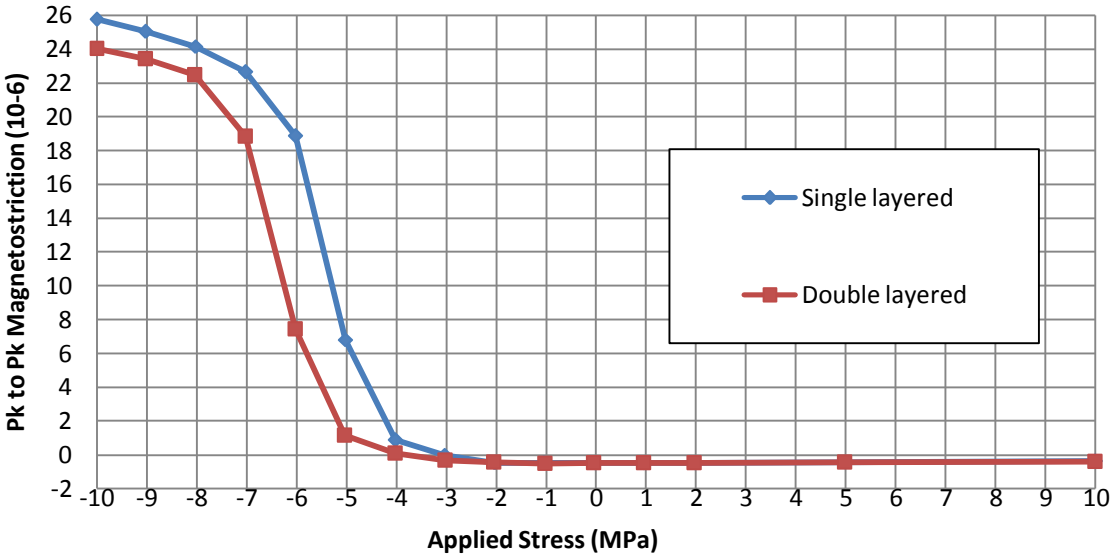

a)

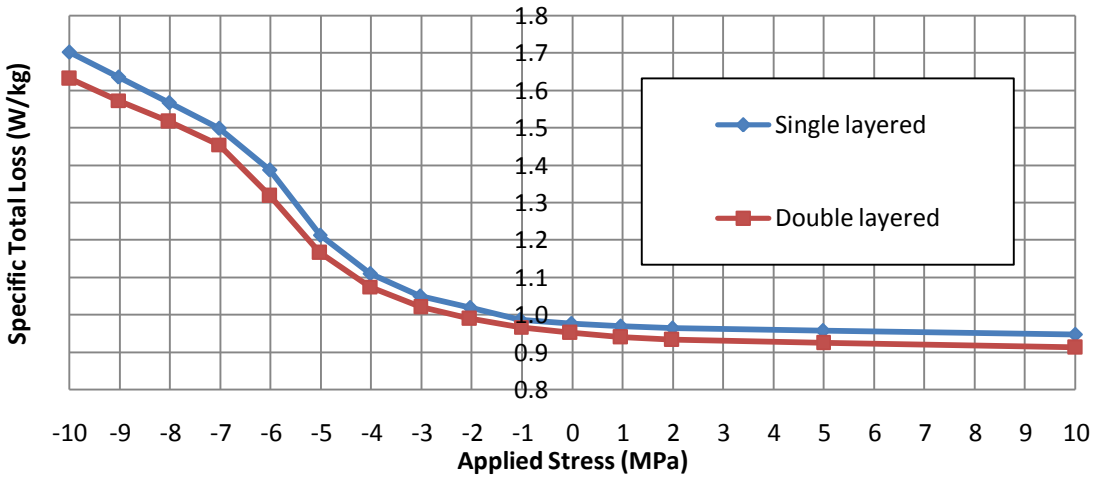

b)

Fig 8.15 Magnetostriction (a) and loss (b) sensitivity curves of the HiB with single and double layered S2 coating of average total weight 11 g/m^2 on the surface measured under 1.7 T at 50 Hz.

In the double coated samples the weight of each coating layer was approximately 2 g/m^2. The magnetostriction and loss of samples with applied single or double layers of Mix26b3 coating present comparable stress sensitivity characteristics. However samples with double layered S2 coatings improve magnetostriction and loss by creating approximately 1 MPa higher shift of magnetostriction and loss compared to that for the single layered sample. This shows that during application of coating weight higher than 4 g/m^2 per side, the multilayer procedure should be used. It seems that adhesion of the multilayered coating is stronger than the singly applied thick coating.

8.4.3.2 Influence of the Coating Weight on the Introduced Stress

To evaluate minimum and maximum stress introduced by all previously mentioned coatings (Mix4, Mix26b3 and S2), magnetostriction of the wide range of samples with applied varying coating weights was investigated. All of the samples with the base coating (approximately 3 g/m^2) were coated using the multilayer coating application procedure with final SRAs, carried out when all cured coating layers were applied. The total weight of coatings applied to the steels, including the primer coating, was in the range from 4 g/m^2 to 110 g/m^2.

Fig 8.16 shows the relationship between the coating weight and the stress shift between "**only glass film**" and "**glass film with applied varying coating thickness**", obtained by the shift of magnetostriction stress sensitivity curves.

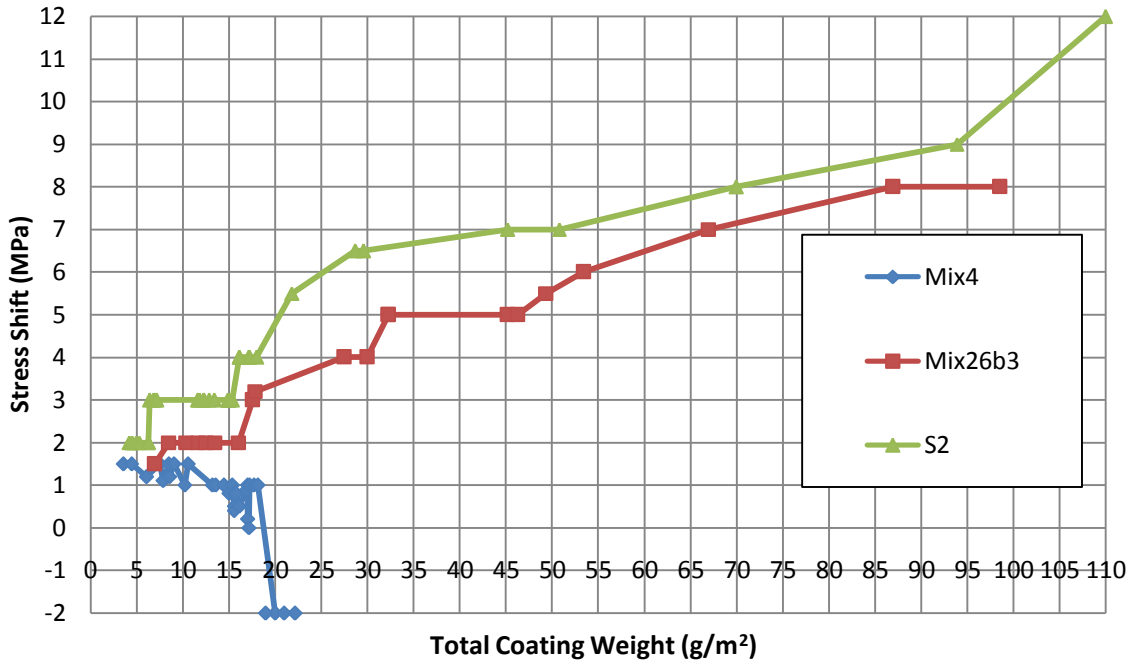

Fig 8.16 Introduced stress shift dependent on the total coating weight of Mix4, Mix26b3, and S2 coating (1.7T, 50 Hz).

The Mix26b3 and S2 coatings are characterised with an increasing trend of tension introduced to the steel surface due to increasing coating weights. However Mix4 is characterised with a decreasing trend. The maximum weight of these three coatings was limited by the quality of the coated surface. To evaluate magnetostriction and loss under

saturation in samples with very high coating weight, the maximum range of applied compressive stress was set up on the magnetostriction measurement system to -20 MPa.

Fig 8.17 shows magnetostriction and loss characteristics under compressive stress up to -20 MPa, for samples prepared in the laboratory (Mix26b3 and S2 with very high coating weight) and from the production line (only the thin single layered Mix4 coating).

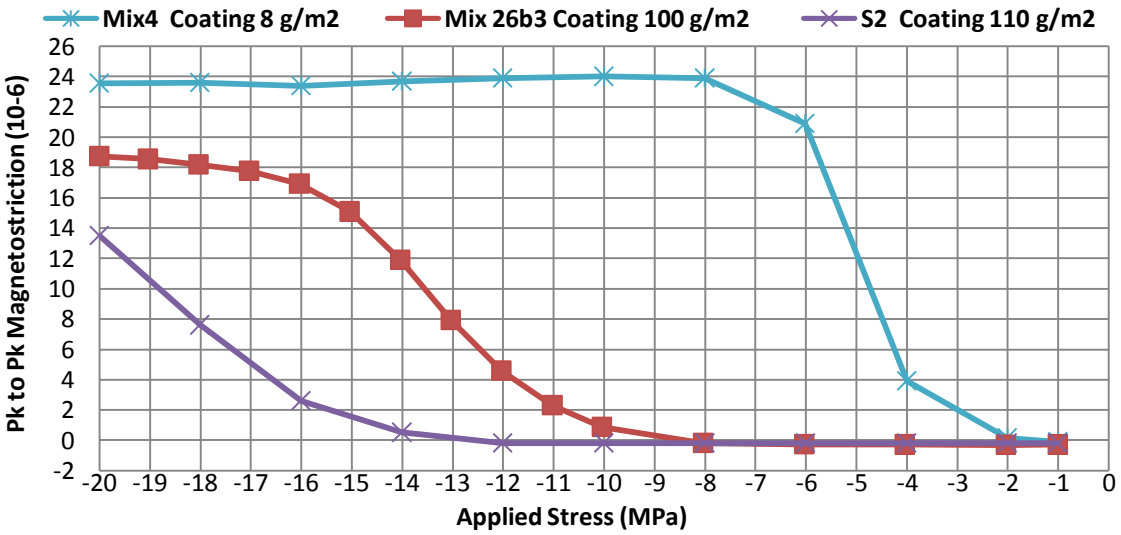

a)

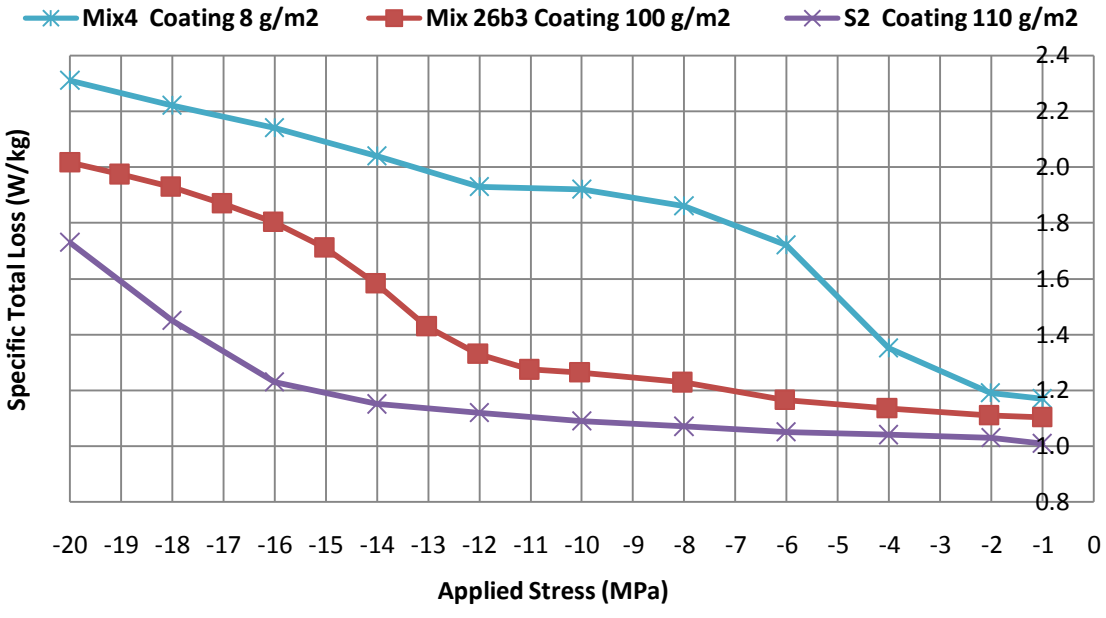

b)

Fig 8.17 Magnetostriction (a) and loss (b) sensitivity curves of the HiB with Mix26b3 coating of average total weight 12 g/m^2 on the surface measured under compressive stress of up to -20 MPa at 1.7 T, 50 Hz.

The stress sensitivity curve for the sample of S2 coating with total weight of 110 g/m^2, the highest coating weight which could be produced in the laboratory, was characterised with rapidly increasing magnetostriction when more than -14 MPa was applied. The tension evaluated from the shift of stress sensitivity curves before and after applied coating is approximately 13 MPa.

8.4.4 Magnetostriction and Loss of Double Coated Samples on the Production Line

Fully finished material with glass film and Mix4 coatings was passed again through the final part of the production line, described in section 2.2.6, in order to double the Mix4 coating weight from 4 g/m^2 to 8 g/m^2 per side. Three samples were cut from sheets before and after passing the coil through the final stage of production for a second time. All samples were SRA after cutting and then tested on the magnetostriction measurement system. The comparison of average values of three samples of magnetostriction and loss of three samples are shown in Fig 8.18.

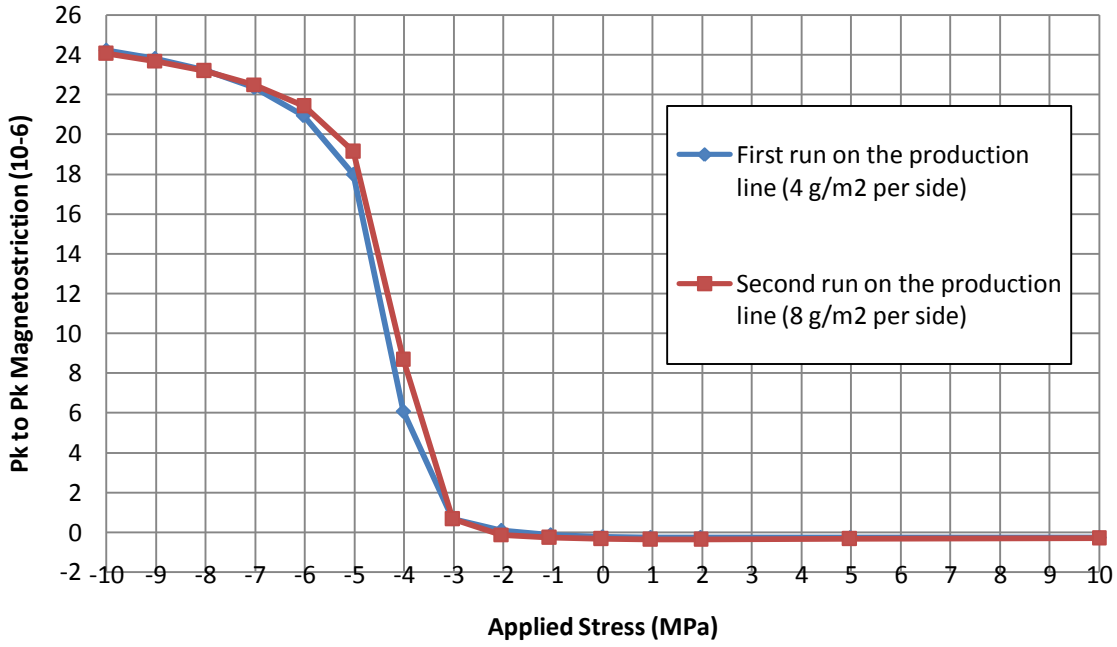

a)

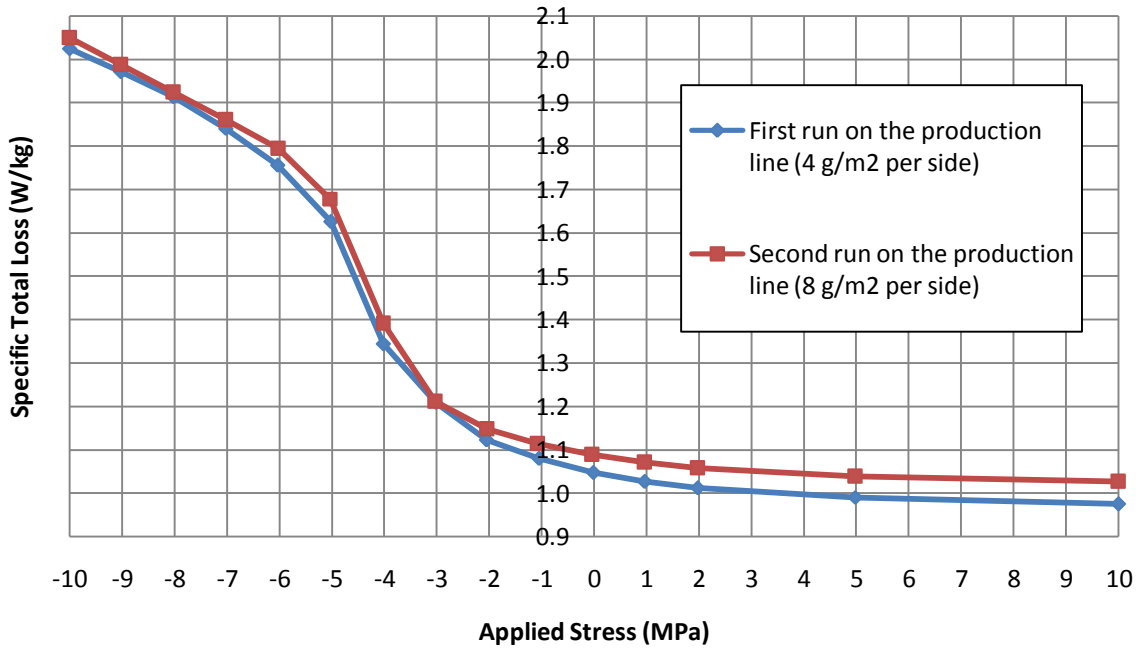

b)

Fig 8.18 Magnetostriction (a) and loss (b) sensitivity curves of the HiB steel with Mix4 coating, passed second time through the final stage of production, measured under 1.7 T at 50 Hz.

The magnetostriction sensitivity curve of the strip with applied Mix4 coating on the surface during the second run on the production line with weight of 8 g/m^2 per side (4 g/m^2 per layer), was compared with the magnetostriction of the strip after first run and showed no improvement in the stress shift stress as shown in Fig 8.18. It is observed that magnetostriction and loss measurements of samples with increased weight of the Mix4 coating on the production line gives similar results to samples prepared in the laboratory (Fig 8.16). This would be the effect of weak mechanical properties of the Mix4 coating which could not resist a high contraction of the steel.

8.4.5 Influence of Surface Coating Stress on the Steel Loss

In this stage the effect of coating stress on the power loss is investigated. The samples coated with varying weight of S2 coating, previously used in Fig 8.16, are plotted as loss under stress characteristics in Fig 8.19.

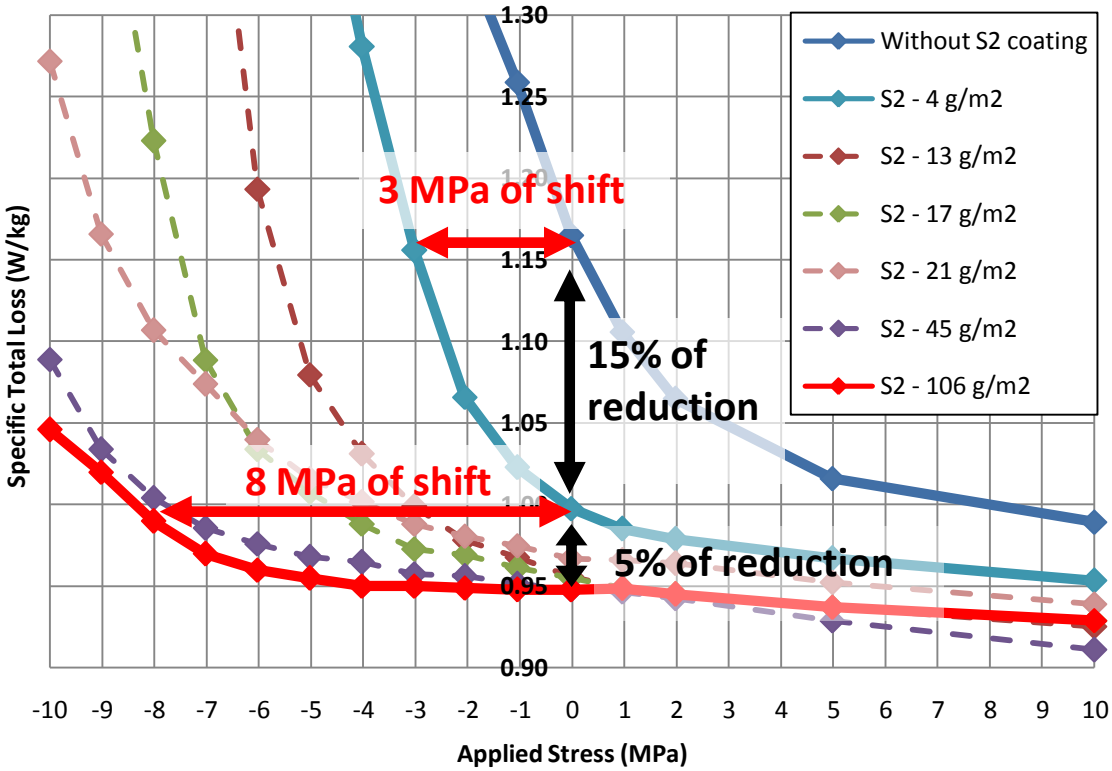

Fig 8.19 Effect of coating stress on loss sensitivity curve measured under 1.7 T at 50 Hz.

Fig 8.19 shows that increasing weight of S2 coating increases the stress shift between the loss curves measured from zero stress up to a certain value of compressive stress. However it must be emphasized that with no external applied stress the ratio of loss reduction to coating weight was most significant for the sample with very thin layer of S2 coating (3.75% per g/m^2). This ratio was shown to be much lower for thicker coatings, e.g. 0.19% per g/m^2 for the thickest (106 g/m^2) S2 coating.

A similar relationship was observed between high coating stress (evaluated by the calculation of a strip curvature after single sided coating removal) and loss in [6] as shown in Fig 8.20. It can be seen that application of greater magnitudes of stress has less substantial effect on loss reduction.

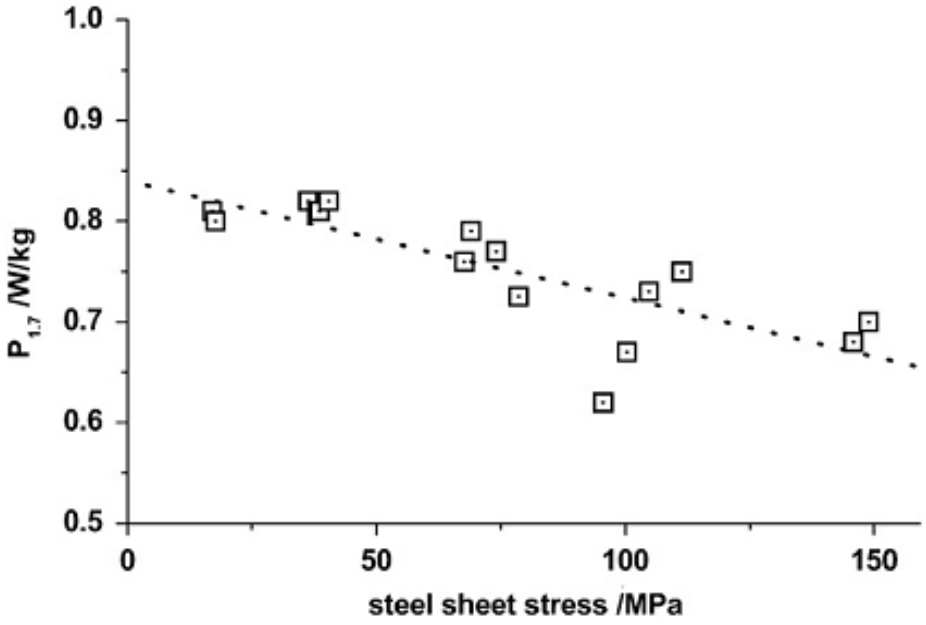

Fig 8.20 Power loss vs. various coating stress introduced to the surface of the HiB steel, measured under no stress at 1.7 T, 50 Hz [6].

Tension applied to the steel surface in the RD direction is created by a high compression applied in the TD direction due to the thermal contraction of the coating and the steel. It was observed that after application of a thin coating layer domains did not become narrower in comparison to the applied very thick coating. The first high decrease in loss would be caused by the reduction of closure domains along the RD direction (15% reduction in Fig 8.19). Furthermore at a certain level of compression in the TD direction, domains will start narrowing. However the domains narrowing would not affect loss with the same magnitude as the reduction of closure domains.

8.4.6 Investigation of Stresses Introduced to the Steel Surface

8.4.6.1 Domain Observations under High Coating Tension

The domain structure of the sample with S2 coating weight of 95 g/m^2 was observed using the Domain Viewer. To prove that a high tension was applied to the steel surface static domain observations under external compressive stress along the RD direction were carried out. Fig 8.21 shows images of domain structures under applied compressive stress correlated to the points on the magnetostriction under stress curve.

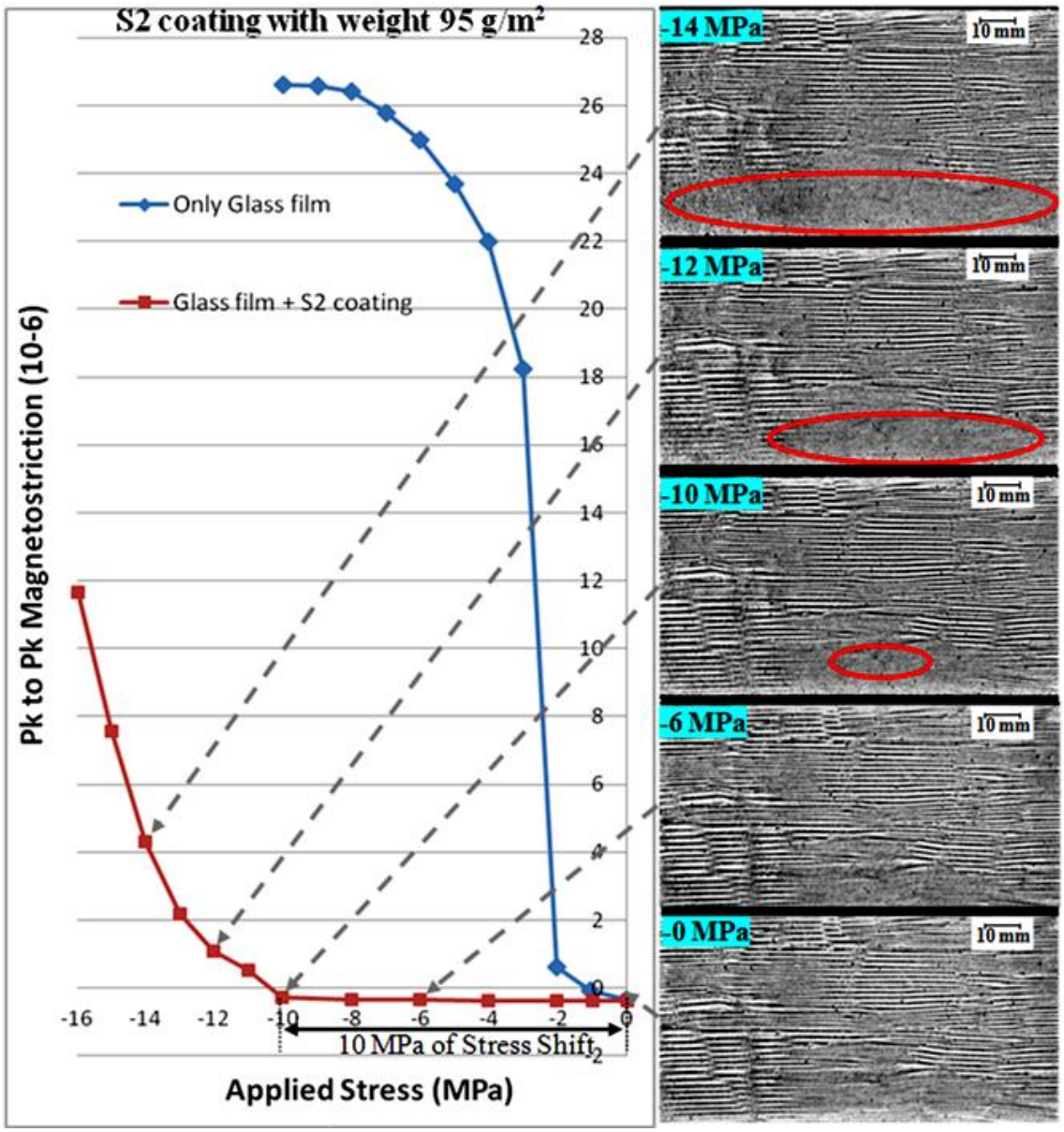

Fig 8.21 Correlation of the Magnetostriction measurements and domain observations under high compression up to -20 MPa of S2 coated HiB steel with average total coating weight 95 g/m^2).

A small area of stress patterns appeared above -10 MPa of applied external compressive stress and these started increasing in volume. This increase in the volume will lead to an increase in the magnitude of the magnetostriction.

8.4.6.2 Single Sided Coated Steel

The same sample with S2 coating weight of 95 g/m^2 as used for domain observations in the section 8.4.6.1 was pickled to achieve an uncoated surface (bare steel) on one side of the steel. The other side the coating was protected by acid resistant tape. Fig 8.22 shows a curvature of the sample after single sided coating removal, introducing tensile stress on the coated side and compressive on the uncoated.

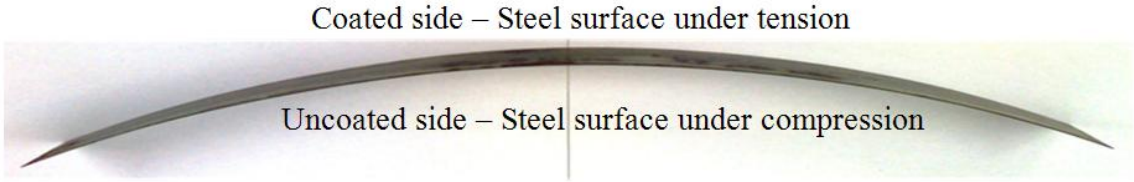

Fig 8.22 Curvature of the S2 coated sample with removed coating from one side.

The radius R of the sample curvature was calculated from

$$R = \frac{a^2}{2x}, \quad if\ x < a \tag{8.3}$$

where **a** and **x** are defined in Fig 8.23.

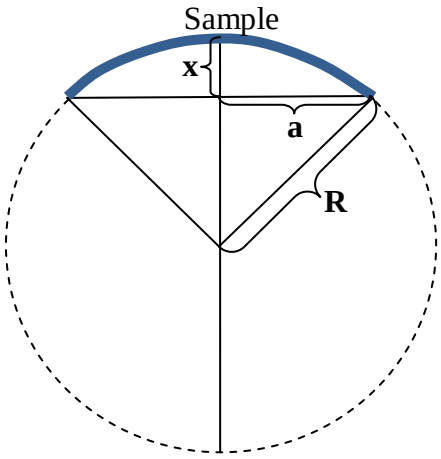

Fig 8.23 Schematic diagram of method to calculate a radius of the strip curvature.

The maximum stress, σ_{max} applied to the steel was calculated from

$$\sigma_{max} = \frac{E \times \left(\frac{t}{2}\right)}{R + \frac{t}{2}} \qquad (8.4)$$

For grain oriented steel with Young`s modulus of 113 GPa in the RD (Table 8.1) and thickness 0.27 mm, the maximum stress σ_{max} applied by the coating on the one side is 35 MPa. The calculated stress is much greater then this evaluated by the domain observation under stress and stress shift of magnetostriction curves (10 MPa).

The curvature of the single side coated sample is an effect of stresses in rolling and transverse directions which are caused by the thermal stresses applied due to the differential contraction of the steel and coating. All stresses in the steel are resisted by the top and the bottom coating layer. If the coating layer of one side is removed then the coating from other side will not resist all stresses applied by the steel, especially the high compressive stress in the TD direction. Therefore the tensile stress will curve the steel in the RD direction and also it could be simultaneously affected by a bending stress in the TD direction.

It is believed that this method for the stress calculation of the residual curvature of the one side coated steel does not give the correct value of a tensile stress applied by the coating in the RD for the double side coated steel.

8.4.6.3 Transverse Stresses

To investigate the effect of a coating stress in the TD, the S2 coating was applied to the surface of a transverse cut HiB sample including glass film. Fig 8.24 shows magnetostriction and loss sensitivity curves measured at 1.4 T, and 50 Hz on a single sample coated with two layers of S2 coating.

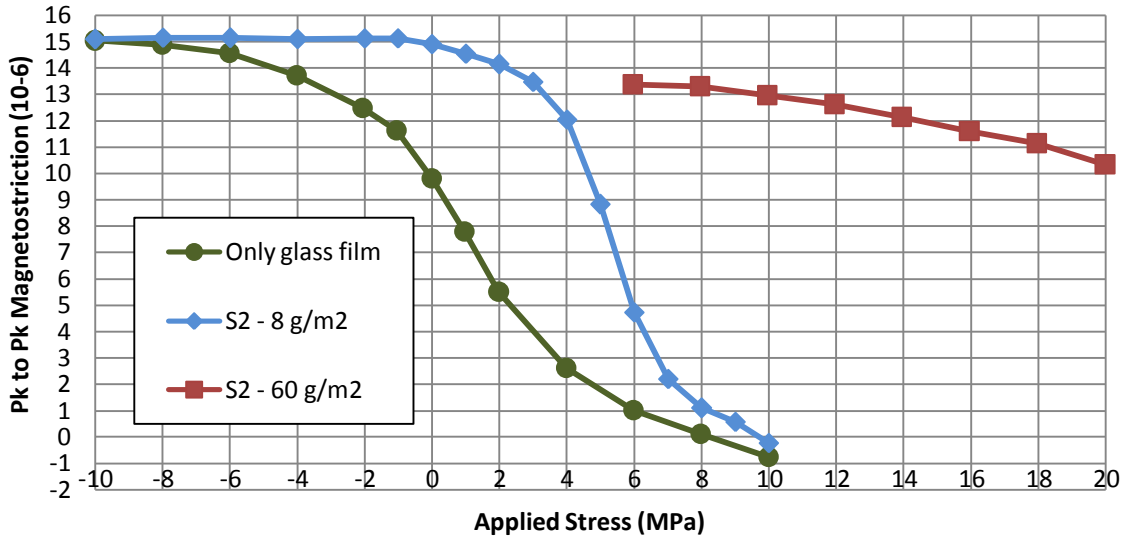

a)

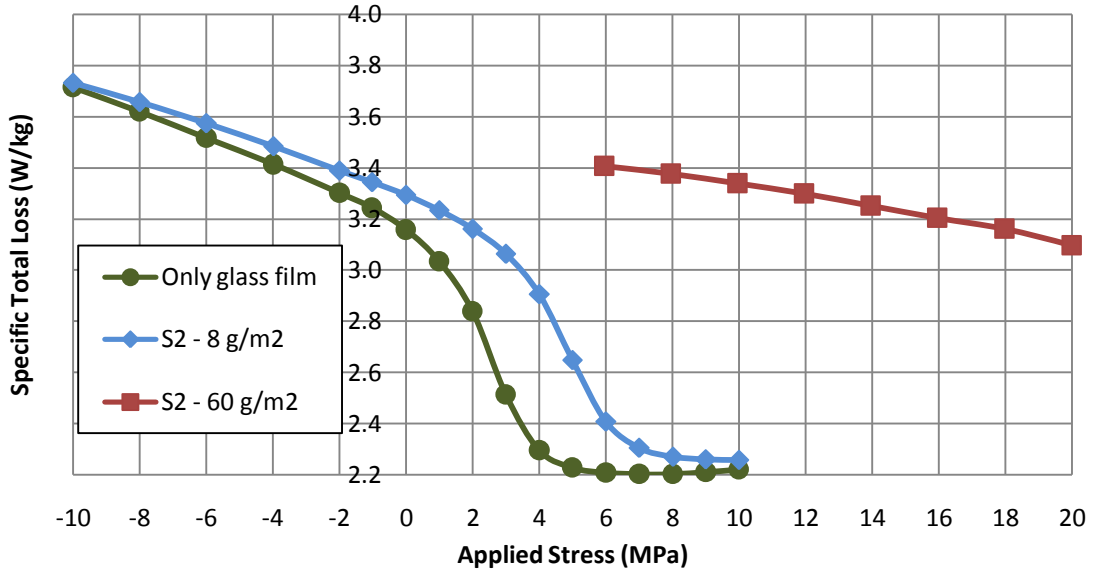

b)

Fig 8.24 Transverse sample with two layers of S2 coating at 1.4T, 50 Hz.

The increase of thickness of S2 coating causes increase in the shift of magnetostriction and loss curves. This shift can be related to a compressive stress applied in the transverse direction. The sample with 60 g/m^2 of S2 coating was initially tested under applied tension of 20 MPa, which was the maximum external tension which could be applied by the magnetostriction measurement system. The high compressive stress in the transverse direction applied in the same direction as the magnetisation would cause difficulties in the magnetisation process. Therefore the minimum tension of 6 MPa was required to enable the magnetisation of the sample at 1.4 T (50 Hz).

It can be seen from Fig 8.16 that the coating weight of 60 g/m^2 applied approximately 8 MPa of tensile stress to the RD direction of the steel. Moreover Fig 8.24(a, b) shows that a compressive stress (stress shift) of approximately 19 MPa was introduced in the TD direction which according to the anisotropic Young`s modulus of the grain oriented steel in these directions gives a value of compression close to that expected.

8.5 The Thermal Contraction Model of Coating Stresses

Stress on the surface of the grain oriented steel is introduced by differential thermal contraction of a coating and the steel. This differential contraction mechanism was first described by Moses, Pegler and Thompson [7], and developed by Stanbury [8] and further by Anderson [3]. However Anderson`s model partially required the experimental data. In this section a purely theoretical model is presented and compared with the obtained experimental magnetostriction data of the samples with different coating thicknesses. Table 8.7 shows definitions of symbols used in the coating stress model.

Table 8.7 Symbols and their values used in the coating stress model

Symbol	Value	Description
σ_S	-	Transverse retained stress in the steel
σ_C	-	Differential thermal contraction stress
E_{RD}	110 GPa	Young`s modulus of the steel in RD
E_{TD}	190 GPa	Young`s modulus of the steel in TD
E_C	-	Young`s modulus of a coating
v_{RT}	0.38	Poisson`s ratio of the steel [8]
v_{TR}	0.69	Transverse retained stress [8]
v_C	0.42	Poisson`s ratio of a coating [2]
$\alpha_{RD} = \alpha_{TD}$	11	Thermal expansion coefficient of the steel
α_C	-	Thermal expansion coefficient of a coating
T_{cure}	400°C	Temperature of a coating curing

In the model stress and strain introduced in the coating and the steel along the RD and the TD as shown in Fig 8.25 are presented.

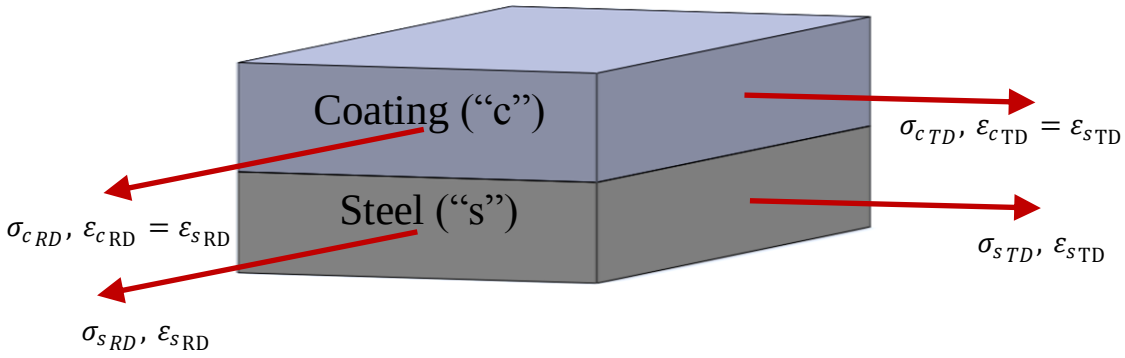

Fig 8.25 Stress and strain directions in a coating and the steel.

Stresses introduced in isotropic coating and anisotropic steel in both directions, taking Poisson’s ratio in to consideration, can be described as

$$\sigma_{c\,RD} = \sigma_{c\,TD} = (\sigma_c - \nu_c\,\sigma_c) \tag{8.5}$$

$$\sigma_{s\,RD} = (\sigma_{s\,RD} - \nu_s\,\sigma_{s\,TD}) \neq \sigma_{s\,TD} \tag{8.6}$$

$$\sigma_{s\,TD} = (\sigma_{s\,TD} - \nu_s\,\sigma_{s\,RD}) \tag{8.7}$$

The strain in the coating and steel can be evaluated using equation 8.8

$$\varepsilon = \frac{\sigma}{E} \tag{8.8}$$

Where for the coating and steel is similar in both directions

$$\varepsilon_s = \varepsilon_c \tag{8.9}$$

Then

$$\frac{1}{E_{RD}}\left(\sigma_{s_{TD}} - v_s\,\sigma_{s_{RD}}\right) = \frac{1}{E_c}\left(\sigma_c - v_c\,\sigma_c\right) \tag{8.10}$$

Hence, the isotropic coating stress is calculated from

$$\boldsymbol{\sigma_c = \frac{E_c}{E_{RD}(1 - v_c^2)}\left[(1 - v_c\,v_{RT})\sigma_{S_{RD}} + (v_c - v_{RT})\sigma_{S_{TD}}\right]} \tag{8.11}$$

The thermal stress in the material can be obtained using

$$\sigma = E * \alpha * T \tag{8.12}$$

The isotropic thermal expansion coefficient is assumed to be lower for the coating then the steel

$$\alpha_s = \alpha_{s_{RD}} = \alpha_{s_{TD}} > \alpha_c \tag{8.13}$$

The difference in the thermal expansion of steel and coating is expressed as

$$\alpha = \alpha_s - \alpha_C \tag{8.14}$$

Therefore the thermal contraction stress in the coating and steel can be expressed as

$$\sigma_C = E_C\,(\alpha - \alpha_C) * T \tag{8.15}$$

$$\sigma_{S_{RD}} = E_{RD}\,(\alpha_s - \alpha) * T \tag{8.16}$$

$$\sigma_{S_{TD}} = E_{TD}\,(\alpha_s - \alpha) * T \tag{8.17}$$

The steel is coated on the both surfaces, therefore the force applied by coating to the steel surface during thermal contraction equals

$$F_S = 2 * F_C \tag{8.18}$$

Then

$$\sigma_S * A_S = 2 * \sigma_C * A_C \tag{8.19}$$

The thermal contraction stress along the RD and the TD direction of the grain oriented steel can be calculated using equations from (8.15) to (8.19) by

$$\boldsymbol{\sigma_{S_{RD}} = \frac{2E_{RD}E_cA_c(\alpha_s - \alpha_c)T}{2E_cA_c + E_{RD}A_s}} \tag{8.20}$$

$$\boldsymbol{\sigma_{S_{TD}} = \frac{2E_{TD}E_cA_c(\alpha_s - \alpha_c)T}{2E_cA_c + E_{TD}A_s}} \tag{8.21}$$

The Young`s modulus and stress of the coating is similar in both directions [2],

$$E_{C_{RD}} = E_{C_{TD}} \tag{8.22}$$

Then,

$$\sigma_{C_{RD}} = \sigma_{C_{TD}} \tag{8.23}$$

The thermal differential contraction stress in the RD direction can be calculated using equation

$$\sigma_{RD} = \sigma_{C_{RD}} - \nu_{TR}\sigma_{C_{TD}} + \nu_{TR}\sigma_{S_{RD}} \tag{8.24}$$

Then,

$$\sigma_{RD} = \sigma_C(1 - v_{TR}) + v_{TR}\sigma_{S_{RD}} \quad (8.25)$$

Also, along the TD direction

$$\sigma_{TD} = \sigma_{C_{TD}} - v_{RT}\sigma_{C_{RD}} - \sigma_{RD} \quad (8.26)$$

Then,

$$\sigma_{TD} = \sigma_C(1 - v_{RT}) - \sigma_{RD} \quad (8.27)$$

However the anisotropic Young`s modulus of the steel requires an additional parameter "**Y**" in (8.26) and (8.27) where:

$$Y = \frac{E_{TD}}{E_{RD}} = \frac{\sigma_{TD}}{\sigma_{RD}} \quad (8.28)$$

Hence,

$$\boldsymbol{\sigma_{RD} = \sigma_c\left(1 - \frac{v_{TR}}{Y}\right) + \frac{v_{TR}}{Y}\sigma_{s_{RD}}} \quad (8.29)$$

$$\boldsymbol{\sigma_{TD} = \sigma_c(1 - Yv_{RT}) - \sigma_{s_{RD}}} \quad (8.30)$$

Fig 8.26 shows differential contraction stresses applied by the coating to the grain oriented silicon steel strip in RD and TD directions.

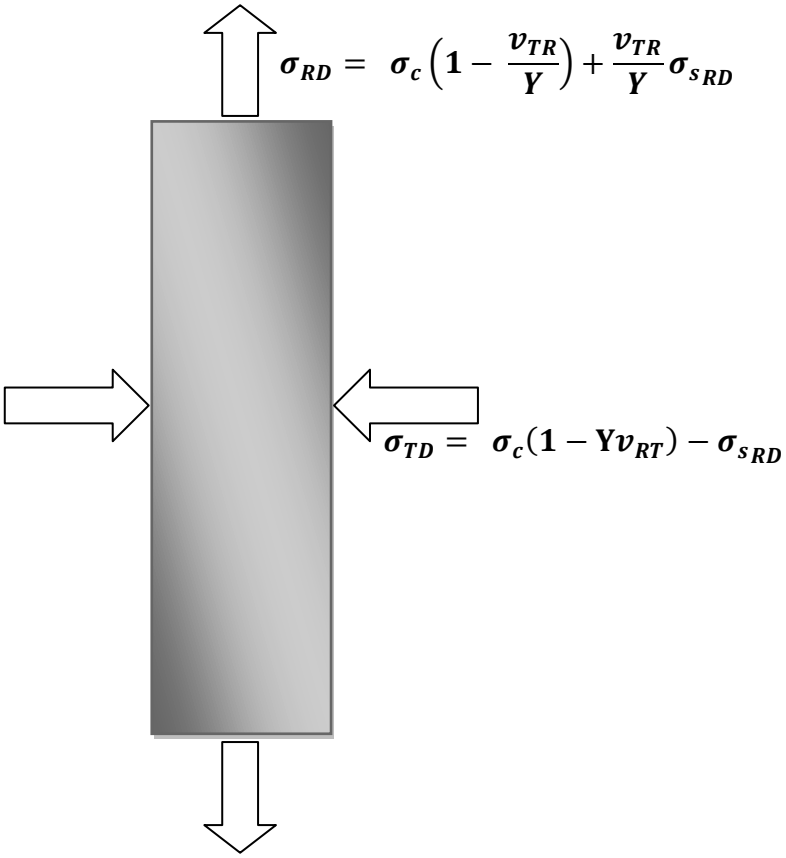

Fig 8.26 Differential contraction stresses applied by the coating to the G-O silicon steel strip in RD and TD directions.

8.5.1 Comparison of Calculated and Measured Results

Stress shifts evaluated by magnetostriction measurements on samples with various coating thickness were compared with the theoretical coating stress model. The brittleness of Mix4, Mix26b3 and S2 coatings causes difficulties in creating of a solid piece of sample for a thermal expansion coefficient test based on the technique described in 8.1.3. However it was found that phosphate ceramic coatings (orthophosphate plus colloidal silica) would have a thermal expansion coefficient in the range 11 to 17 x 10^{-6} °C^{-1} [9]. The coefficient of expansion of the magnesium phosphate (Mix26b3) was approximately 7 x 10^{-6} °C^{-1} [10].

The Young`s modulus of the Mix4 and S2 coatings applied on the surface of the GO steel samples with dimensions 20 mm x 20 mm were measured using a nano-indentation test. The measurement was performed on the nano-test indenter (Micro Material Ltd.)

based at Department of Structure Engineering at Politecbico Mialo (Italy). All tests were carried out with a Berkovitch diamond tip, and a maximum load applied on the samples surface 300 mN. The example of the process of nano-indentation test is shown in Fig 8.27.

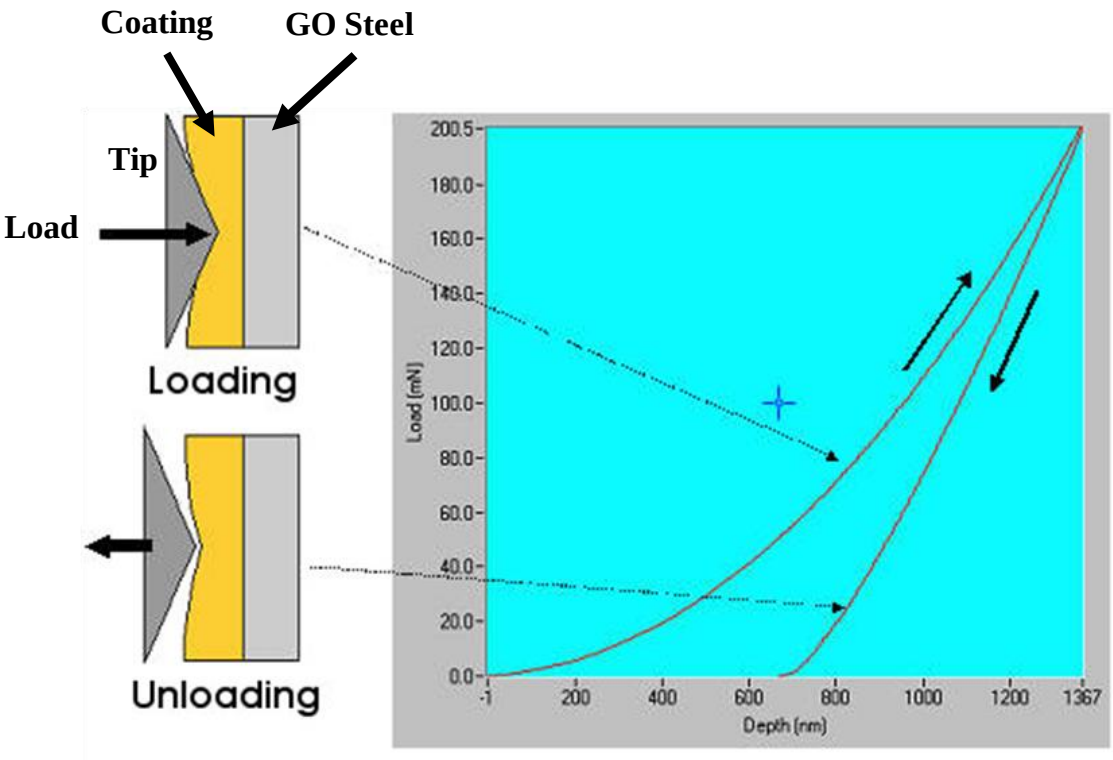

Fig 8.27 The example of the process of nano-indentation test [11].

The evaluated Young`s modulus for Mix4 and S2 coatings was 30 GPa and 80 GPa, respectively. However, the Mix26b3 coating was not measured using nano-indentation test and was estimated to be approximately 60 GPa.

Table 8.8 shows the values of Young`s modulus and thermal expansion coefficient for the steel and all previously used coatings.

Table 8.8 Parameters used in the model of coating stress

Material	**Young`s Modulus (GPa)**		**Thermal Expansion (10^{-6}/°C)**	
	Estimated or Measured	Used for the Calculation	Estimated or Measured	Used for the Calculation
Steel RD	Measured	110	Measured	11
Steel TD	Measured	190	Measured	11
Mix4	Measured	30	Estimated [9] 11 ÷ 17	13
Mix26b3	Estimated	60	Estimated [10] 7 ÷ 9	7
S2	Measured	80	Estimated 7 ÷ 9	8

Coating stresses of Mix4, Mix26b3 and S2 were calculated using equations (8.11), (8.20), (8.29), (8.30) and values from Table 8.8, and compare with measured stress presented in Fig 8.16. These stresses were plotted against coating weights.

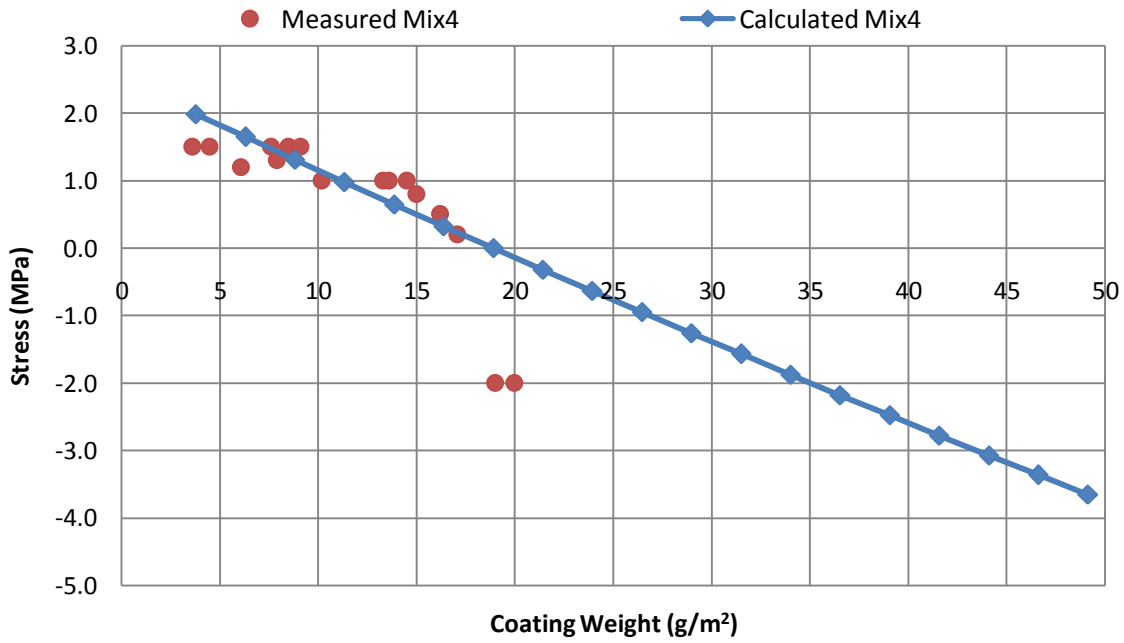

a) Coating Mix4

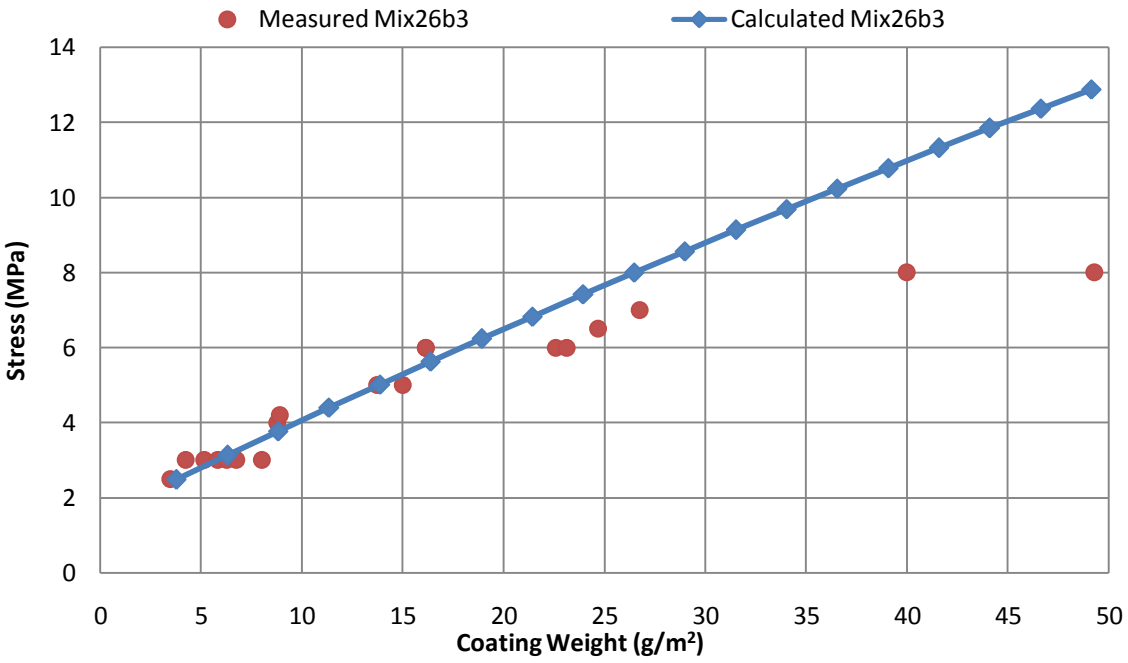

b) *Coating Mix26b3*

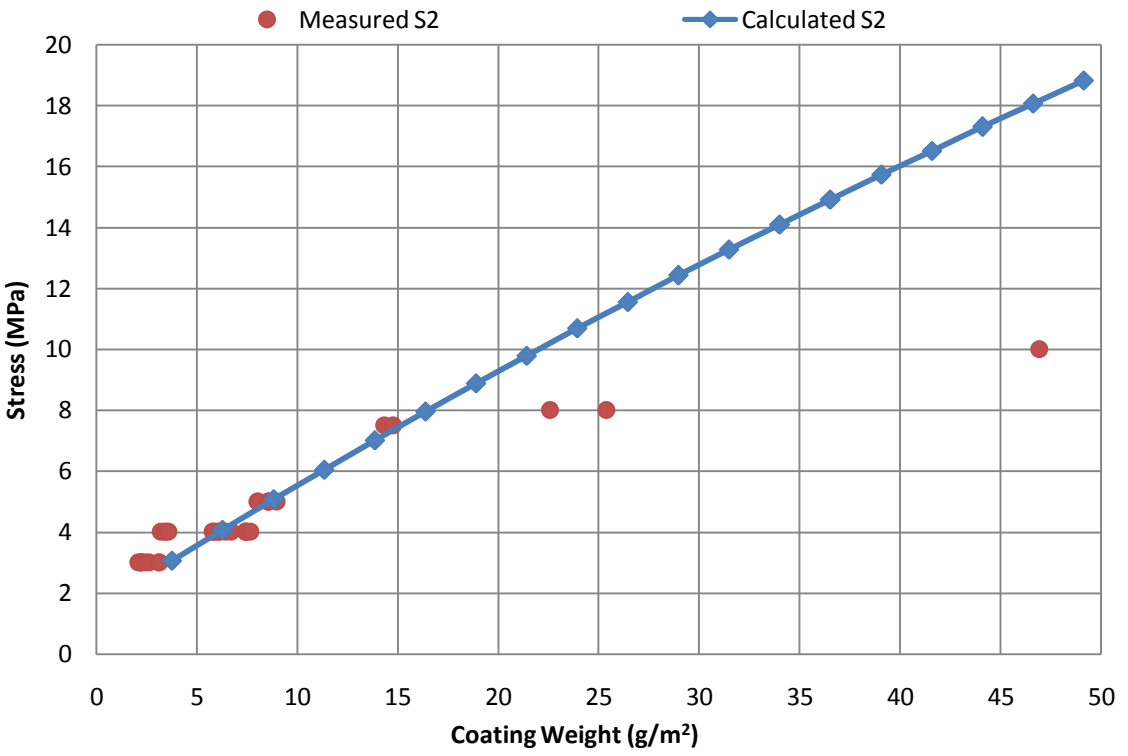

c) *Coating S2*

Fig 8.28 Comparison of calculated and measured stresses applied by Mix4, Mix26b3 and S2 coatings in the RD direction.

The comparison shows that a good agreement was obtained for calculated and measured coating stress for samples with coating thickness up to 18 g/m^2, 19 g/m^2 and 17 g/m^2 for Mix4, Mix26b3 and S2 coatings (Fig 8.28), respectively. However above this weight the measured coating stress saturates for Mix26b3 and S2.

The very thick coating applied as multilayer would be less effective than a very thick singly layered. Moreover the top layers in the very thick coating would create stress transition layers still increasing the total coating stress (as observed for S2 and Mix 26b3 coatings) but with a lower gradient for the layers close to the steel surface. Also it was observed that above 100 g/m^2 the followed applied layers of coating flaked off which means that the bonding between the top layers was weaker after each subsequent layer.

8.6 Summary of the Effect of Coating Stress on Magnetostriction and Loss

Mix4 coating applied in the laboratory was characterised with a similar magnetostriction and loss values to that applied on the production line.

SRA performed once or twice during multilayer coating application does not affect magnetostriction and loss measured under stress.

The glass film as the based coating applied approximately 1 MPa of stress shift in magnetostriction. Also approximately 10% of reduction in loss was observed in the range of -2 to 2 MPa of applied external stress.

The Mix26b3 with and without glass film in the same total coating weight were characterised with similar magnetostriction and loss characteristics. However S2 coating applied more stress to the steel surface when it was applied on the glass film coating.

It was found that application of coating weight with more than 4 g/m^2 per side should be applied as a multilayer. Also the adhesion of the multilayered thick coating is stronger than the singly applied.

S2 coating was characterised with the highest coating stress in comparison to Mix4 and Mix26b3, applied with various coating weights. The very thick Mix4 coating applied compressive stress to the steel surface which results from the lower Young`s modulus and higher thermal expansion coefficient than the steel.

The S2 coating with average total weight 110 g/m^2, the highest weight which could be produced in the laboratory, was characterised with rapidly increasing magnetostriction when more than 14 MPa was applied. The tension evaluated from the shift of stress sensitivity curves before and after applied coating was approximately 13 MPa.

The Mix4 coating applied to the final material by a second run through the production line with weight of 8 g/m^2 per side (4 g/m^2 per layer) compared with the first run did not cause improvement in the stress (tensile) introduced by the coating. It was observed that the highest reduction in loss of approximately 15% was achieved after application of the S2 coating with weight up to 4 g/m^2 per side. Afterwards between 4 g/m^2 and 106 g/m^2 of coating weight maximum 5% of loss reduction was observed.

Domain observation under stress on a sample coated with a very thick coating, confirmed that a high tension was applied to the steel surface. Also in the same sample a high tensile stress was obtained from calculations based on the strip curvature after single sided coating removal. However, the calculated stress from the curvature of the strip showed approximately three times higher stress then that evaluated by domain observations and stress shift of magnetostriction curves.

A high compressive stress in the transverse direction, evaluated by the stress shift, was observed on transverse cut sample coated with very thick S2 coating.

A good agreement was obtained for measured and calculated (based on differential contraction model) coating stress for samples with thickness up to 18 g/m^2, 19 g/m^2 and 17 g/m^2 for Mix4, Mix 26b3 and S2 coatings, respectively.

8.7 References

[1] J. Case, *et al.*, "Strength of materials and structures," *Arnold* 1999.

[2] J. W. Dally and W. F. Riley, *Experimental stress analysis*, Second Edition ed., 1978.

[3] P. Anderson, "A novel method of measurement and characterisation of magnetostriction in electrical steels," PhD Thesis, Cardiff University, Cardiff, 2000.

[4] T. N. Corporation. (2001, Introduction to Fourier Transform Infrared Spectrometry. Available: http://mmrc.caltech.edu/FTIR/FTIRintro.pdf.

[5] A. Technology. *Fischer MP30 Deltascope*. Available: http://ashtead-technology.com/pdfgen/?template=instruments&product=fischer_feritscope_mp30&regi=us.

[6] E. Beyer, *et al.*, "The influence of compressive stress applied by hard coatings on the power loss of grain oriented electrical steel sheet," *Journal of Magnetism and Magnetic Materials*, pp. 1985-1991, 2011.

[7] A. J. Moses, *et al.*, "Role of phosphate coating in determining the magnetic properties of Goss-oriented silicon iron," *Proceedings of the IEE*, vol. 119, 1972.

[8] H. J. Stanbury, "Magnetostriction effects at angles to the rolling direction in grain oriented silicon steel," PhD Thesis, University of Wales, Cardiff, 1984.

[9] S. Nakamura, *et al.*, "Thermal expansion of hydroxyapatite-B-tricalcium phosphate ceramics," *Thermochimica Acta*, pp. 57-72, 1990.

[10] R. Roy, *et al.*, "Mineralogy and thermal behaviour of phosphates; I. magnesium pyrophosphate," *http://www.minsocam.org/ammin/AM33/AM33_458.pdf*.

[11] *Overview of Nanoindentation*. Available: http://micromaterials.net/nanoindentation.asp.

Chapter 9 Influence of Annealing under Tension on Magnetostriction and Loss in GO Steel

9.1 Strips Selection

Epstein strips (305mm x 30 mm) of 0.30 mm thick HiB were cut from high temperature coil annealed (HTCA) sheets, previously coated on the production line only with the forsterite coating as described in chapter 2. After cutting into strips the strips exhibited a curvature dependent on the position from which it was cut out of the coil. Fig 9.1 shows the degree of curvature in strips cut from regions (a) and (b). Therefore two batches of strips were cut from inner (Fig 9.1(a)) and outer (Fig 9.1(b)) turns of the coil. Epstein strips with these two types of curvature were called “inner” and “outer” strips.

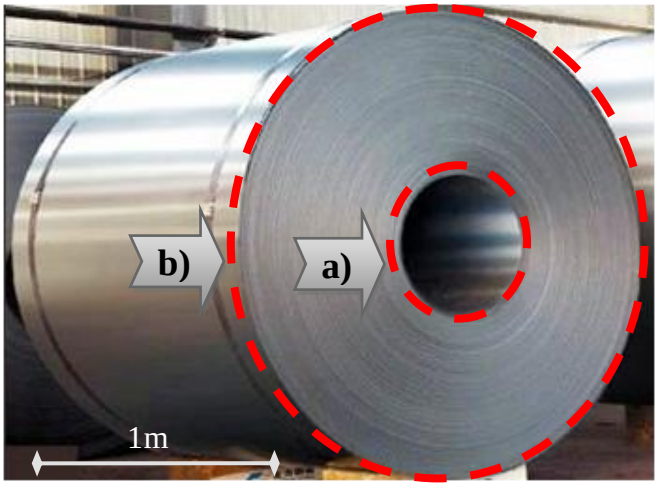

a)

b)

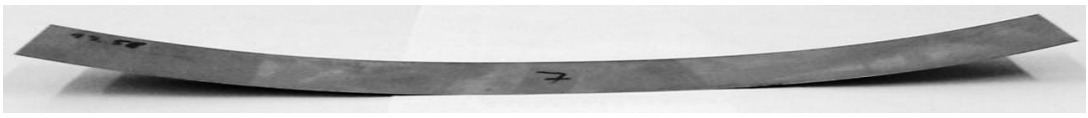

Fig 9.1 Curvature in Epstein strip cut from inner (a) and outer (b) turns of high temperature annealed coil.

9.2 Stressing Rig

The stressing rig shown in Fig 9.2 was designed and built for applying controlled tension to an Epstein strip while it was being annealed.

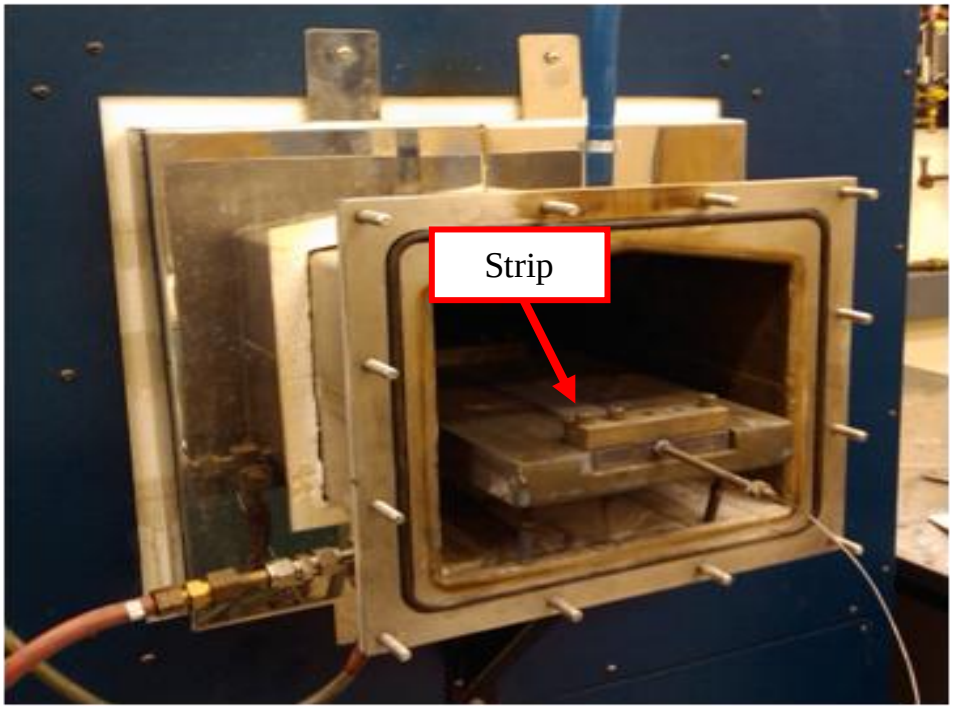

Fig 9.2 Stressing rig placed inside a retort furnace.

A single strip was clamped at one end to a stainless steel base plate whilst the other end was clamped and connected to a stainless steel wire. Weights were hung on the free end of the wire outside the furnace to apply the required tension to the strip.
From preliminary heat treatments it was found that the minimum load required to flatten a curved strip during annealing was 2.2 kg. The maximum load which the wire end clamp could sustain was 9.4 kg. For the 0.30 mm strips used, loads of 2.2 kg, 3.6 kg, 4.4 kg, 5.7 kg, 6.6 kg and 9.4 kg produced tensile stress in the range of 2.4 MPa to 10.2 MPa.

The additional stress introduced to the curved strip after clamping to the stressing rig (strip flattening), before annealing, can be calculated using equation (8.4). Therefore calculated initial flattening stresses in the RD of inner and outer strips equal 63 MPa and 26 MPa, respectively.

The physical condition of each strip after each anneal under tension was examined. It was observed that any possible misalignment of the tension wire connected

with the clamp could cause horizontal and vertical deviation from the direction of an applied stress to a strip as shown in Fig 9.3 which would cause twisting or bending of the strip during annealing process resulting in increase in measured magnetostriction and loss under stress.

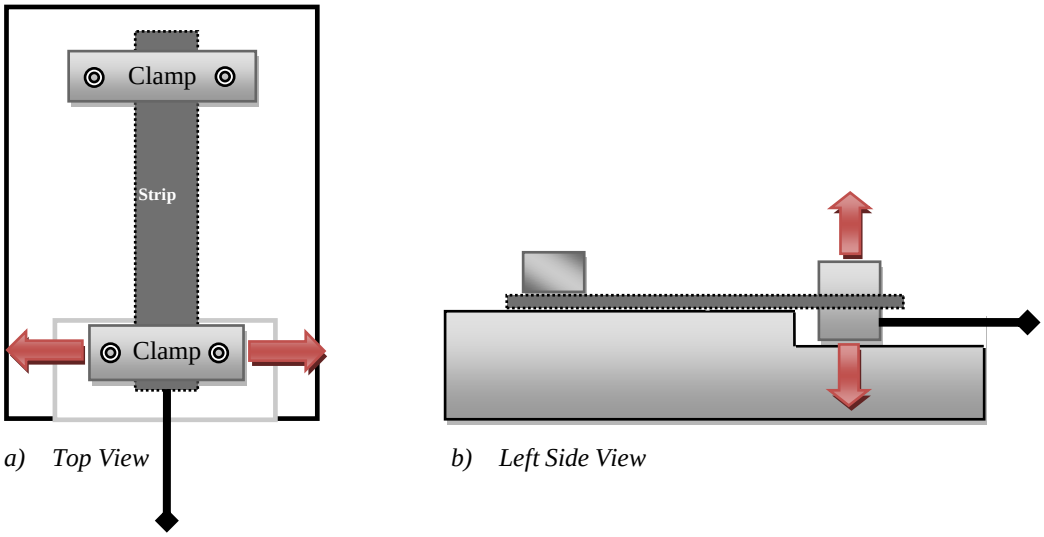

Fig 9.3 Possible deviation of a strip due to misalignment: (a) horizontal and (b) vertical.

Clamps used to fix the strip to the stainless steel plate and wire, resulted in damage to the coating on the upper strip surface. Fig 9.4 shows an example of a trace on the strip surface after clamping and annealing under tension at 810˚C. This visible trace was observed on each end of an annealed strip

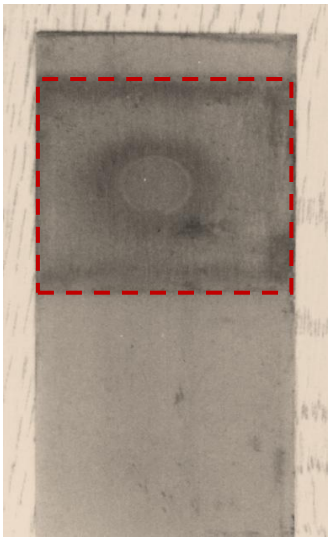

Fig 9.4 Trace on one end of a stripe after clamping and annealing under tension.

As discussed in section 5.3.3 any damage applied to the strip (twisted strip or bent edges) would affect the magnetostriction and loss measurements under stress. Therefore particular care was taken over visual inspection of these samples and only those not exhibiting damage to coating or substrate were chosen.

9.3 Investigation of Annealing under Tension

9.3.1 Annealing under Tension in Nitrogen

Two batches of six Epstein strips cut parallel to the RD from positions (a) and (b), were annealed under the full range of tensile stress. Each strip was placed under tension before heating at 400˚C / hour to 810˚C and held for 1 hour in a nitrogen atmosphere prior to cooling at 100˚C / hour to room temperature of approximately 20˚C.

Peak to peak magnetostriction and specific total loss of each strip were measured under stress at 1.7 T, 50 Hz. Fig 9.5 and Fig 9.6 show curves of pk-pk magnetostriction and specific total loss plotted against applied stress measured on strips cut from the inner and outer turns of the coil. Each data point on the curves is the average of three measurements.

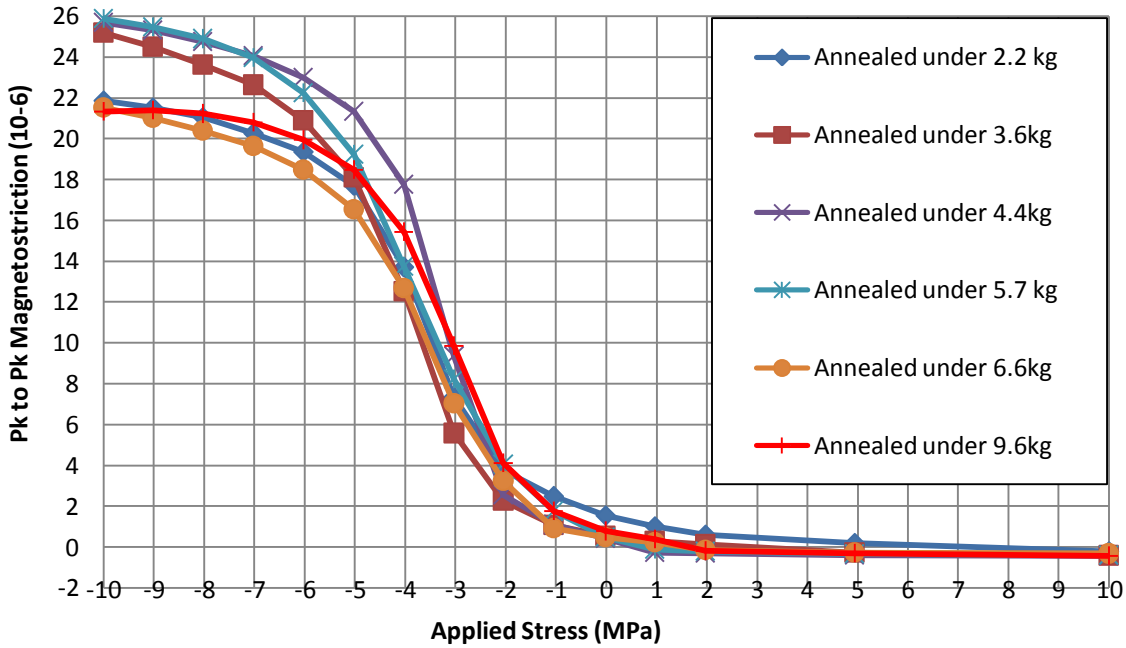

a)

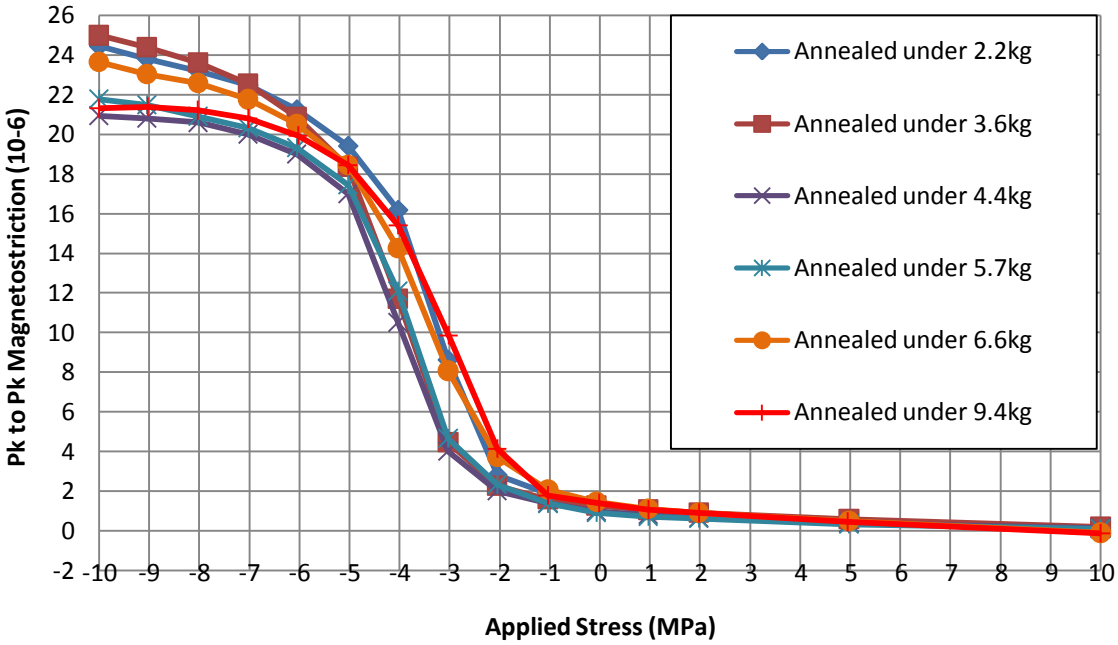

b)

Fig 9.5 Pk-Pk magnetostriction vs. applied stress of strips cut from: (a) inner and (b) outer turn of the coil, measured at 1.7 T, 50 Hz.

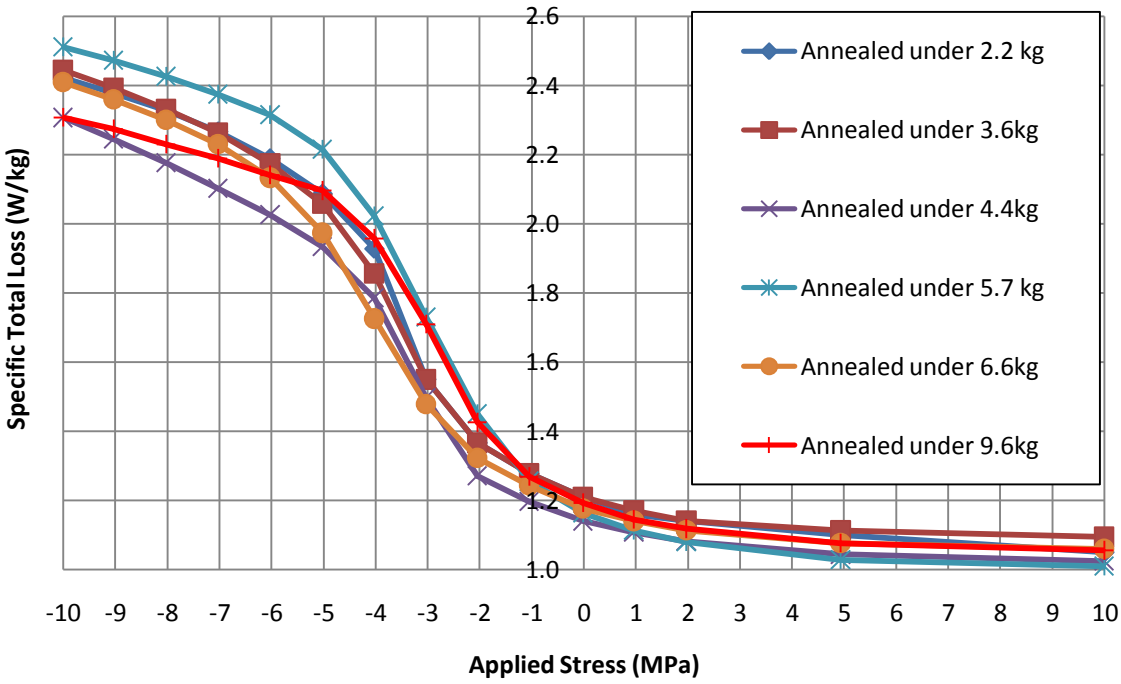

a)

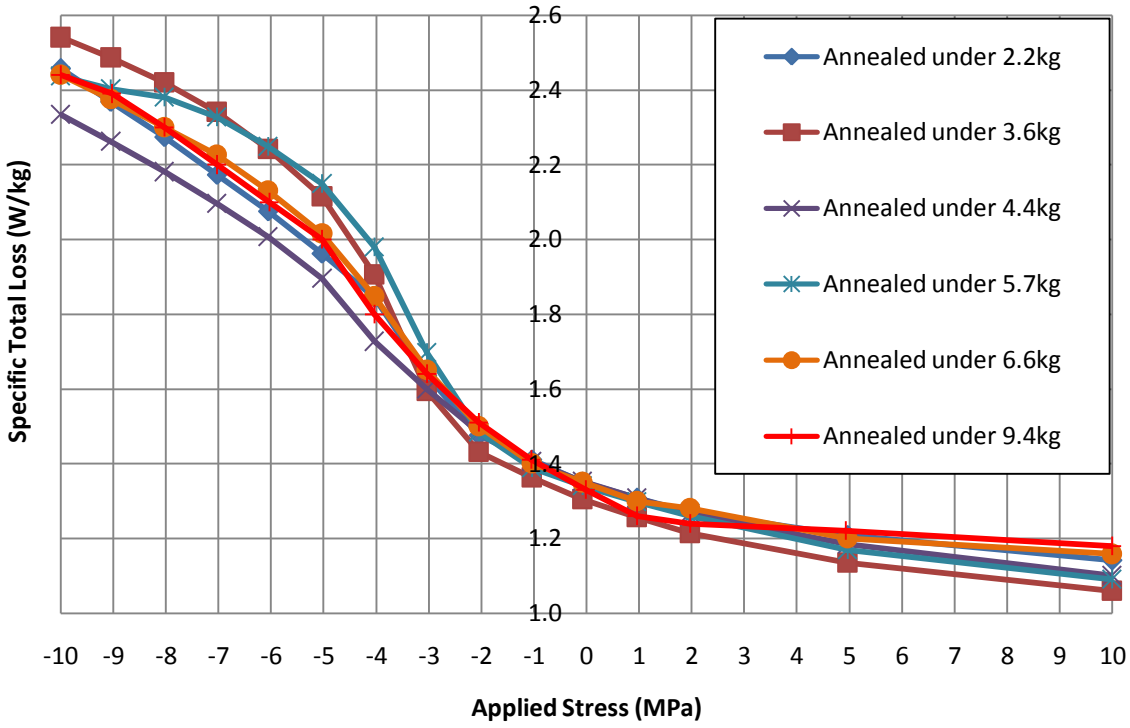

b)

Fig 9.6 Specific total loss vs. stress sensitivity curves of strips cut from: (a) inner and (b) outer turn of the coil, measured at 1.7 T, 50 Hz.

The variation in stress sensitivity curves of magnetostriction and loss for both sets of strips did not show any correlation to the applied stress. Variations between the curves in Fig 9.5 and Fig 9.6, could be caused by a slight damages applied to strips after annealing under tension as explained in section 9.2.

However stress free magnetostriction and loss characteristics of both sets of strip have a parabolic trend as shown in Fig 9.7 and Fig 9.8. Magnetostriction measured without stress decreases for annealed under tension from 2.4 MPa to 4.8 MPa for inner and up to 6.2 MPa for outer strips. Afterwards above this point up to 10.5 MPa of applied tensile stresses under annealing the pk-pk magnetostriction increases. The lowest magnetostriction measured without stress was observed for strips annealed under tensile stress of 4.8 MPa for inner and 6.2 MPa for outer strips (Fig 9.7). Fig 9.8 shows that specific power loss measured without stress decreases for annealed under tension from 2.4 MPa to 4.8 MPa for the inner and 3.9 MPa for the outer strips.

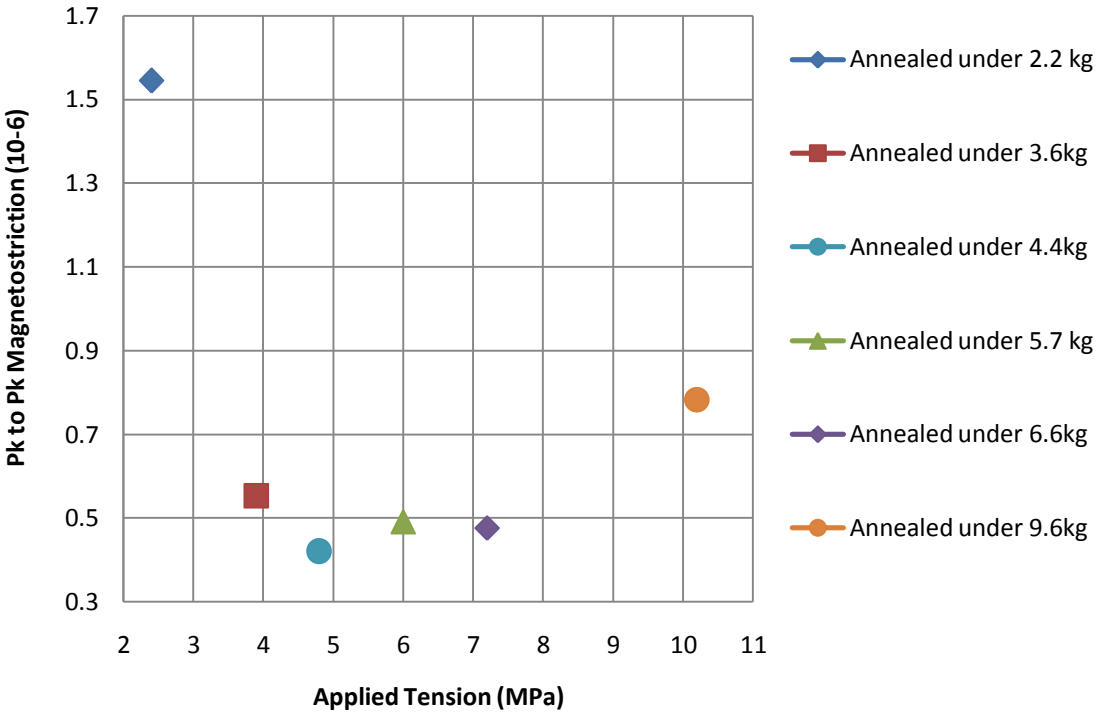

a)

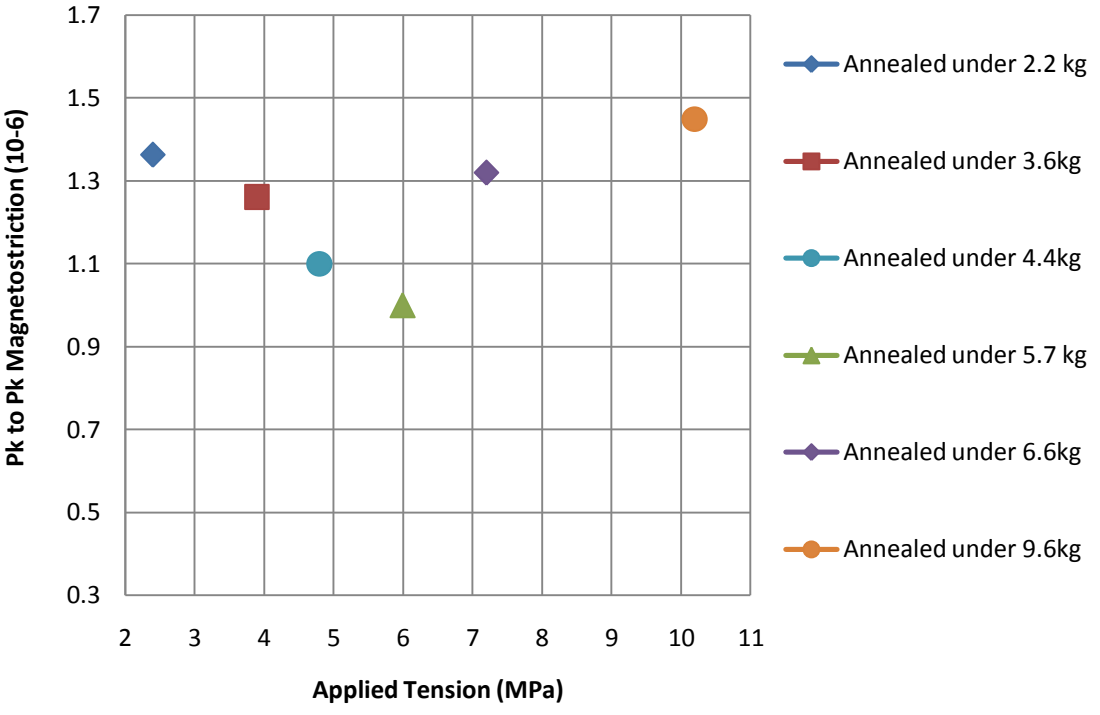

b)

Fig 9.7 Pk-pk magnetostriction of strips cut from: (a) inner and (b) outer turns of a coil without applied stress measured at 1.7 T, 50 Hz.

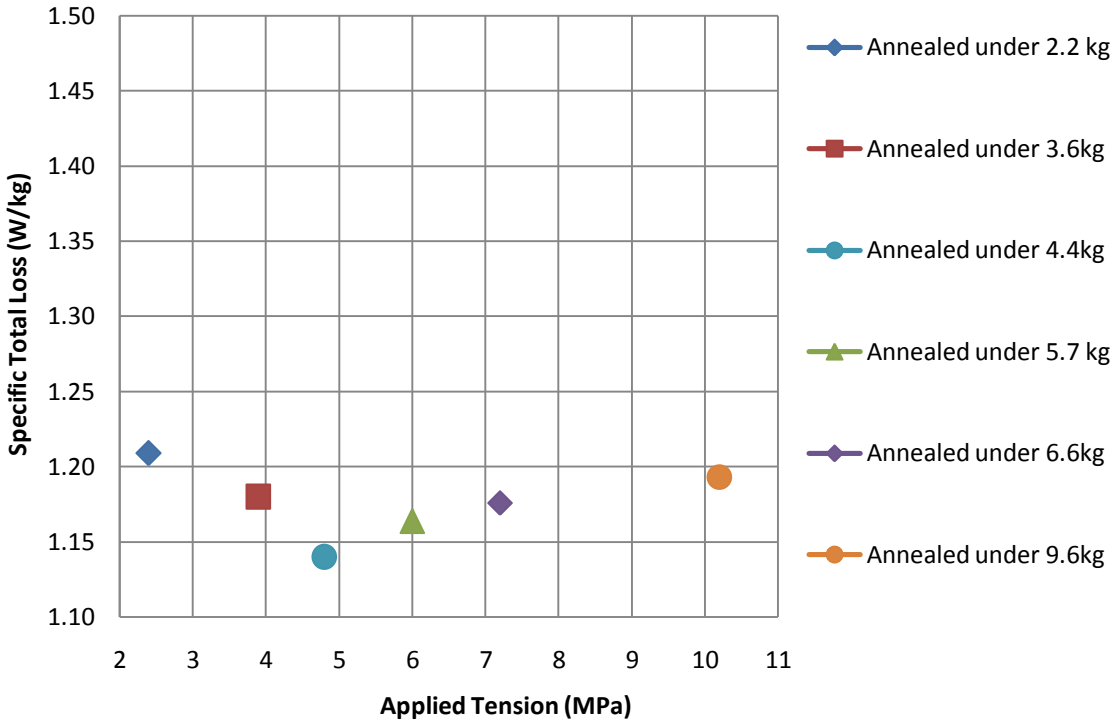

a)

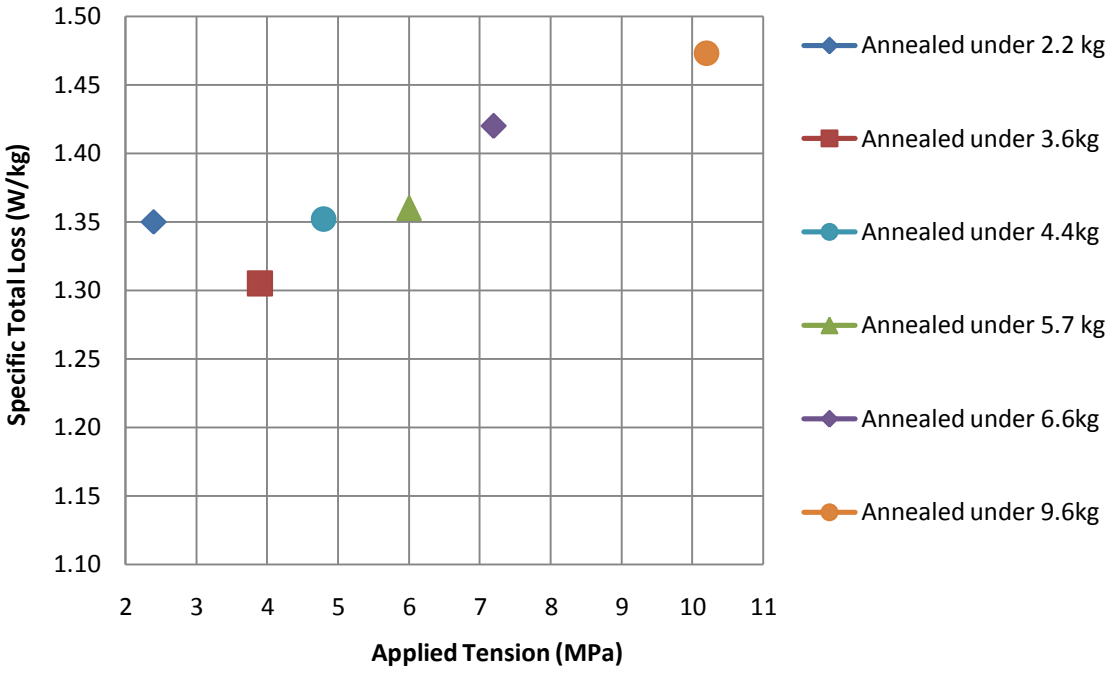

b)

Fig 9.8 Specific total loss of strips cut from: (a) inner and (b) outer turns of the coil under 0 MPa of stress measured under 1.7 T at 50 Hz.

Above these points of stress the measured specific power loss increases. A similar parabolic trend in loss measurement under no applied external stress has been reported previously for Epstein strips cut from GO steel [1] [2]. Differences between loss measured with no applied stress, in the inner and outer strips were observed. The loss of the inner strips varied from 1.10 W/kg to 1.21 W/kg after all annealing tensions whereas the loss in the inner strips were in the range of 1.31 W/kg to 1.47 W/kg at 1.7 T, 50 Hz magnetisation. It is assumes that these differences are due to the difference in the residual stresses introduced before annealing by the flattening of the initially curved material.

The externally applied tension plastically deforms the inner and outer strips at the high temperature. This plastic deformation is the effect of the decreasing yield point of the material as the temperature increases [3]. Moreover the high tension applied to the initially curved strip causes an increased size and density of dislocations due to work hardening at high temperature which could pin domain walls more effectively [4].

Domain observations of highly curved strips were not carried out with the Domain Viewer which can only be used on a flat surface. If the strips were flattened for this measurement, stresses of ± 63 MPa and ± 26 MPa in the RD of inner and outer strips respectively would be set up inducing fine surface stress patterns which would make the observations irrelevant.

9.3.2 Annealing under Constant Tension in Compressed Air

During the HTCA, a forsterite coating forms on the steel surface as described in chapter 2. The process is commercially carried out in an inert atmosphere to avoid the coating reacting with oxygen in the air at high temperature. It was decided to investigate this possible oxidation effect which might occur during annealing under tension in the laboratory furnace in an atmosphere of compressed air on inner strips was carried out.

Four Epstein strips cut parallel to the RD were annealed in turn under 4.8 MPa of tensile stress, evaluated to be the most suitable stress since it produces the lowest magnetostriction and loss as shown in section 9.3.1. Each strip was heated to 810˚C (400˚C / 1h) in pure nitrogen atmosphere followed by the introduction of compressed air for a range of periods prior to cooling in nitrogen at 100˚C / 1h. The dwell period was varied from 1 minute to 3 hours.

Fig 9.9 shows magnetostriction and loss sensitivity curves of four strips measured at room temperature after dwell times in compressed air used to induce oxidation.

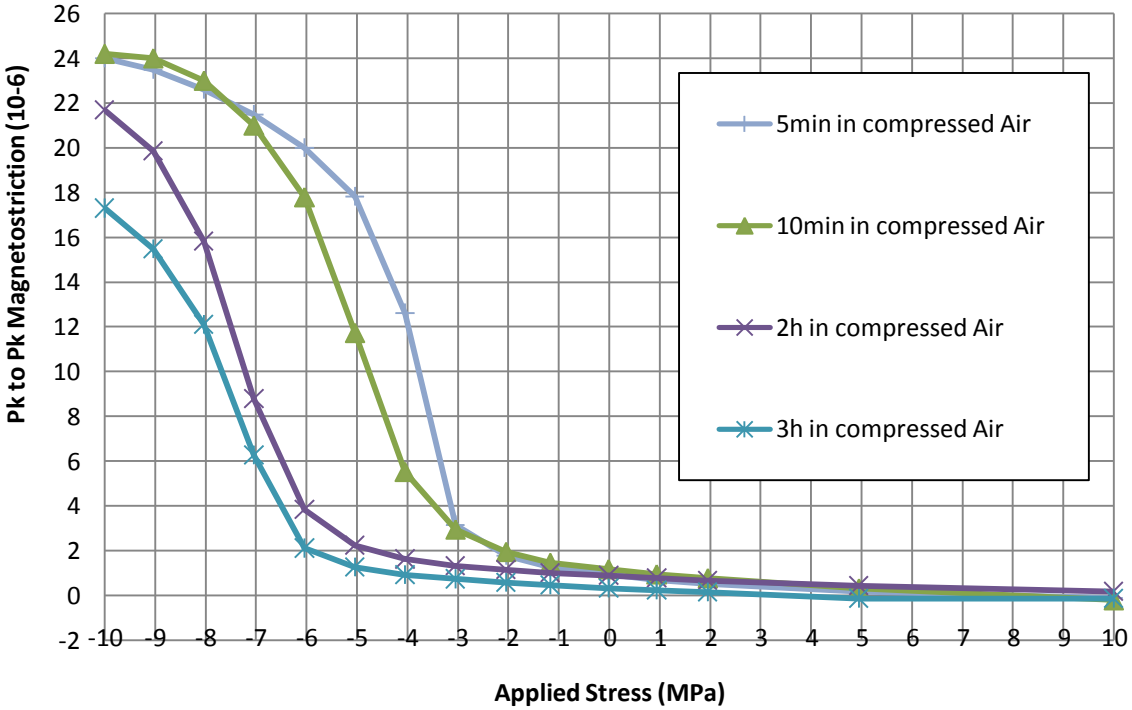

a)

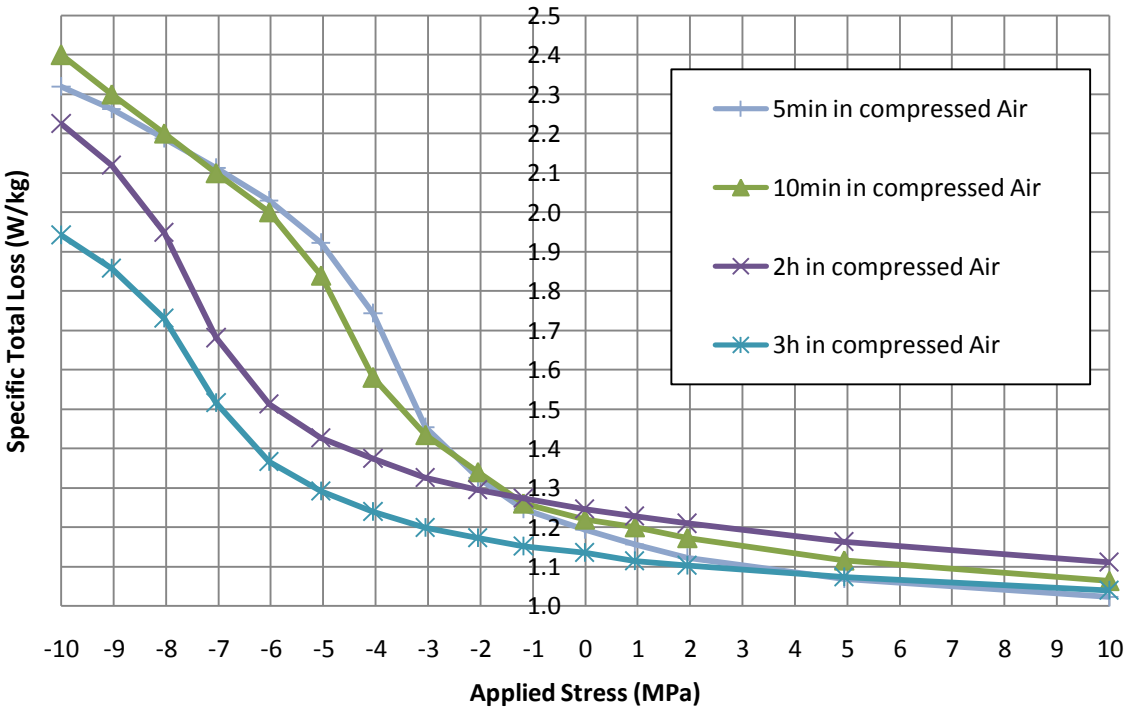

b)

Fig 9.9 Stress sensitivity curves of strips cut from the inner turn of the coil: (a) pk-pk magnetostriction and (b) specific total loss at 1.7T, 50 Hz.

Increasing dwell time in the compressed air decreases the magnetostriction and loss values especially under compressive stress.

The effect of the surface oxidation was also investigated on strips cut from the material after the final stage of the production line. A coil of HTCA material was passed through the thermal flattening process and then continuously annealed at 850°C in air. The steel took approximately 1 minute to pass through the line at high temperature in air (the normal nitrogen gas was not used).

To evaluate the effect of the oxidation on the production line, strips cut from the air annealed coil was compared with strips cut from a coil annealed in nitrogen. The nitrogen annealed coil had a phosphate coating which was removed from the surface by pickling for 10 minutes in a 20% sodium hydroxide solution before the comparison was made. The production process for the both coils, apart from the difference in the gas atmosphere, was similar. Therefore the applied tensile stress due to the driving rolls on the line during production of these two coils was assumed to be similar, but the value of stress was unknown. Fig 9.10 shows average values of magnetostriction and loss under stress of 4 strips annealed on production line in two atmospheres: air and nitrogen.

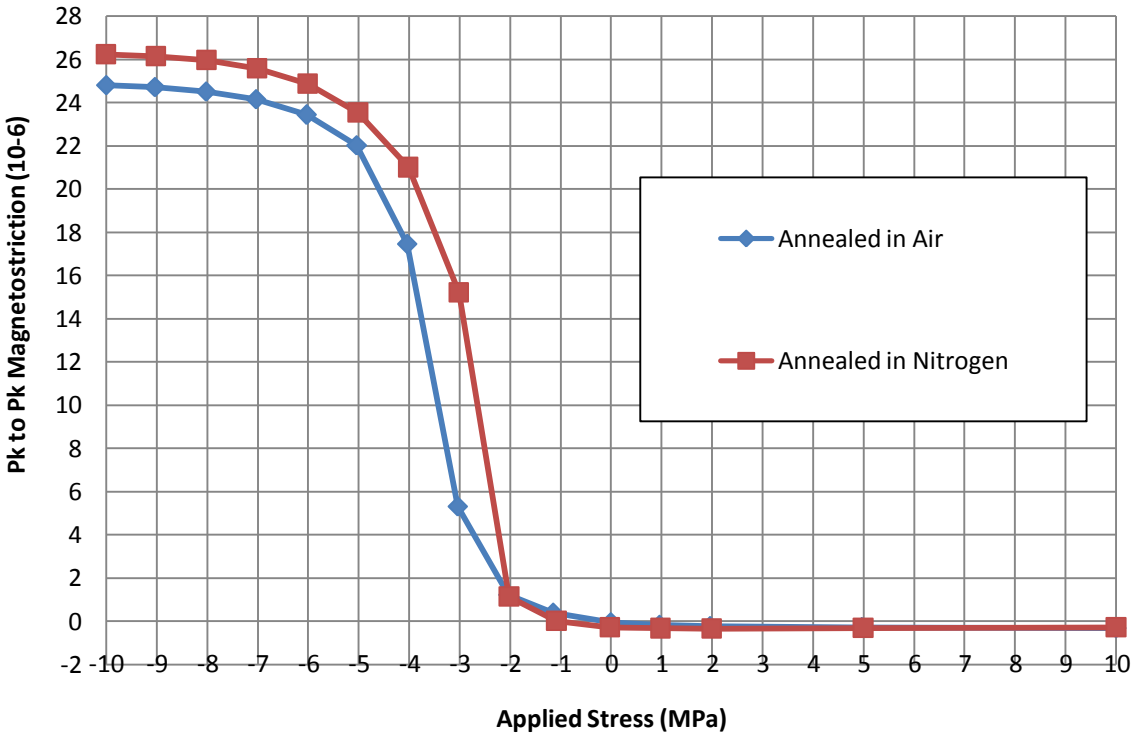

a)

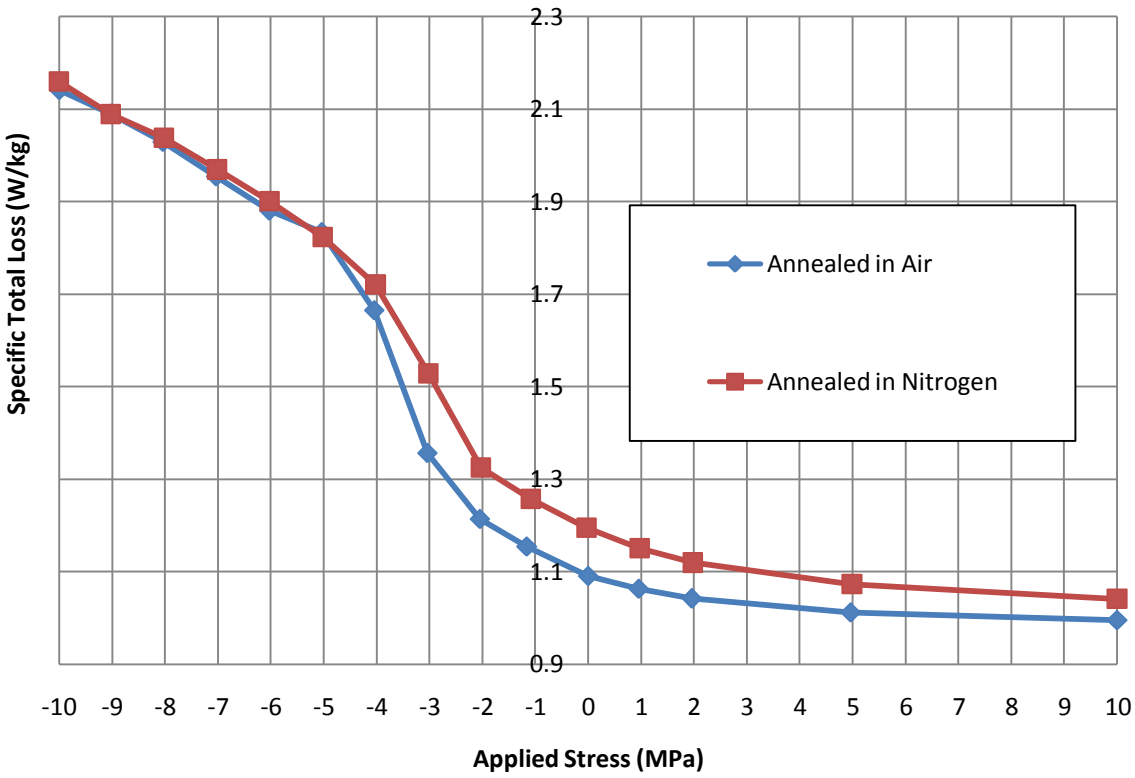

b)

Fig 9.10 Strips annealed on production line in two atmospheres: air and nitrogen (a - pk to pk magnetostriction and b - specific total loss at 1.7 T, 50 Hz).

The magnetostriction decreases under compression in the strips annealed in air. Moreover loss decreases over the full tension and up to - 4MPa compression in strips annealed in air and at higher compression the characteristics are very similar then become similar to those found in the strips annealed in nitrogen.

Surface layers of the laboratory and production line air annealed strips were analysed using a scanning electron microscope (SEM) [5] at the laboratories of the producer. Fig 9.11 shows a surface layers on cross-sections of a strip annealed in air in the laboratory furnace for 3 hours. This strip was characterised with the lowest measured under stress magnetostriction and loss values, therefore as an example is presented.

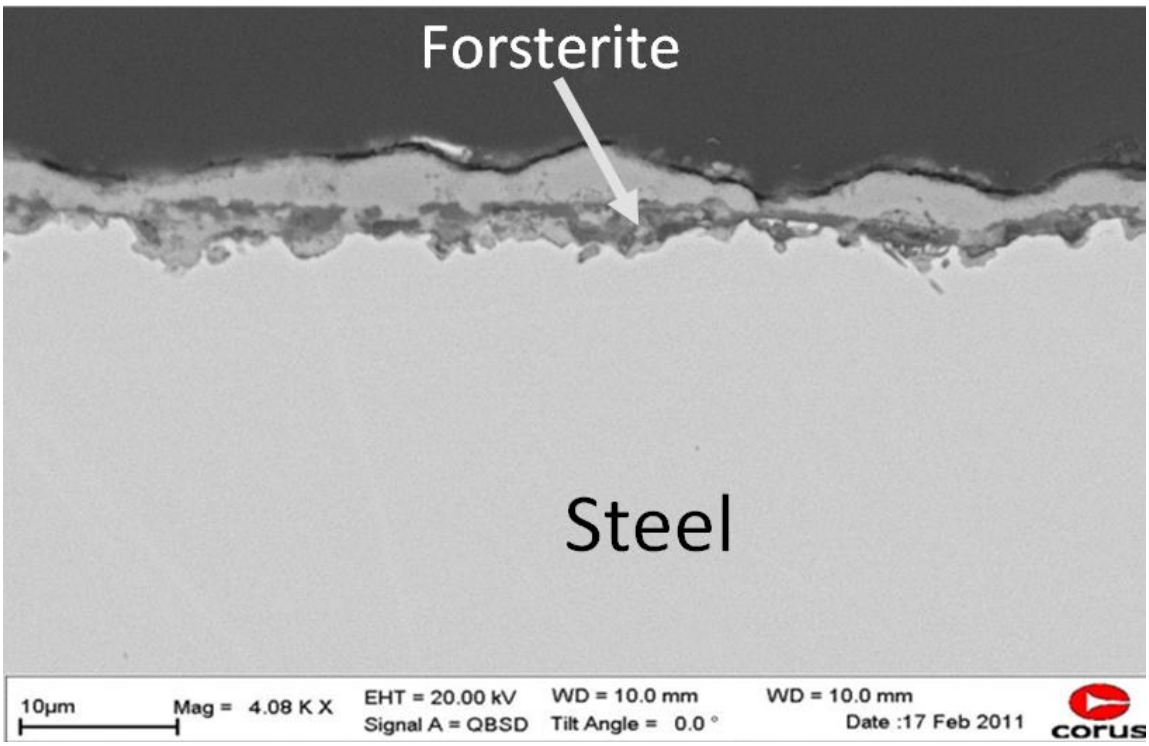

Fig 9.11 The surface layers on cross-sections of the strip annealed in air analysed by SEM.

It was observed that the central darker phase was the forsterite coating (Fig 9.11). On the laboratory annealed strip, the forsterite coating was surrounded above and below by iron oxide. Also traces of sulphur (from complex sulphides), aluminium and titanium were detected in the new created coating layer. However the layers on the strip cut from the production line were mainly forsterite plus sulphur, with little iron oxide detected. It was also observed that after annealing in compressed air for 3h, the new oxidized coating was 8 microns thick on each side, the forsterite coating was only 3 microns thick. As shown in section 8.4.2.1 (Fig. 8.16) an increase in coating thickness increases the coating tension on the steel surface.

The HTCA steel with the forsterite layer was phosphate coated at the final stage of the production line. Therefore the laboratory annealed strips annealed for 2 and 3 hours in compressed air were coated with 3 microns per side thick phosphate coating in order to compare with strips from the production line. Fig 9.12 shows magnetostriction and loss sensitivity curves of the strip annealed under tension in air for 3h, before and after application of the phosphate coating.

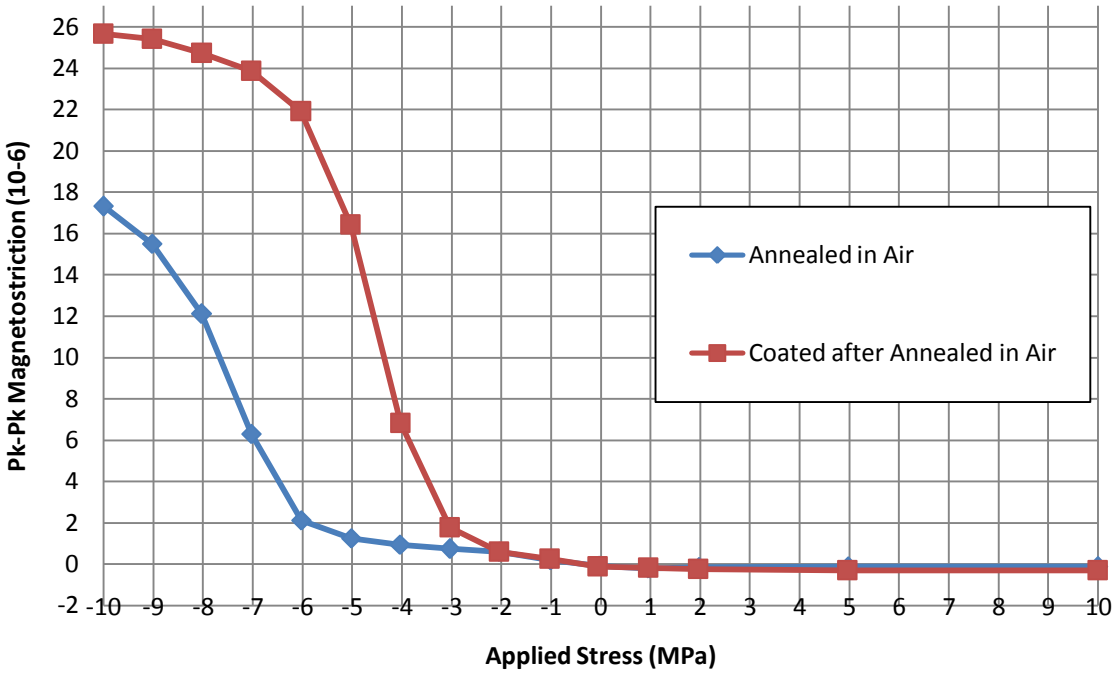

a)

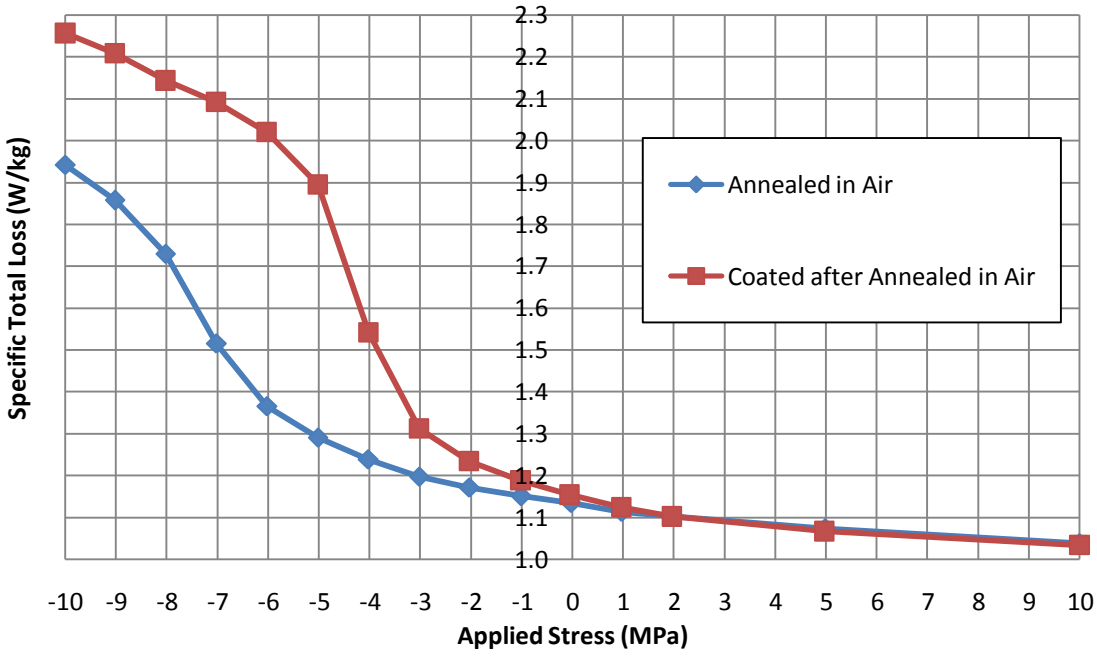

b)

Fig 9.12 Effect of coating application on oxidized surface (a - pk to pk magnetostriction, and b - specific total loss at 1.7 T, 50 Hz).

The phosphate coating removed the beneficial tensile stress from the steel surface as indicated by increased magnetostriction and loss especially under compression. This is likely to be due to the acidic slurry phosphate coating attacking the oxide layer causing a reduction in its thickness or reducing its adhesion to the surface.

9.4 Effect of the Thermal Flattening Process on a Production Line

The final stage of the commercial production process is to apply the phosphate coating, thermally flatten, trim and coil the steel. Before thermal flattening, the phosphate coating is cured on the HTCA material. To observe the effect of thermal flattening on the production line on magnetostriction and loss measurements under stress, the HTCA material was run through rolls with different penetration depths as shown in Fig 9.13.

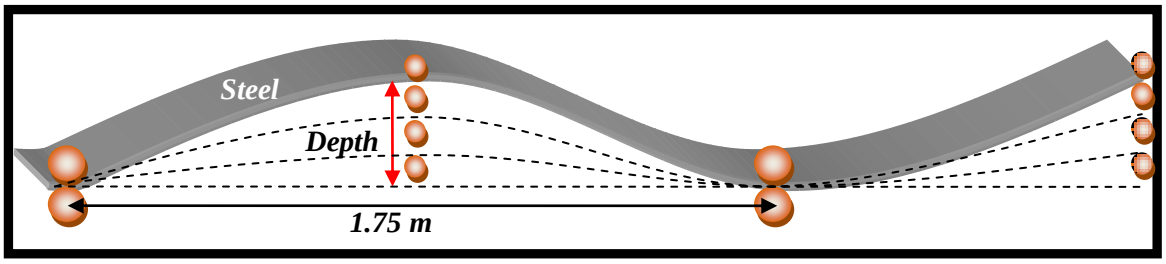

Fig 9.13 Penetration of the GO steel in the thermal flattening chamber.

Four penetration depths were set up: 0, 20, 40 and 60 mm (40 mm is currently used on the production line at Cogent Power). Eight strips cut from four coils, penetrated on production line during thermal flattening under each penetration depth, were measured under stress at 1.7 T, 50 Hz and the average values are presented in Fig 9.14.

Strips with zero penetration depth have the lowest magnetostriction and loss compared to those with the finite depths, especially measured under compressive stress. However no significant improvement in magnetostriction or loss was observed. The steel processed in the thermal flattening line has two coating layers, i.e., the forsterite film and the cured phosphate coating. These two coating resist the stress applied to the steel by the flattening rolls preventing any significant change in magnetostriction or loss occurring.

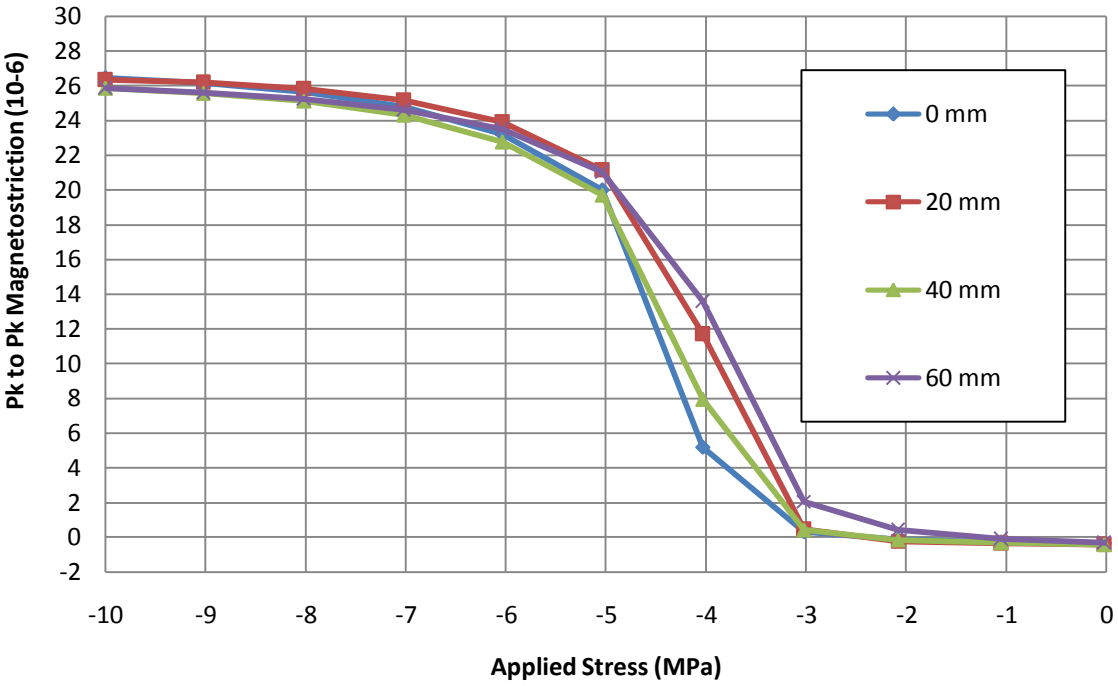

a)

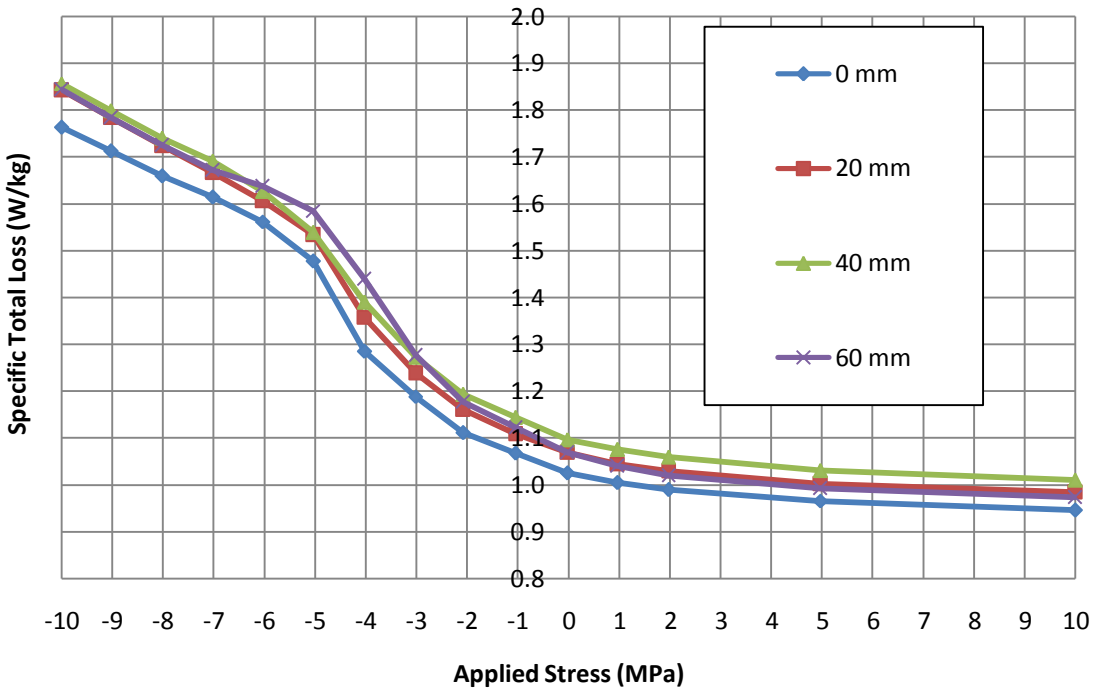

b)

Fig 9.14 Strips cut from coils after thermal flattening with different set up (a - pk to pk magnetostriction and b - specific total loss at 1.7 T, 50 Hz).

9.5 Summary of the Investigation of Annealing under Tension

The lowest value of magnetostriction measured under no external stress was observed in strips annealed under 4.8 MPa of the inner and 6.2 MPa of the outer strips of tensile stress. The inner strips had up to 20% lower losses then the outer strips. Increasing dwell time at 850˚C in compressed air of HTCA material under 4.8 MPa of tension decreased the magnetostriction and loss measured under stress. The new oxidized coating which was thicker than the forsterite film increases tension at the steel surface. The phosphate coating applied on the new oxidized coating removes the beneficial coating tension.

Variation of penetration depth from 0 to 60 mm on the thermal flattening line does not significantly reduce magnetostriction or loss of the steel coated with a forsterite film.

9.6 References

[1] Cogent Power Ltd., "Confidential Internal Communication," 2011.

[2] A. Moses and C. Bakopoulos, "Effect of stress annealing on loss and magnetostriction in grain-oriented silicon-iron," *IEEE Transactions on Magnetics*, vol. 20, pp. 1563-1565, 1984.

[3] S. Lou and D. Northwood, "Effect of temperature on the lower yield strength and static strain ageing in low-carbon steels," vol. 30, pp. 1434-1438, 1995.

[4] H. Bhadeshi and R. Honeycombe, "Steel microstructure and properties," Butterworth-Heinemann, Ed., Third ed, 2006.

[5] M. Ardenne, "Improvements in electron microscopes," British Patent 511204, 1939.

Chapter 10 Influence of Cutting Stress on Magnetostriction in GO Steel

10.1 Sample Selection and Preparation

Three 305 mm x 30 mm Epstein strips of 0.30 mm thick conventional grain oriented (CGO) sheets (500 mm x 240 mm), previously stress relief annealed at a temperature of 810˚C for 2 hours in an atmosphere of 2% hydrogen and 98% nitrogen, were cut parallel to the rolling (RD) and the transverse (TD) direction using guillotining, electrical discharge machining, laser and water jet cutting. These cutting techniques were chosen to compare the influence of cutting stress on magnetostriction in the GO steel when using standard industrial cutting technique (guillotining) and the other alternative cutting techniques commercially available.

10.2 Cutting Techniques

10.2.1 Guillotining

The first cutting technique investigated was a hydraulic metal shear guillotine (Baileigh - SH5210) similar to commonly used by steel manufacturer. This guillotine already available in the laboratory of the Cardiff University has a shear length of 1321 mm and blades at the angle of 1º. The maximum thickness of steel to be cut on this type of guillotine was 3 mm. The guillotine cut strips with an accuracy of ±0.25 mm. The blade was sharpened before use so it cut the strips with burrs less than 10 µm in height. The cutting accuracy and burrs were obtained by using the laboratory facility such as vernier calliper and microscope, respectively.

10.2.2 Electrical Discharge Machining

The second cutting technique is electrical discharge machining (EDM) located at the "EDM Sales & Services" in Bridgend (south Wales). A 0.25 mm diameter brass wire electrode was used for cutting the Epstein strips one at a time. The machine was

designed such that the electrical spark cut the strips to a tolerance of ±0.004 mm (specifications and cutting tolerance were provided by the company). The EDM is not in contact with the material so no mechanical force is applied during cutting. The spark always takes place within deionised water which cools the sample and the electrode as well as flushing away the eroded metal particles. The temperature close to the cut produced by an electrical spark can reach 2000˚C [1]. This high surface temperature generated due to high-density thermal energy discharge, causes a thermal erosion and formation of a recast layer with micro-cracks on machined surface [2].

10.2.3 Laser Cutting

The third cutting technique was a 400 W CO_2 pulsed laser with an assisting stream of oxygen, at "Dragon Laser Ltd" in Bridgend. This was used to cut single strips. The 0.2 mm diameter laser beam cut the steel with a tolerance of ±0.006 mm (specifications and cutting tolerance were provided by the company). During laser cutting, the edge of the strip is rapidly heated to above its melting point then rapidly cooled by the gas stream, which also removes material from the cut edge.

10.2.4 Water Jet Cutting

The final cutting technique was water jet located at "Brecon Water Jet" in Brecon (south Wales). An intensifier is incorporated to generate the water jet at a pressure up to 350 MPa and 0.25 mm in diameter. Abrasive sand particles, around 0.17 mm diameter, were added in to this stream to create the abrasive water jet. This fluid cutting tool is capable of profiling the cut edge of the Epstein strip which is softer than the abrasive itself and cuts with a tolerance of ±0.127 mm (specifications and cutting tolerance were provided by the company).

The benefit of water jet cutting is that it minimises heating near the cut edge compared to EDM. However the water jet cuts strips with burrs whose height depends on the cutting speed. It was observed that higher speed generates lower burrs. However, if the speed is too high it deforms the strip creating visible curvature. Therefore the balance between a cutting speed and a sample condition had to be initially found.

10.2.5 Cutting of Thin CGO Sheets into Epstein Strips

EDM, laser and water jet techniques were designed for cutting strips thicker than 0.50 mm and the 0.30 mm Epstein strips were susceptible to small deformations. Therefore the guillotine was the only acceptable technique to cut strips from a single sheet. It was found that strips cut from stacks of 3 sheets at a time using EDM, laser and water jet techniques showed no sign of distortion or detectable burrs (apart of water jet cutting).

EDM, laser and water jet cutting speeds of 7.5 mm/min and 300 mm/min and 2404 mm/min respectively were chosen taking into consideration the condition of strip edges, corners and final flatness.

10.3 Investigation of the Cutting Stress on Magnetostriction in CGO Steel

It was intended to magnetise the single strips cut parallel to the RD sinusoidally at 1.5 T and 1.7 T (peak), 50 Hz in the magnetostriction measurement system. However during the measurements on the laser cut strips under compressive stress the maximum obtainable sinusoidal flux density was 1.5 T because of the reduced permeability at higher flux density. Therefore the cutting techniques were compared at 1.5 T, where magnetostriction was measured in the range of applied stress of ±10 MPa (also including 0 MPa as included stress point during magnetostriction measurement), directly after cutting and on the same strips after the stress relief annealing at a temperature of 810˚C for 2 hours in an atmosphere of 2% hydrogen and 98% nitrogen.

The level of stress retained in each strip after the stress relief annealing, was assessed by measuring a shift of magnetostriction vs. stress curves before and after the anneal. Comparable shifts of the stress sensitivity curves were observed for three strips cut from the same sheet using each cutting technique. Furthermore within each batch of three samples the pk-pk magnetostriction varied by less than ± 5 % under -10 MPa of compressive stress.

The average values of pk-pk magnetostriction under stress of the 3 strips after cutting using the four techniques and then after subsequent stress relief annealing are shown in Fig 10.1.

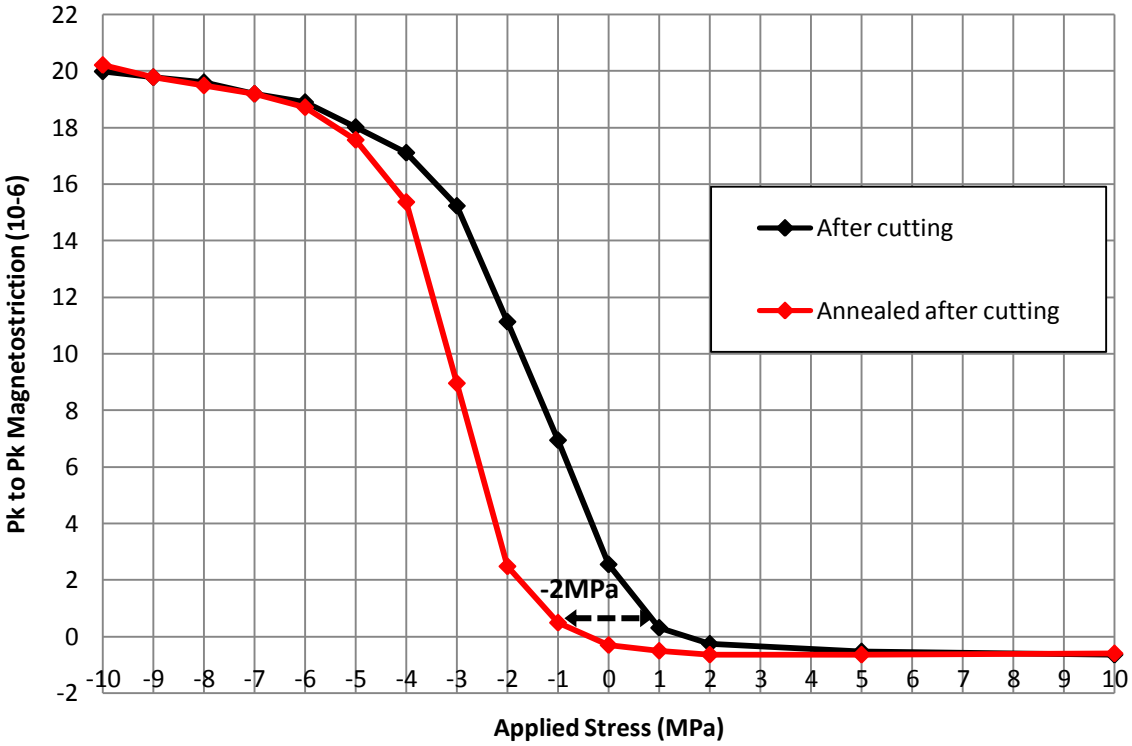

a) Guillotine

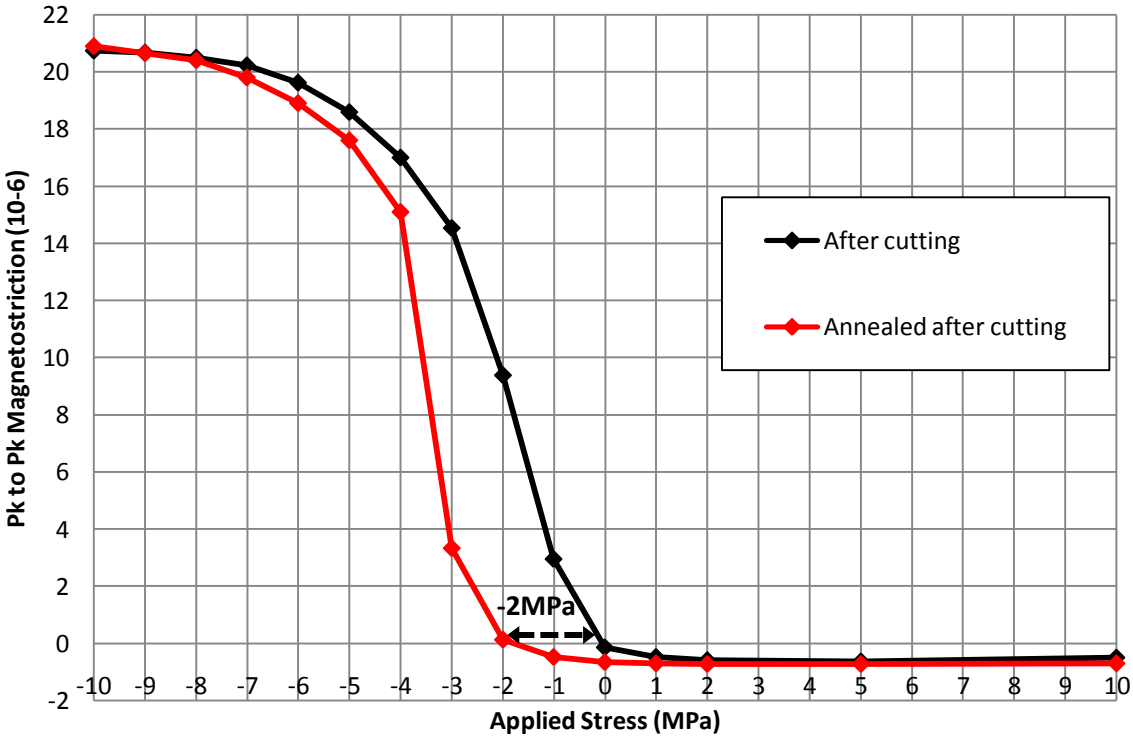

b) *EDM*

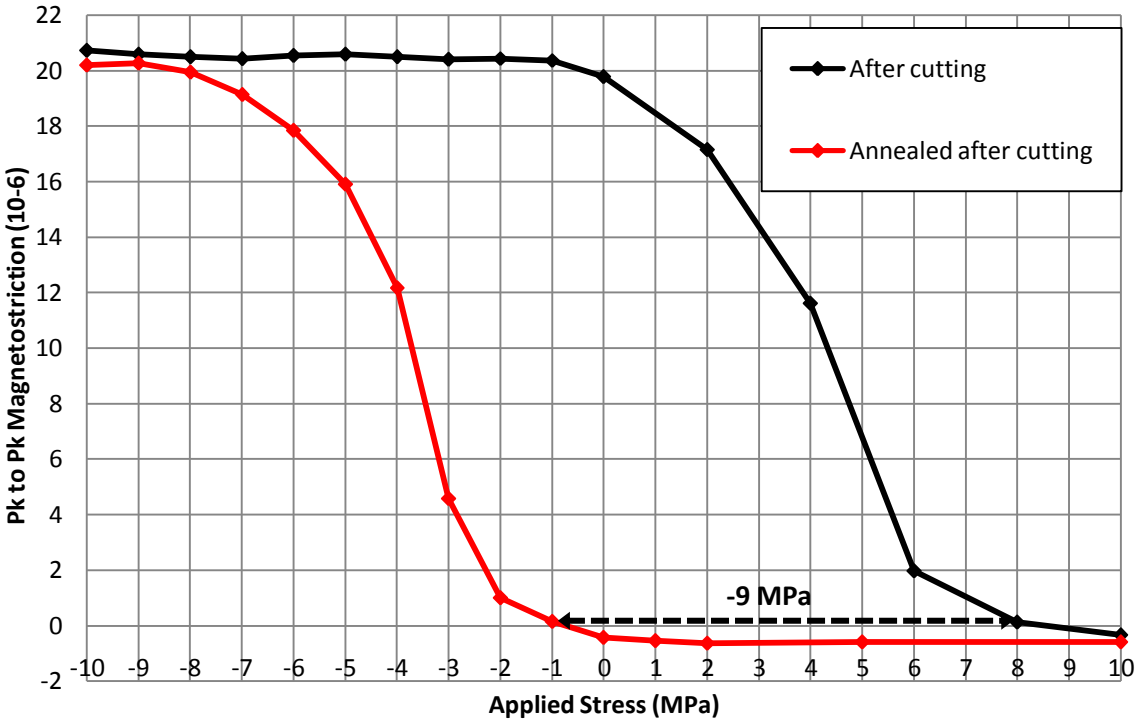

c) *Laser*

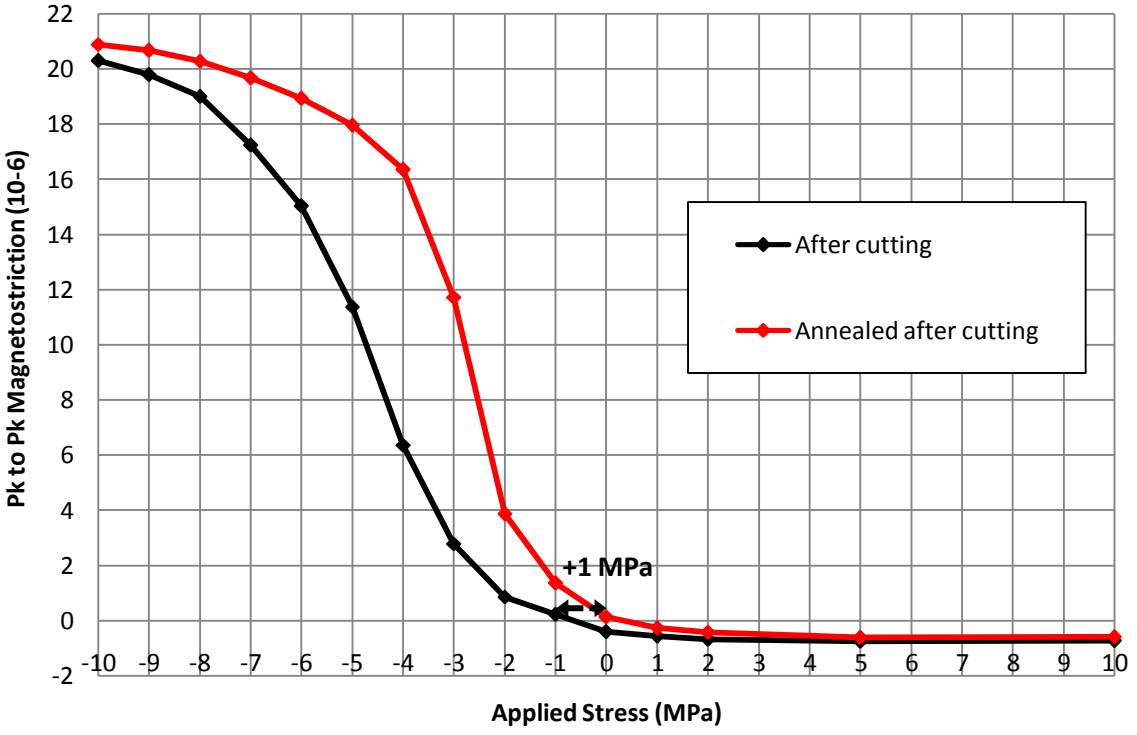

d) Water jet

Fig 10.1 Influence of cutting and subsequent SRA on stress sensitivity of magnetostriction of strips cut parallel to the RD, magnetised at 1.5 T, 50 Hz: a) guillotine, b) EDM, c) laser and d) water jet.

By comparing with the annealed condition, which as stated above was the same in all samples before cutting, guillotining and EDM introduced the effect of a compressive stress of approximately 2 MPa whereas the shift of the stress sensitivity curves of the laser cut strip was about 9 MPa. However water jet cutting introduced a beneficial tensile stress to the cut strip which was characterised by approximately 1 MPa shift of stress sensitivity curve.

A plastically deformed region is created by guillotining up to around 0.1 mm from the cut edge [3]. EDM and laser cutting produces temperatures above the melting point and cause atomic dislocations near the cut edges [1, 4]. The contraction of the steel during rapid cooling causes internal compressive stress in the cut edge region. The difference in the induced cutting stresses set up by EDM and laser could be a result of using different assisting atmosphere (coolants), which could impact the size of heat affected zone (HAZ) and recast layers created by the oxidation of the cut edges [5].

The applied compressive stress along the RD set up during magnetisation caused a rapid increase in the critical magnetic field, which is required to reorient the 90˚ domains (occurring in the stress domain patterns) to the RD [6]. The plastically deformed areas and the stress patterns appearing under compression in the RD, decrease the permeability, which is manifest in the distorted B-H loop. Fig 10.2 shows average B-H loops of 3 strips measured with no external stress after cutting and subsequent stress relief annealing. The loops of all the strips after annealing were similar. A typical curve for the laser cut strip is shown in Fig 10.2 designated as “Annealed after cut”.

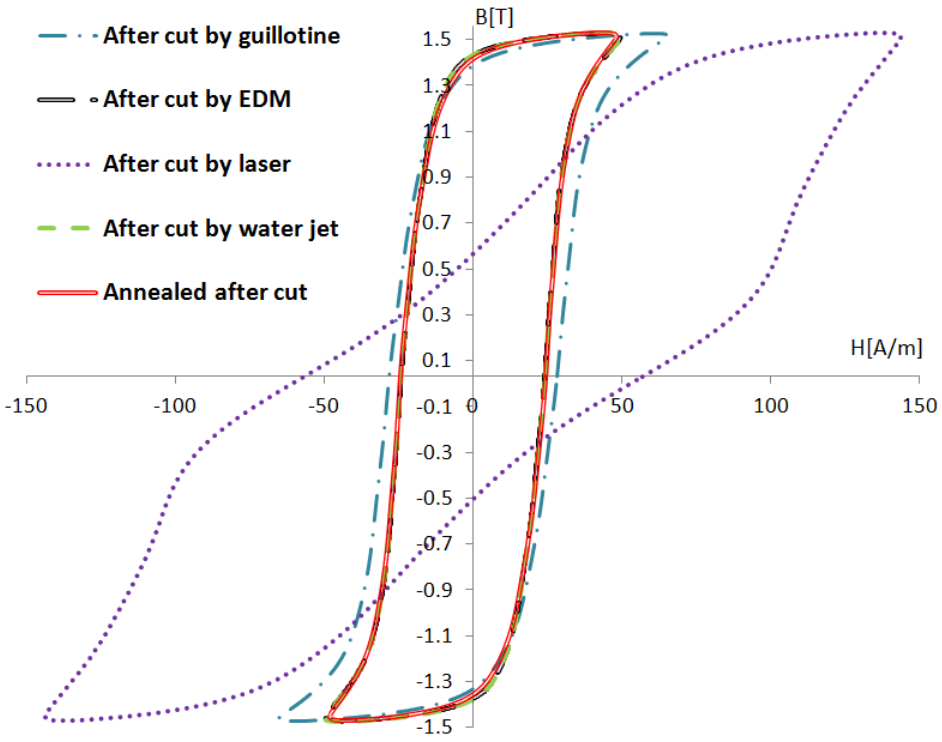

Fig 10.2 B-H loop of samples cut using four techniques measured at 1.5T, 50 Hz.

Furthermore the large reduction in permeability apparent from the B-H loop could divert flux from the stressed area to the unstressed part of the strip.

The beneficial tensile stress set up in the strip after water jet cutting led to the investigation of cutting the CGO sheet under applied high tensile stress in the RD by using a simple tensioning rig as shown in Fig 10.3.

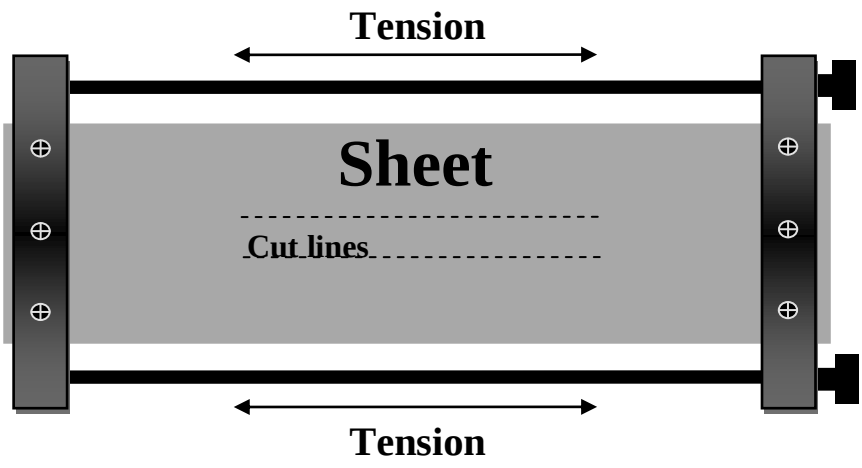

Fig 10.3 Tension rig prepared to cut strips under high tension by using the water jet technique.

The 305 mm lines were cut along the RD under tension by the water jet in the positions shown in Fig 10.3. After cutting, the external tensile stress in the sheet was released, and then the two short ends of Epstein strips were cut using the guillotine in order to avoid applying tensile stress along the TD. Fig 10.4 shows pk-pk magnetostriction under stress of the strip after cutting under tension and after stress relief annealing.

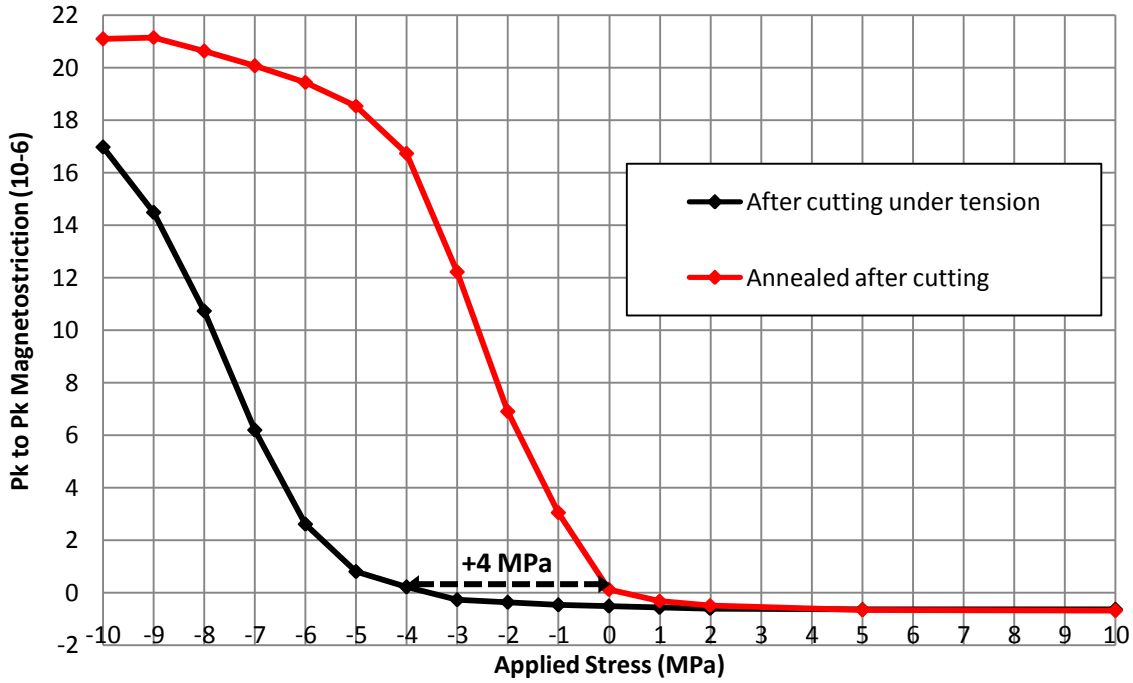

Fig 10.4. Influence of water jet cutting on stress sensitivity of magnetostriction of strip under high tensile stress cut parallel to the RD, magnetised at 1.5 T, 50 Hz.

The external tension extends the shift of magnetostriction vs. stress sensitivity curve from approximately 1 MPa (Fig 10.1d) to 4 MPa (Fig 10.4).

The reason for the difference of magnetostriction vs. stress sensitivity curves of strips after stress relief annealing, especially those cut using EDM and laser with no plastically deformed regions, is not yet understood. Also more research on water jet cutting on a sheet under applied tensile stress in the RD is required.

10.4 Static Domain Observations

The magnetic domain viewer was used for static domain observations on strip surfaces to investigate the compressive stress which causes the shifts of magnetostriction stress sensitivity curves occurring after cutting. No change was

observed in the domain structure for strips after cutting by guillotining or EDM and after stress relief annealing. However, Fig 10.5 and Fig 10.6 show 40 mm x 30 mm domain images obtained when the domain viewer placed near the ends of strips cut by laser and water jet parallel to the RD (Fig 10.5a and Fig 10.6a) and the TD (Fig 10.5b and Fig 10.6b). The laser cutting started and ended slightly above the upper left corner of the strip. The observed domain structures are divided into zones A and B for convenience. In zone A, the domains structure remained unchanged even after stress relief annealing, whereas zone B contains a mixture of: stress pattern I (perpendicular patterns on the surface, oriented along the rolling direction) and stress pattern II (characterised as a zigzag patterns) [7]. Similar patterns were observed on the other surfaces and ends of the strips.

If a compressive stress is applied along the RD of an unmagnetised strip of CGO, the volume of main 180 degree domains oriented along [001] directions close to the RD decreases and the volume of main domains aligned along [100] and [010] directions perpendicular to the RD, including surface closure domains in [001] direction, increase [8]. This is why stress patterns are observed when the laser cuts the strip parallel to the RD (Fig 10.5 "zone B"). If the sample is magnetised along its RD, high magnetostriction occurs as the stress patterns become re-converted to [001] domains.

When strips were cut parallel to the TD the domain structure remained mainly unchanged as shown in Fig 10.5 (there is no evidence of stress patterns near the longitudinal cut edges). This occurs because compressive stress applied in the transverse direction has the same effect as tension in the RD with half the magnitude of magnetostriction [9]. The high tensile stress applied along the RD has the effect of narrowing the domains. However the 4 MPa tension in the RD (half the magnitude of the 8 MPa compression in the TD) is not sufficient to produce a significant change in domain structure. The opposite effect is observed using the water jet technique Fig 10.6(a, b). Cutting the strip parallel to the RD does not affect the domains structure (Fig 10.6 zone "A"). However when it is cut along the TD stress patterns appears (Fig 10.6 zone "B").

The observed stress patterns disappeared after the laser and water jet cut samples were stress relief annealed. This verifies the hypothesis of the appearance of the HAZ

after cutting by the laser. However water jet cutting does not introduce the HAZ, therefore a tensile stress would be set up during creation of burrs on the strip edges.

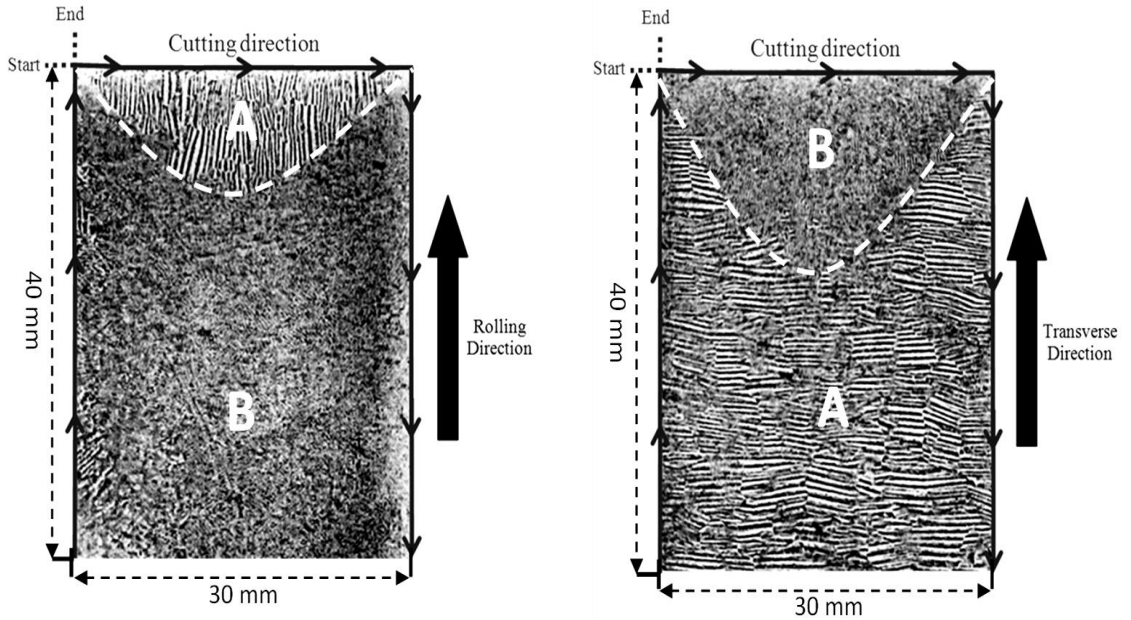

a) *b)*

Fig 10.5 Domain structures after laser cutting of Epstein strips along: a) the RD and b) the TD.

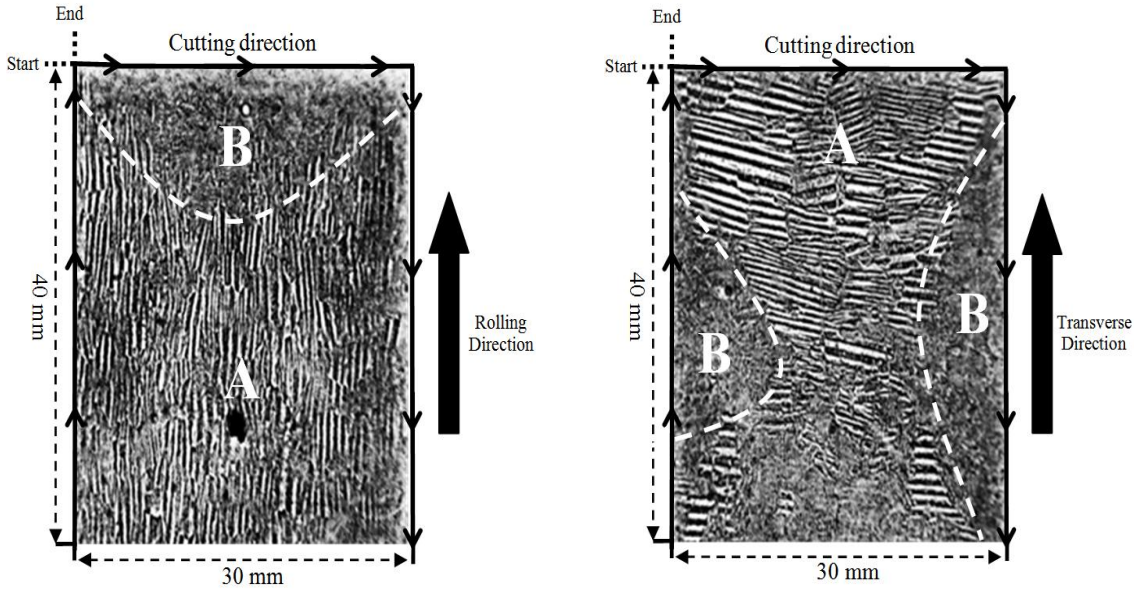

a) *b)*

Fig 10.6 Domain structures after water jet cutting of Epstein strips along: a) the RD and b) the TD.

10.5 Assessment of a Coating Stress in the Measured Strips

Commercial CGO, as used in this investigation, has a double layer coating applied during the production process as described in section 2.2. The coatings create a longitudinal tensile stress at the surface of the steel, which reduces supplementary domain structures oriented away from the RD [10]. Three Epstein strips of CGO were pickled in hydrochloric acid to remove the double coating and the associated tension. Magnetostriction stress sensitivity curves were measured before and after coatings removal to estimate the tension applied to the surface of the steel by the coating. A stress shift of around 2 MPa (tensile) was found as shown in Fig 10.7 which is comparable to this presented in Fig. 8.28(a).

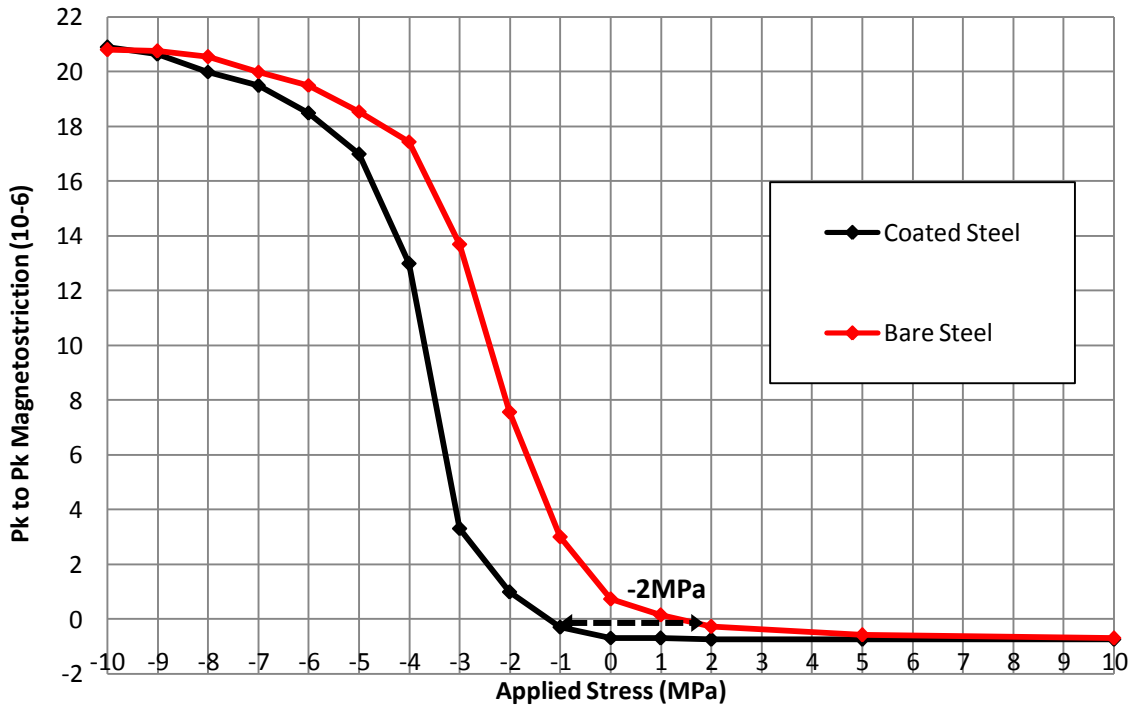

Fig 10.7 Influence of coating tension on magnetostriction measured under stress at 1.5 T, 50 Hz.

The 2 MPa compressive stress set up by guillotining or EDM shown in Fig 10.1 is of the same order of magnitude as the shift in stress sensitivity curves caused by coating removal. In the case of laser cutting, the compressive stress introduced along the cut edge is far higher than the coating tension, hence stress patterns are observed on the cut strip surface.

10.6 Summary of the Effect of Cutting Stress on Magnetostriction in CGO Steel

Guillotining and EDM introduced compressive stress evaluated as a stress shift of approximately 2 MPa in the magnetostriction stress characteristic, whereas the shift of the laser cut strip was about 9 MPa. The opposite effect was observed for water jet cutting which set up approximately 1 MPa of beneficial tensile stress to the cut strip. This tensile stress can be increased to as high as 4 MPa by applying a high tensile stress along the RD of the sheet during the cutting process.

The compressive stress set up in the sample after laser cutting introduced stress domain patterns along the RD. However no visually affected domain structures were observed along the TD. Water jet cutting introduced a low tensile stress which introduced a small amount of stress patterns on the cut strip surface along the TD.

The plastically deformed areas and the stress patterns appearing under compression in the RD, decrease the permeability, which is manifest in the distorted B-H loop.

10.7 Reference

[1] P. Shankar, *et al.*, "Analysis of spark profiles during EDM process," *Machining Science and Technology,* vol. 1, pp. 195-217, 1997.

[2] V. Yadav, *et al.*, "Thermal stresses due to electrical discharge machining," *International Journal of Machine Tools & Manufacture,* vol. 42, pp. 877-888, Jun 2002.

[3] Z. Matheisel, "Blachy elektrotechniczne walcowane na zimno," *WNT,* 1973.

[4] D. Gaworska-Koniarek, *et al.*, "Effect of laser cutting on magnetic properties of electrical steels," *Prace Instytutu Elektrotechniki* pp. 139-152, 2009.

[5] A. Belhadj, *et al.*, "Effect of laser cutting on microstructure and on magnetic properties of grain non-oriented electrical steels," *Journal of Magnetism and Magnetic Materials,* pp. 20-31, 2003.

[6] A. J. Moses and D. Davies, "Influance of compressive stress on magnetic properties of comercial (110) [001] oriented silicon-iron," *IEEE Transactions on Magnetics,* vol. 16, pp. 454-460, 1980.

[7] L. J. Dijkstra and U. M. Martius, "Domain patterns in silicon iron under stress," *Reviews of Modern Physics,* vol. 25, pp. 146-150, 1953.

[8] W. D. Corner and J. J. Mason, "Effect of stress on domain structure of goss textured silicon iron," *British Journal of Applied Physics,* vol. 15, pp. 709-722, 1964.

[9] P. J. Banks and E. Rawlinson, "Dynamic magnetostriction and mechanical strain in oriented 3% silicon iron sheet subject to combined longitudinal and transverse stresses," *Proceedings of the Institution of Electrical Engineers-London,* vol. 114, pp. 1537-1546, 1967.

[10] J. W. Shilling, "Domain structure during magnetisation of grain oriented 3% SiFe as a function of applied tensile stress," *Journal of Applied Physics,* vol. 42, pp. 1787-1789, 1971.

Chapter 11 Influence of Rotational Magnetisation on Magnetostriction in GO and NO Steel

11.1 Samples Selection and Preparation

Samples were taken from 0.30 mm thick grain oriented (GO) electrical steel: conventional (CGO), high permeability (HIB), and 0.35 mm and 50 mm thick non-oriented (NO) electrical steel. They were cut into 80 mm diameter discs and 305 mm long Epstein strips parallel to the rolling direction (RD) and the transverse direction (TD). All disc and Epstein samples (305 mm x 30 mm) were cut by electrical discharge machining (EDM) and then stress relief annealed at 850˚C for 2 hours in an atmosphere of 2% hydrogen and 98% nitrogen. The disc and Epstein sample of each type was cut from adjacent places of the same sheet in a distance to the sheet cut edge.

11.2 Magnetostriction Measurement Techniques

Peak to peak (pk-pk) magnetostriction at 50 Hz of AC magnetisation was determined using two measurement techniques: piezoelectric accelerometers (described in section 5.2.1) for Epstein samples and surface mounted foil resistance strain gauges (described in section 5.1.2.3) for disc samples. Epstein strips were inserted singly into the magnetostriction measurement system previously described in section 5.2. The maximum sinusoidal flux density achievable in GO samples cut along the TD and NO strips was 1.50 T and 1.60 T respectively at magnetisation frequency 50 Hz.

Each disc sample was tested using two-dimensional (2D) magnetisation system shown in Fig 11.1 with a help of a co-researcher, Sakda Somkun [1]. The two phase excitation winding used to produce alternating magnetisation along the RD or TD, or under rotational magnetisation in the flux density ranged from 1.00 T to 1.70 T at 50 Hz is shown in Fig 11.1. In the centre of the discs four holes with 0.5 mm diameter were drilled within 10 mm from the centre of the disc in order to wind two search coils in the

RD and TD direction (Fig 11.1) and then the discs were stress relief annealed to remove the drilling stress.

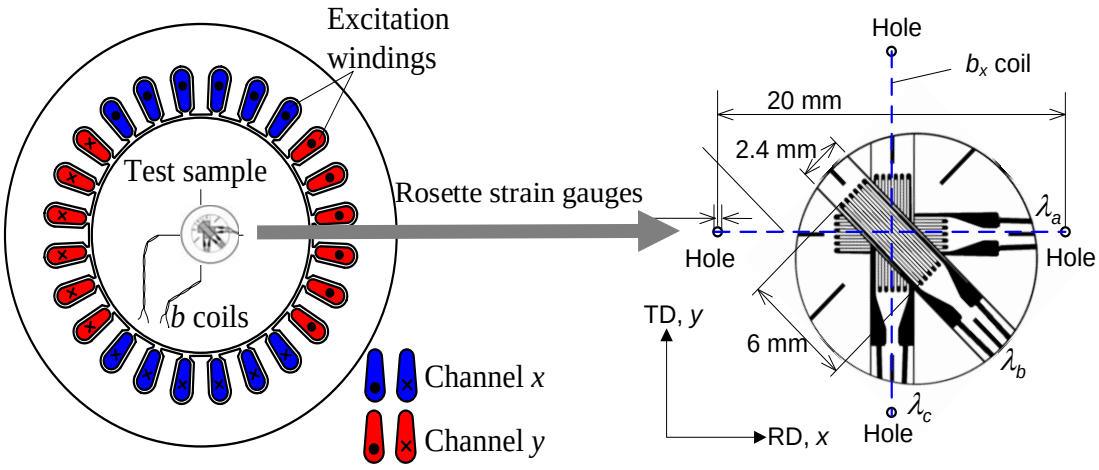

Fig 11.1 Schematic diagrams of two dimensional magnetostriction measurement systems with configuration of excitation windings, and search coils with rosette resistance strain gauges placed at the centre of each disc sample [1].

The flux density in the RD and TD was controlled to be sinusoidal by the LabView feedback algorithm, where the magnetic field applied to the sample was measured by an orthogonal h coils wound on the plastic former and placed on the centre of the disc surface as shown in Fig 11.2.

Components of flux density and magnetic field along the RD and TD directions were calculated from induced voltages in the orthogonal b and h coils.

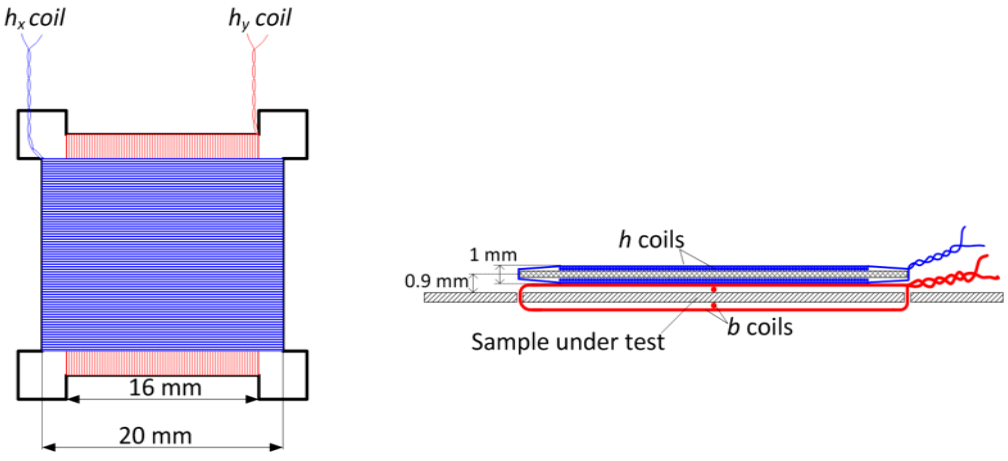

Fig 11.2 Schematic diagram of orthogonal h coils wound on one plastic former (not scaled): (a) top view, and (b) side view when attached with the sample under test [1].

Magnetostriction components along the RD and TD were measured using rosette resistance strain gauges (Fig 11.1), placed in the centre of the disc of CGO, HiB and NO samples. The measurement uncertainty of the average peak to peak magnetostriction was evaluated to be ±12% [2]. Each gauge had a nominal resistance of 120 Ω and an active area 6 mm long and 2 mm wide with a gauge factor of 2.1 (±1%). This resistance change is measured using the half bridge configuration (section 5.1.2.3) with a set of dummy gauges attached to a dummy unmagnetised disc of GO steel for temperature compensation. All Epstein and disc samples were initially demagnetised by stress relief annealing and also by a slow reduction of an alternating field after each magnetisation cycle.

11.3 Static Domain Observations on the GO Steel

A static domain observations were carried out on the uncoated steel surface of two selected CGO Epstein strips under two separate conditions: applied compressive stress in the RD and magnetisation in the TD, to help understand the magnetostriction mechanism under rotational magnetisation. The domain viewer was used to observe domain patterns of the first strip under compressive stress of up to -10 MPa in the RD presented in Fig 11.3(a). However to observe domain patterns under DC magnetisation in the TD without stress, the surface of the second strip was mechanically polished down to 1 micrometer by the magnetic disc polisher to enable domain observations using Kerr magneto optic microscope which is described in [3]. Fig 11.3(b) shows domains present on the polished surface due to DC magnetisation along the TD of the strip with no external applied stress.

It was observed that similar transverse closure domains were obtained for the CGO strips under compression in the RD, and also during magnetisation in the TD.

a)

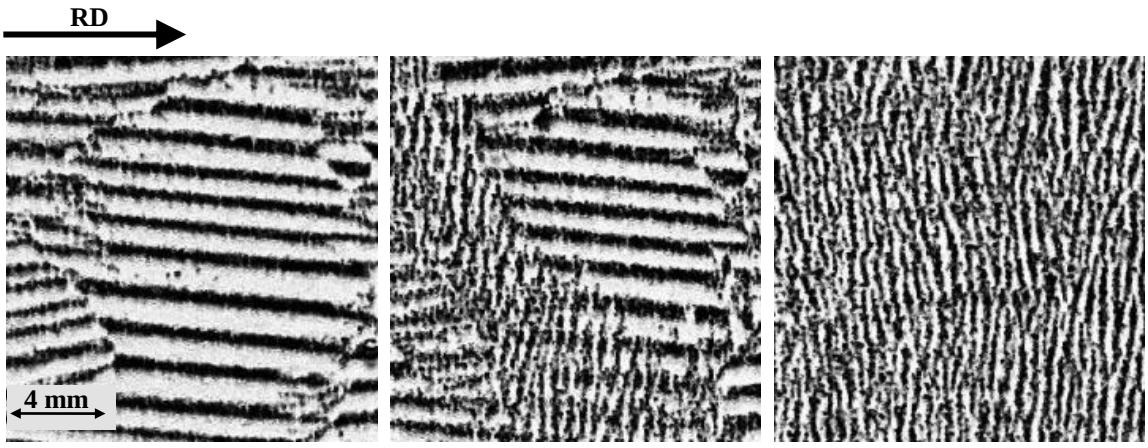

$\sigma = 0$ $\sigma_1 = -4$ MPa $\sigma_2 = -10$ MPa

b)

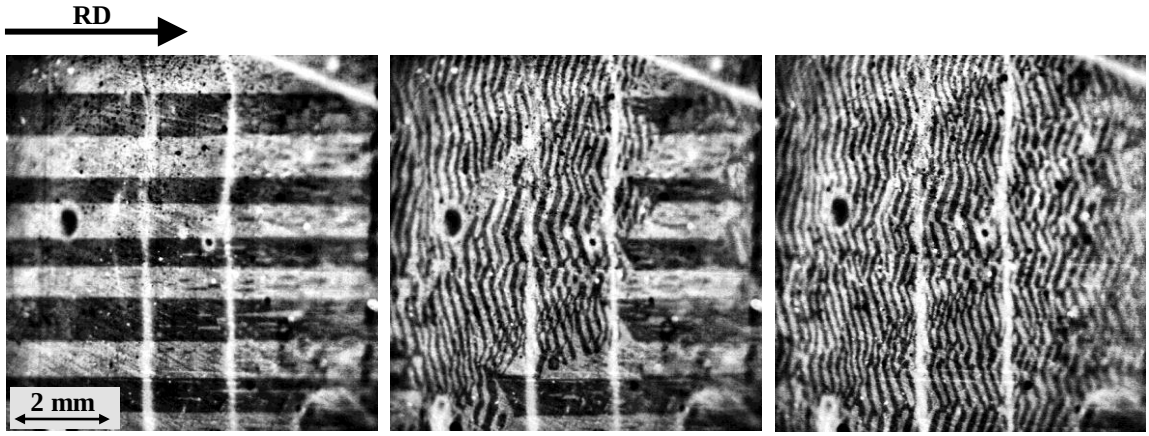

$H = 0$ $H_1 > 0$ $H_2 > H_1$

Fig 11.3 Static domain structures on the surface of a strip of CGO steel under: (a) compressive stress along the RD, and (b) DC magnetisation along the TD.

11.4 Investigation of Effect of Rotational Magnetisation on Magnetostriction in GO Steel

The components of peak to peak magnetostriction of the single CGO, HiB and two (0.35 mm and 0.50 mm) NO disc samples were measured along the RD and the TD under rotational ("Rotational Disc") and uniaxial ("Uniaxial Disc") magnetisation with no external applied stress.

The Epstein strips of the single CGO, HiB and two NO (0.35 mm and 0.50 mm) were magnetised along the RD and the TD, where magnetostriction was measured under

various magnitudes of applied stress (+10 MPa to -10 MPa) [3]. Two values of pk-pk magnetostriction were chosen for analysis from the measurements under stress: maximum magnetostriction under compression of -10 MPa ("Uniaxial Epstein High Compression") and magnetostriction with no external applied stress ("Uniaxial Epstein No Stress"). The collation of magnetostriction measurements under reference conditions are presented in Table 11.1.

Table 11.1 Collation of magnetostriction with reference conditions

Sample designation	**Applied stress**	**Excitation along**	**Component of magnetostriction measured along**
Uniaxial Epstein No Stress	No Stress	RD	RD
		TD	TD
Uniaxial Epstein High Compression	Compression in RD	RD	RD
	Compression in TD	TD	TD
Uniaxial Disc	No Stress	RD	RD
		TD	TD
Rotational Disc	No Stress	Rotational	RD and TD

The error bars at each measured point presented in Fig 11.4 to Fig 11.7 represent the uncertainty of the two measurement systems, i.e. for the 2D system is ± 12%, and magnetostriction measurement system: ± 0.5% at 0 MPa and ± 4.3% at -10 MPa of compressive stress.

The disc sample of the 0.50 mm thick NO steel, magnetised under rotational magnetisation was found to have a comparable characteristic of magnetostriction to the NO Epstein strip under high compression as shown in Fig 11.4(a). A similar tendency was found for NO disc and Epstein samples under uniaxial magnetisation in the RD with no applied external stress (Fig 11.4(a)).

Epstein strips cut along the TD and magnetised with and without external applied stress, had a lower magnetostriction than disc samples under uniaxial and rotational magnetisation Fig 11.4(a).

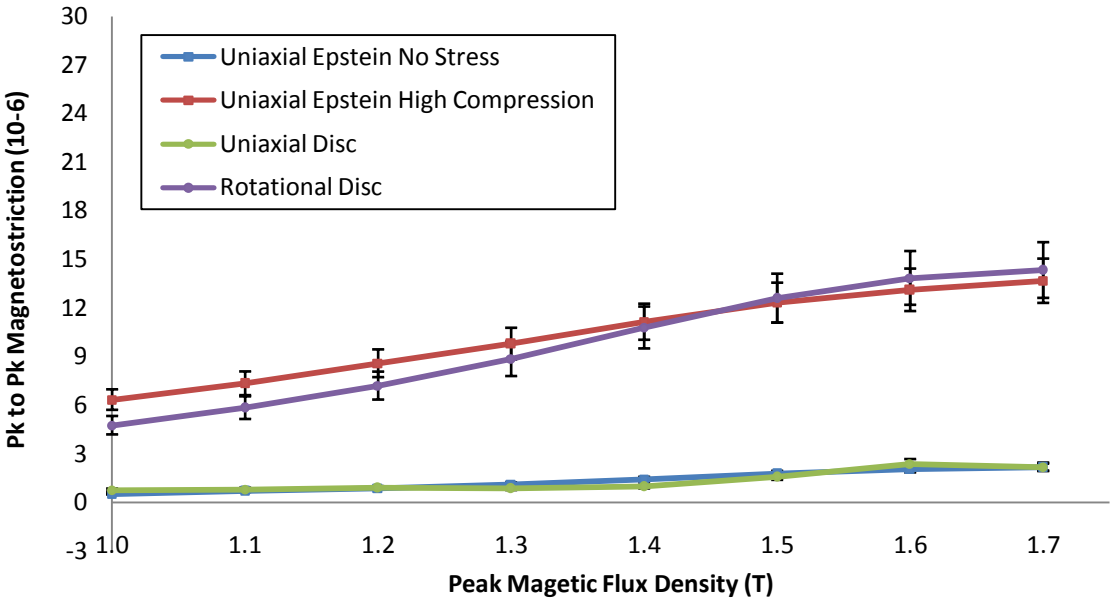

a) NO 0.50 mm in the RD

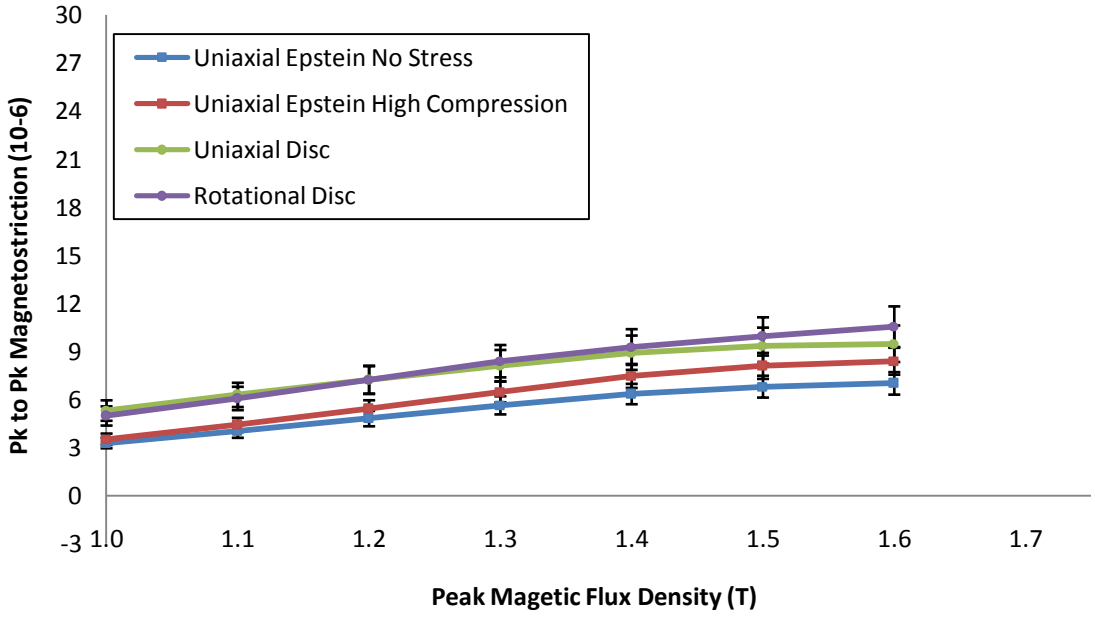

b) NO 0.50 mm in the TD

Fig 11.4 Variation of rotational and uniaxial pk-pk magnetostriction with flux density of 0.50 mm NO electrical steel measured along: (a) the RD, and (b) the TD.

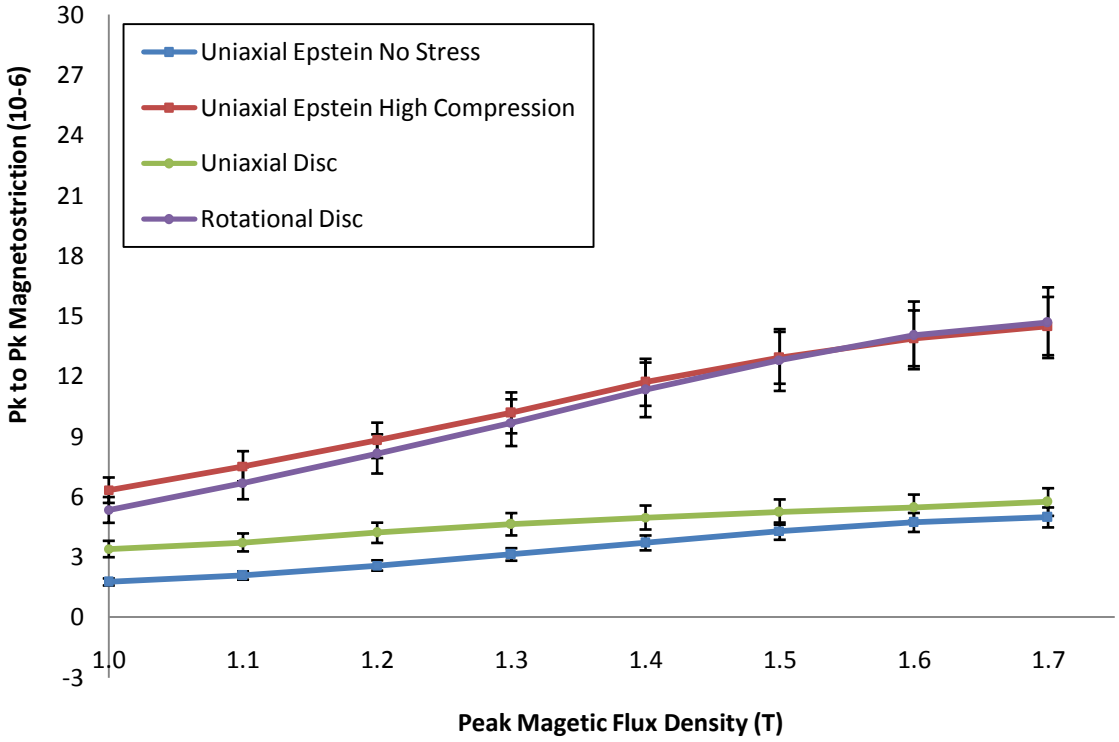

a) NO 0.35 mm in the RD

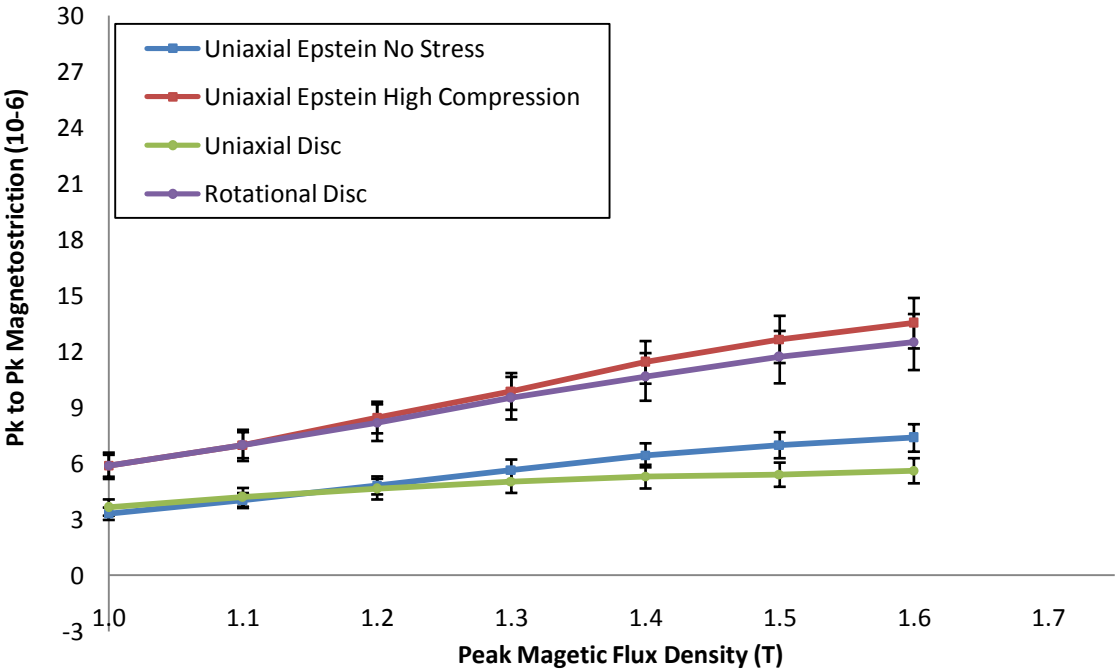

b) NO 0.35 mm in the TD

Fig 11.5 Variation of rotational and uniaxial pk-pk magnetostriction with flux density of 0.35 mm NO steel measured along: (a) the RD, and (b) the TD.

Epstein strips cut along the TD and magnetised in the same direction with and without external applied stress, had a lower magnetostriction than disc samples under uniaxial and rotational magnetisation (Fig 11.4 (b)). A similar relationship was obtained for 0.35 mm thick NO steel disc magnetised in a rotational field and Epstein strip under higher compression (Fig 11.5(a)). However 0.35 mm thick NO steel Epstein strip under uniaxial magnetisation, exhibited lower magnetostriction along the RD than the disc sample magnetised in the same direction up to 1.4 T and comparable above that flux density level. Magnetostriction measured along the TD was comparable to that of Epstein strip under stress and the disc sample under rotational magnetisation at lower flux density and higher for disc sample above 1.2 T (Fig 11.5(b)). A similar variation of magnetostriction can be observed due to uniaxial magnetisation for disc and Epstein samples with no applied stress (Fig 11.5(b)). The magnetostriction of the 0.30 mm thick CGO and HIB disc samples under rotational magnetisation was higher than that of Epstein strips under high compression measured along both directions as shown in Fig 11.6 and Fig 11.7.

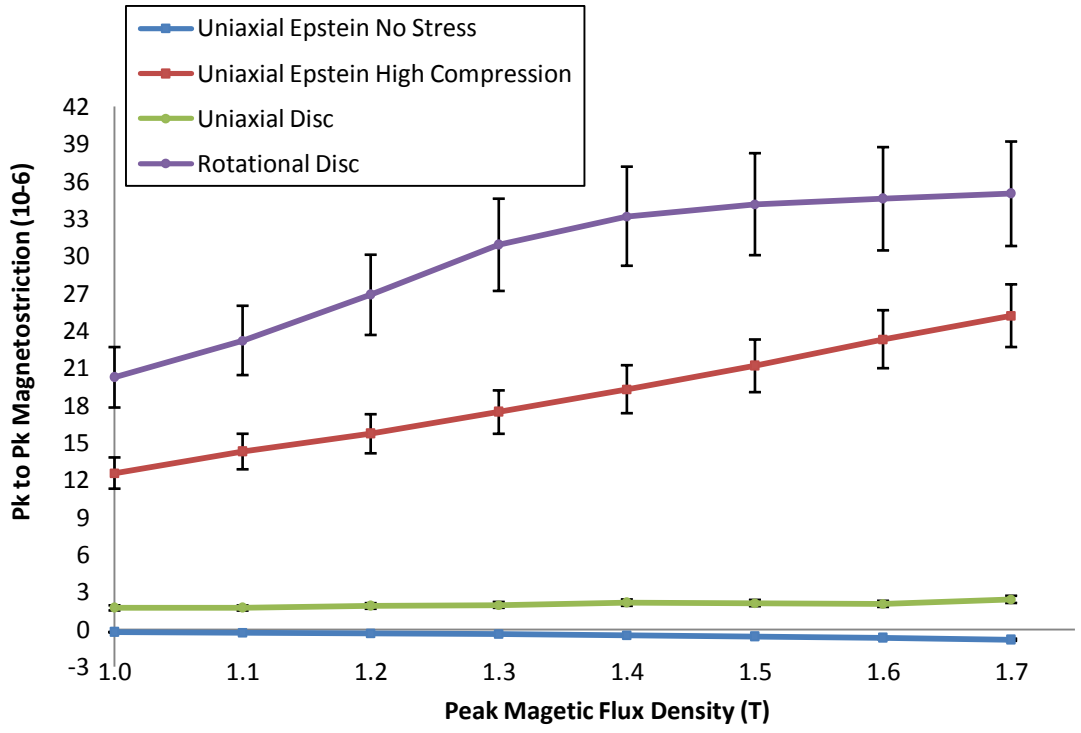

a) CGO 0.30 mm in the RD

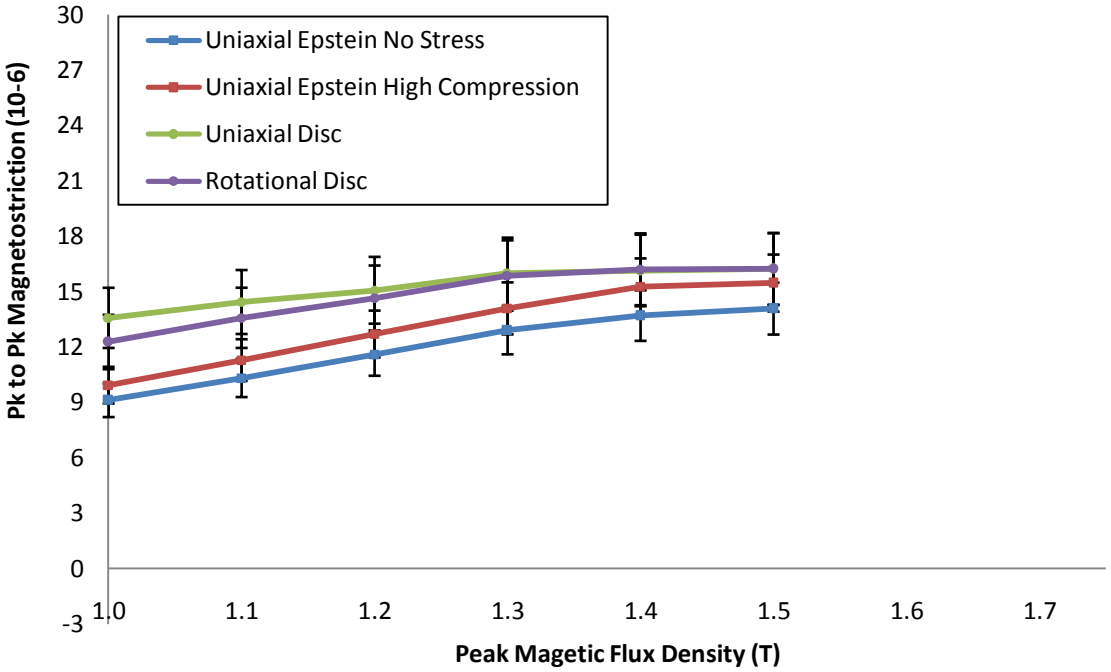

b) CGO 0.30 mm in the TD

Fig 11.6 Variation of rotational and uniaxial pk-pk magnetostriction with flux density of 0.30 mm CGO electrical steel measured along: (a) the RD, and (b) the TD.

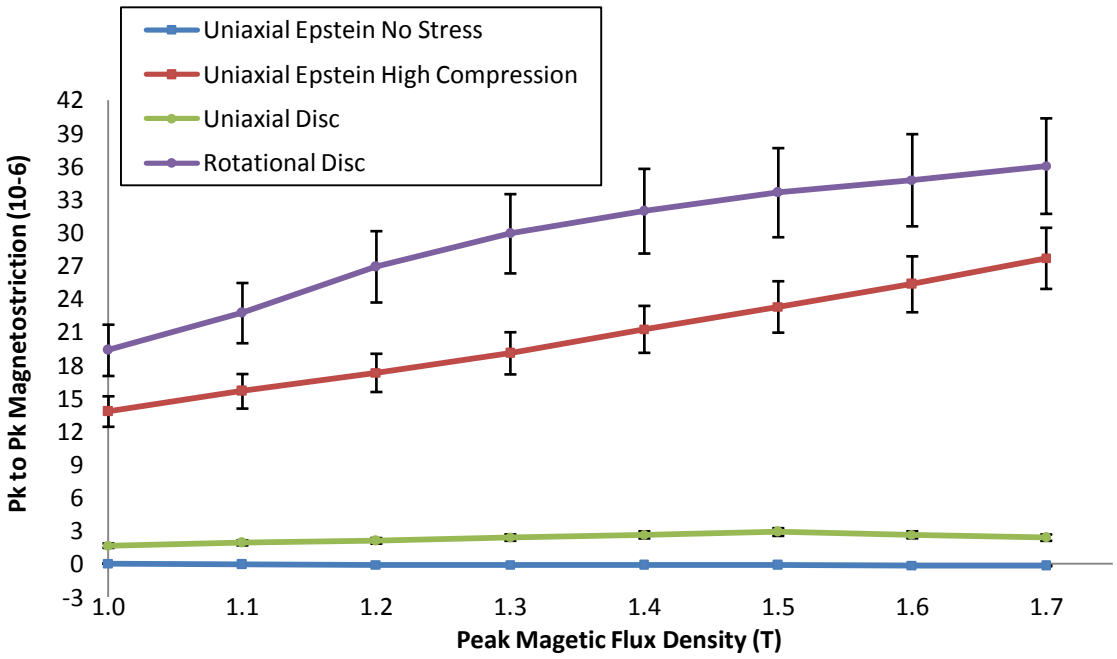

a) HIB 0.30 mm in the RD

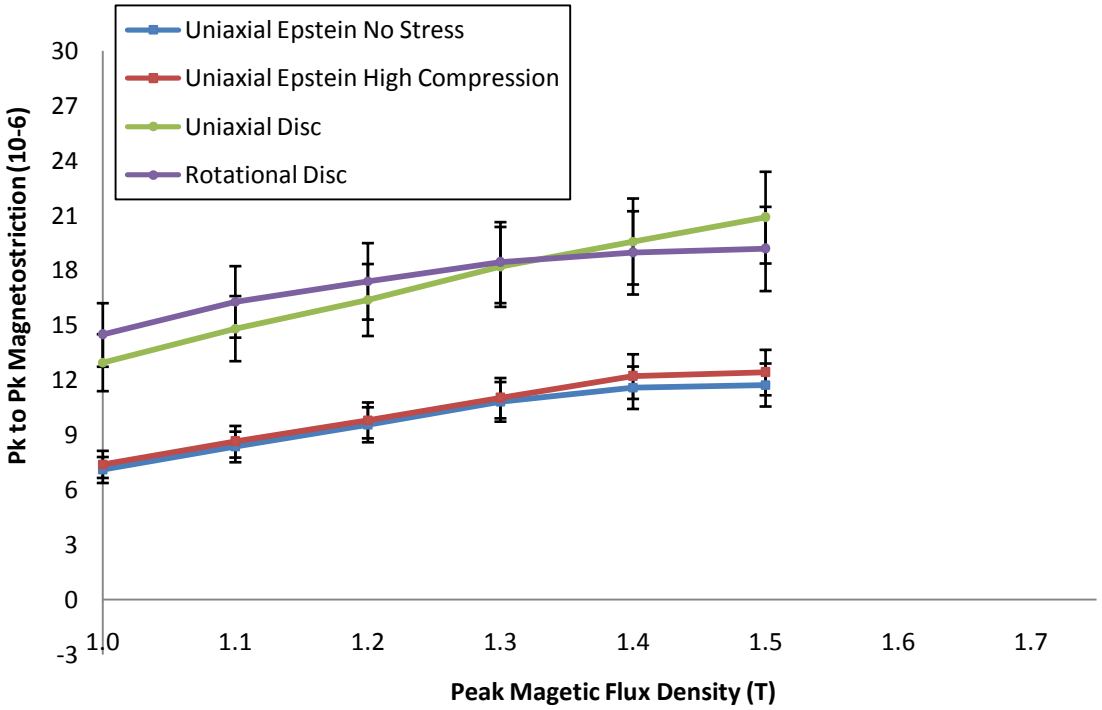

b) HIB 0.30 mm in the TD

Fig 11.7 Variation of rotational and uniaxial pk-pk magnetostriction with flux density of 0.30 mm HIB electrical steel measured along: (a) RD, and (b) TD.

Also magnetostriction under uniaxial magnetisation with no external applied stress was slightly higher for disc samples than for Epstein strips along the RD and significantly higher along the TD. Table 11.2 shows collation of pk-pk magnetostriction measured at 1.5 T along the RD and the TD of all samples of each reference condition.

Table 11.2 Collation of pk-pk magnetostriction at 1.5 T in the RD and TD direction at each reference condition

Type	**Sample designation**	**Component of magnetostriction in the RD at 1.5 T**	**Component of magnetostriction in the TD at 1.5 T**
NO 0.50 mm	Uniaxial Epstein	1.8	6.8
	Uniaxial Epstein High Compression	12.3	8.1
	Uniaxial Disc	1.6	9.4
	Rotational Disc	12.6	9.9
NO 0.35 mm	Uniaxial Epstein	4.3	7.0
	Uniaxial Epstein High Compression	12.9	12.7
	Uniaxial Disc	5.2	5.4
	Rotational Disc	12.8	11.7
CGO 0.30 mm	Uniaxial Epstein	-0.6	14.1
	Uniaxial Epstein High Compression	21.2	15.5
	Uniaxial Disc	2.1	16.2
	Rotational Disc	34.2	16.2
HiB 0.30 mm	Uniaxial Epstein	-0.1	11.7
	Uniaxial Epstein High Compression	23.3	12.4
	Uniaxial Disc	2.9	20.9
	Rotational Disc	33.6	19.2

The Becker-Döring [4] equation (3.4) is used to calculate the saturation magnetostriction of a single crystal (grain) of ideal GO steel. If a perfectly oriented (110)[001] grain in a sheet of CGO is magnetised to saturation, switching of magnetic moments from the [001] to [110] directions would cause the magnetostriction along the RD to change from λ_{100} to $-\lambda_{100}/2$, and from $-\lambda_{100}/2$ to $(\lambda_{100}+3\lambda_{111})/4$ along the [110] direction as shown in Fig 11.8 [5].

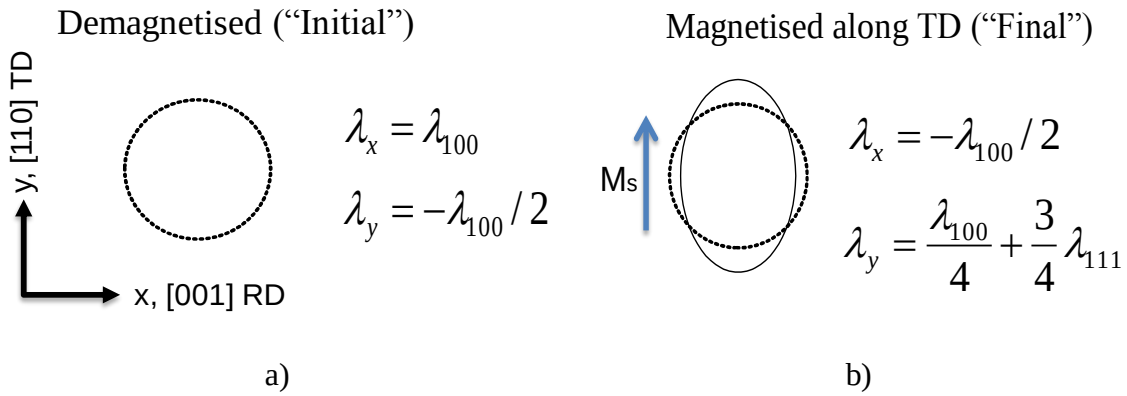

Fig 11.8 Schematic diagram of magnetostriction components in a single crystal of GO steel at the demagnetised state (a) and magnetised to saturation along the TD (b).

The observed magnetostriction is the difference between initial (Fig 11.8(a)) and final (Fig 11.8 (b)) magnetostriction. Thus, in a perfectly oriented material, the pk-pk magnetostriction along the RD and the TD, when an initially demagnetised material is magnetised to saturation in the TD, are $-3\lambda_{100}/2$ = -36 μm/m and $3(\lambda_{100}+\lambda_{111})/4$ = 14.7 μm/m respectively (assuming values of λ_{100} = 24 μm/m and λ_{111} = -4.1 μm/m for 3% SiFe [6]).

This agrees closely with the measured magnetostriction along the RD of CGO and HiB under rotational magnetisation at saturation level.

The samples cut along the TD as well as the RD under high compression could not be magnetised to saturation because of its complicated domain structure [7] so the ideal theoretical values would not be reached.

If Epstein strips of CGO and HiB cut along the TD are magnetised to saturation, the pk-pk magnetostriction along the sample length would be close to $3(\lambda_{100}+\lambda_{111})/4$. Similarly, the pk-pk magnetostriction of Epstein strips of CGO and HiB cut along the RD under a high compression magnetised at saturation along the strip length would be

close to $-3\lambda_{100}/2$. These trends can be observed in Fig 11.6 and Fig 11.7 even though the samples were not saturated and there were the presence of flux closure domains.

It is not possible to quantify the significance of the small difference in magnetostriction between the Epstein strips and disc samples of NO 0.50 mm and CGO due to the low number of samples used since difference observed is within the combined uncertainty. Also the large difference in the HiB sample could be caused by the localization of the strain gauge on the boundary of two grains.

However a similar relation between the Epstein and disc samples of NO 50 mm was observed in [5]. The difference in magnetostriction between Epstein strips and disc samples along the TD of the 0.50 mm thick NO steel was considered to be due to the form effect [6]. The form effect gives rise to spontaneous magnetostriction of an ellipsoid of rotation shown in Fig 11.9(a) magnetised along its length in order to reduce the magnetostatic energy so that the total energy of the system will be minimised [6].

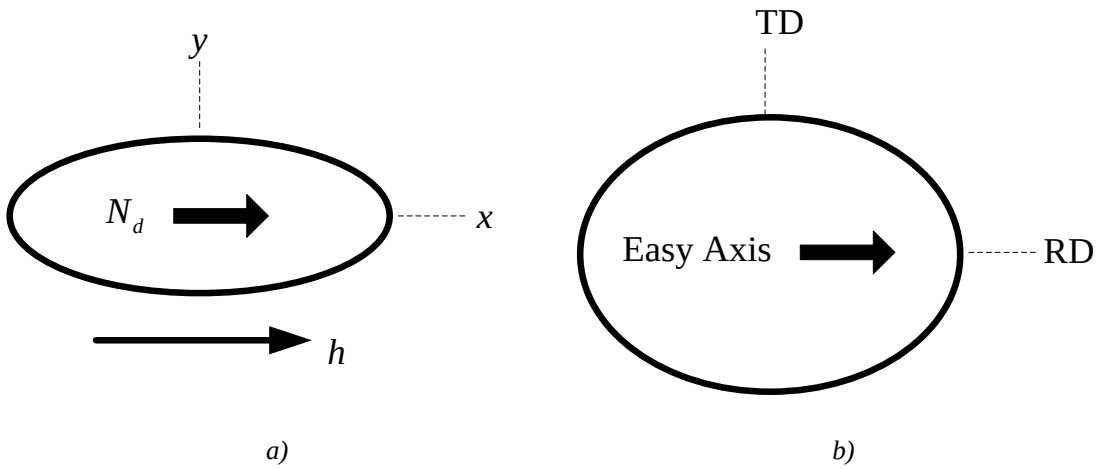

Fig 11.9 Demagnetisation factor "Nd" in an ellipsoid of rotation under external applied field "h" (a), equivalent shape of the 0.50 mm disc sample due to the magnetic anisotropy (b).

In samples exhibiting significant anisotropy the magnetostatic energy is the highest if magnetised along the TD. Additional magnetostriction occurs with more magnetostatic energy due to the form effect.

11.5 Summary of the Rotational Magnetostriction Investigation

The strip of GO steel under applied high compressive stress shows similar transverse closure domains on the polished surface to this under DC magnetisation along the TD of the strip with no external applied stress.

The pk-pk magnetostriction of GO steel under rotational magnetisation reaches 35 μstrain which is higher than due to uniaxial magnetisation under high compression (approximately 24 μstrain).

Magnetostriction measured in the TD of 0.30 mm GO and 0.50 mm NO samples under uniaxial magnetisation in the TD is higher for disc shape then for Epstein samples which was considered to be due to the form effect.

.

11.6 References

[1] S. Somkun, *et al.*, "Magnetostriction anisotropy and rotational magnetostriction of a nonoriented electrical steel," *IEEE Transactions on Magnetics*, vol. 46, pp. 302-305, 2010.

[2] S. Somkun, "Magnetostriction and magnetic anisotropy in non-oriented electrical steels and stator core laminations," PhD Thesis, Cardiff University, Cardiff, 2011.

[3] A. Moses, *et al.*, "Real time dynamic domain observation in bulk materials," *Journal of Magnetism and Magnetic Materials*, pp. 150-154, 2006.

[4] R. Becker and W. Döring, "Ferromagnetism," *Springer*, 1939.

[5] S. Somkun, *et al.*, "Comparisons of AC magnetostriction of non-oriented electrical steels measured in epstein and disc samples," *Journal of Electrical Engineering*, vol. VOL 61, pp. 89-92, 2010.

[6] R. Gersdorf, "Uniform and non-uniform form effect in magenetostriction," *Physica*, vol. 26, pp. 553-574, 1960.

[7] J. W. Shilling and G. L. Houze, "Magnetic proprties and domain structure in gain-oriented 3% Si-Fe," *IEEE Transactions on Magnetics*, vol. MAG10, pp. 195-223, 1974.

Chapter 12 Control of Magnetostriction Characteristic under Applied Stress

12.1 Control of Magnetostriction under Stress

The strip thickness, coating stress and cutting stress covered in chapters 7, 8 and 10 were selected as factors having the most impact on the shape of magnetostriction stress sensitivity curves. Fig 12.1 presents an example of a three transformation phases of a stress sensitivity curve caused by decrease in the steel thickness and increase in the coating thickness of GO electrical steel strip. Moreover "Phase 3" can be modified by application of the beneficial cutting stress using the water jet technique discussed in chapter 10.

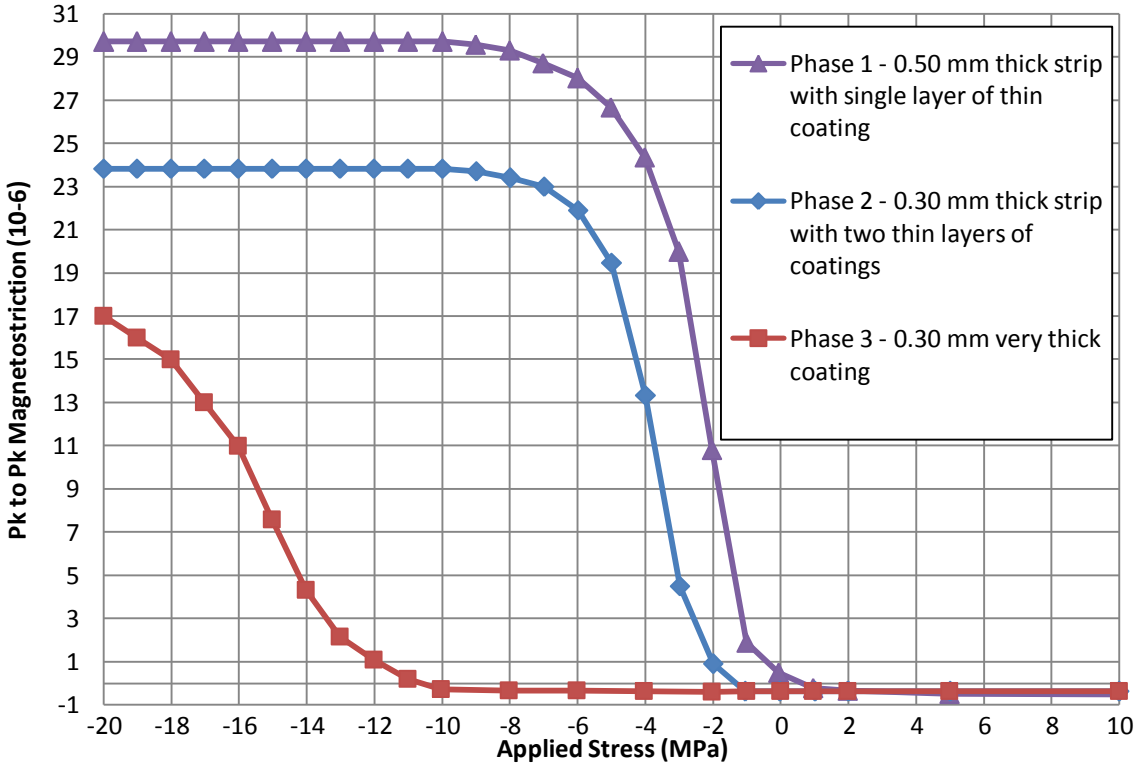

Fig 12.1 Three phases of magnetostriction stress sensitivity curve transformation under 1.7 T, 50 Hz.

It is shown that the three main parts of the curves, especially under compression are changed. Three variable parameters A, B and C representing the changed sections of the curve were chosen to describe the horizontal and vertical shifts and the slope of stress sensitivity curve as shown in Fig 12.2.

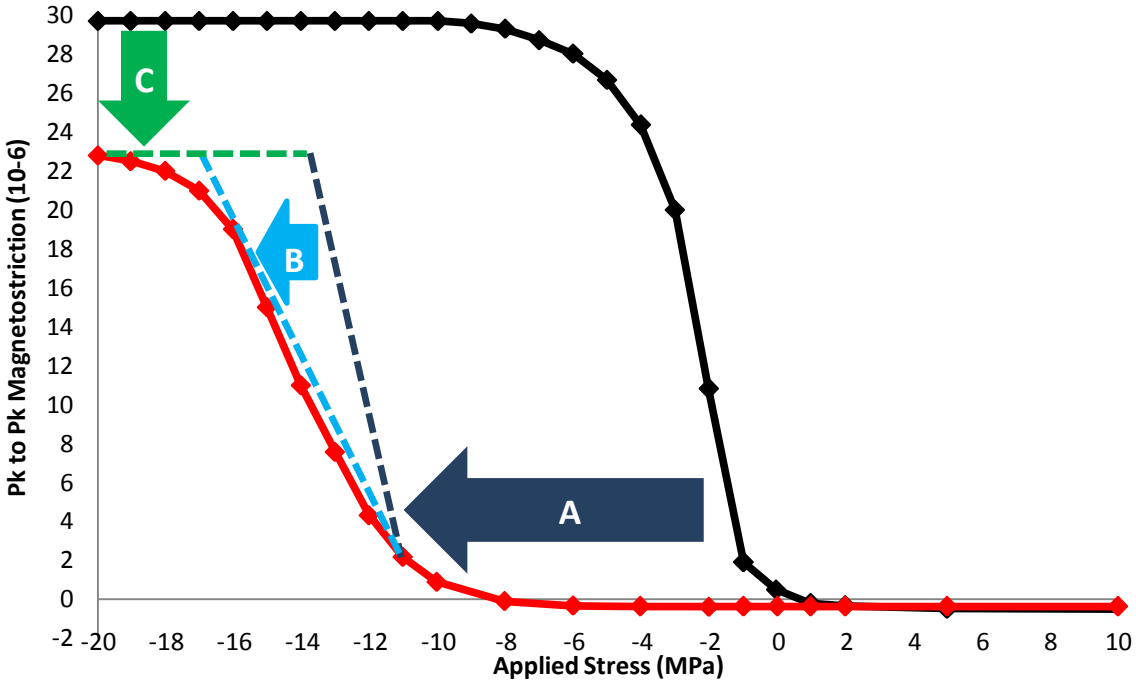

Fig 12.2 Horizontal and vertical shifts with change in a slope of magnetostriction under stress curves described by parameters A, B and C.

The parameter A characterises a shift in the rapid increase in magnetostriction and parameters B and C define changes in the slope of the curve and level of magnetostriction saturation, respectively. Each presented variable can be controlled by one or more factors as shown in Table 12.1.

Table 12.1 Selected factors affecting parameters A, B and C

Parameter	**Factor**		
A	Strip thickness	Coating thickness	Cutting stress
B	Strip thickness	-	-
C	Strip thickness	-	-

12.2 Prediction Model of Magnetostriction under Stress

The magnetostriction stress sensitivity curve can be modelled using the Boltzmann function [1]. This model was modified to fit parameters A, B and C (Fig 12.2) and can be expressed by

$$y = \frac{C}{1 + e^{\frac{(x_\sigma - A)}{B}}} - y_0 \qquad (12.1)$$

where,

y - Magnetostriction (µstrain)

C – Parameter describing magnetostriction saturation (µstrain)

x_σ - Applied stress in the range of ±10 MPa

A - Parameter describing value of applied stress, where magnetostriction is characterised with approximately middle value of saturation (MPa)

B - Parameter describing standard deviation of the stress which determines the smoothness of the magnetostriction stress sensitivity curve

y_0 – Magnetostriction offset (µstrain)

To plot the initial curve of magnetostriction stress sensitivity the prediction model requires fitting parameters A, B and C to the magnetostriction curve measured under applied stress as shown in Fig 12.3.

The prediction model was fitted to the measurement data with the following assumptions were made:

a) Strips with very thick coatings could only be tested up to -10 MPa compression which made it impossible to obtain the magnetostriction saturation level. Therefore in the model the saturation level was set to be unchanged under increasing coating thickness.
b) The model is valid only in the range of flux densities between 1.5 T to 1.7 T which was limited by the measurement data.

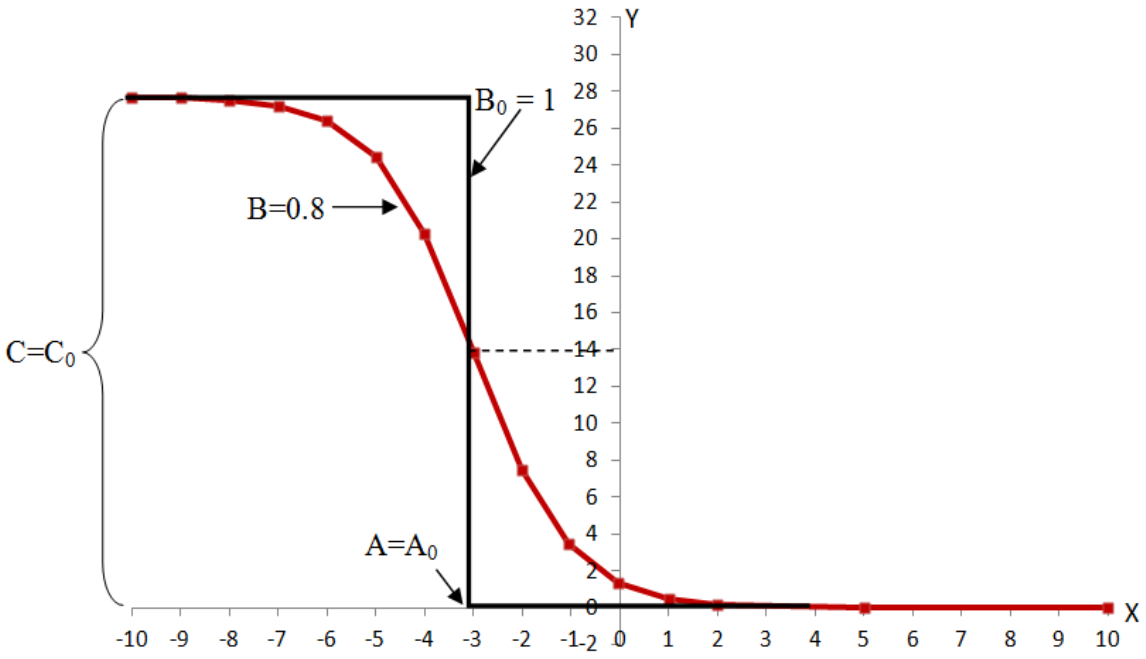

Fig 12.3 Boltzmann function used to model magnetostriction sensitivity curve.

Parameters A, B and C can be defined as follows:

$$A = a_0 - (a_1 * T) + (a_2 * C_T) + (a_3 * C_S) \quad (12.2)$$

$$B = b_0 - (b_1 * T) \quad (12.3)$$

$$C = c_0 + (c_1 * T) - (c_2 * C_T) \quad (12.4)$$

where,

a, b, c – Constant values required to fit the parameters to measured data

T – Strip thickness parameter

C_T – Measured coating thickness (µm)

C_S – Measured cutting stress (MPa)

Parameters C and A were defined from measurement data such as that shown in Fig 12.4. However, B, which is the slope of magnetostriction curve, must be fitted manually to the measured curve.

Strip Thickness			
Stress (MPa)	0.23 mm	0.30 mm	0.50 mm
10.0	-0.5	-0.5	-0.5
9.0	-0.5	-0.5	-0.5
8.0	-0.5	-0.5	-0.5
7.0	-0.5	-0.5	-0.5
6.0	-0.5	-0.5	-0.5
5.0	-0.5	-0.5	-0.5
4.0	-0.5	-0.5	-0.5
3.0	-0.5	-0.5	-0.5
2.0	-0.5	-0.5	-0.4
1.0	-0.4	-0.4	-0.3
0.0	-0.3	-0.1	0.3
-1.1	0.0	0.7	1.9
-2.0	0.9	2.6	5.5
-3.0	3.3	7.1	12.4
-4.0	8.0	13.9	20.0
A -5.0	13.7	19.6	24.8
-6.0	17.6	22.6	26.8
-7.0	19.4	23.7	27.5
-8.0	20.0	24.1	27.7
-9.0	20.3	24.2	27.8
C -10.0	20.3	24.2	27.8

Coating Thickness				
Stress (MPa)	4 g/m^2	12 g/m^2	18 g/m^2	24 g/m^2
10.0	-0.5	-0.5	-0.5	-0.5
9.0	-0.5	-0.5	-0.5	-0.5
8.0	-0.5	-0.5	-0.5	-0.5
7.0	-0.5	-0.5	-0.5	-0.5
6.0	-0.5	-0.5	-0.5	-0.5
5.0	-0.5	-0.5	-0.5	-0.5
4.0	-0.5	-0.5	-0.5	-0.5
3.0	-0.5	-0.5	-0.5	-0.5
2.0	-0.5	-0.5	-0.5	-0.5
1.0	-0.4	-0.5	-0.5	-0.5
0.0	-0.1	-0.5	-0.5	-0.5
-1.1	0.7	-0.4	-0.5	-0.5
-2.0	2.6	-0.3	-0.5	-0.5
-3.0	7.1	0.0	-0.4	-0.5
-4.0	13.9	1.1	-0.3	-0.5
-5.0	19.6	3.9	0.0	-0.4
-6.0	22.6	9.4	1.1	-0.3
-7.0	23.7	16.2	3.9	0.1
-8.0	24.1	20.9	9.5	1.2
-9.0	24.2	23.0	16.3	4.0
-10.0	24.2	23.8	20.9	9.6

Cutting Stress				
Stress (MPa)	"-8 Mpa"	"-2 MPa"	"+1 MPa"	"+5 MPa"
10.0	-0.5	-0.5	-0.5	-0.5
9.0	-0.4	-0.5	-0.5	-0.5
8.0	-0.3	-0.5	-0.5	-0.5
7.0	0.0	-0.5	-0.5	-0.5
6.0	1.0	-0.5	-0.5	-0.5
5.0	3.5	-0.5	-0.5	-0.5
4.0	8.4	-0.5	-0.5	-0.5
3.0	14.2	-0.4	-0.5	-0.5
2.0	18.0	-0.2	-0.5	-0.5
1.0	19.7	0.3	-0.5	-0.5
0.0	20.3	1.9	-0.4	-0.5
-1.1	20.5	5.6	-0.1	-0.5
-2.0	20.5	10.9	0.5	-0.5
-3.0	20.6	16.0	2.3	-0.4
-4.0	20.6	18.9	6.4	-0.3
-5.0	20.6	20.0	12.2	0.3
-6.0	20.6	20.4	16.9	1.7
-7.0	20.6	20.5	19.2	5.1
-8.0	20.6	20.5	20.1	10.7
-9.0	20.6	20.6	20.4	15.9
-10.0	20.6	20.6	20.5	18.8

Fig 12.4 Example of assessing parameter A (stress) and C (magnetostriction) from measurement data.

Magnetostriction measurements from strip thickness and coating thickness investigations (chapter 7 and 8) were made at 1.7 T. However the maximum flux density obtained for samples from the cutting stress investigation was 1.5 T. Fig 12.5 shows the variation of magnetostriction saturation level for a typical measured CGO strip at 1.5 T and 1.7 T.

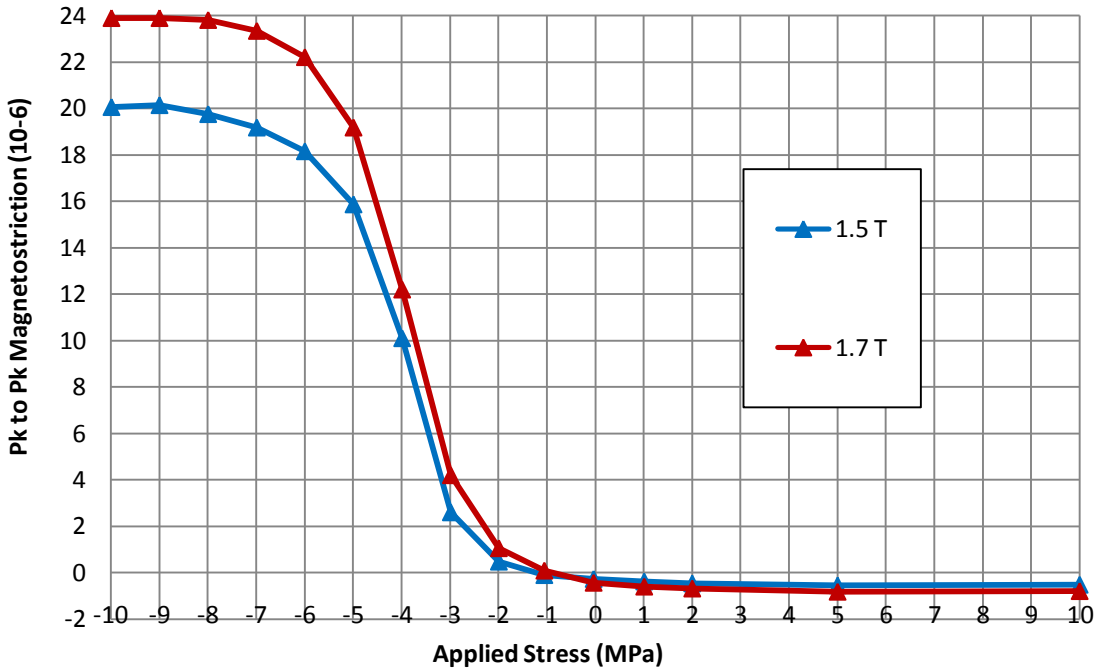

Fig 12.5 Magnetostriction stress sensitivity curve obtained under 1.5 T and 1.7T.

It shows that a variation of approximately 4 μstrain in the saturation can be obtained in this range of measured flux density (B_m). Therefore a factor $\left(\frac{B_S}{B_m}\right)$ has to be added to the parameter C, where B_S is the saturation flux density of the GO steel (2.03 T). Also the parameter "T" related to strip thickness in the calculation of maximum magnetostriction for the GO steel can be expressed as a function of $\left(\frac{1}{t^2}\right)$ where t is the strip thickness according to equation (7.7). This relation was previously described in section 7.4.

To prepare the final equations for the prediction model the parameters A, B and C have to be optimised according to eleven measured curves (based on data from Fig 12.4) and can be presented as follows:

a) Parameter A:

$$A_1 = a_0 + (a_1 * (\frac{1}{{t_1}^2})) + (a_2 * C_{T1}) + (a_3 * C_{S1})$$

$$A_2 = a_0 + (a_1 * (\frac{1}{{t_2}^2})) + (a_2 * C_{T2}) + (a_3 * C_{S2})$$

...

$$A_{11} = a_0 + (a_1 * (\frac{1}{{t_{11}}^2})) + (a_2 * C_{T11}) + (a_3 * C_{S11})$$

b) Parameter B:

$$B_1 = b_0 + (b_1 * (\frac{1}{{t_1}^2})) + (b_2 * (\frac{B_s}{B_m}))$$

$$B_2 = b_0 + (b_1 * (\frac{1}{{t_2}^2})) + (b_2 * (\frac{B_s}{B_m}))$$

...

$$B_{11} = b_0 + (b_1 * (\frac{1}{{t_{11}}^2})) + (b_2 * (\frac{B_s}{B_m}))$$

c) Parameter C:

$$C_1 = c_0 + (c_1 * (\frac{1}{{t_1}^2})) + (c_2 * (\frac{B_s}{B_m}))$$

$$C_2 = c_0 + (c_1 * (\frac{1}{{t_2}^2})) + (c_2 * (\frac{B_s}{B_m}))$$

...

$$C_{11} = c_0 + (c_1 * (\frac{1}{{t_{11}}^2})) + (c_2 * (\frac{B_s}{B_m}))$$

MATLAB software was used to obtain optimal parameters for a, b and c. An "over determined solution system" algorithm (12.5) was used to calculate a system of eleven linear equations (separately for A, B and C), where a greater number of columns (m) than rows (n) was presented in the matrix.

$$D = E_{(m \times n)} \setminus F \qquad (12.5)$$

where,

D – Column vector with n entries vector ($a_0 \ldots a_3$, $b_0 \ldots b_2$ and $c_0 \ldots c_2$)

E– (m×n) matrix

F – Column vector with m entries ($A_1 \ldots A_{11}$, $B_1 \ldots B_{11}$ and $C_1 \ldots C_{11}$)

Results of solving linear equations of A, B and C are presented in Table 12.2.

Table 12.2 Solving of linear equations for A, B and C parameters

A	**B**	**C**
$a_0 = -1.511$	$b_0 = -1.196$	$c_0 = +49.551$
$a_1 = +0.079$	$b_1 = -0.001$	$c_1 = -0.502$
$a_2 = -0.339$	$b_2 = +1.653$	$c_2 = -16.688$
$a_3 = +0.932$		

Table 12.3 shows maximum differences between measured A, B and C calculated by using the optimal parameters of a, b and c from Table 12.2.

Table 12.3 Maximum error between measured and calculated A, B and C

Parameters A, B, C	**Difference in A (%)**	**Difference in B (%)**	**Difference in C (%)**
A_1, B_1, C_1	4.0	20.4	1.4
A_2, B_2, C_2	3.9	12.2	0.5
A_3, B_3, C_3	6.1	22.4	1.1
A_4, B_4, C_4	3.9	12.2	0.5
A_5, B_5, C_5	3.6	57.1	0.5
A_6, B_6, C_6	1.1	1.8	0.5
A_7, B_7, C_7	0.3	1.8	0.5
A_8, B_8, C_8	7.3	19.2	2.1
A_9, B_9, C_9	14.3	50.0	2.1
A_{10}, B_{10}, C_{10}	6.4	4.5	2.1
A_{11}, B_{11}, C_{11}	5.1	4.5	2.1
Maximum	14.3	50	2.1

The prediction model based on equation (12.1) and Table 12.2 with three variables "t", "C_T" and "C_S" is presented in the following final equations:

$$A = -1.511 + \left(0.079 * (\frac{1}{t^2})\right) - (0.339 * C_T) + (0.932 * C_S) \quad (12.6)$$

$$B = -1.196 - \left(0.001 * (\frac{1}{t^2})\right) + \left(1.653 * \left(\frac{B_S}{B_m}\right)\right) \quad (12.7)$$

$$C = 49.551 - \left(0.502 * (\frac{1}{t^2})\right) - \left(16.688 * (\frac{B_S}{B_m})\right) \quad (12.8)$$

Measured and calculated (based on measurements and predicted) magnetostriction stress sensitivity curves with an extended scale for compressive stress up to -15 MPa are presented in Fig 12.6:

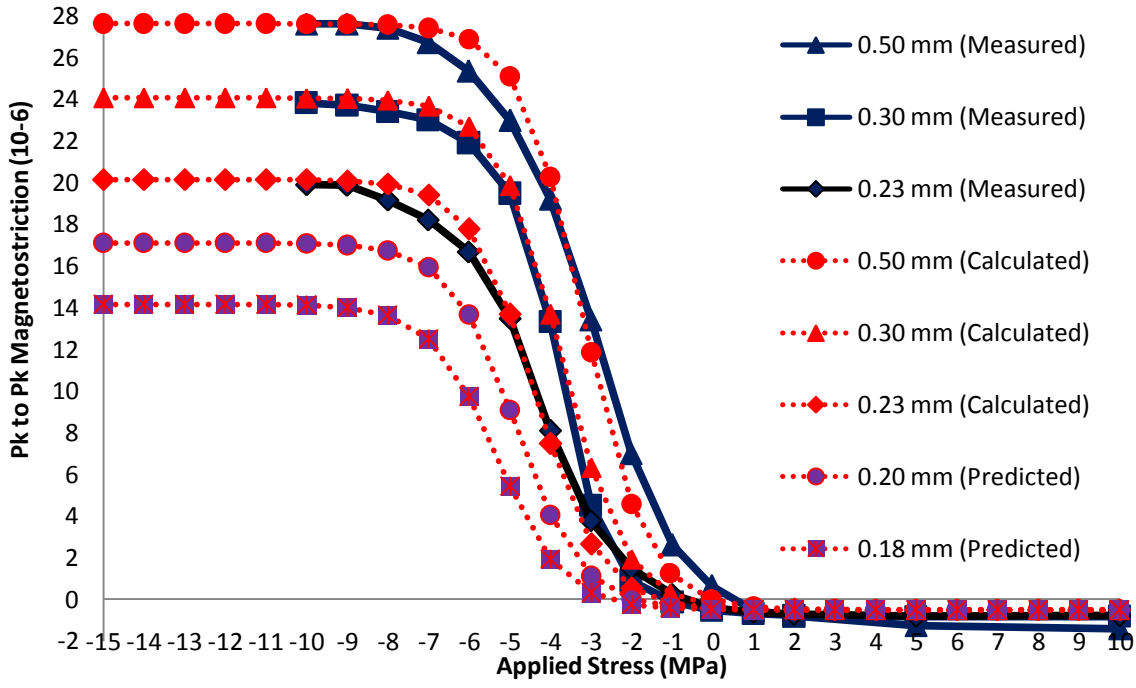

a) Prediction of strip thickness

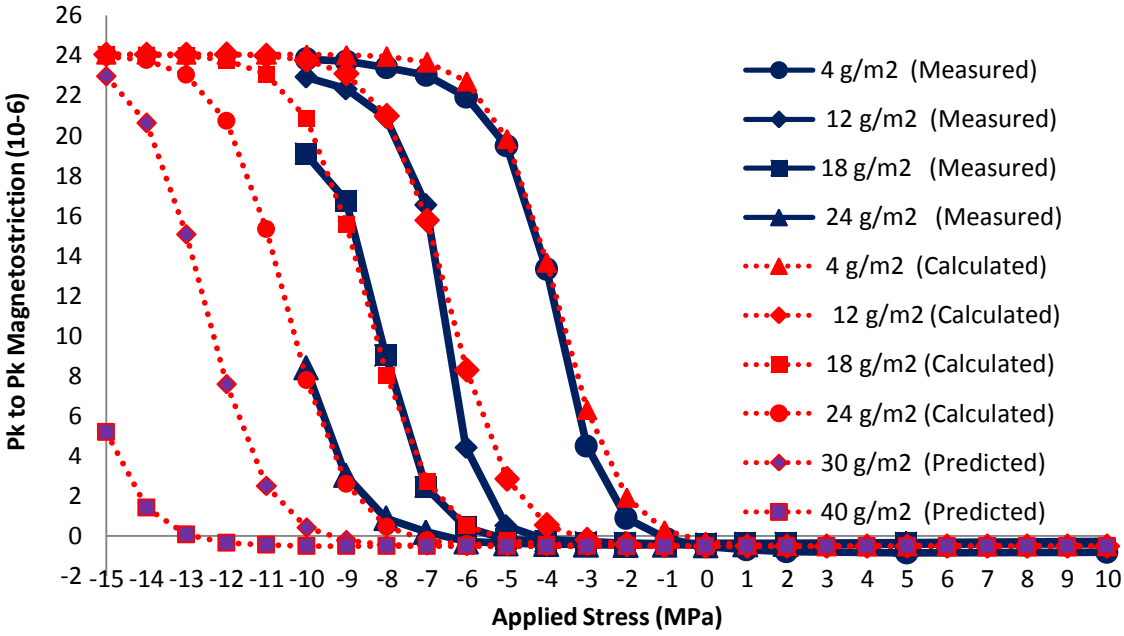

b) Prediction of coating stress

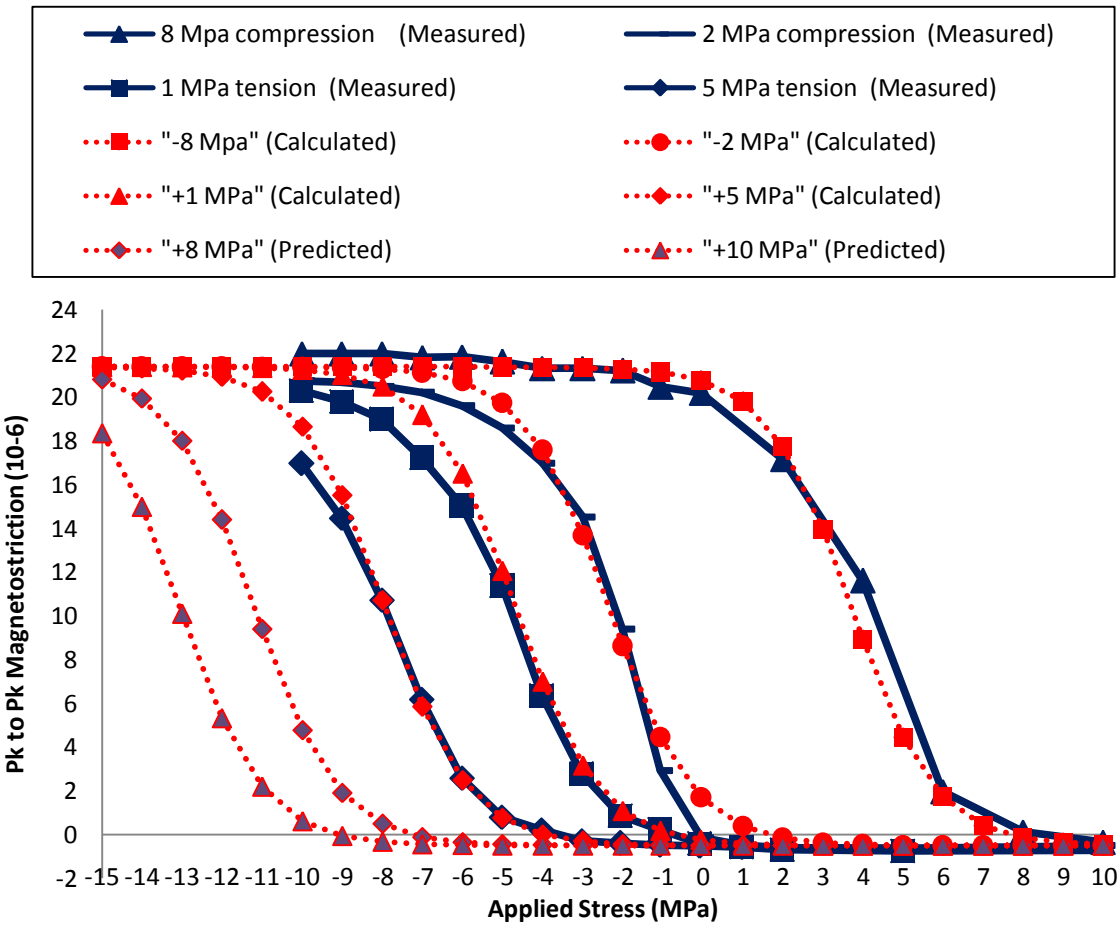

c) Prediction of cutting stress

Fig 12.6 Measured and calculated stress sensitivity curves for predicted strip thickness (a), coating thickness (b) and cutting stress (c).

The correlation coefficient between the measured and calculated parameters A, B and C were obtained as, 1.00, 0.57 and 0.99 respectively. Moreover physical expressions for parameters A, B and C were also considered in order to eliminate fitting of the model to the measurement data:

The parameter A can be correlated to any external applied stress to the GO steel which causes a horizontal stress shift of the magnetostriction sensitivity curve. Creation of a numerical stress table for a wide range of coatings and also cutting techniques would enable the value for parameter A to be defined.

The parameter B would be affected by the misorientation of the GO steel. Fig 12.7 shows that typical CGO steel has lower change of slope than HiB. However due to unavailability of samples with a range of average misorientation while maintaining the values of other variables it has not been possible to investigate the correlation between misorientation and parameter B. Further investigation to define the influence of material parameters on the slope of the magnetostriction stress sensitivity curve of the CGO and HiB material could be carried out on laboratory produced samples.

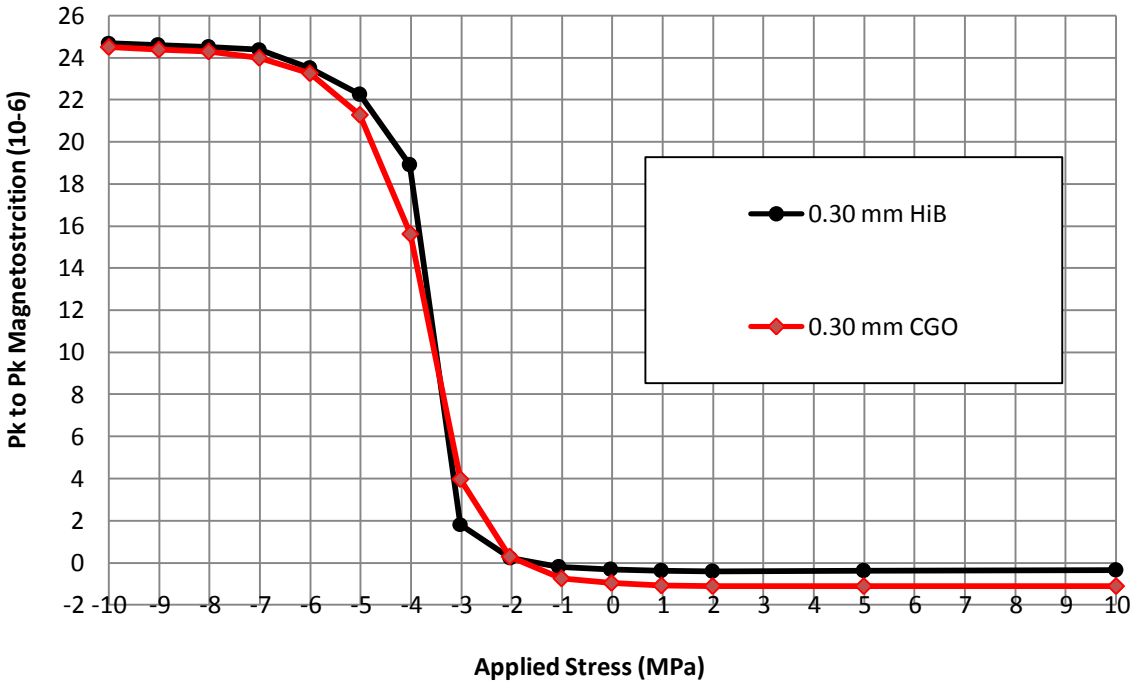

Fig 12.7 Magnetostriction stress sensitivity curves of typical CGO and HiB Epstein samples under 1.7 T, 50 Hz.

The parameter C represents the magnetostriction saturation which, for the GO steel, can be calculated using equation (7.1).

The prediction model developed can be a very powerful quantitative tool for evaluating the influence of single or even combinations of various factors such as strip thickness, coating stress, misorientation and cutting stress on magnetostriction of GO steel. Therefore it can be used by electrical steel manufactures to further improve their product to become more efficient and environmental friendly.

12.3 References

[1] C. M. Bender and S. A. Orszag, "Advanced mathematical methods for scientists and engineers," *McGraw-Hill, New York*, 1978.

Chapter 13 Conclusions

- **Magnetostriction Measurement System**

A novel measurement system has been developed to measure magnetostriction under applied stress of ±10 MPa at flux densities of 1.5 T and 1.7 T and frequency of 50 Hz. The system has greater operating range than any other single strip system in the world, and also proven repeatability and high reliability.

It was confirmed that care with several aspects of the design including alignment, frames to restrain the sample from slight buckling and use of guides to eliminate any torsion effects, improve repeatability of magnetostriction measurements.

The uncertainties of magnetostriction in three stress regions: 5 MPa, -5 MPa and -10 MPa, were evaluated to be ±0.5%, ±5.5% and ±4.3% respectively.

The magnetostriction measured by the system agrees well with the results from calculations based on domain pattern observations giving a high degree of confidence in the measurements.

- **Strip Thickness**

Magnetostriction measurements on a range of strips under stress showed that a change in thickness caused a vertical increase in magnitude of magnetostriction vs. stress sensitivity curves. An increase in the measured magnetostriction under high compressive stress is approximately proportional to the strip thickness.

The results obtained using the magnetostriction model of stress pattern I taking into account the angle θ of the surface closure domain walls showed a good agreement with magnetostriction measurements under 10 MPa of compressive stress. The angle θ was estimated to be inversely proportional to strip thickness. Therefore it is assumed that the increase of strip thickness leads to the decrease of the magnetostatic energy and therefore a reduction in the volume of closure domains in the stress patterns.

This could have a significant bearing on future transformer designs. If magnetostriction is shown to be the most important parameter in transformer noise then by constructing cores from thinner grades of steel could reduce magnetostriction amplitude under stress.

This would have to be offset against the practicalities of building cores from thinner laminations (increased building factors) and the overall increase in cost.

- **Applied Coating Stress**

A laboratory applied coating was characterised with a similar magnetostriction and loss values to this applied on the production line.

In the case of two out of the three studied coatings (S2 and Mix36b3) it was shown that a gradual increase in coating weight resulted in an effective increase of tensile stress introduced to the surface of the GO steel which was evaluated by analysis of the stress shift of the magnetostriction curve. This was further confirmed by surface domain observations under stress. The highest tensile stress magnitude of 14 MPa was observed to be introduced by the S2 coating with an average total weight 110 g/m^2.

A purely theoretical differential thermal contraction model based on coating stress dependence on mechanical properties of the GO steel and coating material was developed. This model was proven to successfully estimate the influence of coating weight on stress introduced to steel surface in cases of samples with coating thickness up to 18 g/m^2, 19 g/m^2 and 17 g/m^2 for Mix4, Mix26b3 and S2 coatings, respectively.

- **Annealing under Tension**

The new oxidized coating with higher thickness than the forsterite coating increases tension on the steel surface. The phosphate coating applied on the new oxidized coating removes the beneficial coating tension. Although there are many practical obstacles preventing this coating technology from being implemented commercially, it gives a direction for future coatings research.

A different level of penetration depth (from 0 to 60 mm) on the thermal flattening production line does not significantly improve values of magnetostriction and loss of the steel previously coated with forsterite coating. A similar effect was observed in the laboratory environment for Epstein strips annealed under various magnitudes of applied tension.

- **Applied Cutting Stress**

An investigation of sample cutting techniques showed for the first time that the water jet cutting introduced an advantageous tensile stress along the cut edge in RD of the CGO steel. Also the high compressive stress introduced by the laser cutting performed along the TD could also have beneficial effect resulting in a low tension in the RD.

The future application of this effect could see significant improvements in stress sensitivity and therefore reduced magnetostriction and losses in transformer cores.

- **Rotational Magnetostriction**

A strip of GO steel under applied high compressive stress shows similar transverse closure domains on the polished surface to that due to DC magnetisation along the TD of the strip with no external applied stress.

Measurement of the pk-pk magnetostriction of GO steel under rotational magnetisation reaches 35 μstrain (close to $-3\lambda_{100}/2$) which is significantly higher than due to uniaxial magnetisation under high compression (approximately 24 μstrain).

This high magnetostriction under rotation should be considered when designing three phase transformers. Minimisation of the region around the T joint where rotational flux density is observed could have a large impact on the total noise of the core.

- **Magnetostriction under Stress Prediction Model**

The prediction model developed was shown to effectively evaluate the influence of various factors such as strip thickness, coating stress and cutting stress on magnetostriction of GO steel. The Boltzmann function used in the model was able to accurately describe the effect of all studied aspects being present during the production of the steel and affecting the magnetostriction sensitivity of the final material.

This model can be used by electrical steel manufacturers to evaluate the impact of future production technologies.

Chapter 14. Future Work

- **Investigations on Coated Laminations Assembled in a Core**

The future work of this study would be to assemble transformer cores using the thin and thick S2 coated laminations in order to quantify the influence of magnetostriction reduction on the vibration and noise generated by transformer.

- **Further Development of the Prediction Model**

The prediction model was used to evaluate the influence of various factors on magnetostriction of GO steel with different types of misorientation. Therefore to obtain the full picture of applicability of this model the following investigations should be carried out:

a) Investigations of strip thickness, coating stress and cutting stress on the GO steel sample with the same average misorientation in order to define the parameter B
b) Magnetostriction measurements under stress at a wider range of flux densities and frequencies in order to verify the functionality of the model for different magnetisation conditions.

- **Application of Water Jet Cutting to GOSS Laminations**

The feasibility of utilising water jet cutting in the place of slitting or other lamination cutting technologies should be investigated in collaboration with the sponsor. This is unlikely to provide a universal solution due to the additional cost but may be applicable to high performance cores.

List of Publications

International Journals

1. **P. Klimczyk**, A. Moses, P. Anderson, M. Davies, "Challenges in Magnetostriction Measurements under Stress", Przegląd Elektrotechniczny (Electrical Review), ISSN 0033-2097, R. 85 NR 1, pp. 100-102, 2009.

2. **P. Klimczyk**, S. Somkun, P. Anderson, A. Moses, "Comparison of Uniaxial and Rotational Magnetostriction of Non-oriented and Grain-oriented Electrical Steel", Przegląd Elektrotechniczny (Electrical Review), ISSN 0033-2097, R. 87, No 9b, pp. 33-36, 2011.

3. **P. Klimczyk**, A. Moses, P. Anderson, M. Davies, "Influence of Cutting Techniques on Magnetostriction Under Stress of Grain Oriented Electrical Steel", IEEE Transactions on Magnetics, Vol. 48, No. 4, pp. 1417-1420, April 2012.

4. S. Somkun, **P. Klimczyk**, A. J. Moses and P. I. Anderson, "Comparisons of AC magnetostriction of non-oriented electrical steels measured in Epstein and disc samples," Journal of Electrical Engineering, Vol 61. NO 7/s, pp. 89-92, 2010.

5. S. Somkun, A. J. Moses, P. I. Anderson and **P. Klimczyk**, "Magnetostriction anisotropy and rotational magnetostriction of a nonoriented electrical steel," IEEE Transaction on Magnetics, Vol. 46, pp. 302-305, February 2010.

International Conferences

1. **P. Klimczyk**, A. J. Moses, P. I. Anderson and M. Davies, "Effect of Strip Thickness on Magnetostriction of Grain Oriented Silicon Steel", conference digest accepted for presentation at 19th Soft Magnetic Materials Conference (SMM) in Turin, Italy 2009.

2. **P. Klimczyk**, S. Somkun, P. I. Anderson and A. J. Moses, "Comparison of Uniaxial and Rotational Magnetostriction of Non-oriented and Grain-oriented Electrical Steel" conference digest accepted for presentation at 11th International Workshop on 1&2 Dimensional Magnetic Measurement and Testing in Oita, Japan 2010.

3. **P. Klimczyk**, A. J. Moses, P. I. Anderson and M. Davies, Anderson "Influence of Cutting Techniques on Magnetostriction Under Stress of Grain Oriented Electrical Steel" conference digest accepted for presentation at 20th Soft Magnetic Materials Conference (SMM) in Kos, Greece 2011.